Development of a method for evaluation of liquefaction potential of sands based on a dynamic penetrometer

Sebastián Lòpez Retamales

École des Ponts ParisTech

THÈSE DE DOCTORAT

de l'École des Ponts ParisTech

Development of a method to evaluate the risk of liquefaction of sands from a dynamic penetrometer test

École doctorale N° 531, Sciences, Ingénierie et Environnement (SIE)

Spécialité : Géotechnique

Thèse préparée au laboratoire Navier

Soutenue le 5 Juillet 2022, par

Sebastián LÓPEZ RETAMALES

Composition du jury :

Pierre BREUL Professeur, Polytech Clermont	*Rapporteur*
Mahdia HATTAB Professeur, Université de Lorraine	*Rapporteur*
Philippe REIFFSTECK Directeur de recherche, Université Gustave Eiffel	*Examinateur*
Jean, CANOU Chercheur, École des Ponts ParisTech	*Examinateur*
Miguel, BENZ Docteur, Sol Solution	*Examinateur*
Jean-Claude DUPLA Chargé de recherche, Université Gustave Eiffel	*Directeur de thèse*

ABSTRACT

Liquefaction is currently a problem with the capacity to generate significant damage to human beings and their activities, and therefore the evaluation of this phenomenon requires attention. Currently, the liquefaction potential evaluation can be carried out through laboratory and in situ tests, but each equipment and methodology has advantages and disadvantages that may limit its use. Based on this, it is possible to state that the creation of new liquefaction potential evaluation methods is necessary. In this context, a liquefaction potential evaluation method has been proposed based on the execution of dynamic penetration tests of variable energy using a dynamic penetrometer instrumented with accelerometers and deformation sensors that allow the measurement of dynamic signals for each hammer impact. For the development of the proposed method, dynamic penetration tests have been performed on specimens of Hostun HN31 and Fontainebleau NE34 sands in a K0 calibration chamber, in addition to cyclic triaxial tests to evaluate liquefaction properties of both sands. With the results obtained from the tests performed, it is possible to conclude that the proposed method is capable of evaluating the liquefaction properties of the sands.

RESUME

La liquéfaction est un phénomène qui peut engendrer des dommages importants pour les êtres humains et leurs activités, et l'évaluation de ce phénomène nécessite donc une attention particulière. Actuellement, l'évaluation du potentiel de liquéfaction peut être réalisée à partir d’essais en laboratoire ou in situ, mais chaque équipement et méthodologie présente des avantages et des inconvénients qui peuvent limiter leur utilisation. Sur cette base, le développement de nouvelles méthodes d'évaluation du potentiel de liquéfaction est nécessaire. Dans ce contexte, une méthode d'évaluation du potentiel de liquéfaction, basée sur la réalisation d'essais de pénétration dynamique à énergie variable, à l'aide d'un pénétromètre dynamique instrumenté d'accéléromètres et de capteurs de déformation permettant la mesure de signaux dynamiques pour chaque impact de marteau, a été proposée. Pour le développement de la méthode proposée, des essais de pénétration dynamique ont été réalisés sur des massifs de sables d’Hostun (HN31) et de Fontainebleau (NE34) dans une chambre d'étalonnage K0. Des essais triaxiaux cycliques pour évaluer les propriétés de liquéfaction des deux sables ont également été réalisés. Avec l’ensemble des résultats obtenus, on peut conclure que la méthode proposée permet d'évaluer les propriétés de liquéfaction des sables.

ACKNOWLEDGEMENTS

Este trabajo fue realizado en el laboratorio NAVIER de la Ecole des Ponts ParisTech en conjunto con la Empresa Sol-Solution en el marco del proyecto FUI-EMERG3R. Me gustaría expresar mi gratitud por la confianza depositada en mí y tu apoyo en este trabajo.

Quisiera agradecer a todas las personas que me apoyaron durante la realización de esta investigación y confiaron en que esto podía ser posible. En primer lugar, debo agradecer a mi familia: A mi esposa Camila y a mis hijos Sebastián y Santiago, quienes llegaron a mi vida entregándome amor y fueron pacientes y comprensivos siempre y sin condiciones, esto es también para ustedes. También quiero agradecer a mi padre Hugo y a mi madre Cristina, quienes desde siempre han estado conmigo y me han apoyado en cada sueño y cada meta propuesta, siempre y sin condiciones. Tampoco puedo olvidar mencionar a mis hermanos y familiares cercanos que siempre estuvieron conmigo con una palabra de aliento y soporte, muchas gracias a ustedes, Juan José, Patricia, Fabian y Hugo.

Debo también agradecer a quienes me confiaron este proyecto de investigación: Jean Canou y Jean-Claude Dupla de la Ecole des Ponts ParisTech y a Miguel Benz Navarrete, de la empresa Sol-Solution. Siempre estuvieron disponibles ante cualquier duda o necesidad del proyecto y solo puedo decir gracias.

Gracias al equipo de la empresa Sol-Solution y a su directora Anne Sophie Veret por la confianza depositada en mi y al equipo técnico del laboratorio Navier de la Ecole des Ponts ParisTech. Sin ustedes nada hubiera sido posible. Su ayuda fue un punto importante en el desarrollo de la investigación y la consecución de los objetivos planteados

Finalmente, un agradecimiento al jurado revisor de la investigación, quienes con sus conocimientos fueron capaces de ser justos y respetuosos con mi trabajo y aportar en que este fuera mejor.

Muchas gracias a todos.

NOTATIONS

a	ground acceleration
a_{max}	max ground acceleration
A_r	rod cross section
A_t	cone cross section
B	Skempthon's B value
CRR	cyclic resistance ratio
CSR	cyclic stress ratio
$CRR_{7.5;1atm}$	normalized cyclic resistance ratio
$CSR_{7.5;1atm}$	normalized cyclic stress ratio
CPT	cone penetration test
C_U	uniformity coefficient
C_c	curvature coefficient
C_{p3}	penetration resistance normalization factor
C_{kd}	dynamic modulus normalization factor
D_{50}	mean grain size
c_r	wave velocity at rod
D_r	relative density
DCP	dynamic cone penetrometer
e	void ratio
e_{max}	maximum void ratio
e_{min}	minimum void ratio
e_c	post consolidation void ratio
E_{p3}^d	unloading secant elastic modulus
E_{p3}^r	reloading secant modulus
E_k	kinetic energy
E_p	potential energy
E_{pd}	maximum deformation potential energy
E_{pds}	potential elastic deformation energy of the system
E_{pes}	restitutive elastic potential energy of the soil
E_{nc}	non conservative energies
E_h	dynamic driving energy
E_{kd}	dynamic modulus
$E_{kd\ (min)}$	minimum dynamic modulus
$E_{kd\ (max)}$	maximum dynamic modulus
E_{kdN}	normalized dynamic modulus
E_r	elastic modulus of rod
$EPWP$	excess pore water pressure
F	force
F_d	dynamic penetration force
FS_{liq}	liquefaction safety factor
γ	total soil specific weight
γ_d	soil dry specific weight
γ_w	water specific weight
I_c	CPT soil behavior index
I_D	density index
k_σ	overburden correction factor
k_α	sloping ground correction factor
k_d	dynamic stiffness
k_M	Mindlin coefficient
l_r	rod length
M_w	seismic magnitude
MSF	magnitude scaling factor
M	hammer mass
n	porosity

$(N_1)_{60}$	corrected SPT number of blows
N_{cyc}	number of cycles
N_{crit}	critic number of cycles
ν	Poisson's coefficient
$PANDA$	*pénétromètre autonome numérique dynamique assisté par ordinateur*
P_a	atmospheric pressure
ϕ'	effective friction angle
q_c	CPT cone penetration resistance
q_{c1N}	normalized CPT penetration resistance
q_{dyn}	dynamics resistance component
q_d	tip penetration resistance
q_{dN}	normalized tip penetration resistance
q_s	pseudo-static penetration resistance
Δq_{cyc}	cyclic deviator amplitude
r_d	reduction factor
SPT	standard penetration test
t	time
σ'_{v0}	vertical effective stress
σ'_c	effective consolidation stress
u	pore water pressure
UCA	central data acquisition unit
V_v	volume of voids
V_S	shear wave velocities
W_{nc}	total work done by non-conservative forces
Z_r	rod mechanical impedance
Z_t	cone mechanical impedance

TABLE OF CONTENT

GENERAL INTRODUCTION 14
1 BIBLIOGRAPHIC ELEMENTS 17
1.1 General concept and definitions 19
1.1.1 Physical characteristics of sands 19
1.1.2 Multiphase interaction of granular soils 21
1.1.3 Stresses and strains in soil masses 22
1.1.4 Stress paths 23
1.1.5 Contractancy and dilatancy in soils 27
1.1.6 Critical state and steady state 29
1.1.7 Characteristic state or transformation line 31
1.2 Behavior under cyclic loading 32
1.2.1 Behavior observed upon undrained conditions 35
1.2.2 Behavior observed seismic loading 36
1.2.3 Cyclic mobility 38
1.2.4 Cyclic liquefaction 39
1.3 Soil liquefaction analysis 41
1.3.1 Liquefaction Potential Evaluation 41
1.3.2 Overburden correction factor 46
1.3.3 Sloping ground correction factor k_α 47
1.3.4 Cyclic resistance ratio CRR 48
1.3.5 In-situ CRR evaluation 50
1.3.6 Liquefaction potential evaluation with a light dynamic variable energy penetrometer 61
1.4 Conclusions 69
2 EXPERIMENTAL SETUP AND TEST PROCEDURES 71
2.1 Tested sands characterization 71
2.1.1 Hostun sand (HN31) 71
2.1.2 Fontainebleau NE34 sand 72
2.2 Lightweight dynamic variable energy penetrometer 72
2.2.1 Operating principle 74
2.2.2 Data acquisition and processing 75
2.2.3 Rod friction analysis 75
2.2.4 Wave reconstruction at the cone-soil interface 77
2.3 Analysis of dynamic variable energy penetrometer results 89
2.3.1 Determination of the dynamic driving energy 89
2.3.2 Dynamic penetration resistance determination 92
2.3.3 Elastic response of soil 96

2.3.4 Polar shock method 98
2.3.5 Analysis of soil response in the frequency domain 101
2.4 k_0 Calibration chamber 103
2.4.1 Description and operating principle 103
2.5 Experimental procedure 107
2.5.1 Specimen reconstitution 107
2.5.2 Specimen saturation 109
2.5.3 Dynamic Penetration Test 110
2.6 Conclusions 112
3 VARIABLE ENERGY DYNAMIC PENETRATION TESTS IN A CALIBRATION CHAMBER 114
3.1 Presentation and analysis of dynamic penetration test results in the calibration chamber 114
3.1.1 Experimental program 114
3.1.2 Typical dynamic penetration test results 116
3.1.3 Repeatability of dynamic stress-strain paths 123
3.1.4 Penetration velocity effects 126
3.1.5 Penetration energy 130
3.1.6 Typical results obtained on dry test study 137
3.1.7 Typical results obtained for saturated sand 143
3.2 Dynamic penetration resistance 145
3.2.1 Vertical effective stress influence 148
3.2.2 Influence of density index on dynamic penetration resistance 150
3.2.3 Influence of sand type on results obtained 152
3.2.4 Penetration resistance normalization 155
3.2.5 Dynamic module E_{kd} 157
3.3 Other parameters analyzed 172
3.3.1 Elastic modulus E_{p3}^{d} 173
3.4 Conclusions on dynamic variable energy penetration tests 174
4 LIQUEFACTION PROPERTIES OF THE TESTED SANDS 177
4.1 Cyclic triaxial equipment 177
4.1.1 Experimental procedure 178
4.2 Undrained behavior of saturated sands under cyclic shearing 183
4.2.1 Experimental program 183
4.2.2 Typical cyclic triaxial test results 183
4.2.3 Parametric study 190
4.2.4 Cyclic resistance curves 195
4.2.5 Conclusion 197

5 PREPOSITION OF A METHOD FOr THE EVALUATION OF LIQUEFACTION POTENTIAL OF SANDS 198
5.1 Soil type characterization 200
5.1.1 Soil Type definition 200
5.1.2 Soil Type Identification 202
5.1.3 Density index determination 203
5.2 Dynamic penetration test result database 204
5.2.1 Dynamic signal database 204
5.2.2 $q_{dN} - CRR$ parameter data base 205
5.3 Liquefaction potential evaluation method 208
5.3.1 Dynamic penetration test 209
5.3.2 Establish in situ stress conditions (σ_{v0} and σ'_{v0}) 210
5.3.3 Parameter normalization 210
5.3.4 Soil type identification 210
5.3.5 Cyclic resistance $CRR_{7.5;1atm}$ determination 211
5.3.6 Liquefaction Safety Factor calculation 214
5.4 Example of cyclic resistance evaluation 214
5.5 Conclusions 217
6 GENERAL CONCLUSION AND PERSPECTIVES 218
7 BIBLIOGRAPHY 222

GENERAL INTRODUCTION

The liquefaction phenomenon is described as a soil failure in which there is a loss of shear strength, losing its structure and being able to behave as a fluid. It has been established that this loss of shear strength is related to an increase in the cumulative excess pore water pressure (EPWP) produced by the application of successive cyclic shear stresses such as those produced during an earthquake. The occurrence of this phenomenon produces critical failures on structures and human facilities, such as those reported in the 1964 Niigata earthquake in Japan, in which residential buildings collapsed, or in the 2012 Christchurch earthquake in New Zealand, where damage to structures and urban infrastructure was reported.

Although the occurrence of liquefaction was reported earlier, the evaluation of the potential for liquefaction began in the 1960s after the Niigata earthquake in Japan in 1964. Based on the observations obtained from this earthquake and others reported in the literature, the first in situ liquefaction potential evaluation methodology was initiated through the application of Standard Penetration Tests SPT. This assessment methodology became the starting point and precursor of other methods based on in-situ testing with other equipment such as the Cone Penetration Test CPT. Since then other evaluation methods have been developed using techniques such as V_s shear wave analysis and extension to other penetrometers by correlations such as the Becker penetrometer or the Dynamic Cone Penetration test DCP.

Currently, the methods for evaluating liquefaction potential are based on the use of historical data from tests carried out in places where liquefaction has or has not occurred and through a process of probabilistic analysis, a relationship is established that establishes equations relating the cyclic resistance ratio and a parameter associated with the test carried out. In the case of penetrometers, the main parameter is the penetration resistance.

Currently, liquefaction properties of soils are evaluated both in the laboratory and in situ. In the case of the laboratory, the most usual tests are the cyclic single shear and cyclic triaxial equipment. In both cases the results allow establishing relationships between the cyclic resistance ratio and a number of shear cycles necessary to cause the liquefaction phenomenon. In the case of in situ testing, the three most common methodologies currently in use are based on the execution of Standard Penetration Tests SPT, Cone Penetration Tests CPT and shear wave analysis V_s. Although the currently available methods for the evaluation of liquefaction potential are still in use, they present advantages and disadvantages, which must be evaluated according to each case of application, this, together with the persistence of the liquefaction problem, justifies the creation of new methods for evaluation of liquefaction properties of soils.

Since the 1990s, a new dynamic variable energy penetrometer has been developed in France. Since the first version, the equipment based its analysis on the measurement of waves produced by the impact of a hammer on the penetrometer head, and from these to evaluate the energy for each impact and apply a dynamic driving equation. The current version of this penetrometer (PANDA3®) bases the analysis of the soil response on a method of decoupling and reconstruction of waves at the soil-soil interface. This advance has allowed the establishment of a framework that allows a multiparametric analysis of the soil subjected to cone penetration. Using this technology, a new methodology for the evaluation of liquefaction potential is proposed in this research.

In this manuscript the results of this research are presented in 5 main chapters. *Chapter 1* presents the most important bibliographical elements required for the understanding of the problem and the proposal of a method for the analysis of the soil response to cone penetration. *Chapter 2* presents the main aspects of the variable energy dynamic penetrometer used in the research, the modified K_0 calibration chamber used for the reconstitution of sand specimens, as well as the procedures carried out for the execution of the dynamic penetration tests. *Chapter 3* presents the results of the analysis of the dynamic penetration test results on Hostun HN31 and Fontainebleau NE34 sand specimens. *Chapter 4* presents the results of cyclic triaxial tests carried out to establish the liquefaction properties of the sands studied in this research. *Chapter 5* presents the proposed liquefaction potential evaluation method and a procedure for identifying the type of soil penetrated by the cone based on a multiparametric approach. Finally, the main conclusions and perspectives associated with the objectives of this research are presented.

1 BIBLIOGRAPHIC ELEMENTS

Historically, the concept of liquefaction has been used to describe a group of soil behavior phenomena in which there is a loss of critical shear strength and the generation of excess pore water pressure (EPWP) due to the presence of an external static or dynamic stress, these effects on human activities are usually catastrophic and lead to both material and human losses. This is why an analysis that allows predicting its occurrence is important.

Some of the most commonly damages associated with soil liquefaction phenomena are associated with damage or loss of critical infrastructure such as: road infrastructure, buildings, port facilities and even basic service systems such as potable water or sewage disposal, among others. In Figure 1-1 are some examples of damage caused by the occurrence of soil liquefaction phenomena.

The problem of soil liquefaction has been extensively studied since the 60's, where one of the most important works was presented by Seed and Idriss (1967). This paper presents some of the most important consequences associated with liquefaction during the 1964 Niigata (Japan) earthquake, as well as some proposals for the analysis of the phenomenon. Later Seed and Idriss (1971) presented a simplified method for the evaluation of liquefaction potential based on SPT dynamic penetration tests and the use of a database with records of tests performed at sites where liquefaction did and didn´t occur, becoming one of the starting points regarding the use of this equipment for the evaluation of cyclic resistance in the field.

Later, multiple investigations have led to the development of new methods for the evaluation of liquefaction potential by means of penetration tests such as Cone Penetration Test (CPT), Becker, Dynamic Cone Penetrometer (DCP), light dynamic penetrometer PANDA (*pénétromètre autonome numérique dynamique assisté par ordinateur*), as well as the application of shear waves measurements. (Alam, Azad, and Rahman 2008; Jara 2013; Lepetit 2002; Sebastián López et al. 2021; Robertson and Campanella 1985; Youd and Idriss 1997).

Nowadays, soil liquefaction continues to be a problem that requires attention due to the negative effects on the safety of people and human activities. Therefore, the improvement and updating of the current evaluation methods and the creation of new methods to improve the analysis of this phenomenon and avoid negative externalities continues to be necessary.

Figure 1-1 – Damage caused by soils liquefaction during earthquakes, (a) Loma Prieta 1989 (USGS 1989) **, (b) Niigata 1964** (Ishihara and Koga 1981) **and (c) Christchurch 2011** (GEONET 2022)**.**

1.1 General concept and definitions

1.1.1 Physical characteristics of sands

Soil is a mineral material composed of individual particles that are grouped together, whose response is governed by interaction mechanisms and internal and boundary conditions. The response associated with a soil is variable and its characteristic is a function of multiple factors, so its study must be performed through a multiparametric approach, trying to capture its highly anisotropic and variable behavior.

In its natural state, the soil will be composed of multiple elements whose characteristics will depend on the factors that intervened in its formation and deposition, thus the intervention of mechanical phenomena will result in the creation of granular elements from a parent rock and chemical phenomena to mostly fine elements (clays). A combination of these elements together with interstitial fluids will give rise to the composition of a three-phase material, in which the response will depend on the interaction of solid (grains), liquid (water) and gaseous (air) elements.

The three-phase interaction of the soil is associated with the triggering of internal mechanical phenomena of the soil mass, the results of which can be catastrophic for the stability of the internal structure. At this point, the engineering study of granular and fluid component characteristics allows to avoid or predict the occurrence of these phenomena, such as liquefaction.

The importance of a thorough knowledge of the physical characteristics of the grains lies in the fact that they define the overall behavior of the granular mass. Characteristics such as the size and shape of the grains, breaking strength or structural accommodation of the particles, directly influence the mechanical properties of the granular mass. An example of this is given by the angular characteristics of the contacts, where more angular particles with higher surface roughness are able to generate higher frictional resistance.

Among the most important physical characteristics to consider in the analysis of granular soils, the following can be mentioned: (a) particle size distribution, (b) mechanical properties, (c) characteristic parameters of granular soils. The knowledge of these characteristics allows predicting the response of a soil, however, it is always necessary to study the conditions in the field and the variations that may occur.

Granular soils have a characteristic composition that differentiates them from fine soils. However, granular soils also have different responses to internal and external stresses. These differences are based on the wide range of forms that the granular arrangement can adopt, where

one of the main characteristics is the size of the particles that constitute the structure, or granulometry.

Directly, particle size can affect other characteristics of the granular arrangement, such as the ratio of inter-particle spaces, fluid flow velocity, density, among others. Granular soils in general present a varied granulometry, however, sometimes the particles tend to a similar size being called uniformly graded soil and which is represented by a very steep slope of the granulometric curve, on the contrary, a soil with a variable granulometric size will be called well graded and the slope of the curve will be smoother if the granulometric curve presents an erratic shape, the soil is called open graded (Figure 1-2).

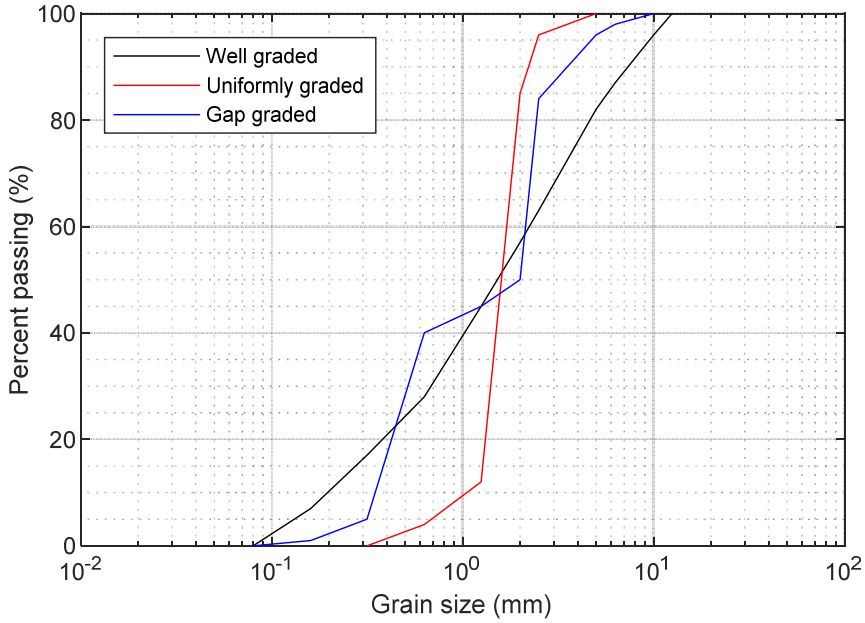

Figure 1-2- Typical particle size distribution curves

If particle size is considered, those soils with different particle sizes (well graded soil) will allow a tighter packing of the particles, since a greater number of spaces can be filled. Otherwise, a soil composed of particles of similar sizes (poorly graded soil) does not contain the right size elements that can fit into the inter-particle spaces. Note that this characteristic also directly influences the fluid drainage capacity.

From the granulometric analysis of the granular arrangement, it is possible to establish the values of uniformity coefficient C_U and coefficient of curvature C_c. The uniformity coefficient (eq. 1-1) is defined as the ratio between the diameter corresponding to 60% and 10% of the material weight passing through the sieves, where the higher the ratio, the better the gradation. The coefficient of curvature (eq. 1-2) or also called shape factor, allows to establish whether the soil is well or poorly graded.

$$C_U = \frac{D_{60}}{D_{10}} \quad \textbf{eq. 1-1}$$

$$C_c = \frac{(D_{30})^2}{D_{60} \cdot D_{10}} \quad \textbf{eq. 1-2}$$

By considering the relationships between solids and inter-particle spaces (Figure 1-3), it is possible to define parameters indicative of the level of voids in the arrangement and the degree of densification of the soil. The parameters used in this characterization are void ratio, porosity and density index. The void ratio e (eq. 1-3), is the ratio of void volume V_v and the volume of solids. It is possible to set maximum and minimum void ratio values (e_{max} and e_{min} respectively), where a lower void ratio indicates a higher density and a higher void ratio indicates a lower density. The maximum and minimum void ratio values can be used to calculate the relative density D_r of a soil or density index I_D (eq. 1-4).

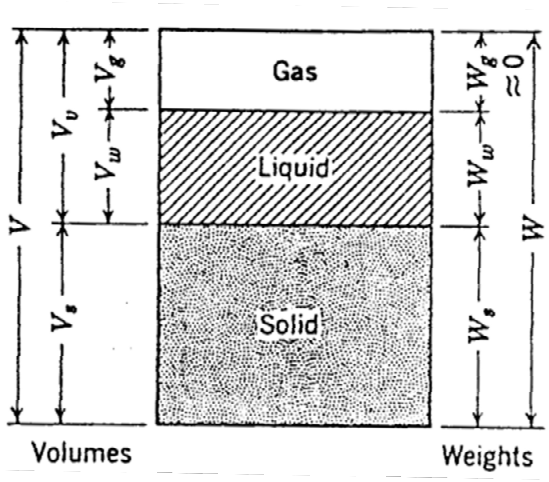

Figure 1-3 – Relationships of solid, liquid and gaseous elements in a soil mass (Lambe and Whitman 1969)**.**

$$e = \frac{V_v}{V_s} \quad \textbf{eq. 1-3}$$

$$I_D = \frac{e_{max} - e}{e_{max} - e_{min}} \quad \textbf{eq. 1-4}$$

It is also possible to define the porosity value of the soil n, establishing the relationship between the volume of voids and the total volume of the soil mass (eq. 1-5).

$$n = \frac{V_v}{V} \quad \textbf{eq. 1-5}$$

1.1.2 Multiphase interaction of granular soils

The multiphase composition of soil determines the mechanical response of the granular aggregate. The proportion of each of its components and their individual characteristics generate different responses to stresses. A soil with a higher proportion of fine (clayey) soil will

show a different behavior with respect to water content and time of application of stresses; on the other hand, the mostly granular soils show behavior more associated to the direct interaction of the grains, thus it has been defined that the resistant stress of the granular aggregate is defined by the effective stress established in the inter-particle contacts.

When considering the effective stresses developed in a granular structure, it is necessary to consider the interstitial water content and its behavior. In general, it is necessary to consider the possibility of finding dry, partially saturated and saturated granular soils. Identifying the water content present in the granular mass allows to determine the type of response that the structure will present under different loading conditions.

1.1.3 Stresses and strains in soil masses

The analysis of internal stresses in the soil mass requires the analysis of its multiphase components and their properties. A saturated soil is composed of two elements with different behaviors. On the one hand there are the solid particles capable of interacting with each other and generating frictional resistance and on the other hand the fluid whose static shear strength can be considered zero. This multiphase interaction allows the establishment of two basic concepts of soil behavior, effective and total stresses.

If the stress states of the soil mass at an arbitrary depth z are analyzed, the total stress generated by a soil mass will correspond to the total density of the soil, which corresponds to the sum of the density of each of the granular elements, as a function of the volumetric space they occupy. Then, the total stress is represented by the sum of the solid and liquid components of the mass (eq. 1-6).

$$\underline{\underline{\sigma}} = \underline{\underline{\sigma}}' - u \qquad \textbf{eq. 1-6}$$

with:

z: soil depth.
γ: total soil specific weight.
γ_d: soil dry specific weight.
γ_w: water specific weight.

If the saturated soil is in stable equilibrium and the solid particles interact with each other by means of contacts (red arrows), the fluid will exert isotropic interstitial pressures (white arrows) (Figure 1-4). The formulation representing these stresses is called effective stress (σ'_v),

acting on the soil mass and is given by the difference between the total stress and the pore water pressure (eq. 1-7).

$$\underline{\sigma}' = \underline{\sigma} - u \qquad \textbf{eq. 1-7}$$

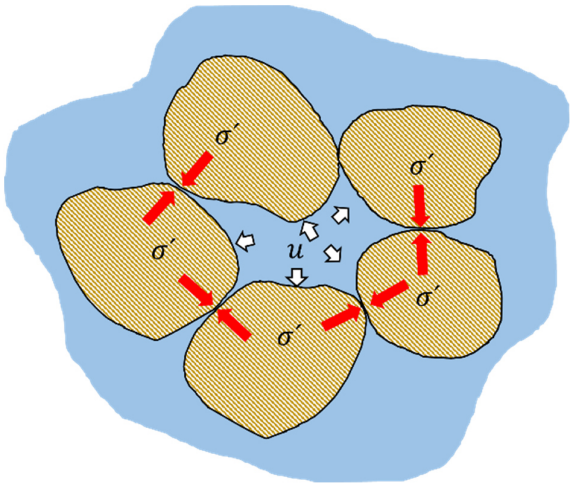

Figure 1-4 - Schematic representation of the effective stress principle.

1.1.4 Stress paths

The stress path represents the behavior of the soil under the application of loads, and allows describing some characteristics of the soil response. The paths can be presented in stress planes, where the most usual ones are the Lambe plane (τ, σ, σ') and Cambridge plane (q, p, p'). From this it is possible to construct Mohr circles, considering the relationship between the major and minor principal stress (Figure 1-5a).

In a drained triaxial test, when successive tests are performed considering higher confining pressures, the deviator stresses will be higher and therefore the circle will have a larger diameter (Figure 1-5b). Then, it is possible to visualize the results of the triaxial tests for different confining pressures considering the different stress points obtained (Figure 1-5c).

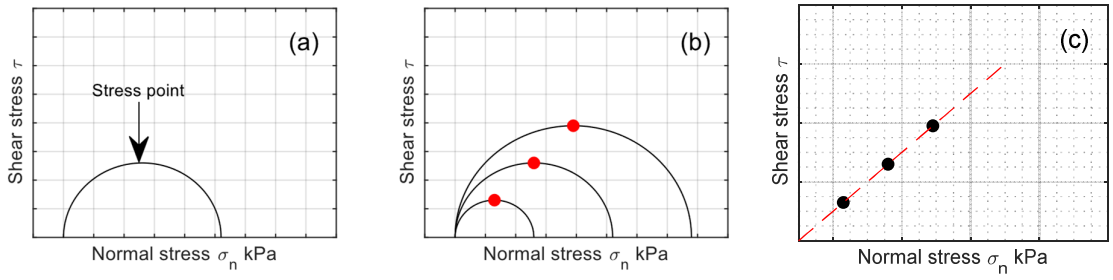

Figure 1-5 - Description of Mohr circles and stress path in the (τ, σ) Lambe plane.

The line formed by the points is called the "stress path" of a soil and is usually represented by a straight line. In clean sand the higher the number of measured points, the more the

trajectory tends to zero and to a curved shape, However, for most geotechnical problems, the linear regression of the stress points is sufficient to describe the resistant behavior of the soil and can be defined as the Mohr-Coulomb theory.

$$\tau' = \sigma'_v \tan\phi' + c' \qquad \textbf{eq. 1-8}$$

In a drained triaxial test, all the stresses will be developed at the granular contacts and the effects of interstitial fluids are neglected because the permeability is sufficient to dissipate the pore pressure. In this case the effective stress will be equal to the total stress. In the case of a triaxial test in undrained conditions, where the EPWP are not dissipated, the trajectories would vary by the development of the EPWP, which can produce phenomena such as liquefaction and cyclic mobility.

By analyzing the Peacock diagram relating volumetric variations, confining pressures and void ratio, it is possible to observe that a soil specimen subjected to a triaxial test that is in a state of post consolidation void ratio e_c and at an isotropic consolidation stress σ'_c above critical value σ'_{3cri} (stress at which the change in volumetric behavior occurs) will tend to contract (Figure 1-6). On the other hand, if the test is in undrained conditions and no volumetric variations are allowed, the pressure increase is assumed by the interstitial fluid and positive pore pressures will be generated $+\Delta u$ causing a decrease in the effective stresses.

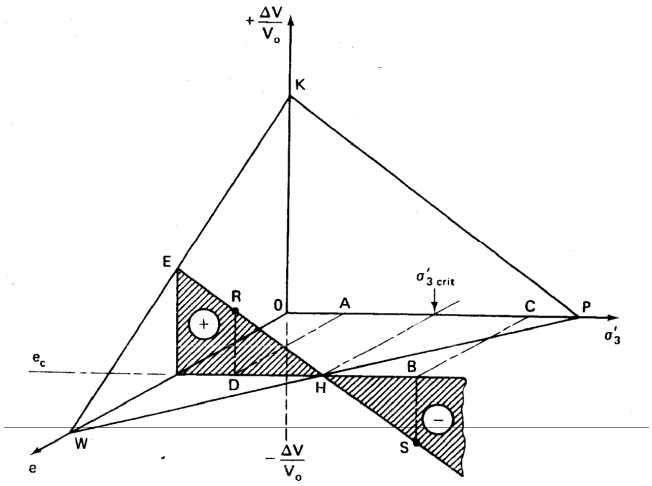

Figure 1-6 – Peacock Diagram (Holtz and Kovacs 1981)**.**

The decrease in effective stresses is easily observed in the plane (τ, σ, σ') by means of the displacement of the Mohr circle in effective stresses to the left by a magnitude of Δu (Figure 1-7).

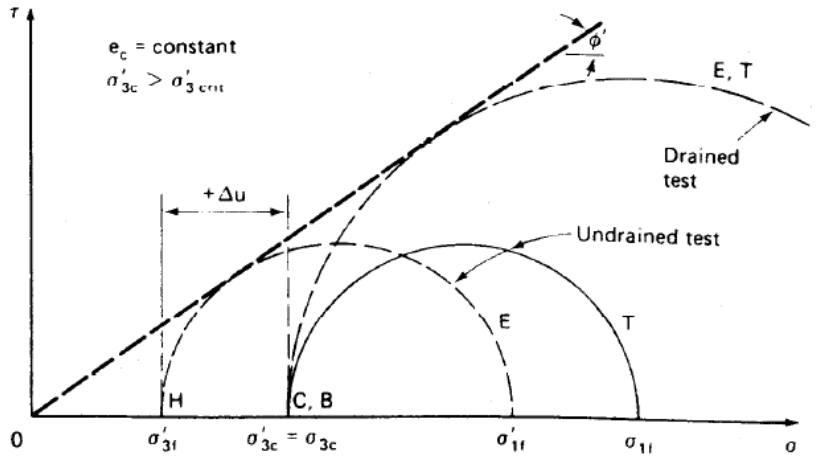

Figure 1-7 – Mohr's circles for drained and undrained triaxial tests with $+\Delta u$ (Holtz and Kovacs 1981)**.**

In the case of a soil tested with a consolidation stress less than the critical one, in the Peacock diagram (Figure 1-6) it can be observed that the soil would tend to expand and therefore generate a negative pore pressure ($\Delta u < 0$), which would generate an increase in the resistant response of the soil, shifting the Mohr circle in effective stresses to the left (Figure 1-8).

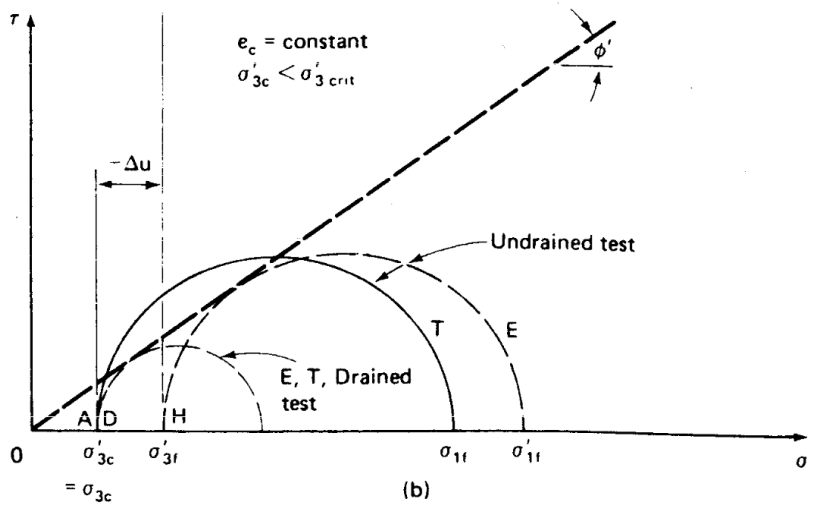

Figure 1-8– Mohr's circles for drained and undrained triaxial tests with $\Delta u < 0$ (Holtz and Kovacs 1981)**.**

Another possible case is the application of an effective consolidation stress equal to the critical pressure ($\sigma'_c = \sigma'_{3cri}$) and with a post-consolidation voids ratio (e_c) specific. Theoretically the volumetric variations will be zero and therefore the pore pressure should be zero since the deformations of the granular arrangement are already in a critical state (Figure 1-6).

The use of the Cambridge plane (q, p, p') presents advantages in the representation of the results of a triaxial test since it allows the representation of the total and effective stresses in the same diagram, showing the variation during the application of the deviator stress (Figure 1-9).

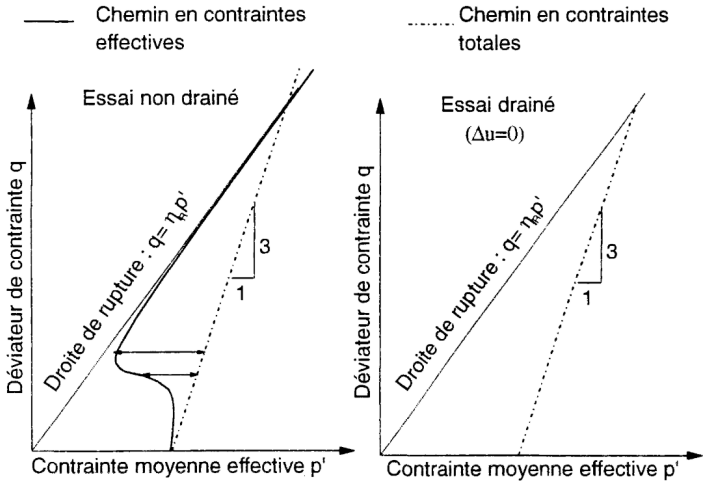

Figure 1-9 - Stress path represented in a (q, p, p') plane. (a) case of an undrained test; (b) case of a drained test (Benahmed 2001)**.**

Observing the plan (q, p') of Figure 1-9(a) (undrained test) it can be seen that the effective stress path (solid line) varies with respect to the increase in deviatoric stress and the total stress increases linearly (dashed line). The shift of the effective stress path to the left shows the reduction caused by the increase in pore pressure ($\Delta u > 0$). The decrease in effective stress (or increase in pore pressure) is maintained until reaching a point of inversion (characteristic state point) to later begin to increase the effective stress, which asymptotically approaches the rupture line.

In the case of a drained test (Figure 1-9b), the visualization of the failure point is simple since it is represented by the maximum stress deviator. However, for the undrained case failure may be difficult to identify, since it is not simple to find the point where the stresses reach the failure line represented by eq. 1-9.

$$q = \eta_R p' \qquad \textbf{eq. 1-9}$$

With:

$$\eta_R = \frac{6 \sin \phi'}{3 - \sin \phi'} \qquad \textbf{eq. 1-10}$$

For the case of triaxial test in extension, the slope of the failure line is represented by:

$$\eta_t = \frac{6 \sin \phi'}{3 + \sin \phi'} \qquad \textbf{eq. 1-11}$$

1.1.5 Contractancy and dilatancy in soils

Since soil is a material composed of a group of particles, the deformations of the granular structure depend on the behavior of the grain and its interaction with the surrounding grains and these, in turn, can be affected by other elements such as fluids that may be located in the inter-particle spaces. This is why the behavior of the granular structure of the soil must be addressed at micro, meso and macro scales.

When considering the inter-particle interaction, the deformation of the granular arrangement will be dominated by three main mechanisms: sliding and rolling, elastic deformations at contacts and grain breakage. These mechanisms of internal soil interaction, together with the boundary conditions, will define the contractant or dilatant behavior of the soil.

When considering the presence of other elements in the inter-particle spaces interacting with the grains, the soil will present variations in its behavior. In the drained case, the spaces will be occupied by air, which, although it is a fluid, the pressure generated on the grain surfaces can be neglected for most geotechnical solutions. In the case of presence of water, or saturated state, the deformation analysis becomes more complex due to the high variability of responses presented by the granular structure.

Under saturated conditions, the response of the soil will also depend on other external factors such as external loads applied, as well as their magnitude and shape. The slow application of load will allow the dissipation of water flow and the deformation can be defined as a function of the interaction between particles (allowed drainage velocity greater than the generated flow velocity), however, the rapid and/or cyclic application could generate undrained conditions (allowed drainage velocity less than the generated flow velocity), which would give greater importance to the behavior of the pore fluid in the definition of the deformation stresses in the granular arrangement.

Although it has been indicated that the deformation response of the soil depends on the granular elements and their interaction with other elements, the analysis is carried out considering the soil mass as a deformable continuum and the factors are reduced to descriptive parameters such as void ratio, "e" and water content.

A dry soil with a low initial void ratio (an initially dense soil) will present an increase of the deviatoric stress until it reaches a maximum peak and then it will decrease until it reaches the critical state. (Figure 1-10a) and volumetrically, will first tend to contract and then to expand (Figure 1-10b).

A soil with an initially high void ratio (initially loose soil) will present an increase in the deviatoric stress without reaching a peak magnitude until the critical state is reached (Figure 1-10a) and will tend to contract (Figure 1-10b).

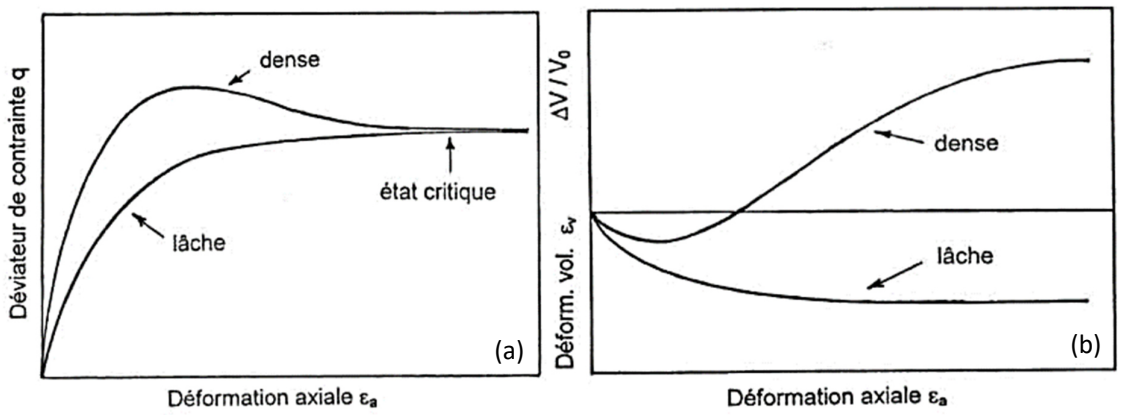

Figure 1-10 – Typical behavior observed in dry sands: (a) $p - \varepsilon_a$; (b) $\Delta V/V_0 - \varepsilon_a$ (Canou et al. 2002)**.**

When considering a perfect undrained condition where no volumetric deformations are allowed ($\varepsilon_v = 0$), the pore pressure defines the behavior of the soil mass. If an initially dense soil is subjected to a deviator stress (Figure 1-11a), the granular structure will be rearranged decreasing the interstitial spaces and generating an increase in pore pressure, however, this increase will be transitory and will lead to a decrease due to the occurrence of dilatation, by which an increase in the interstitial spaces will occur and therefore a relaxation of the pore pressure (Figure 1-11b). In the opposite case, a loose soil having a greater volume of voids will allow the initial redistribution of pore pressure, however, the decrease of interstitial spaces due to contraction will generate an increase in pore pressure (Figure 1-11b).

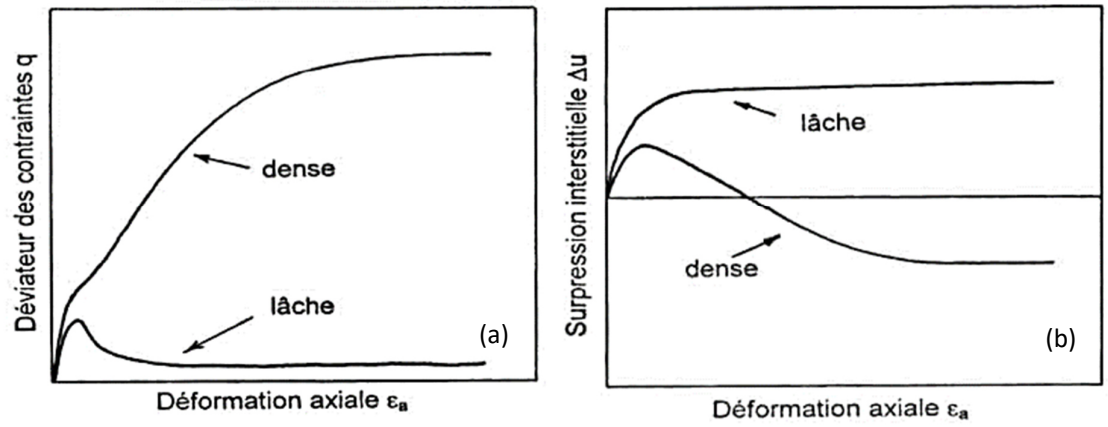

Figure 1-11 – Typical behavior observed in saturated sands: (a) $p - \varepsilon_a$; (b) $\Delta u - \varepsilon_a$ (Canou et al. 2002)**.**

When considering a perfect undrained condition where no volumetric deformations are allowed ($\varepsilon_v = 0$), the pore water pressure defines the behavior of the soil mass. If an initially dense soil is subjected to a deviator stress (Figure 1-11a), the granular structure will be rearranged decreasing the interstitial spaces and generating an increase in pore water pressure, however, this increase will be transitory and will lead to a decrease due to the occurrence of dilatancy, by which an increase in the interstitial spaces will occur and therefore a relaxation of the pore pressure. In the opposite case, a loose soil having a greater volume of voids will allow the initial redistribution of pore pressure, however, the decrease of interstitial spaces due to contraction will generate an increase in pore pressure (Figure 1-11b).

The contractant or dilatant behavior of a sandy soil is highly related to the state of the granular structure, so the density index can be used as a reference parameter to establish the possible occurrence of one of these behaviors. Another factor that must be considered in the analysis of the soil deformation behavior is the magnitude and form of application of the stresses, being necessary to establish differences between monotonic and cyclic and/or dynamic application.

1.1.6 Critical state and steady state

The terms critical state and steady state are used to describe the behavior and state of a soil when large deformations develop at a stable or constant strength. The understanding of these states has allowed the analysis of the soil against external effects such as the application of static and dynamic loads in a state of large deformations.

The establishment of a difference between steady state and critical state is currently complex, as there are arguments for and against the equivalence of these states (Kang et al. 2018). However, for practical purposes in this research, both terms can be considered indistinctly.

The steady state can be defined as the state in which the soil mass is subjected to constant deformations at constant volume, constant shear stress, constant effective normal stress and constant strain rate. One of the most important characteristics of this state is that a soil under the same initial loading conditions but at different levels of initial density (Figure 1-12a), will reach steady state at the same or approximately the same value of void ratio (Figure 1-12b). This void ratio will be unique for these conditions, however, at different initial loading conditions, the ratios will result in a unique steady state line for the soil (Figure 1-13)

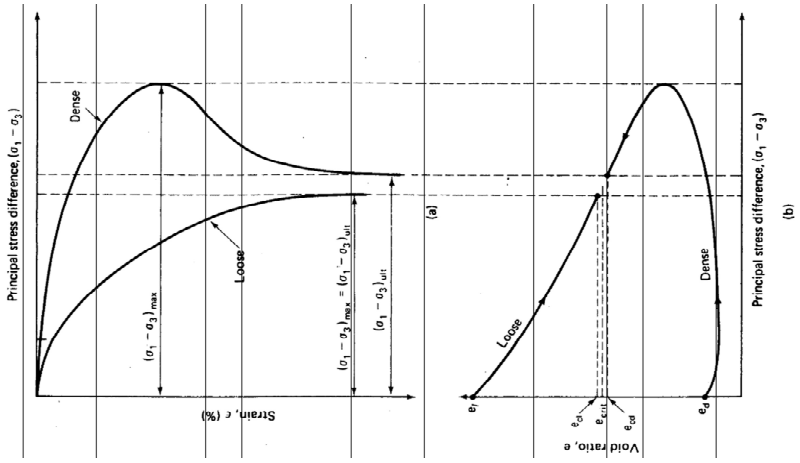

Figure 1-12 – Typical triaxial test results for loose and dense sands. (a) Stress-strain curves (b) changes in void ratio (Holtz and Kovacs 1981)**.**

Figure 1-13 an example of a steady state line is shown. An initially loose soil (point A), when subjected to shear stress will show an increase in strength and a decrease in void ratio (e) as a product of the contractancy of the material until reaching point C on the steady state line. On the other hand, if the soil is initially dense (point B), and is subjected to a shear stress it will present an increase in its resistance until reaching a maximum value (Figure 1-12a) and a decrease of the void ratio due to an initial contractancy, which will be followed by a dilatancy that will increase the value of the void ratio until reaching the same point C on the steady state line.

By analyzing the contractant and dilatant response of the soil by means of the steady state line, it is possible to subdivide the space $(p' - e)$ in two subspaces. A space below the SSL where the soil response will be mostly dilatant and a subspace above the SSL where the soil response will be characterized by a contractive behavior.

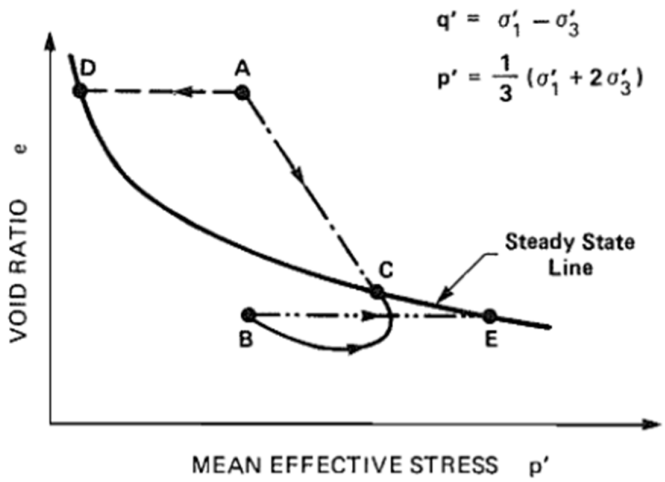

Figure 1-13 – Example of a typical steady-state line in $(p' - e)$ space (Sladen et al. 1985)**.**

1.1.7 Characteristic state or transformation line

When performing a drained triaxial test on dense sands, considering different initial consolidation stress, it is observed that the specimen begins to deform volumetrically describing a contractancy until reaching a point of maximum deformation in which a volumetric behavior of dilatancy begins (Figure 1-14). The point where this change in behavior occurs is called the characteristic state point (Ishihara, Tatsuoka, and Yasuda 1975; Luong 1978, 1980)

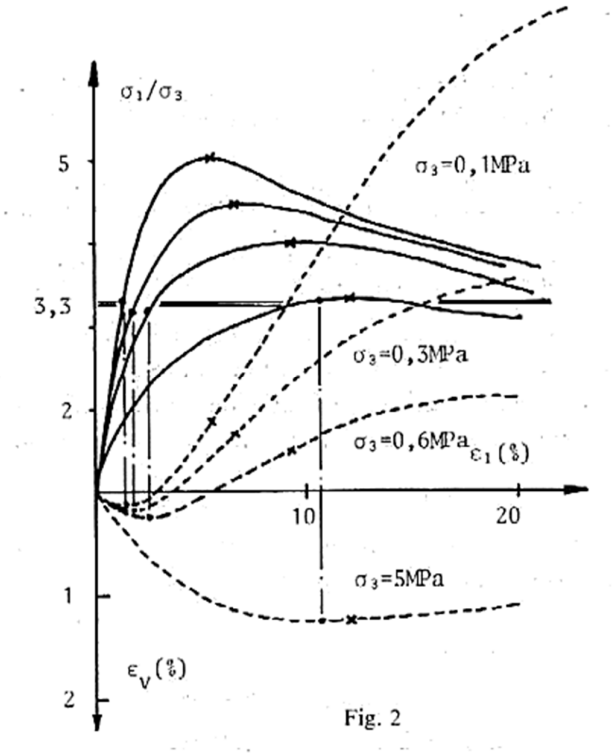

Figure 1-14 – Typical volumetric stress and strain paths of triaxial tests (Luong 1978)**.**

If the stress states associated with the characteristic state points of the specimens are plotted in the $(p' - q')$ stress plane, the characteristic line is obtained, which starts at the origin of the coordinates and is characterized by an inclination that describes an angle of inclination called characteristic angle and is located below the Mohr-Coulomb failure line of the soil (Figure 1-15).

The characteristic state line divides the stress space into three subspaces associated with the type of volumetric deformation reached. Between the two characteristic lines LC (compression and extension), and two other dilating subspaces in compression and extension, above and below the characteristic lines respectively (Figure 1-15).

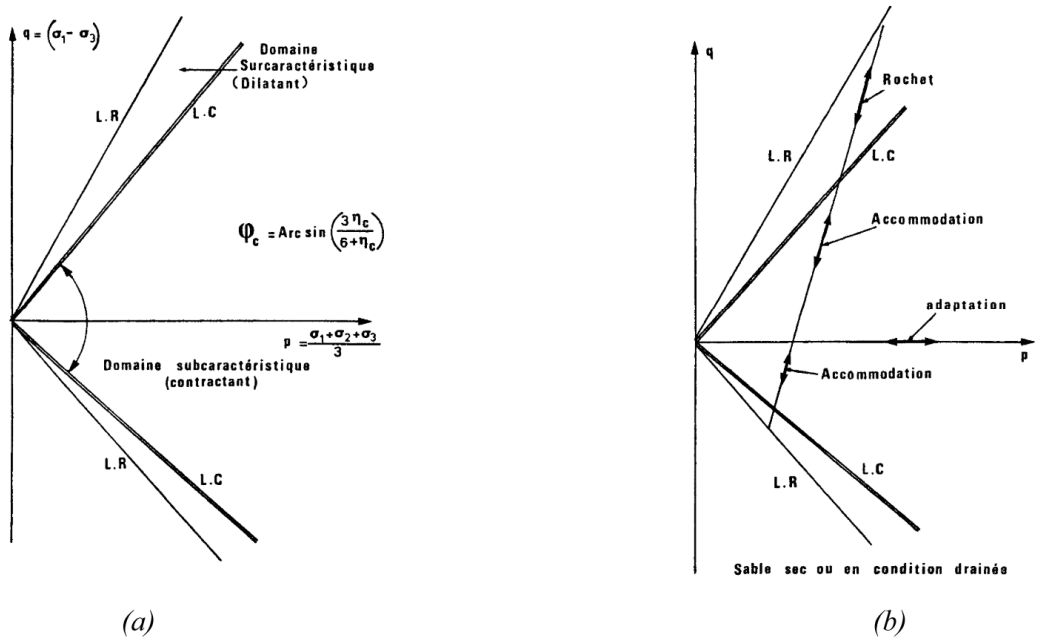

Figure 1-15 - Diagram of characteristic state spaces (Luong 1980)**. (a) Behavior under monotonic loading, (b) behavior under cyclic loading.**

In the case of undrained conditions the characteristic state is also an intrinsic parameter associated with the control of the effective stress path, however, due to the presence of pore water, there are pore pressure effects associated with the volumetric variation, The tendency to shrinkage during the execution of a triaxial test on a dense sand will generate an increase in pore pressure and a decrease in effective stress, however, a reversal of the pressure value will occur due to expansion effects, so that in the undrained case the phase change can also be defined by the point at which the pore pressure is zero ($u = 0$).

1.2 Behavior under cyclic loading

Cyclic loads are characterized by being imposed on the soil in a repetitive motion, presenting some distinctive characteristics such as frequency, amplitude, duration and regularity of the load. When applied to the soil, they are capable of inducing mechanical responses associated with a decrease in resistance and the occurrence of large deformations.

Although these loads can have multiple origins (vehicular traffic, effect of sea waves, machinery operations, explosions, etc.), one of the most important in engineering applications is that generated by earthquakes. The loads associated with earthquakes are usually rapid, limited in time and irregular, and in the case of saturated soils, they are capable of inducing an undrained behavior capable of generating phenomena such as liquefaction and cyclic mobility.

The analysis of the cyclic response of a soil can be complex considering the main characteristics of the shear waves produced during an earthquake, which are three-dimensional

and irregular. However, it is possible to reproduce the conditions and stresses induced in the soil by means of elementary tests such as the cyclic simple shear and cyclic triaxial tests.

Cyclic tests are capable of reproducing the conditions of soil subjected to repetitive cyclic loading and are even capable of reproducing the paths generated by an earthquake. These characteristics have made it possible to understand and predict the response of the soil under this type of stress.

Figure 1-16 shows a typical example of cyclic triaxial testing performed on a specimen of Fontainebleau NE34 sands reconstituted at a I_D value of 0.50, subjected to an isotropic consolidation stress of 400 kPa and to a cyclic deviator amplitude Δq_{cyc} 144 kPa. The results show the cyclic loading signal, axial deformation of specimen and excess pore water pressure generation versus number of cycles.

As observed in the response of the soil under monotonic loading, in the cyclic case the mechanical response is closely related to the volumetric behavior of the soil (higher deformations imply a contraction of the granular structure and an increase in pore pressure), and this in turn on the state of the soil and the imposed boundary conditions, however, the characteristics of a cyclic loading (cumulative variations) must be considered. This feature is especially critical in the undrained case, where two different phenomena can be triggered: liquefaction and cyclic mobility.

I.3.2 Behavior observed upon drained conditions

Under drained condition, the behavior of the soil under cyclic stress will be governed by the inter-particle interaction, so the effective stress would be equal to the total stress and the deformation mechanism will be a function of the characteristics of the contractancy and dilatancy properties and these in turn are a function of the initial state of the granular material, in addition to the characteristics and magnitude of the applied load, however, the final tendency will be towards densification.

One way to describe the cyclic response of a drained soil is to consider the characteristic state of the soil (Luong 1978, 1980). Under this consideration, the $(p - q)$ plane where the stress trajectories develop, would be subdivided into two subspaces. A characteristic subspace (below the line of the characteristic limit) where the soil would present a contractive behavior and a characteristic subspace where the soil deformations would be dilatant (above the line of the characteristic limit).

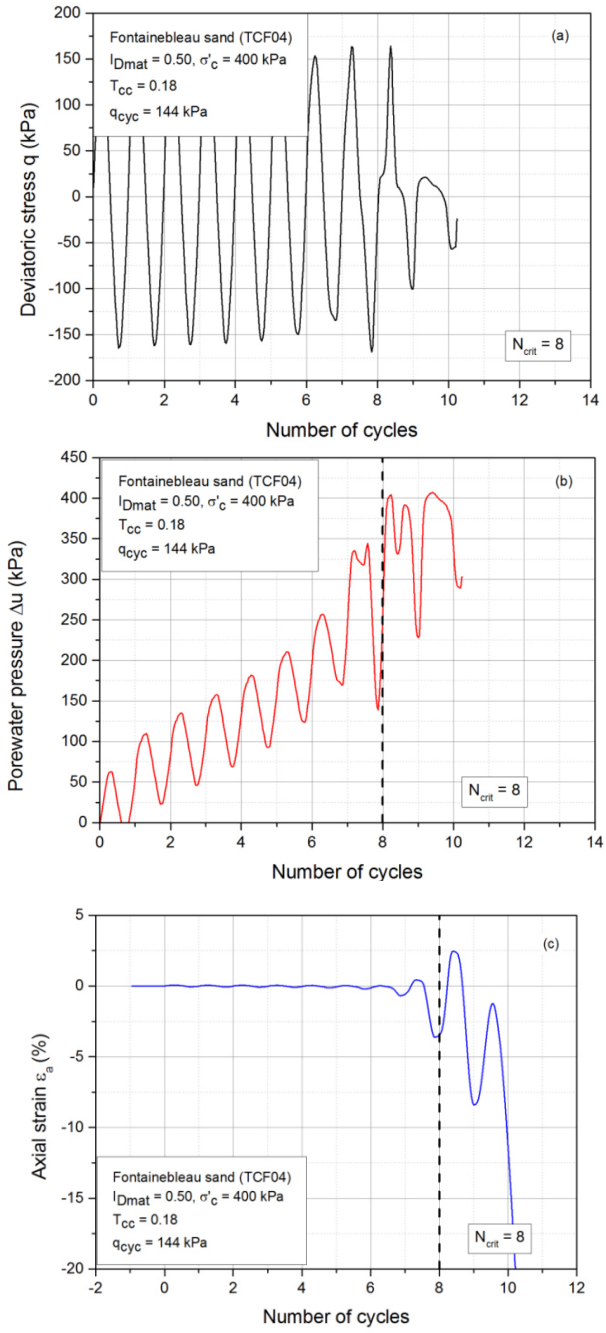

Figure 1-16 - Example of results of load-controlled cyclic triaxial tests, (a) deviatoric stress; (b) pore water pressure variation; (c) cyclic axial strain (Jradi 2018)**.**

In the Figure 1-17 (Tatsuoka and Ishihara 1974), the stress ratio - volumetric strain relationship is shown in a test performed on loose sand specimens. Both specimens were cyclically tested with two different load amplitudes. In Figure 1-17a the amplitude of the cyclic loading is below the characteristic line so that volumetric deformation is observed initially rapid and apparently not recoverable and then cycles where the volumetric deformation is less each time and the soil will tend to a state of higher density. In Figure 1-17b The cyclic stress exceeds the characteristic limit, observing a dilatant response towards the occurrence of the peak load

(point on the characteristic line). During subsequent loading cycles this dilatancy phenomenon continues to repeat, however, the specimen tends to stabilize at a higher density.

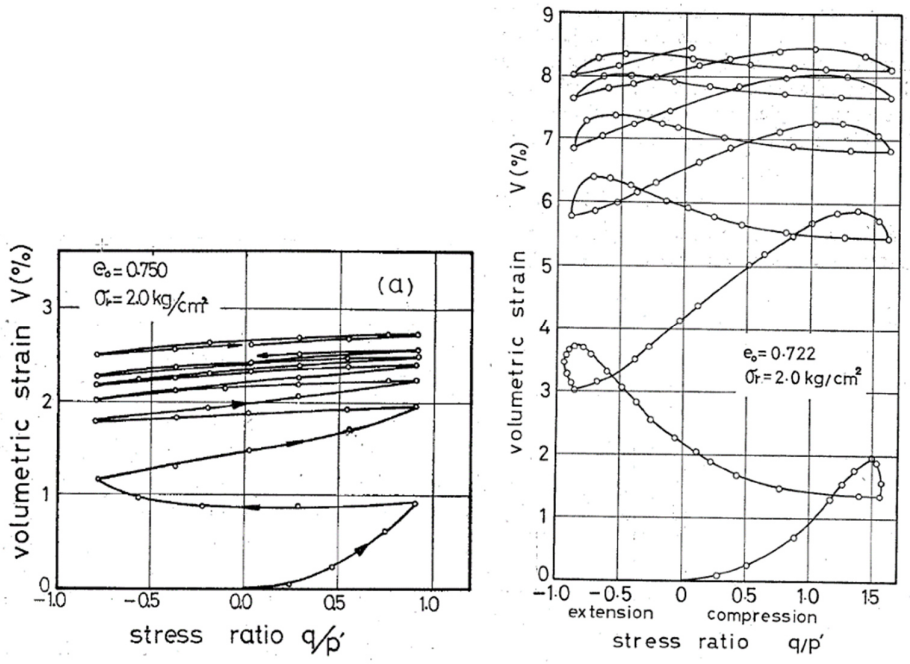

Figure 1-17 – Relationship stress ratio – volumetric strain in a drained test on loose sand specimen (Tatsuoka and Ishihara 1974)**.**

1.2.1 Behavior observed upon undrained conditions

This behavior is induced in a soil when it is subjected to load and the volumetric deformations of the granular structure are prevented, producing an increase in EPWP, because the fluid cannot be drained. This behavior can be reproduced in the laboratory by undrained tests and in the field by applying stresses such as those generated by an earthquake.

The EPWP will gradually increase with the application of loading cycles (Figure 1-18a). This EPWP increase results in a corresponding decrease of effective stress following Terzaghi principle until the loss of the strength of the granular skeleton (Figure 1-18b), at which point two failure mechanisms can be observed. In the case of dense sands, a failure associated with the accumulation of deformations, or "cyclic mobility" is generally observed, on the contrary, in loose sands, a failure associated with the total loss of strength and consequently large deformations or "true liquefaction" is generally observed.

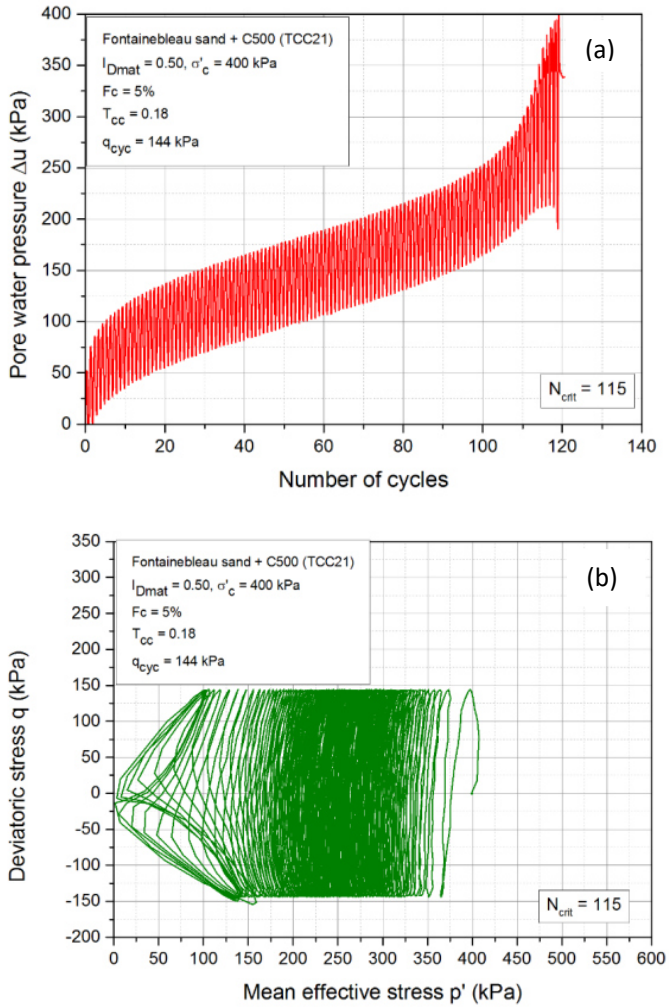

Figure 1-18 – Variations of effective stress and pore pressure during undrained cyclic triaxial testing (Jradi 2018)**.**

1.2.2 Behavior observed seismic loading

When an earthquake occurs, large amounts of energy are released in waves that travel through the layers of soil and reach the surface. These waves can be classified into two main groups: body waves and surface waves.

The body waves can be subdivided into waves *P* or longitudinal and *S* or shear waves (transversal). The passage of *P* waves generate compression and rarefaction cycles due to the longitudinal direction of propagation. On the other hand, the *S* waves move generating a motion perpendicular to the direction of propagation (Figure 1-19). Due to the perpendicular motion, *S*-waves can be divided into two motion components: motion in the vertical plane (*SV*) and motion in the horizontal plane (*SH*).

Surface waves are the result of the interaction of body waves and soil surface and their characteristics will be a function of the propagation medium characteristics. For engineering purposes, the most important surface waves are Rayleigh and Love waves. Rayleigh waves

arise from the interaction between P and SV waves, on the other hand Love waves result from the interaction between SH waves and soft surface soils.

During displacement, waves are affected by the medium in which they propagate and may be affected by dissipative phenomena associated with the characteristics of the medium (density, geological faults, presence of water, etc.). This phenomenon that decreases the amount of energy contained in the wave is called damping.

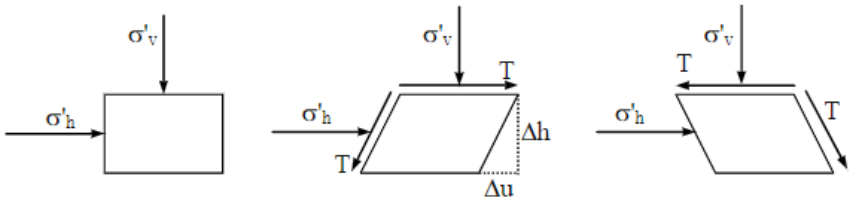

Figure 1-19 – Stresses induced by shear wave propagation (Pecker 2007).

Due to the variability and complexity of earthquakes, their quantitative evaluation is complex, so their characterization must be performed by means of a multiparametric approach. Some of the parameters commonly used are those describing the motion of surface phenomena such as acceleration, velocity and displacements. The velocity and displacement can be obtained from the integration of the acceleration signal (Figure 1-20).

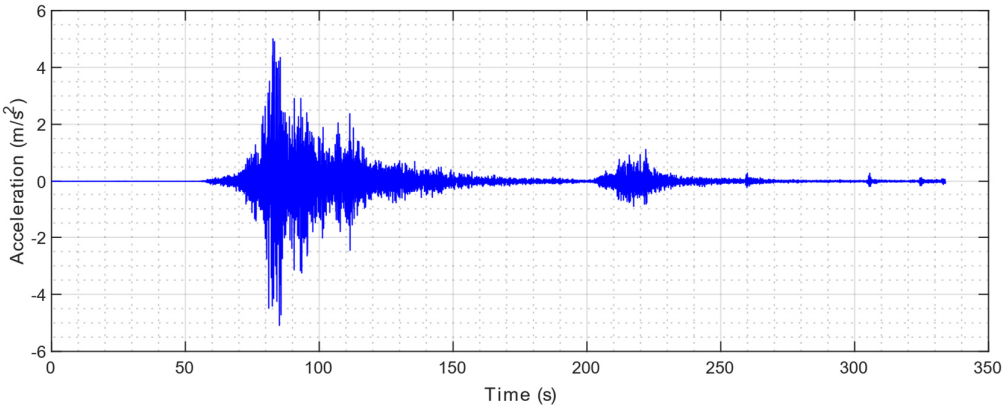

Figure 1-20 - Seismic acceleration measurements (Iquique earthquake 2014) (CSN 2014).

Another way to characterize an earthquake is a response spectrum (Figure 1-21), which is obtained from the response of a simple structure with one degree of freedom. This spectrum allows the determination of the maximum horizontal force that can be applied on a structure when it is subjected to an earthquake, knowing its damping properties and its natural frequency. The construction of these spectra must consider the direction of motion and depends on the seismic recording equipment.

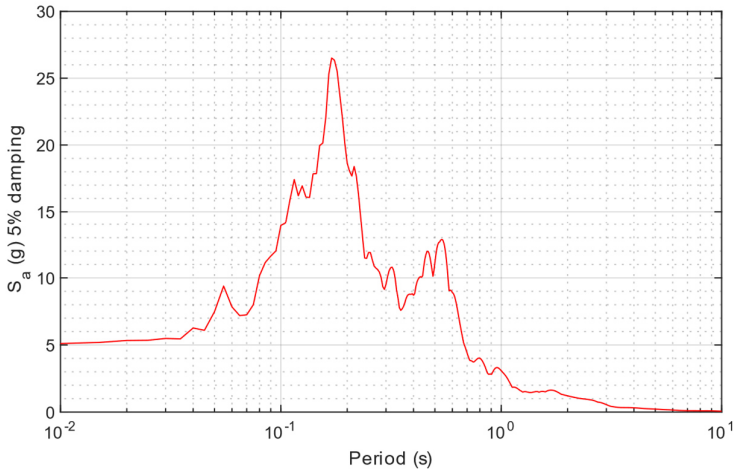

Figure 1-21 - Response spectrum (Iquique earthquake 2014) (CSN 2014)**.**

1.2.3 Cyclic mobility

Initially, the cyclic mobility phenomenon was called liquefaction (Seed and Lee 1966) However, the mechanisms involved in liquefaction and cyclic mobility phenomena are different, as are their consequences. The differentiation between these two phenomena was established by Castro (1969) by monotonic and cyclic triaxial tests. Later, extensive research has been carried out to evaluate and understand this phenomenon (Benahmed 2001; Canou 1989; Casagrande 1975; Castro 1975; Castro and Poulos 1977; Ishihara 1985; Ishihara et al. 1975; Seed 1979).

Cyclic mobility is a phenomenon that occurs in medium to high density sands ($I_D > 0.60$), in which the soil fails due to an accumulation of significant deformations when it first crosses the phase transformation line (characteristic state line), and a state of zero or near zero effective stresses is reached followed by a recovery of the soil strength in the extension phase, so it can be considered a stable phenomenon (Dupla 1995).

The phenomenon of cyclic mobility can be observed in a cyclic triaxial test, in which the evolution of the soil response can be appreciated. Once the cyclic loading is initiated, very small but perceptible axial deformations will occur and the pore pressure will gradually increase until it reaches a value equal or close to the confining pressure, at which point cyclic mobility occurs. (Figure 1-22).

During the cyclic mobility phase the pore pressure reaches a maximum peak twice in each cycle, in which the magnitude is equal to the consolidation pressure and the soil will temporarily liquefy producing important and cumulative deformations.

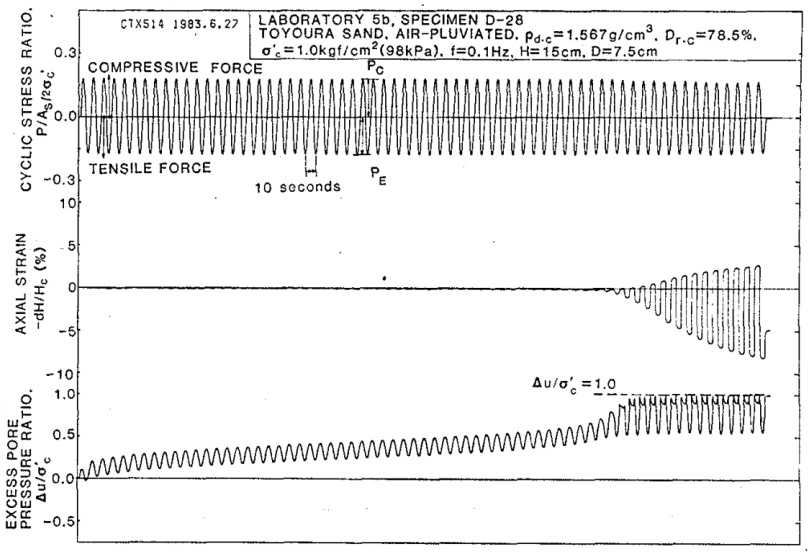

Figure 1-22 – Cyclic triaxial test with cyclic mobility results in dense sands (Toki et al. 1986)**.**

Another way to observe the occurrence of cyclic mobility is through the representation of the effective stress path in the $(q - p')$ plane (Figure 1-23). Observing the effective stress trajectory, it is possible to observe the cyclic decrease of the effective stress until reaching a value close to zero, where the cyclic mobility phenomenon occurs, characterized by a cyclic recovery of the effective resistance.

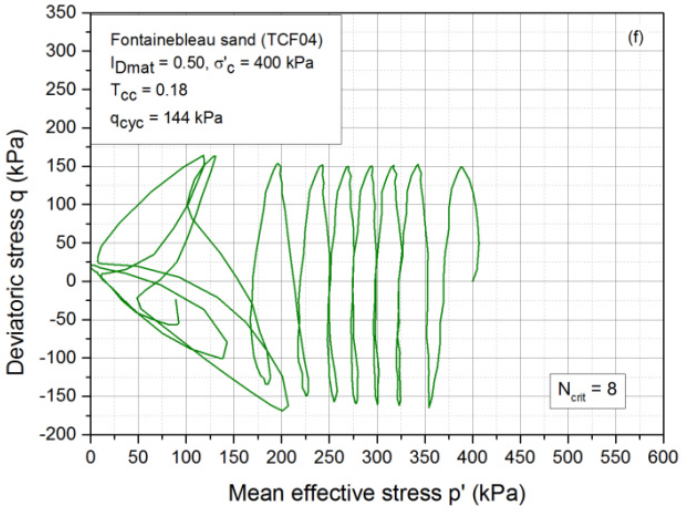

Figure 1-23 – effective stress path in the $(q - p')$ plane corresponding to cyclic mobility phenomenon (Jradi 2018)**.**

This phenomenon will always occur if a sufficiently high load level and a sufficient number of load cycles are applied, regardless of whether the density level is high.

1.2.4 Cyclic liquefaction

The phenomenon of cyclic liquefaction or "true liquefaction" occurs in loose or very loose sands subjected to a cyclic shear applied upon undrained conditions, which, when will

experience a progressive increase in EPWP with a initially very low axial deformation, until reaching a "critical" cycle, after which the pore pressure will increase sharply until reaching a value close to or equal to the initial confining pressure and will produce large deformations in the form of flow and an abrupt loss of shear strength, which decreases to a residual value that will depend on the characteristics of the soil.

Figure 1-24 shows a typical cyclic triaxial force-controlled test with true liquefaction result presented by Castro (1969). In the results it is possible to observe the mechanical response of the soil and the differences with respect to the cyclic mobility phenomenon.

In the first stage, the loading cycles generate limited deformations, but the EPWP gradually increases until the critical cycle (cycle number 5) is reached, at which time there is a rapid increase in pore pressure to the value of the initial consolidation pressure and a rapid decrease in shear strength. This phenomenon of loss of stability occurs in a very short time (0.15 seconds) and produces large deformations (25%). Unlike the cyclic mobility phenomena, during liquefaction the material maintains its fluid behavior until it reaches a stable state in which the imposed stress is equal to or less than the residual resistance.

By observing the effective stress path in the $(q - p')$ plane, it is observed that the effective stress trajectory is directed to the right, which is associated with a contractive behavior, which is related to the increase in EPWP. After the critical cycle, the trajectory migrates towards the origin, showing the loss of soil resistance.

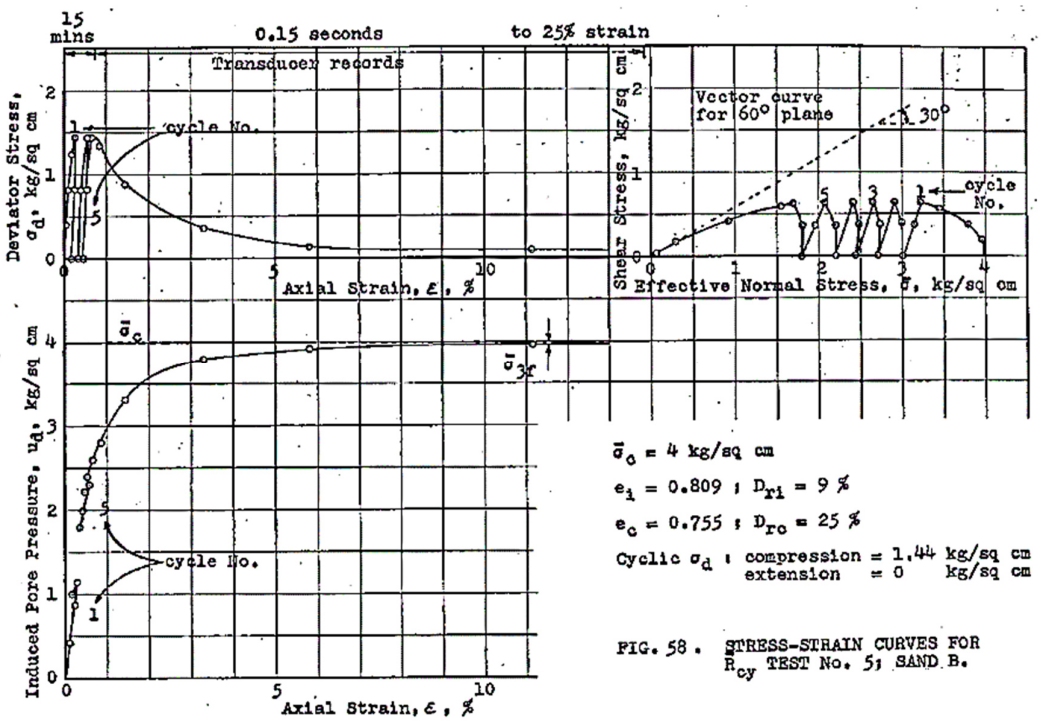

Figure 1-24 - Cyclic triaxial test with cyclic liquefaction result in loose sands (Castro 1969).

1.3 Soil liquefaction analysis

1.3.1 Liquefaction Potential Evaluation

1.3.1.1 Liquefaction potential evaluation method

The general method of liquefaction potential evaluation proposed by Seed and Idriss (1971), is based on the consideration of the soil characteristics collected both in the field and in the laboratory, to establish the possible seismic load generated by an earthquake and to obtain the cyclic resistance that it can mobilize. With these data it is possible to establish a safety factor based on the maximum resistance of the soil.

In general terms, the liquefaction potential evaluation method proposed by Seed and Idriss (1971) can be summarized in four steps:

1. Determine seismic-induced shear stress measurements at different depth levels (prior establishment of the soil and design earthquake conditions is required).
2. Convert the stress level associated with the various seismic dynamic load cycles to a number of equivalent load cycles and plot it as a function of depth (Figure 1-25) (Note that this consideration takes into account soil shaking, its duration and variation with respect to depth).
3. Establish the cyclic resistance of the soil CRR at different depth levels, through laboratory or field tests. Resistance can be plotted as a function of depth. (Figure 1-25).
4. By comparing the cyclic resistance CRR with the cyclic seismic-induced stress CSR, establish the zones where liquefaction may occur (Figure 1-25).

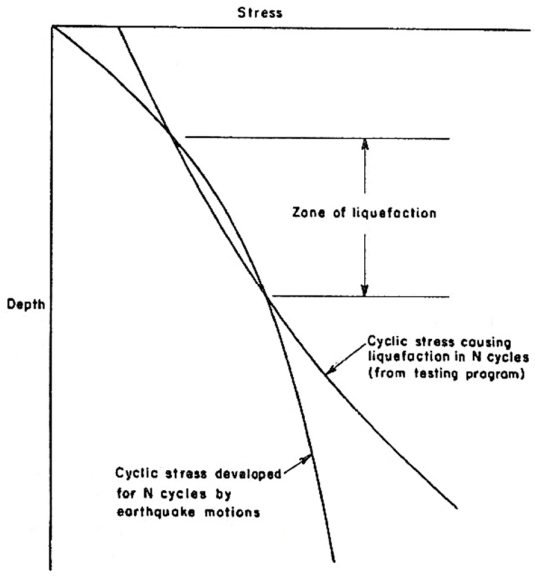

Figure 1-25 – Comparison of cyclic resistance and solicitation at depth (Seed and Idriss 1971)**.**

1.3.1.2 Cyclic Stress Ratio CSR

The cyclic stress ratio represents the shear stress generated on a soil deposit by the occurrence of a seismic movement. The magnitude of this stress depends directly on the characteristics of the earthquake likely to occur at a site and on the properties and conditions of the soil.

For the calculation of the cyclic stress ratio, a level or very slightly sloping terrain must be considered. Likewise, it should be considered that the portion of soil used in the theoretical analysis behaves as a rigid body (Figure 1-26).

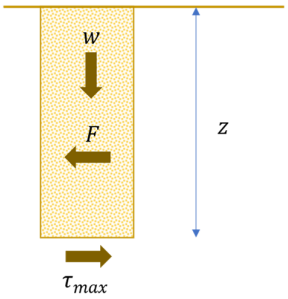

Figure 1-26 – Idealization of the soil as a rigid body subjected to seismic loading.

with:

w: weight of the soil column.
z: depth of the soil column.
F: force generated by the earthquake.
τ_{max}: shear strength generated at the base of the soil column.

The rigid column problem can be analyzed using a Newtonian approach, obtaining a relation between the force, the seismic acceleration (PGA), and the weight of the soil column, as follows:

$$F = m \cdot a = \left(\frac{w}{g}\right) \cdot a_{max} \qquad \textbf{eq. 1-12}$$

If a force F is applied to the soil column, the response τ_{max} is a function of the properties and response of the soil.

$$\tau_{max} = F = \frac{\gamma \cdot z}{g} \cdot a_{max} \qquad \textbf{eq. 1-13}$$

Note that $\sigma_{v0} = \gamma \cdot z$.

$$\tau_{max} = F = \sigma_{v0} \cdot \left(\frac{a_{max}}{g}\right) \qquad \textbf{eq. 1-14}$$

with:

σ_{v0}: total vertical stress at base of soil column.
γ: total unit weight of the soil column.

Then, by dividing on both sides by the effective vertical stress, the equilibrium in the equation is maintained and the following is obtained:

$$\frac{\tau_{max}}{\sigma'_{v0}} = \left(\frac{\sigma_{v0}}{\sigma'_{v0}}\right) \cdot \left(\frac{a_{max}}{g}\right) \quad \textbf{eq. 1-15}$$

The idealization of the soil as a rigid body is deficient when considering that the soil is a deformable granular material that allows the dissipation of energy through the movement of the constituent particles of the soil structure. In addition, the deformation generated in the column is affected by the stiffness of the specimen which varies with depth due to the pressures associated with the internal stresses of the soil. In order to make a more rational analysis, the method includes a reduction factor r_d (eq. 1-16), which allows to relate the real and theoretical shear stresses to the theoretical stresses.

$$\frac{\tau_{max}}{\sigma'_{v0}} = \left(\frac{\sigma_{v0}}{\sigma'_{v0}}\right)\left(\frac{a_{max}}{g}\right) r_d \quad \textbf{eq. 1-16}$$

On a typical seismographic record one will usually observe an irregular behavior (Figure 1-27), and the consideration of an arbitrary acceleration does not represent the reality of soil dynamics. An erroneous or non-representative consideration of seismic accelerations may result in obtaining unrealistic dynamic stress values.

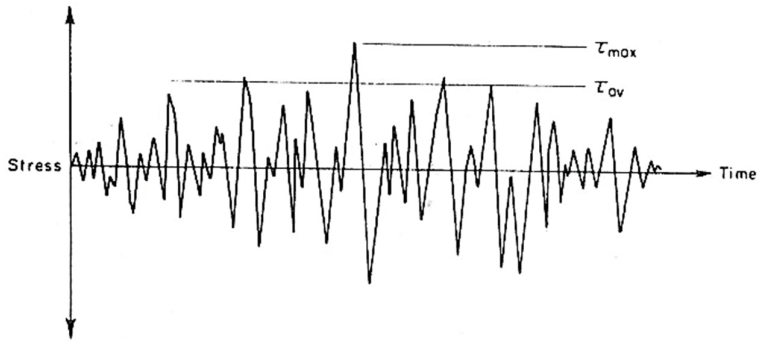

Figure 1-27 – Shear stresses during earthquakes (Seed and Idriss 1971)**.**

For the correction and consideration of the irregularity of the seismographic measurement, an attempt is made to convert the measurement to a series of equivalent cycles of uniform stress with the application of a factor of 0.65 (Figure 1-27). Then, the cyclic stress equation is expressed as follows:

$$CSR = \frac{\tau_{av}}{\sigma'_{v0}} = 0.65\left(\frac{a_{max}}{g}\right)\left(\frac{\sigma_{v0}}{\sigma'_{v0}}\right) r_d \quad \textbf{eq. 1-17}$$

1.3.1.3 Reduction factor r_d

The reduction factor r_d is the ratio between the real expected behavior of a soil and the assumed rigid body response of the soil (eq. 1-18), so that its function is to obtain more rational resistance results.

$$r_d = \frac{(\tau_{max})_{real}}{(\tau_{max})_{rigidbody}} \qquad \text{eq. 1-18}$$

This reduction factor can be considered as a measure of energy dissipation in the soil structure, so its value presents variability associated with multiple factors, where some of the most important are the stratigraphy and depth of the soil, geotechnical properties of the soil and characteristics of the load applied to the soil.

Several studies have been carried out for the evaluation of this correction factor. The reduction factor has been widely discussed in the available literature. (Cetin et al. 2004; Cetin and Seed 2004; Golesorkhi 1989; Idriss 1999; Idriss and Boulanger 2006; Ishihara 1977; Liao and Whitman 1986; Youd and Idriss 1997). These studies have presented calculation equations for r_d based on different conclusions and hypotheses, so their application must be carried out in a rational way. Some of the equations for calculating r_d are presented in Table 1-1, below.

Table 1-1 - Equations for calculating the reduction factor r_d.

Equation	Condition	Reference
$r_d = 1 - 0.00765z$	$z \leq 9.15m$	(Liao and Whitman, 1986)
$r_d = 1.174 - 0.0267z$	$9.15m < z \leq 23m$	(Liao and Whitman, 1986)
$r_d = 0.744 - 0.008z$	$23m < z \leq 30m$	(Youd and Idriss 1997)
$r_d = 0.5$	$z > 30m$	(Youd and Idriss, 1997)
$r_d = \frac{(1 - 0.4113z^{0.5} + 0.001753z^{1.5})}{(1 - 0.4177z^{0.5} + 0.5729z - 0.006205z^{1.5} + 0.001210z^2)}$		(Youd and Idriss, 1997)
$\ln(r_d) = \alpha(z) + \beta(z)M_w$ With : $\alpha(z) = -1.012 - 1.126\sin\left(\frac{z}{38.5} + 5.133\right)$ $\beta(z) = 1.106 - 0.118\sin\left(\frac{z}{37.0} + 5.142\right)$ $M_w = Seismic\ Magnitude$ $z = depth\ in\ foot$	$z \leq 34m$	(Idriss 1999) and (Golesorkhi 1989)
$r_d = 0.12e^{0.22M_w}$	$z > 34m$	
$r_d = 1 - 0.015z$	Not informed	(Iwasaki et al. 1978)

1.3.1.4 Magnitude scaling factor

For the development of the simplified liquefaction potential evaluation method, they were based on the construction of a database built with data from sites where earthquakes of magnitudes close to 7.5 magnitude occurred (Youd and Idriss 2001). However, this would be a limitation if it is considered that the magnitudes are variable and multifactorial. This is why an extension of the method to earthquakes of other magnitudes is included through the inclusion of the magnitude scale factor (MSF). The application of the MSF makes it possible to analyze any earthquake by converting it to one of equivalent magnitude 7.5 and vice versa. Note that it is possible to apply the factor to the calculation of both CRR and CSR.

$$CRR_{7,5;1} = \frac{CRR_{M_w}}{MSF} \quad \textbf{eq. 1-19}$$

$$CSR_{7,5;1\ atm} = \frac{CSR_{M;\sigma'_V}}{MSF} \quad \textbf{eq. 1-20}$$

Through a study of accelerograms of strong motions, a relationship was established between the magnitude of an earthquake and the number of equivalent load cycles (Seed and Idriss 1982; Youd and Idriss 1997). In the case of an earthquake of magnitude 7.5, a correspondence was established with 15 cycles and 10 and 26 equivalent cycles for earthquakes of magnitude 6.5 and 8.5 respectively. Later, through the realization of cyclic tests on clean reconstituted sands, on specimens of different densities, a relationship between the seismic magnitude and the MSF was established (Seed and Idriss 1982) (Figure 1-28).

From the conclusions reached by Youd et al., (1997) the recommendation to calculate the MSF by means of the eq. 1-21, using an exponent that limits a subspace with a value of n equal to -2.56 at the bottom and -3.3 at the top (Figure 1-28)

$$MSF = \left(\frac{M_w}{7,5}\right)^n \quad \textbf{eq. 1-21}$$

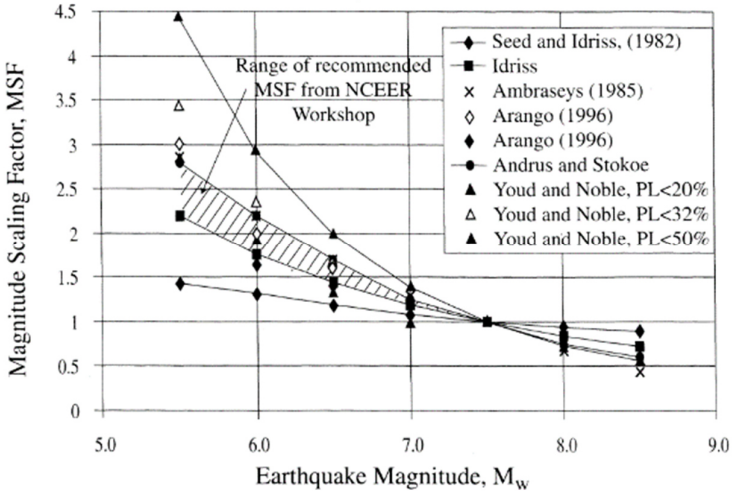

Figure 1-28 - Magnitude scaling factor proposed in the bibliography (Youd and Idriss 1997)**.**

Other equations for calculating MSF have been reported in the literature (Figure 1-28) (Ambraseys 1988; Arango 1996; Boulanger and Idriss 2007, 2014; Idriss 1999; Idriss and Boulanger 2008; Youd and Idriss 2001) A summary of some of the calculation expressions is presented in the Table 1-2

Table 1-2 - Summary of MSF calculation equations.

Equation	Condition	Reference
$MSF = \left(\frac{M_w}{7.5}\right)^{-3.3}$		(Andrus and Stokoe, 1997)
$MSF = 6.9e^{\left(\frac{-M_w}{4}\right)} - 0.06$	$M_w > 5.2$	(Idriss 1999)
$MSF = 1.82$ $MSF = \left(\frac{M_w}{7.5}\right)^{-2.56}$	$M_w \leq 5.2$	(Youd and Idriss 1997)
$MSF = \frac{10^{3.81}}{M_w{}^{4.53}}$	$LP < 20\%$ $M_w < 7$	Youd and Noble (Youd and Idriss 1997)
$MSF = \frac{10^{3.74}}{M_w{}^{4.33}}$	$LP < 32\%$ $M_w < 7$	
$MSF = \frac{10^{4.21}}{M_w{}^{4.81}}$	$LP < 50\%$ $M_w < 7.5$	

1.3.2 Overburden correction factor

The basic considerations of the simplified evaluation method indicate that the results obtained below 15 meters depth may not be accurate (Seed and Idriss 1971; Youd and Idriss 2001). On the other hand, based on cyclic triaxial tests, it has been shown that the cyclic resistance increases with the consolidation stress (Youd and Idriss 2001), which also increases as the soil depth increases. To incorporate these overburden effects, a correction factor is implemented k_σ (eq. 1-23), which has been recommended for overburden stress greater than 100 kPa (Bolton Seed 1983).

The k_σ factor was initially introduced by Seed (1983), and corresponds to the ratio between CRR and $CRR_{\sigma'_{vc}=1atm}$ (CRR when $\sigma'_{vc} = 1\ atm \approx 100\ kPa$).

$$k_\sigma = \frac{CRR_{\sigma'_{vc}}}{CRR_{\sigma'_{vc\,=\,1\ atm}}} \qquad \textbf{eq. 1-22}$$

Boulanger (2003) derived an equation for the calculation of k_σ (eq. 1-23). This equation requires knowledge of σ'_{vc} and of the C_a coefficient.

$$k_\sigma = 1 - C_a \ln\left(\frac{\sigma'_{vc}}{P_a}\right) \qquad \leq 1.1 \qquad \textbf{eq. 1-23}$$

C_a is a coefficient that can be obtained based on the results of CPT and SPT tests and through the density index (eq. 1-24, eq. 1-25 y eq. 1-26) (Boulanger 2004; Boulanger and Idriss 2004; Idriss and Boulanger 2004, 2008).

$$C_a = \frac{1}{18.9 - 17.3 I_D} \leq 0.3 \quad \textbf{eq. 1-24}$$

$$C_a = \frac{1}{18.9 - 2.55\sqrt{(N_1)_{60}}} \leq 0.3 \quad \textbf{eq. 1-25}$$

$$C_a = \frac{1}{37.3 - 8.27(q_{c1N})^{0.264}} \leq 0.3 \quad \textbf{eq. 1-26}$$

1.3.3 Sloping ground correction factor k_α

The original methodology presented by Seed and Idriss (1971) considered flat or slightly inclined surface conditions, excluding the effects of static shear stresses. To account for the effects of inclined soil surfaces (static shear stresses), a k_α correction factor has been proposed. (Idriss and Boulanger 2003, 2008; Seed 1983).

By definition, the k_α factor corresponds to the ratio between the cyclic resistance for a specific value of α and the cyclic resistance for $\alpha = 0$. Where α is the ratio of the static shear stress to the effective vertical consolidation stress ($\alpha = \tau_{st}/\sigma'_{vc}$).

$$k_\alpha = \frac{CRR_\alpha}{CRR_{\alpha=0}} \quad \textbf{eq. 1-27}$$

Several relationships have been presented for the calculation of k_a (Youd and Idriss 1997). These ratios have been developed mainly on the basis of laboratory tests (simple shear tests). Idriss and Boulanger (2003) presented an equation for the calculation of k_α.

$$k_\alpha = a + be^{\left(\frac{-\xi_R}{c}\right)} \quad \textbf{eq. 1-28}$$

with:

$$a = 1267 + 636\alpha^2 - 634e^{\alpha} - 632e^{-\alpha}$$

$$b = e^{\left(-1.11 + 12.3\alpha^2 + 1.31\ln(\alpha + 0.0001)\right)}$$

$$c = 0.138 + 0.126\alpha + 2.52\alpha^3$$

$$\alpha = \frac{\tau_{st}}{\sigma'_{vc}}$$

ξ_R as a function of $(N_1)_{60}$ and/or q_{c1n}

$$\xi_R = \frac{1}{Q - \ln\left(\frac{100(1+2k_0)\sigma'_{vc}}{3P_a}\right)} - \sqrt{\frac{(N_1)_{60}}{46}}$$

$$\xi_R = \frac{1}{Q - \ln\left(\frac{100(1+2k_0)\sigma'_{vc}}{3P_a}\right)} - (0.478(q_{c1n})^{0.264} - 1.063)$$

with:

$$q_{c1n} \geq 21$$

$$\alpha \leq 0.35$$

$$-0.6 \leq \xi_R \leq 0.1$$

1.3.4 Cyclic resistance ratio CRR

The cyclic resistance ratio CRR represents the capacity of a loaded soil to resist the occurrence of liquefaction. The magnitude of this resistance can be evaluated by laboratory and field tests. In the case of laboratory tests, cyclic loading equipment are usually used, and for field evaluations, static and dynamic penetration tests are commonly used, in addition to methods based on shear wave measurements.

Laboratory tests allow the CRR parameter to be obtained directly, however, penetrometers are not able to obtain the cyclic resistance directly, so they use correlations and databases of measurements taken in the field of historical cases, where the occurrence of liquefaction has been observed or not. Some of the most commonly used tests in the calculation of CRR are summarized in the diagram shown in Figure 1-29.

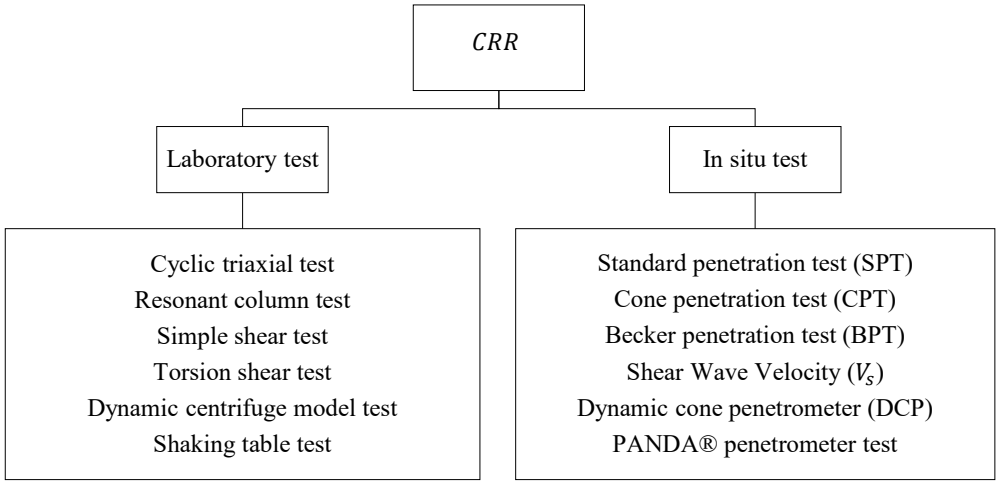

Figure 1-29 – Laboratory tests and in-situ equipment used for CRR evaluation.

1.3.4.1 Laboratory evaluation of CRR

Evaluation of CRR as defined in eq. 1-29 is performed in the laboratory by applying cyclic tests on reconstituted specimens, which should be representative of the soil characteristics in the field (density, moisture, loading conditions, granulometry, etc.). On the other hand, loads applied to the specimens should be controlled and, if possible, several tests should be performed with different loading conditions to capture the behavior of the soil over a range of possible conditions.

$$CRR = \frac{\tau_{cyc}}{\sigma'_c} = \frac{q_{cyc}}{2\sigma'_c} \quad \textbf{eq. 1-29}$$

In the evaluation of liquefaction potential, it is necessary to compare the load applied by an earthquake with respect to the ultimate load that the soil is capable of developing before generating the liquefaction phenomenon. For this, it is necessary to establish a common reference point between the load and the resistance through a common factor. In the case of these methods, a number of cycles equivalent to a reference earthquake is established as a reference (for example, 15 cycles are equivalent to an earthquake of magnitude 7.5). The establishment of the relationship allows the construction of $CRR - N_{cyc}$ curves, through which it is possible to obtain the cyclic resistance of a soil for different seismic conditions.

If the cyclic resistance ratio CRR is obtained based on laboratory experiments, it is possible to use it directly for the evaluation of liquefaction potential (eq. 1-30). However, carrying out such experiment programs can be complex and expensive in most cases of applications, so it is usually feasible only in those cases in which the occurrence of this phenomenon results in critical negative effects.

$$FS_{liq} = \frac{CRR}{\mathrm{CSR}} \quad \textbf{eq. 1-30}$$

Although laboratory tests allow obtaining the response of the soil under controlled conditions, they have disadvantages associated with the reconstitution of the specimens. One of the main disadvantages associated with this method of evaluating the CRR is the difficulty in reproducing soil conditions, especially in granular soils, where the resistance is mostly due to the contact between particles and where the extraction of samples represents an almost immediate modification of the internal structure of the soil and its stress states. This disadvantage can be minimized if controlled boundary conditions and reconstitution procedures are applied to ensure, among other factors, sample homogeneity.

1.3.5 In-situ CRR evaluation

1.3.5.1 Standard Penetration Test (SPT)

The Standard Penetration Test is one of the most widely used equipment for obtaining the cyclic resistance ratio (CRR) in the field since the publication of the pioneering paper on liquefaction risk analysis originally published by Seed and Idriss (Seed and Idriss 1970, 1971).

Although this equipment has disadvantages with respect to repeatability and quality control (Youd et al. 1997), the robust database of cases analyzed with this equipment, complemented by new cases available, has allowed the construction of abacuses to determine the susceptibility of a soil to liquefaction (Figure 1-30).

The SPT analysis is based on the number of blows needed to penetrate a soil by 30 centimeters, which can be affected by factors associated with the procedure (hammer energy, sampler details, length of the rods, borehole dimensions, operator experience) and boundary conditions. To reduce the effect of factors that affect the number of blows obtained in the field N_1, correction factors are applied (eq. 1-31) (Some recommended values for the correction factors are summarized in Table 1-3.).

$$(N_1)_{60} = C_N C_E C_R C_B C_S N_m \qquad \text{eq. 1-31}$$

With:

C_N : overload correction factor.
C_E : hammer energy correction factor
C_R : correction factor for rod length.
C_B : borehole size correction factor.
C_S : correction factor associated with sampler type.
N_m: number of blows.

The fines content (quantity of fines contained in the soil mass) modifies the resistance properties of the soil, so it is necessary to apply a correction factor that considers the percentage of fines contained in the granular material. This consideration can be presented by a set of additional curves presented in the (CRR-$(N_1)_{60}$) plane or present the results of SPT blow numbers in terms of clean sand by applying a correction factor.

For the correction of $\boldsymbol{(N_1)_{60}}$ for the content of fines multiple equations have been presented (Boulanger and Idriss 2014; Cetin et al. 2004; Idriss and Boulanger 2008, 2010; Kayen and Mitchell 1997; Seed 1986; Tokimatsu, Oshiaki, and Oshimi 1983; Youd and Idriss 1997). In the Table 1-4 a summary of some equations used for correcting of SPT test results for fines content is presented.

Table 1-3 - Correction factors for *SPT* test (Idriss and Boulanger 2008; Youd and Idriss 1997)

Factor	Correction factor
Overburden pressure	$C_N = \left(\frac{P_a}{\sigma'_{v0}}\right)^{0.5} \leq 2$
Energy ratio	$C_E = \frac{ER_m}{60}$ $For\ rods > 10m$ $C_E = 0.5 - 1.0$ (Doughnut hammer) $C_E = 0.7 - 1.2$ (Safety hammer) $C_E = 0.8 - 1.3$ (Automatic triphammer) Seed et al. (1984) Skempton (1986) NCEER (1997)
Borehole diameter	$C_B = 1.0$ (Diameter of 65 - 115 mm) $C_B = 1.05$ (Diameter of150 mm) $C_B = 1.15$ (Diameter of 200 mm) Skempton (1986)
Rod length	$C_R = 0.75$ (Rod length < 3 m) $C_R = 0.80$ (Rod length 3 - 4 m) $C_R = 0.85$ (Rod length 4 – 6 m) $C_R = 0.95$ (Rod length 6 – 10 m) $C_R = 1.00$ (Rod length 10 – 30 m) Youd et al., (2001)
Sampler	$C_S = 1.00$ Standards split spoon (no room for liners) Split spoon sampler with room for liners $C_S = 1.10$ for $(N_1)_{60} \leq 10$ $C_S = 1 + \frac{(N_1)_{60}}{100}$ for $10 \leq (N_1)_{60} \leq 30$ $C_S = 1.30$ for $(N_1)_{60} \geq 30$ Seed et al. (1984); Seed et al. (2001)

Table 1-4 – Summary of the equation for calculating the correction factor for fines content.

Reference	Equation
(Youd and Idriss 1997)	$(N_1)_{60cs} = k_s(N_1)_{60}$ Where: $k_s = 1 + \left[\left(\frac{0.75}{30}\right)(FC - 5)\right]$
(Youd and Idriss 1997)	$(N_1)_{60cs} = A + B(N_1)_{60}$ Where: $A = 0$ For $FC \leq 5\%$ $A = e^{[1.76-(190/FC^2)]}$ For $5\% < FC \leq 35\%$ $A = 5$ For $FC \geq 35\%$ $B = 1$ For $FC \leq 5\%$ $B = [0.99 + (FC^{1.5}/1000)]$ For $5\% < FC \leq 35\%$ $B = 1.2$ For $FC \geq 35\%$
(Boulanger and Idriss 2014)	$(N_1)_{60cs} = (N_1)_{60} + \Delta(N_1)_{60}$ Where the delta value can be obtained from multiple sources:
(Tokimatsu et al. 1983)	$\Delta(\mathrm{N_1})_{60} = \mathrm{e}^{\left[1.63+\frac{9.3}{\mathrm{FC}+0.01}-\left(\frac{15.7}{\mathrm{FC}+0.01}\right)^2\right]}$ FC (%) | $\Delta(\mathrm{N_1})_{60}$ $0-5$ | 0 $5-10$ | Interpolate >10 | $0.1\mathrm{FC}+4$
(Kayen and Mitchell 1997)	$\Delta(\mathrm{N_1})_{60} = 0$ For $\mathrm{FC} \leq 5\%$ $\Delta(\mathrm{N_1})_{60} = (\mathrm{FC}-5)\left(\frac{7}{30}\right)$ For $5\% < \mathrm{FC} \leq 35\%$ $\Delta(\mathrm{N_1})_{60} = 7$ For $\mathrm{FC} \geq 35\%$
(Seed 1986)	FC (%) | $\Delta(\mathrm{N_1})_{60}$ ≤ 5 | 0 $\simeq 15$ | 3 $\simeq 35$ | 5 $\simeq 50$ | 7
(Cetin et al. 2004)	$(\mathrm{N_1})_{60\mathrm{cs}} = (\mathrm{N_1})_{60}\mathrm{C_{FINES}}$ $\mathrm{C_{FINES}} = (1 + 0.004\mathrm{FC}) + 0.05\left(\frac{\mathrm{FC}}{(\mathrm{N_1})_{60}}\right)$ For $5\% \leq \mathrm{FC} \leq 35\%$

Once the correction factors and normalizations have been applied, it is possible to obtain the value of the cyclic resistance of the soil as a function of the number of corrected SPT blows $(N_1)_{60cs}$, by means of equations proposed in the literature and which have been subject to updates that include new case studies associated with observed and unobserved liquefaction in the field.

One of the most commonly used equations for calculating cyclic resistance is presented in Idriss and Boulanger (2004) (eq. 1-32). Other equations for the calculation of cyclic resistance can be obtained from bibliography (Boulanger and Idriss 2014; Cetin et al. 2004; Youd and Idriss 1997, 2001). These equations divide the space $(N_1)_{60cs} - CRR$ in two subspaces. A subspace under the curve where the analysis of the cases represents mostly no liquefaction occurrence, and in contrast, the subspace above the curve represents the space where the cases present mostly soil liquefaction (Figure 1-30).

$$CRR_{M=7.5;\sigma'_v=1\ atm} = e^{\left(\frac{(N_1)_{60cs}}{14.1}+\left(\frac{(N_1)_{60cs}}{126}\right)^2-\left(\frac{(N_1)_{60cs}}{23.6}\right)^3+\left(\frac{(N_1)_{60cs}}{25.4}\right)^4-2.8\right)} \qquad \textbf{eq. 1-32}$$

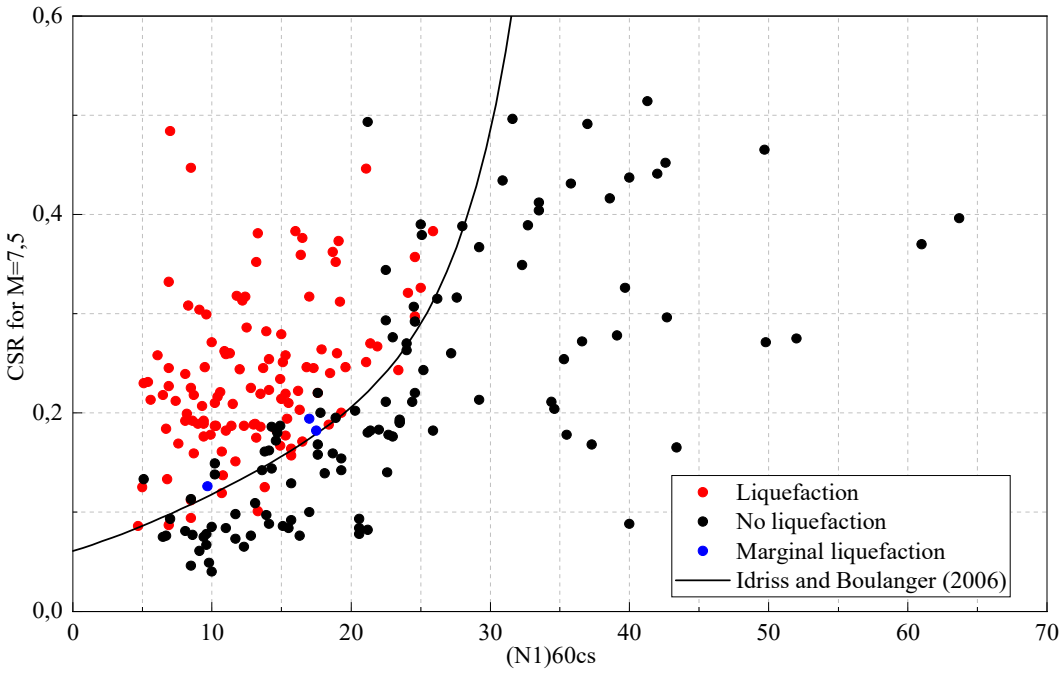

Figure 1-30 – Simplified curve for the calculation of CRR from data of $(N_1)_{60cs}$-SPT (Seed et al. 1985).

1.3.5.2 Cone penetration test (CPT)

The penetration test (CPT), also called static penetration test because the cone is driven at a constant speed, allows to determine the properties of a soil based on the continuous measurement of the penetration resistance of a cone q_c (Q_c/A_c), lateral friction and, depending on the configuration of the equipment, the possibility of pore pressure measurements (Figure 1-31).

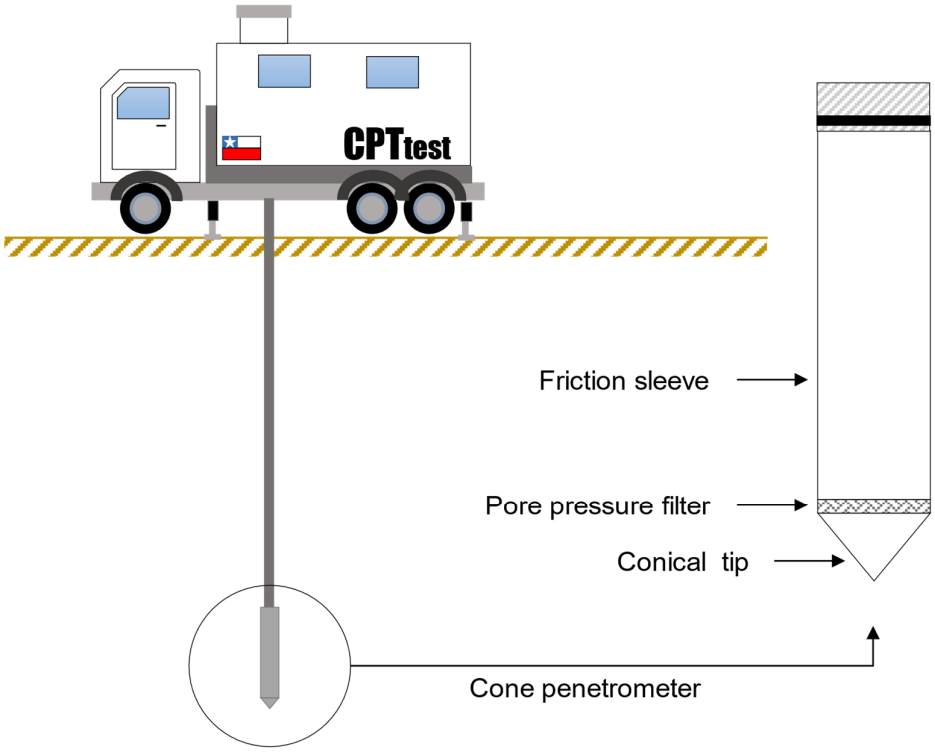

Figure 1-31 – Scheme of cone penetration test (CPT) setup.

Like the SPT-based liquefaction risk analysis method, the CPT-based method is based on the generation of a database with results of in situ analysis regarding the occurrence or not of the liquefaction phenomenon, in addition to accessing the database of cases associated with the SPT equipment by means of correlations.

A first methodology for the evaluation of liquefaction potential can be performed by normalizing the resistance results (eq. 1-33) and correlations developed from the SPT test database and from CPT test databases (Figure 1-32) (Olsen 1988; Olsen and Koester 1995; Olsen and Malone 1988; Robertson and Campanella 1985; Robertson and Fear 1995; Seed and de Alba 1986; Shibata and Teparaksa 1988; Suzuki, Tokimatsu, Koyamada, et al. 1995; Suzuki, Tokimatsu, Taya, et al. 1995; Timothy Stark and Olson 1995).

$$q_{c1N} = \left(\frac{q_c}{P_{a2}}\right) C_Q = \frac{q_{c1}}{P_{a2}} \qquad \textbf{eq. 1-33}$$

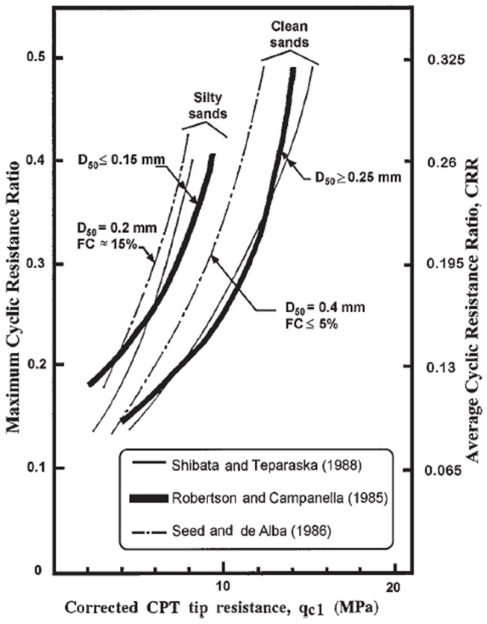

Figure 1-32 – Graph for estimation of cyclic resistance value from corrected tip resistance q_{c1} (Robertson and Wride 1998)**.**

In order to include the soil characteristics in the liquefaction potential assessment Robertson and Wride (1998), presented some modifications to update the method by including a correction factor associated with the fines content of the soil. With this modification, it is possible to obtain the resistance as a function of the strength and granular characteristics of the soil.

$$(q_{c1N})_{cs} = k_c q_{c1N} \quad \textbf{eq. 1-34}$$

With k_c = correction factor.

For the identification of the soil type, and based on the classification proposed by Robertson (1990), the definition of a soil behavior index is possible (I_c) (eq. 1-35).

$$I_c = [(3.47 - Q)^2 + (\log F + 1.22)^2]^{0.5} \quad \textbf{eq. 1-35}$$

Where:

$$Q = \left(\frac{q_c - \sigma_{v0}}{P_{a2}}\right)\left(\frac{P_a}{\sigma'_{v0}}\right)^n \quad \textbf{eq. 1-36}$$

Q corresponds to the normalized CPT penetration resistance, with $n = 1$, f_s sleeve friction, $F = (f_s/(q_c - \sigma_{v0})) * 100$ (Normalized friction ratio), σ_{v0} and σ'_{v0} total and effective overload stresses, P_a reference pressure (100 kPa), P_{a2} reference pressure (100 kPa), in the same unit as q_c.

The calculation of this behavioral index is critical because it is able to identify a fine soil from a mostly granular one, however, there are suggestions on the value that the power n should take. Olsen and Malone (1988), indicated that this value varies from 0.5 for sands to 1.0 for clays, however, the application of this value can be complex and iterative (Robertson and Wride 1998).

Taking into account the above, the proposed recommendation is the initial use of a value of $n = 1.0$ as it was applied in the original method of Robertson (1990) for the calculation of Q. Therefore, if the value of I_c is greater than 2.6, it is possible to use $q_{c1N} = Q$, otherwise, with I_c less than or equal to 2.65, Q should be recalculated using a value of $n = 0.5$.

If recalculating Q with $n = 0.5$, the value of I_c continues to be less than 2.6 normalization of the resistance is maintained with the eq. 1-36. Otherwise, the value normalization should be made using $n = 0.75$ and recalculate the value of the I_c. Note that this behavioral index allows a general characterization of the type of soil penetrated (Table 1-5).

Table 1-5 – Soil behavior index limits (I_c).

Soil behaviour type index, I_c	Zone	Soil type
$I_c < 1.31$	7	Gravelly sand to dense sand
$1.31 < I_c < 2.05$	6	Sand: Clean sand to silty sand
$2.05 < I_c < 2.60$	5	Sand mixtures: silty sand to sandy silt
$2.50 < I_c < 2.95$	4	Silt mixtures: clayey silt to silty clay
$2.95 < I_c < 3.60$	3	Clays: silty clay to clay
$I_c > 3.60$	2	Organic soil: peats

With the value of I_c defined, the calculation of the k_c correction factor is possible (eq. 1-37 and eq. 1-38). If the value of I_c is less than or equal to 1.64, caution must be taken due to the possible confusion of identification of loose sands with sands containing fines, yielding lower resistance values, this is the reason why for behavior indexes less than 1.64, it is indicated to approximate the result to a constant value of 1.

$$I_c \leq 1.64 \quad k_c = 1 \qquad \textbf{eq. 1-37}$$

$$I_c > 1.64 \quad k_c = -0.403{I_c}^4 + 5.581{I_c}^3 - 21.63{I_c}^2 + 33.75I_c - 17.88 \qquad \textbf{eq. 1-38}$$

Finally, with the normalized penetration resistance, it is possible to calculate the cyclic resistance (eq. 1-39 and eq. 1-40). This relationship is not unique, and different ones have been proposed in the bibliography (Christian and Swiger (1975), Liao et al. (1988), Liao and Lum (1998), Youd and Nobel (1997), Toprak et al. (1999), Juang et al. (2002), Cetin et al. (2002, 2004), and Moss et al. (2006)).

$$CRR_{7.5} = 93\left(\frac{(q_{c1N})_{cs}}{1000}\right)^3 + 0.08 \qquad \textbf{eq. 1-39}$$

For: $50 \leq (q_{c1N})_{cs} < 160$

$$CRR_{7.5} = 0.833\left(\frac{(q_{c1N})_{cs}}{1000}\right) + 0.05 \qquad \textbf{eq. 1-40}$$

For: $(q_{c1N})_{cs} < 50$

Note that the equations divide the space $CSR - q_c$, in two subspaces. These subspaces are characterized by representing the response of liquefied and non-liquefied soil, so the equation represents the limiting resistance of the soil CRR (Figure 1-33).

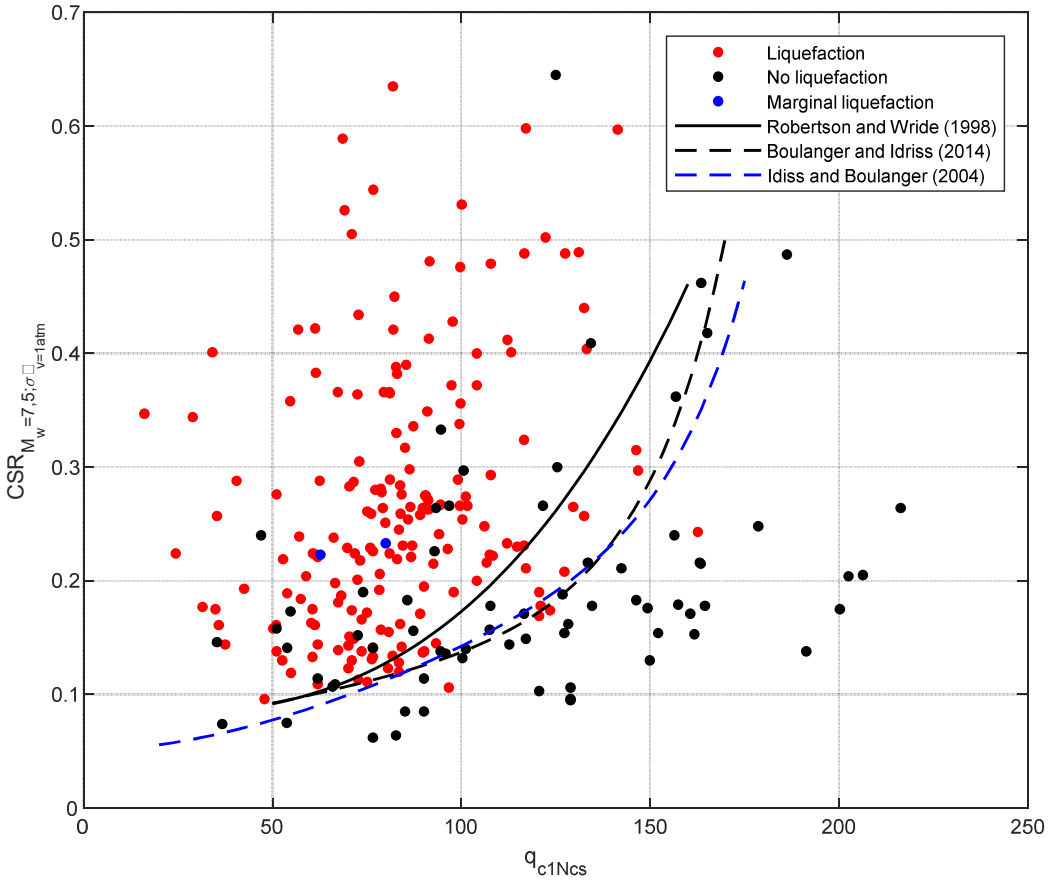

Figure 1-33- Summary graph of relationships between penetration resistanceq_c and cyclic resistance.

The general flow diagram of the method is presented in Figure 1-34.

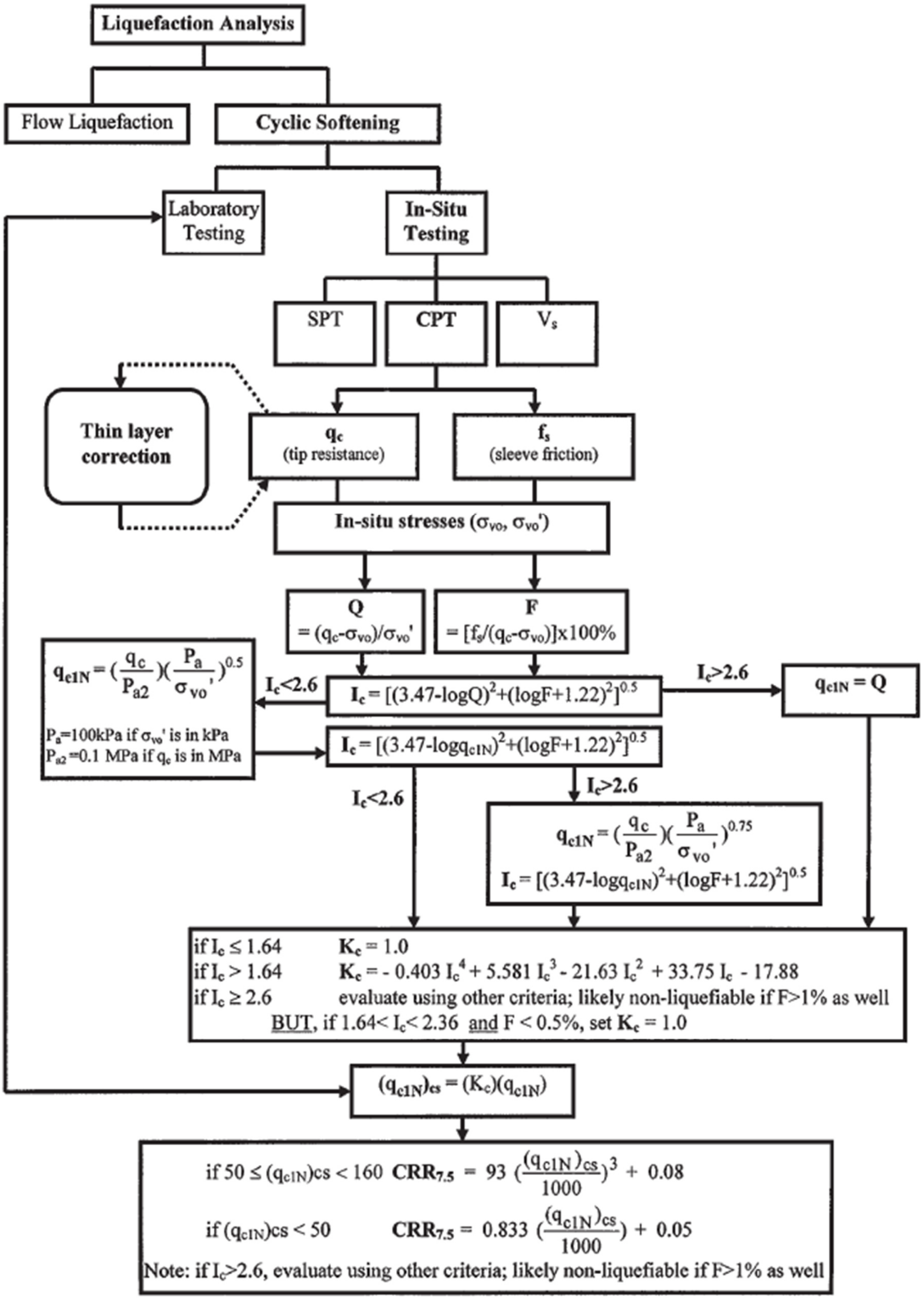

Figure 1-34 – Flow chart of application of the liquefaction potential evaluation method using CPT penetration tests (Robertson and Wride 1998)**.**

1.3.5.3 Other liquefaction potential evaluation methods and equipment

Other geotechnical methods and equipment have been used to evaluate liquefaction potential, such as the Becker penetrometer (Harder 1993; Rollins, Youd, and Talbot 2016) and shear wave velocity (Andrus and Stokoe 1998, 2000; Youd et al. 1997). The Becker penetrometer (Figure 1-35) has been used in the evaluation of liquefaction potential in gravelly soils, due to the difficulty in using SPT or CPT tests, wich results are strongly disturbed by the presence of large particles, yielding unrealistic penetration resistance values (Harder 1993). Due to the limited availability of tests that allow the construction of a database with historical cases, the method based on this equipment is based on the use of correlations with the SPT test (Figure 1-36).

Figure 1-35 - Becker penetrometer (UCD 2022)**.**

The liquefaction potential evaluation method based on in-situ measurement of shear wave velocities V_s which can be measured in situ through tests such as spectral analysis of surface waves ($SASW$), is based on the establishment of a relationship between the cyclic resistance and V_s considering that both parameters are similarly influenced by effective consolidation stress, void ratio, geologic age and stress history. In its development, several procedures have been presented (Andrus 1994; Kayen et al. 1992; Robertson, Woeller, and Finn 1992; Stokoe et al. 1988; Tokimatsu, Tamura, and Kuwayama 1991) However, the current standard has been presented by Andrus and Stokoe (2000).

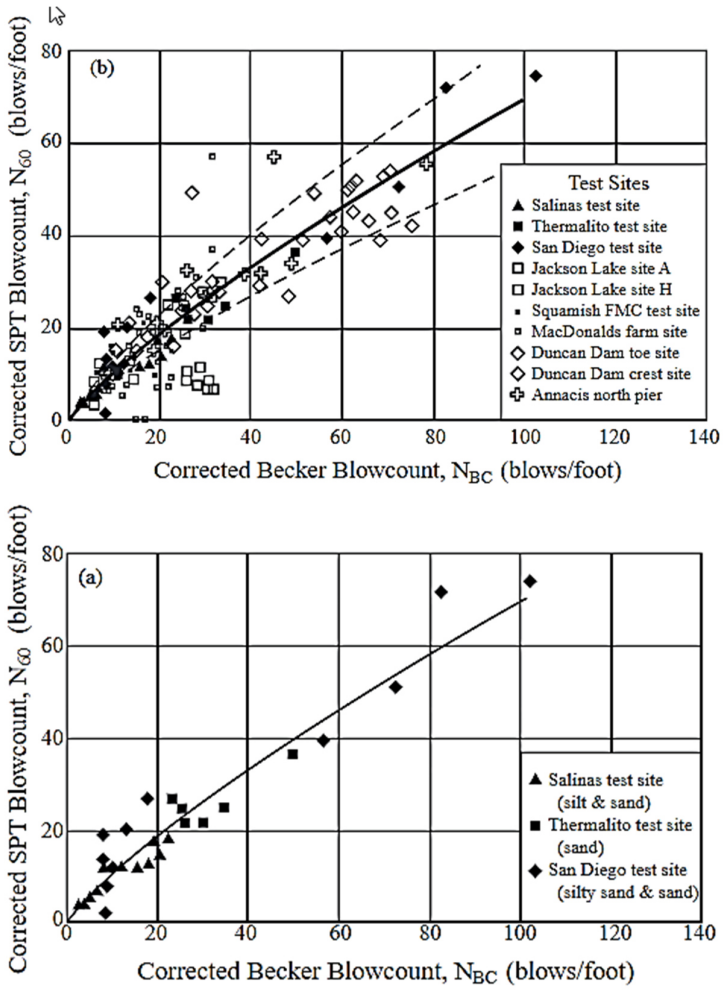

Figure 1-36 – SPT – Becker penetrometer correlation (Youd and Idriss 1997)**.**

The calculation of the cyclic resistance by means of shear wave velocity measurements can be performed by means of the eq. 1-41. The curve generated by this equation divides the space $CRR - V_{s1}$ in two subspaces describing liquefaction behavior above the CRR line and non-liquefaction behavior below the curve CRR (Figure 1-37).

$$CRR = \left[a\left(\frac{K_c V_{s1}}{100}\right)^2 + b\left(\frac{1}{V_{s1}^* - V_{s1}} - \frac{1}{V_{s1}^*}\right)\right] MSF \qquad \textbf{eq. 1-41}$$

Where:

$a = 0.022$
$b = 2.8$

$V_{s1}^* = 215\ m/s$ For $FC \leq 5\%$

$V_{s1}^* = 25 - 0.5(FC - 5)\ m/s$ For $5\% < FC < 35\%$

$V_{s1}^* = 200\ m/s$ For $FC \geq 35\%$

$$MSF = \left(\frac{M_w}{7,5}\right)^n$$

$$n = -2.56$$

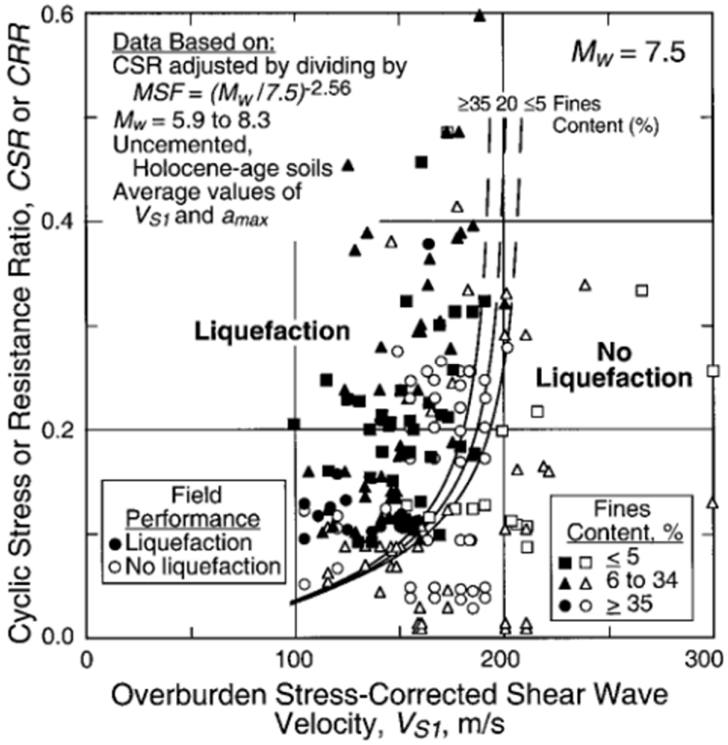

Figure 1-37 – CRR curve based on corrected shear wave velocity (Youd and Idriss 2001)**.**

1.3.6 Liquefaction potential evaluation with a light dynamic variable energy penetrometer

This part presents the liquefaction potential evaluation methods developed for applications by means of dynamic penetration tests. PANDA (AFNOR 2000b). The methods have been developed based on the application of correlations and comparative analysis of parameters obtained from other tests such as SPT or CPT, as well as using other equipment that allows the characterization of the soil based on geoendoscopy (Haddani 2001, 2004; Haddani et al. 2016). The methods developed have been initially based on fine granular soils from mine tailings for the stability analysis of tailings dams (Espinace et al. 2013; Jara 2013; Lepetit 2002; Villavicencio et al. 2012; Villavicencio et al. 2016).

1.3.6.1 Approach developed by Lepetit (2002)

Lepetit (2002) proposed liquefaction potential evaluation method using a dynamic penetrometer (PANDA 2) and based on correlations between the dynamic penetration

resistance q_d^{P2} and tip resistance q_c obtained by means of the penetrometer (eq. 1-42) (Chaigneau 2001; Langton 1999)

$$q_c \cong (0.93\ to\ 1.05) q_d \qquad \textbf{eq. 1-42}$$

Lepetit (2002) considers it a good approximation to establish an equivalence between the dynamic penetration resistance q_d^{P2} and static penetration resistance of CPT ($q_d^{P2} = q_c$). Based on this equivalence and the use of permeability k measurements for the definition of the behavioral index (I_c), Lepetit (2002) applies the method of liquefaction potential evaluation originally proposed by Robertson (Robertson and Campanella 1985; Robertson and Wride 1998).

The relationship between k and I_c is obtained from the hydraulic conductivity values proposed by Manassero (1994) and the soil classification proposed by Robertson and co-workers (Robertson 1990; Robertson et al. 1986) (Table 1-6). By means of linear regression it is possible to obtain the relationship that allows the calculation of the behavioral index I_c through a permeability measurement (Figure 1-38).

Table 1-6 - Relationship between permeability and soil behaviour index (I_c) (Lunne, Robertson, and Powell 1997; Manassero 1994)**.**

Soil type	I_c	$\frac{k}{m/s}$
Gravel	<1.31	$10^{-3} - 10^{0}$
sand	$1.31 < I_c < 2.05$	$10^{-5} - 10^{-3}$
Sandy mixtures	$2.05 < I_c < 2.60$	$10^{-7} - 10^{-5}$
Silty mixtures	$2.60 < I_c < 2.95$	$10^{-9} - 10^{-7}$
Clays	$2.95 < I_c < 3.60$	$10^{-10} - 10^{-9}$

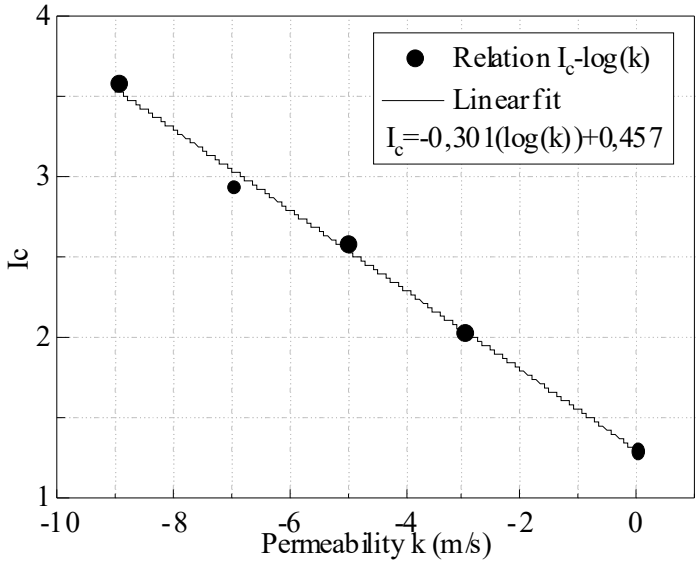

Figure 1-38 - I_c – k relationship (Lunne et al. 1997; Manassero 1994)**.**

Using the relationship between k and I_c it is possible to replace the behavior index I_c and reformulate the equation for the calculation of the k_c correction factor as a function of the permeability k (eq. 1-43 and eq. 1-44).

$$\mathrm{k}_c = 1 \qquad \textbf{eq. 1-43}$$

for $k > 1.4 \cdot 10^{-4}(m/s)$

$$\mathrm{k}_c = 0.26 \cdot (\log(k))^2 + 2.6 \cdot (\log(k)) + 5.49 \qquad \textbf{eq. 1-44}$$

For $k < 1.4 \cdot 10^{-4}(m/s)$

The general flow diagram of the method is presented in Figure 1-39.

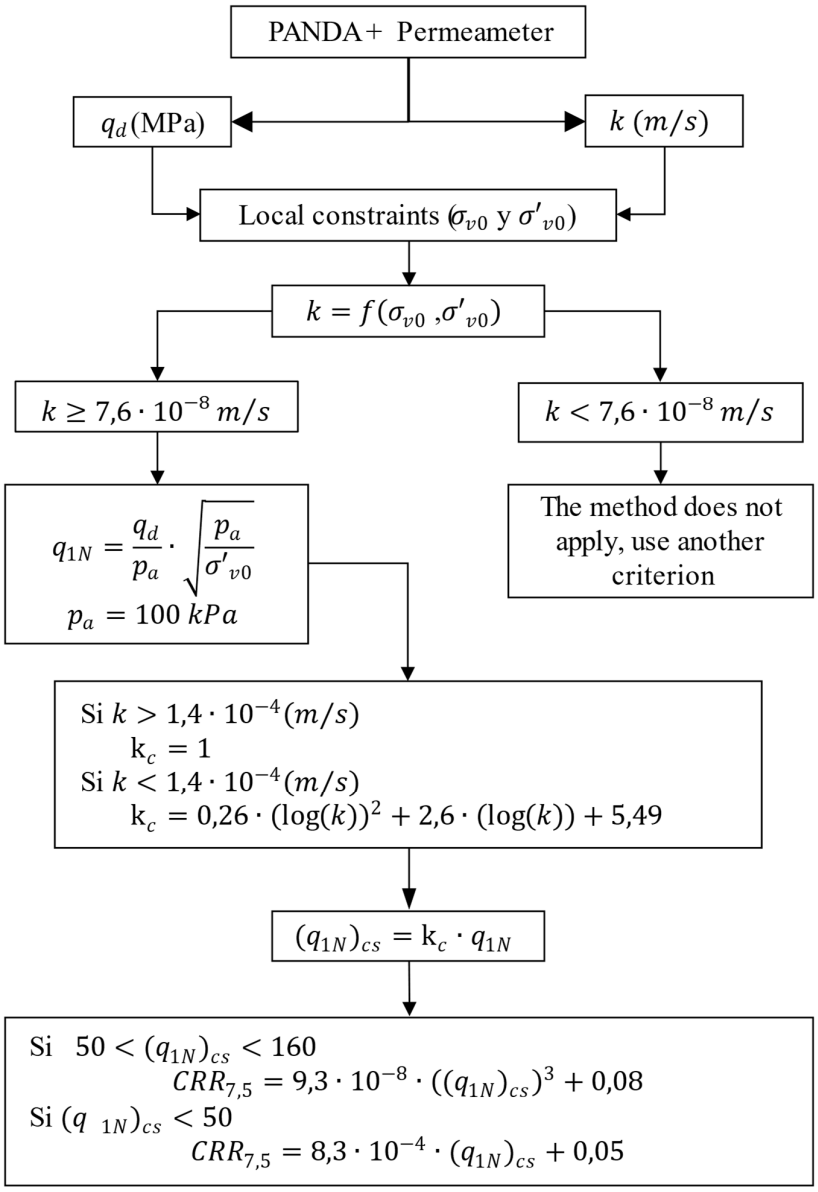

Figure 1-39. Scheme of Lepetit method proposed for liquefaction potential evaluation using light dynamic variable energy penetrometer (Lepetit 2002)**.**

1.3.6.2 Approach developed by Jara (2013)

Using a PANDA 3 dynamic penetrometer and geoendoscopy equipment (Haddani 2001, 2004; Haddani et al. 2016), Jara, (2013) proposed two methods for the evaluation of liquefaction potential initially intended for the analysis of fine sands from mining tailings. Both methods are based on the evaluation of dynamic penetration resistance q_d^{P3} and soil characteristics using geoendoscopy results.

In the first method Jara, (2013) proposes an equivalence between PANDA 3 dynamic and CPT static penetration resistance ($q_d^{P3} = q_c$) and later applying the liquefaction potential evaluation method proposed by Robertson (Robertson and Wride 1998). In the second method Jara, (2013) proposes an equivalence between the shear wave velocity obtained by analyzing the dynamic signals of the PANDA 3 penetrometer C_s^{P3} and the shear wave velocity v_s thus making it possible to apply the methodology proposed by Andrus and Stokoe (2000).

a. First method proposed by Jara (2003)

The first method proposed by Jara, (2013) is based on the same principles as the approach proposed by Robertson and Wride (1998), in which one of the most important steps is the knowledge of the density state of the soil, which can be obtained through previous studies or by applying $q_d - \gamma_d$ relations predetermined for the penetrometer (eq. 1-45) (Chaigneau, 2001; Gansonré et al., 2019; López Retamales et al., 2020; López Retamales et al., 2021).

$$\gamma_d = \mathrm{A}\ln(q_d) + B \qquad \textbf{eq. 1-45}$$

With A and B, being two factors associated with soil types and soil conditions.

If the density of the soil is known, it is possible to establish the value of σ'_{v0} and it is possible to apply the correction for the overburden stress. For this purpose an exponent $n = 0.5$ is used (Jara 2013). Then, the correction is carried out by the application of the eq. 1-46.

$$q_{d1N} = \frac{q_d}{P_a}\left(\frac{P_a}{\sigma'_{v0}}\right)^n \qquad \textbf{eq. 1-46}$$

In the original method of Robertson and Wride, it is possible to obtain the fines content by means of the behavioral index I_c. However, in the case of Jara (2013), this index is not available. On the other hand, it is possible to evaluate the fines content through a geoendoscopy test and the analysis of images obtained from this test (Haddani 2001, 2004; Haddani et al. 2016), and through this it is possible to calculate the index I_c solving it from the equation proposed by (Robertson and Wride 1998) (eq. 1-47).

$$I_c = \left(\frac{FC + 3.7}{1.75}\right)^{\frac{1}{3.25}} \qquad \textbf{eq. 1-47}$$

for:

$$FC \in [0.01\%; 99\%]).$$

If the value of the CPT behavioral index is available, it is possible to calculate the k_c correction factor to obtain the corrected penetration resistance value, which allows obtaining the CRR value corrected for magnitude and fines content by using the eq. 1-48 (Idriss and Boulanger 2004) (The general flow diagram of the Jara (2013) method is presented in Figure 1-40).

$$CRR_{7.5;1\,atm} = e^{\left(\frac{q_{c1Ncs}}{540}+\left(\frac{q_{c1Ncs}}{67}\right)^2-\left(\frac{q_{c1Ncs}}{80}\right)^3+\left(\frac{q_{c1Ncs}}{114}\right)^4-3\right)} \qquad \textbf{eq. 1-48}$$

b. Second method proposed by Jara (2003)

The second method proposed by Jara (2013) is based on the consideration of equivalence between the shear wave velocity obtained by means of the PANDA 3 penetrometer (C_s^{P3}) and shear wave velocity conventionally obtained by in-situ tests such as SASW (V_s). With this hypothesis, it is possible to perform an evaluation of the liquefaction potential by applying the same concepts as used in the ones the method presented by Andrus & Stokoe (2000).

For the application of this method, it is necessary to apply the normalization or correction for vertical overburden stress. For this it is necessary to establish the density value of the soil in the same way as in method 1. For this it is necessary to obtain the density through previous studies of the soil or through the application of pre-stabilized $q_d - \gamma_d$ relations for different soil types and conditions (Chaigneau, 2001; Gansonré et al., 2019; López Retamales et al., 2020; López Retamales et al., 2021). Knowing the variables of density and C_s^{P3}, it is possible to obtain the corrected shear wave velocity measurement (eq. 1-52).

$$(Cs_{P3})_1 = Cs_{P3}\left(\frac{P_a}{\sigma'_{v0}}\right)^{0.25} \qquad \textbf{eq. 1-49}$$

The fines content is obtained by analysis of images taken through the geoendoscopy test (Haddani 2001, 2004; Haddani et al. 2016), With this, it is possible to calculate the k_{cs} correction factor for fines content (eq. 1-50, eq. 1-51 and eq. 1-52).

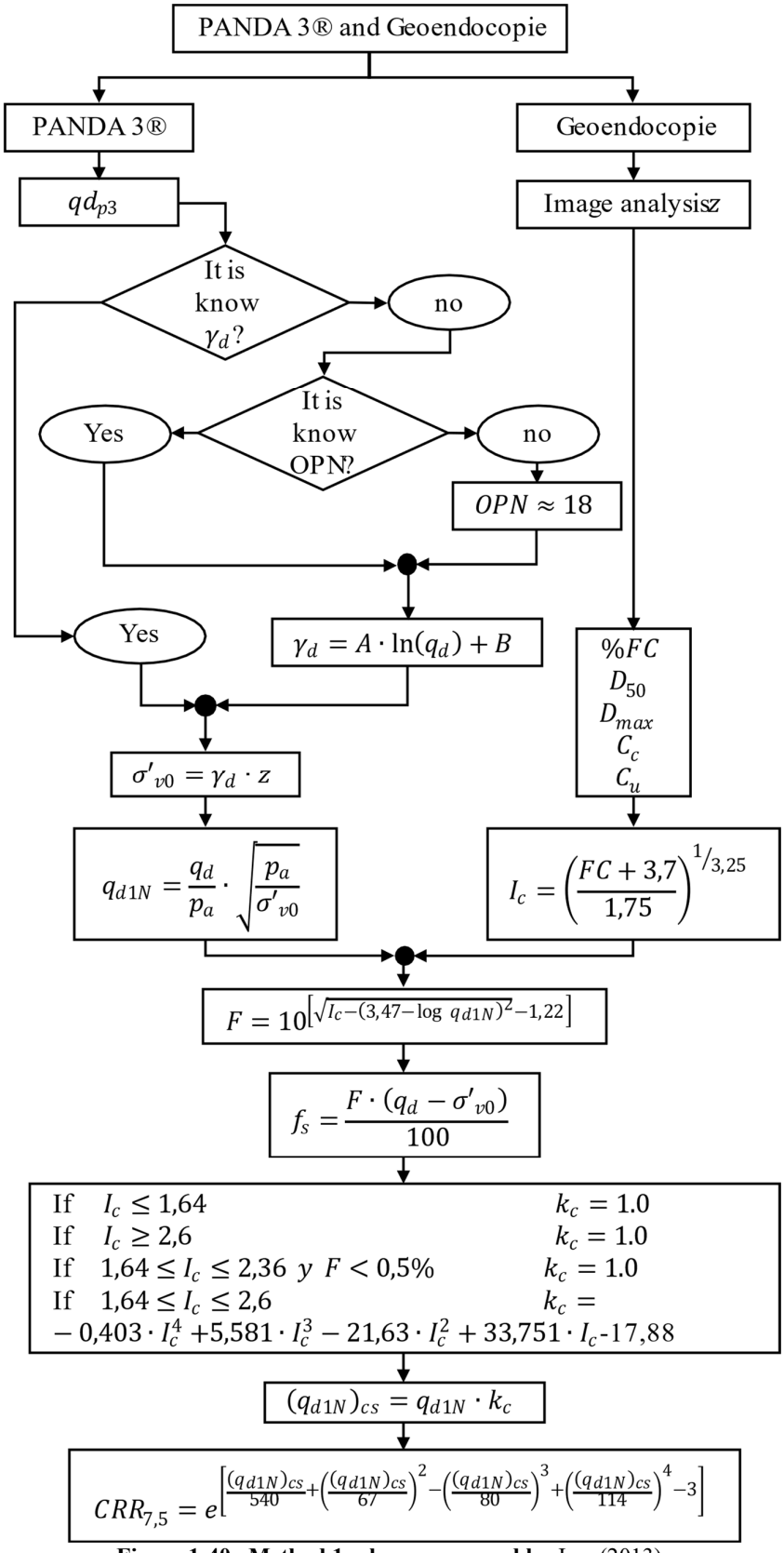

Figure 1-40. Method 1 scheme proposed by Jara (2013)**.**

$$k_{cs} = 1 \qquad FC \leq 5\% \qquad \textbf{eq. 1-50}$$

$$k_{cs} = 1 + T(FC - 5) \qquad 5\% < FC < 35\% \qquad \textbf{eq. 1-51}$$

$$k_{cs} = 1 + 30T \qquad FC \geq 35\% \qquad \textbf{eq. 1-52}$$

Where T is a factor as a function of the shear wave velocity (Juang et al. 2002) (eq. 1-53).

$$T = 0.009 - 0.0109\left(\frac{(Cs_{P3})_1}{100}\right) + 0.0038\left(\frac{(Cs_{P3})_1}{100}\right)^2 \qquad \textbf{eq. 1-53}$$

Then, the value of the corrected cyclic resistance ($CRR_{7,5cs}$) is obtained through the eq. 1-54.

$$CRR_{7,5cs} = 0.022\left(\frac{(Cs_{P3})_{1CS}}{100}\right)^2 + 2.8\left(\frac{1}{V_{s1c} - (Cs_{P3})_{1CS}} - \frac{1}{V_{s1c}}\right) \qquad \textbf{eq. 1-54}$$

Where V_{s1c} corresponds to the upper limit of liquefaction occurrence indicated by the Andrus & Stokoe (2000) method. The limit value is calculated by the eq. 1-55

$$V_{s1c} = 200 + \frac{35 - FC}{30} \cdot 15 \qquad \textbf{eq. 1-55}$$

The general flow diagram of the method is presented in the Figure 1-41

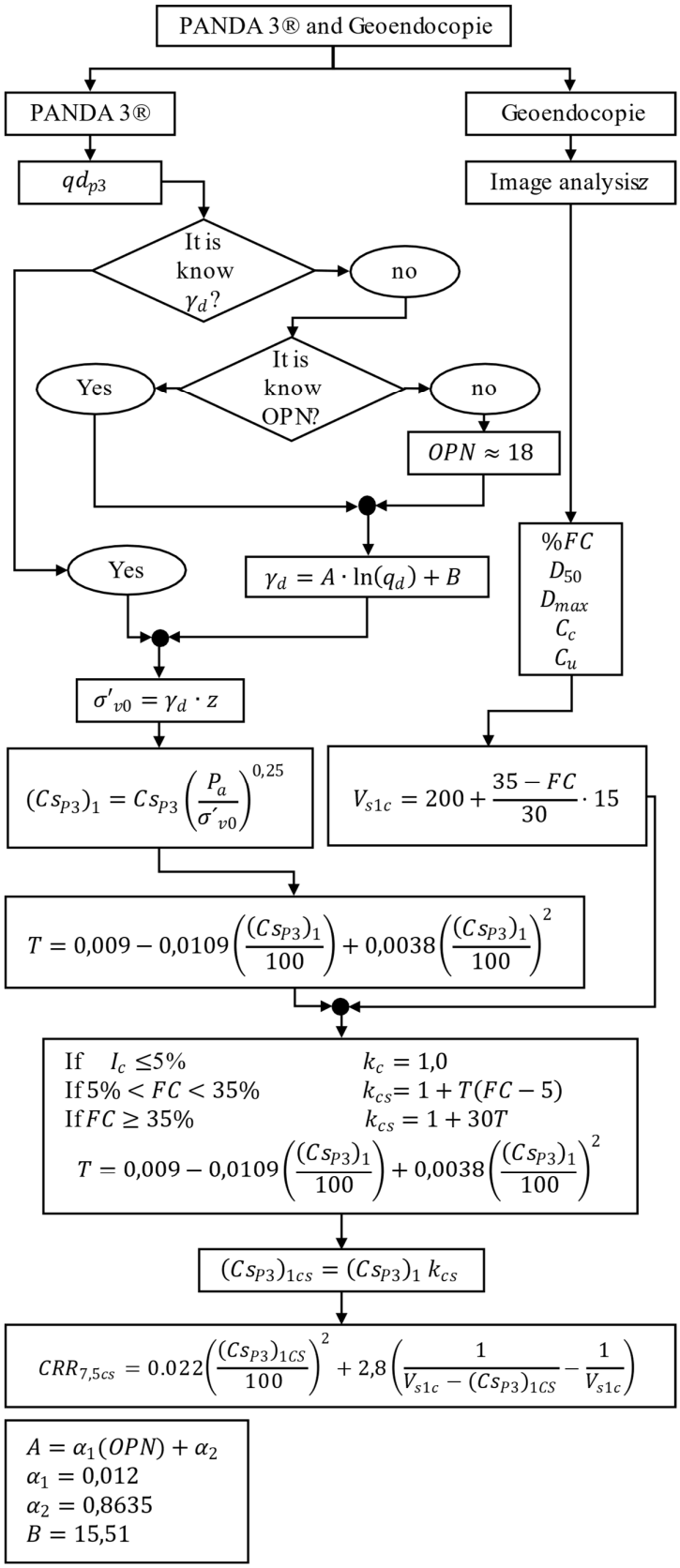

Figure 1-41. Method 2 scheme proposed by Jara (2013)**.**

1.4 Conclusions

In consideration of the bibliographic review presented, it is possible to conclude that the study of the liquefaction phenomenon is still a work in progress, which seeks the continuous improvement of the understanding and evaluation of this phenomenon, both with laboratory equipments and field tests. However, it was also found that the methodologies for the evaluation of liquefaction potential still present some elements that require improvement.

In general, laboratory tests present a high degree of accuracy in the measurements obtained during their application; however, in the case of cyclic strength evaluation, one of the disadvantages observed is related to the representativeness of the tested soil. A specimen reconstituted in the laboratory may not be representative of the real soil conditions because, during extraction, the stress states and the sand structure are highly altered.

Field tests have the advantage of obtaining data from the soil in its natural state. However, the main disadvantages observed are related to the repeatability of the results and the complexity of their interpretation. The most commonly used in situ tests are the standard penetration test (SPT) and the cone penetration test (CPT) as well as shear wave propagation test. The SPT presents difficulties associated with the repeatability and the difficulty in the interpretation of the test, since this is a dynamic test, where variables such as the driving energy are difficult to control. Although presenting a high degree of accuracy and repeatability, CPT test presents difficulties in its implementation, because it requires a reaction mass greater than that required in dynamic tests, and the results can be disturbed by the presence of large rocks in the soil, which result in unrealistic resistance results. In the case of the use of shear waves, this presents difficulties in the consideration of the range of deformations in the operation, since shear waves operate in the range of small deformations and liquefaction is a phenomenon associated with large deformations.

Although there are disadvantages and difficulties for both laboratory and field tests, both methods allow the evaluation of liquefaction potential and can be complementary, thus allowing a more accurate result.

The dynamic variable energy penetrometer is presented as an alternative to the methods currently in use. However, this type of test lacks its own frame of reference on which to base the construction of a liquefaction evaluation method, therefore the methods presented are based on correlation with other methods to access databases of historical cases. The possibility of establishing correlations between variable energy dynamic penetration tests and penetration tests commonly used in the evaluation of liquefaction potential would allow expanding the use

of dynamic penetrometers and making available a portable rapid test for the evaluation of liquefaction potential.

2 EXPERIMENTAL SETUP AND TEST PROCEDURES

2.1 Tested sands characterization

2.1.1 Hostun sand (HN31)

Hostun HN31 sand is a sand whose particles are mostly light gray in color and composed mainly of silica ($SiO_2 > 99\%$), and of a uniform gradation (Figure 2-1). The grains have angular to subangular shapes. Due to their mineralogical composition, the individual particles have a high breaking strength. The main properties of the granular assemblage are presented in Table 2-2.

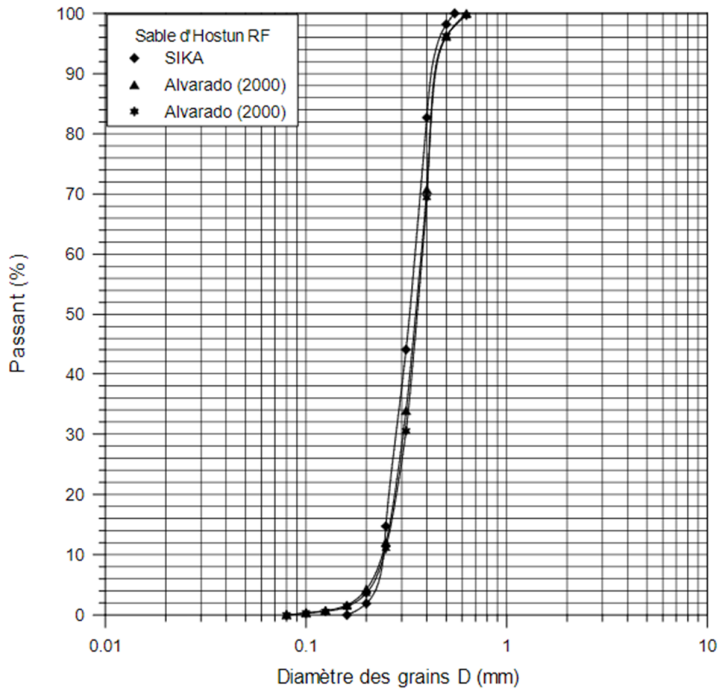

Figure 2-1 - Hostun HN31 sand granulometry (Benahmed 2001)**.**

Table 2-1. Hostun HN31 sand parameters.

Parameter	Value
Specific gravity ρ_s	$2.65\ g/cm^3$
D_{50}	0.35
C_u	1.57
ρ_{min}	$1.33\ g/cm^3$
ρ_{max}	$1.60\ g/cm^3$

Different values of e_{min} and e_{max} were found in the available literature (Benahmed 2001; Zhu et al. 2021). In order to obtain these parameters, a laboratory study was carried out using a standardized procedure (AFNOR 2000a). The test results provided values of $e_{min} = 0.67$ and $e_{max} = 1.03$ for the minimum and maximum void ratio respectively.

2.1.2 Fontainebleau NE34 sand

Fontainebleau NE34 sand is a sand whose particles are mostly light beige in color, composed mainly of silica ($SiO_2 > 98\%$), and of uniform gradation (Figure 2-2). The individual grains have a sub-rounded shape and a high breaking strength. The main properties of this sand are presented in Table 2-2

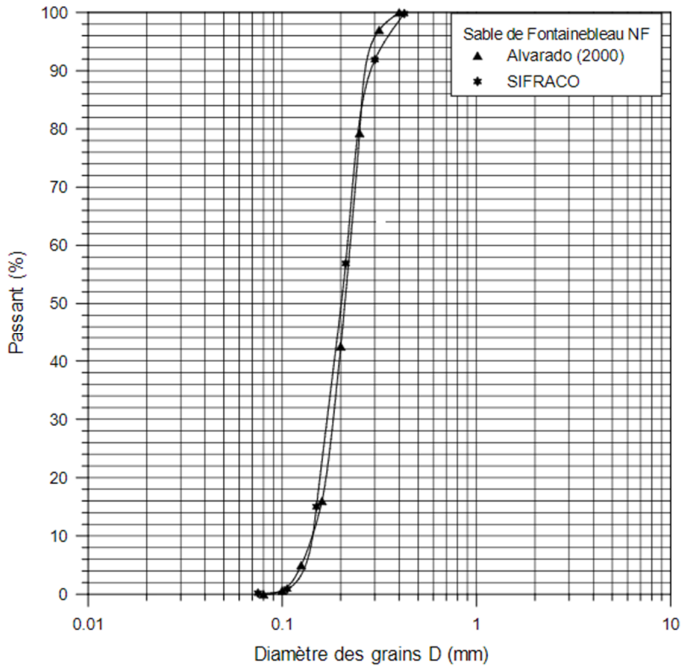

Figure 2-2. Fontainebleau NE34 sand granulometry (Benahmed 2001)**.**

Table 2-2. Fontainebleau NE34 sand parameters.

Parameter	Value
Specific gravity (ρ_s)	2.65 g/cm^3
D_{50}	0.21
C_u	1.52
ρ_{min}	1.37 g/cm^3
ρ_{max}	1.72 g/cm^3

Different values of e_{min} and e_{max} were found in the available literature for this sand (Benahmed 2001; Latini and Zania 2016; Li, Escof, and Kotronis 2013; Serratrice 2002; Thiet 2005), however, measurements performed in the laboratory by standardized procedure (AFNOR 2000a), provided values of $e_{min} = 0.55$ and $e_{max} = 0.85$ for minimum and maximum void ratio respectively.

2.2 Lightweight dynamic variable energy penetrometer

To perform the tests, a penetrometer (PANDA3®) (Figure 2-3), with the capacity to measure and process the dynamic signals generated by the dynamic driving of a hammer is used (Benz 2009b;

Benz et al. 2022; Gourvès 1991; Langton 1999). This equipment, developed in France in the 1990s, has been widely used in geotechnical applications associated with road, mining, airport, railway infrastructure, among others (Benz Navarrete et al., 2013; Escobar et al., 2014; Escobar Valencia et al., 2016; Espinace A et al., 2013; López Retamales et al., 2020; López et al., 2018, 2019; López & Benz, 2019; López Retamales et al., 2021; López Retamales et al., 2021).

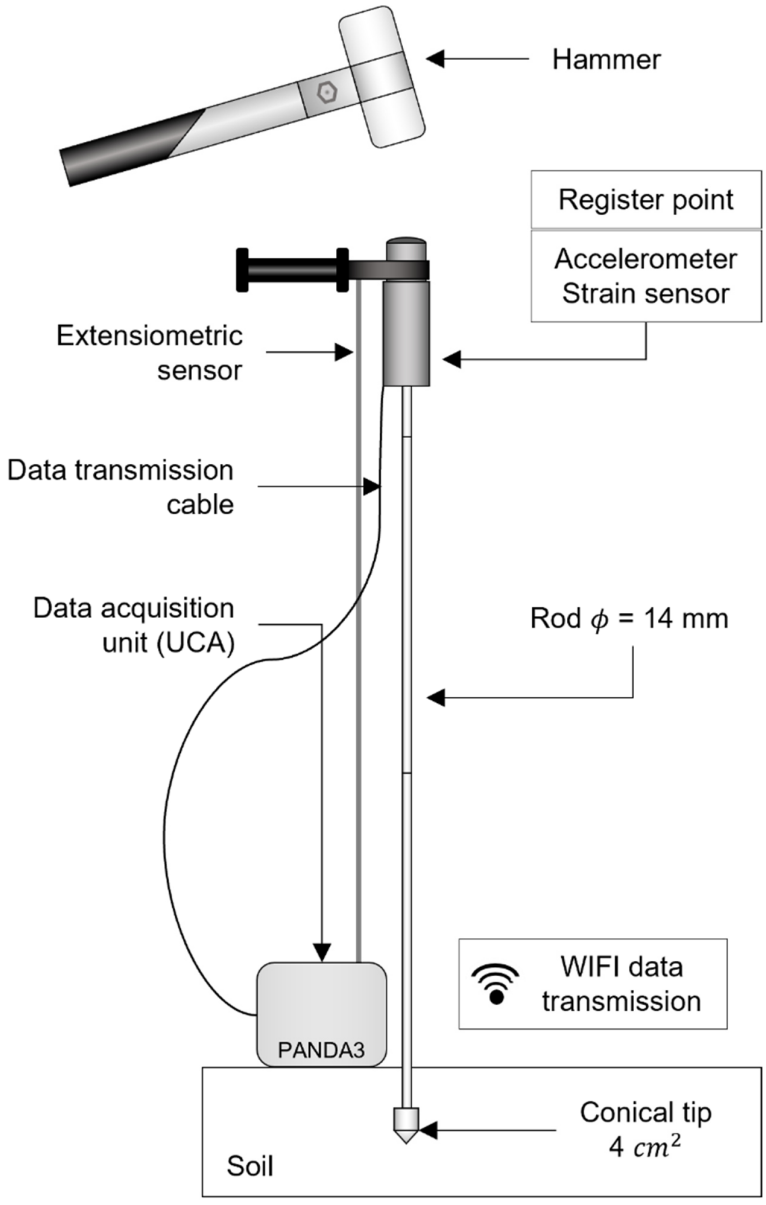

Figure 2-3 - Schematic diagram of light dynamic variable energy penetrometer (PANDA3).

The penetrometer consists of a standardized hammer, the penetrometer body, and a data acquisition unit (UCA). The penetrometer body consists of an instrumented impact head with accelerometers with a measuring range of ± 20,000 g and strain sensors with a measuring range of ±45 kN. Bolted to this are 500 mm long and 14 mm in diameter rods, which can be extended to

recorded depths of up to 21 meters. At the opposite end of the bars a 2 or 4 cm^2 conical tip is installed, with an angle of 90° according to the standard (ISO 22476-2, 2005) (Figure 2-3).

The central data acquisition unit (*UCA*) is a device that is located on the surface of the soil and at the side of the bar train and is also instrumented with a displacement sensor, which is connected to the striking head by means of a strap (Figure 2-3). This device receives and store the data generated, and also serves as a guide for the rod train.

The visualization of data and test results can be performed in real time on any portable device (tablet or cell phone), through wireless connection (Wi-Fi), and through an application specially developed for this purpose by Sol Solution. The application allows the configuration and control of the dynamic penetration test, the transfer of the test results from the UCA and storage of these in the required device.

The results can be post-processed using SigmaSprint software. The software contains the tools to perform a correction and treatment of the signals for the subsequent evaluation of the dynamic response of the soil. In addition, the implemented algorithms allow the calculation of the geotechnical parameters of the soil associated with the dynamic penetration test.

2.2.1 Operating principle

The operating principle of the dynamic penetrometer is based on the evaluation of dynamic strain and acceleration signals generated by the impact of a hammer driven by dynamic energy.

When the hammer impacts the penetrometer body, two compression waves are generated, one propagating downward through the rods of the penetrometer and the other propagating upward through the hammer. This compression wave will propagate through the penetrometer until it reaches the cone-soil interface, at which point an energy transfer to the soil will occur (Figure 2-4). The wave will be reflected and detected by the sensors and accelerometers located in the striking head.

In the measured signals, the incident and reflected wave fronts are superimposed, so an iterative process of decoupling and wave reconstruction is applied to obtain the force and velocity signals at the cone-soil interface. These signals allow a parametric evaluation of the soil and the construction of dynamic cone load test curves of the soil also called $DCLT$ curve.

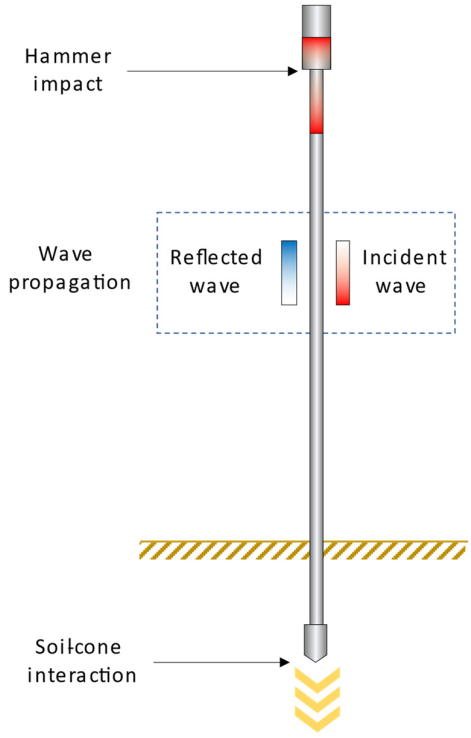

Figure 2-4 – Diagram showing the principle of operation of the DPT.

2.2.2 Data acquisition and processing

The signals measured by the deformation sensors and accelerometers are sent to the data acquisition unit *UCA (*from French *unite centrale d´acquisition)*, a device in which they are stored. The data acquisition is made at 250 kHz frequency and 24 $bits$ resolution and the data are recorded in a time interval of 100 to 200 ms (Benz Navarrete et al. 2022).

The signals are affected by boundary conditions and sensor-specific problems. To solve this problem, baseline corrections and filtering are applied by applying a low-pass filter and a cutoff frequency of 25 kHz (Benz Navarrete et al. 2022).

2.2.3 Rod friction analysis

The compression wave generated by the impact of the hammer travels downward through the penetrometer, generating a particular localized displacement. When this wave reaches the surface of the soil it starts an interaction with the soil that produces a lateral friction (Figure 2-5). This lateral friction is capable of producing a partial reflection of the wave. (Nishida, Sekiguchi, and Matsumoto 1986).

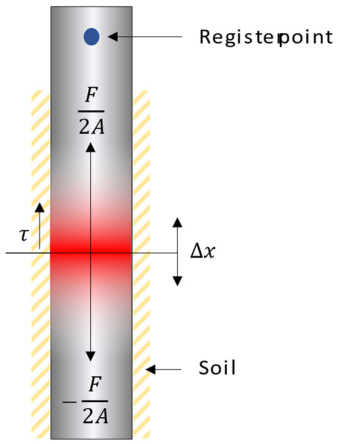

Figure 2-5 - Lateral rod-soil interaction diagram.

Since the disturbance generated by the passing wave is small, the mobilized frictional resistance can be considered as a concentrated force, which will depend on the lateral frictional resistance of the soil (τ_f), the extent of the zone disturbed by the wave front (Δx), and the perimeter of the rod (P_r) (eq. 2-1). Considering the above, it is possible to deduce that the longer the length of the set of rods, the larger the frictional effects on the dynamic signals.

$$F_f = \tau_f \Delta x P_r \qquad \textbf{eq. 2-1}$$

The measurement of friction effects in a penetrometer test is complex due to the high number of factors that can affect the dynamic signals (impedance changes, external vibrations, secondary reflections, among others). However, in the case of a penetrometer, it is possible to quantify friction effects under the hypothesis that at time interval $2\, l_r/c_r$ (with l_r the rod length and c_r wave velocity), the measurements are disturbed only by lateral friction effects.

In the range of $2\, l_r/c_r$, a cycle of reflected waves is theoretically produced, and the force and velocity signals represented as force signal should maintain a proportional line (Figure 2-6). After the first reflection, it is not possible to perform this analysis due to the superposition of waves and to the fact that the vector sum of forces and velocities behave in opposite ways. In the case of the force measurement, the wave is normally reflected as a traction wave and the superposition of the measurements corresponds to a subtraction, in the case of the velocities the vectors are superimposed as a sum of magnitudes and the net result is an increase in magnitude.

Figure 2-6a shows the signals obtained from the dynamic driving generated on a set of rods of 4 meters in length. The proportionality of the force and velocity signals in the time interval 2 l_r/c_r is shown here (Figure 2-6b).

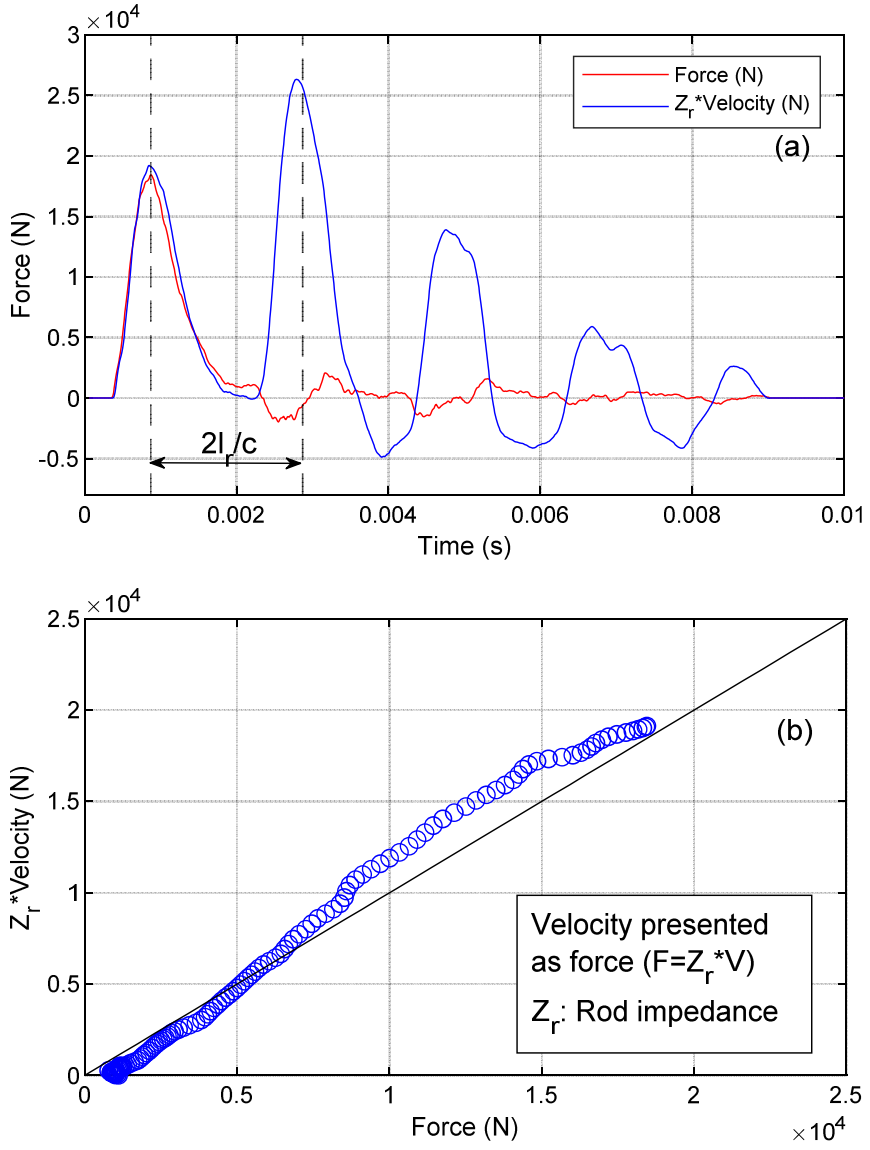

Figure 2-6 – Dynamic force and velocity ($Z * V$) measurements for a set of 4 m rods.

For of this research, penetrometer configurations with rod lengths of 1 meter were used, so the magnitude of lateral friction forces can be considered negligible.

2.2.4 Wave reconstruction at the cone-soil interface

2.2.4.1 Initial conditions for the generation of elastic waves

A wave is considered elastic if it propagates through an elastic medium and in its passage can disturb the particles by displacing them from their initial point with a wave motion that ends at the

initial point. This stress wave propagating through the elastic body can be generated in different ways, such as an earthquake in the case of the soil, an explosion, the forced deformation of an elastic body, and in the case of a penetrometer, the impact of a mass such as a hammer.

The wave propagation characteristics will depend on the materiality and shape of the body. However, it is considered that the wave propagation through the steel bar will be within the range of elastic behavior. In this case, it is necessary to establish the limit of validity of the analysis to that perturbation generated that does not imply the development of plastic deformations or failure in the material due to the effects of vibrations. In case of plastic deformations, the analysis becomes more complex because the energy contained by the wave is dissipated by other mechanisms and not only by the penetrometer-soil interaction.

Considering that the velocity at which the wave propagates (c_r), is constant as the homogeneity and elasticity of the material and the dimensions of the body are maintained. The equation that allows the calculation of the propagation velocity is expressed as a function of the elasticity modules (E), density (ρ) and Poisson's coefficient of the medium (ν), as follow:

$$c_r = \sqrt{\frac{1}{\rho}\frac{E(1-\nu)}{(1+\nu)(1-\nu)}} \qquad \textbf{eq. 2-2}$$

Taking into account the geometry of the penetrometer, the wave will travel mainly through the rod, whose characteristics correspond to those of a thin body. The propagation of a wave in this type of element will generate zones of compression and traction in its passage, generating zones of radial extension and compression in the rod (Figure 2-7). his deformation can be described by means of Poisson's coefficient (ν) and is an important factor in the evaluation of the wave propagation velocity in a material.

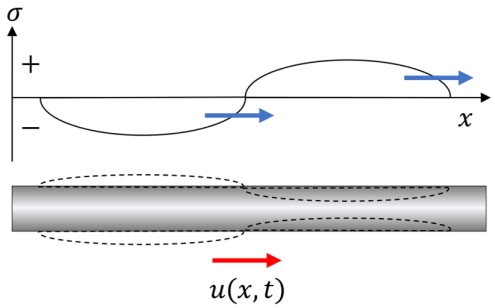

Figure 2-7 – Deformational effect of the passage of a compression wave in a thin body (after Graff, 1991).

In the case of the penetrometer, the radial deformations produced by the passage of the wave in the thin body can be considered negligible and the propagation velocity in the body is considered to

be independent of Poisson's coefficient (Timoshenko and Goodier 1975). Thus the displacement velocity of the wave can be described in a simplified manner as follows:

$$c_r = \sqrt{\frac{E_r}{\rho}} \qquad \textbf{eq. 2-3}$$

2.2.4.2 Elastic wave propagation

A wave is produced by a disturbance generated in the medium, which can be triggered by multiple elements and sources, where examples of these can be: impacts, earthquakes, explosions, traffic, etc. In the case of the PANDA 3 dynamic variable energy penetrometer, the source generating the wave is the impact of the hammer on the penetrometer head.

It is possible to analyze the behavior and interaction of the wave generated in the penetrometer using the one-dimensional wave equation (eq. 2-4), however, it requires the consideration of some previous hypotheses:

- Constant wave propagation velocity.
- Elastic, homogeneous rods with uniform A_r cross-section.
- The external lateral forces applied to the rods are negligible.
- The rods are considered as a thin body (diameter d_r small in relation to its length l_r).

$$\frac{\partial^2 u}{\partial x^2} = \frac{1}{c_r}\frac{\partial^2 u}{\partial t^2} \qquad \textbf{eq. 2-4}$$

The one-dimensional wave equation can be analyzed by means of D'Alembert's solution (1756). This solution proposes the superposition of two waves propagating in opposite directions after their generation (eq. 2-5). Applying this solution implies the generation of an incident u_d and a reflected u_r wave, which can be obtained by decoupling methods (Casem et al. 2003; Jung et al. 2006; Lundberg and Henchoz 1977).

$$u(x,t) = u_i(x - c_t t) + u_r(x + c_t t) \qquad \textbf{eq. 2-5}$$

2.2.4.3 Force, velocity, and strain relationships upon wave propagation

It is possible to establish relationships between the force, velocity and deformation produced by the wave as it passes through the penetrometer, from the acceleration and deformation measurements in the instrumented equipment.

Using the solution to the wave equation (eq. 2-4) and the penetration equipment configuration $u_d(x - c_r t)$ will be considered as the wave displacing towards the tip or downward and $u_r(x + c_r t)$ as the wave reflected from the tip or upward. Then, from this solution, it is possible to define the unit strain $\varepsilon(x,t)$ and the particular velocity $v(x,t)$ of the wave, applying derivative with respect to displacement and time. The above can be expressed as follows:

$$\frac{\partial u(x,t)}{\partial x} = \frac{\partial u_d(x - c_r t)}{\partial (x - c_r t)} \frac{\partial (x - c_r t)}{\partial x} + \frac{\partial u_r(x + c_r t)}{\partial (x + c_r t)} \frac{\partial (x + c_r t)}{\partial x} \quad \textbf{eq. 2-6}$$

Note that:

$$\frac{\partial (x \pm c_r t)}{\partial x} = \frac{\partial (x)}{\partial x} \pm \frac{\partial (c_r t)}{\partial x} = 1 \quad \textbf{eq. 2-7}$$

Then, considering eq. 2-6 and eq. 2-7 and eq. 2-8, the unit deformation (ε) generated by the passage of the wave is expressed as follows:

$$\frac{\partial u(x,t)}{\partial x} = \frac{\partial u_d(x - c_r t)}{\partial x} + \frac{\partial u_r(x + c_r t)}{\partial x} \quad \textbf{eq. 2-8}$$

$$\varepsilon(x,t) = \varepsilon_d(x - c_r t) + \varepsilon_r(x + c_r t) \quad \textbf{eq. 2-9}$$

To obtain the particulate velocity, we proceed to the derivation of the solution with respect to time, as follows:

$$\frac{\partial u(x,t)}{\partial t} = \frac{\partial u_d(x - c_r t)}{\partial (x - c_r t)} \frac{\partial (x - c_r t)}{\partial t} + \frac{\partial u_r(x + c_r t)}{\partial (x + c_r t)} \frac{\partial (x + c_r t)}{\partial t} \quad \textbf{eq. 2-10}$$

Note that:

$$\frac{\partial (x \pm c_r t)}{\partial t} = \frac{\partial u_d(x)}{\partial t} \pm c_r \frac{\partial u_r(t)}{\partial t} = \pm c_r \quad \textbf{eq. 2-11}$$

Considering equations eq. 2-10 and eq. 2-11, it is possible to obtain a solution of the wave equation that allows to obtain the particulate velocity at a point of measurement x on the rod:

$$v(x,t) = \frac{\partial u(x,t)}{\partial t} = c_r \left(-\frac{\partial u_d(x - c_r t)}{\partial x} + \frac{\partial u_r(x + c_r t)}{\partial x} \right) \quad \textbf{eq. 2-12}$$

The eq. 2-12 can be rewritten as a function of the unit deformations generated by the passage of the wave, as follows:

$$v(x,t) = c_r\left(-\varepsilon_d(x - c_r t) + \varepsilon_r(x + c_r t)\right) \quad \textbf{eq. 2-13}$$

One of the main potentialities of the application of wave theory in the analysis of the mechanics of dynamic penetration is the possibility of calculating the force and particulate velocity of the wave from at least one measurement. However, the use of only one sensor limits the possibilities of analysis to the first reflection cycle of the wave front. In the case of the penetrometer used in this research, this limitation is eliminated by the use of an accelerometer and a strain sensor.

If the strain measurement is available, it is possible to use Hooke's law to relate force, strain and penetrometer characteristics as follows:

$$\sigma(x,t) = E\frac{\partial u(x,t)}{\partial x} \quad \textbf{eq. 2-14}$$

$$F(x,t) = EA_r\frac{\partial u(x,t)}{\partial x} \quad \textbf{eq. 2-15}$$

Note that the force is dependent on the unit strain of the material, which can be obtained from the wave deformation measurements. With this, the equation is expressed as follows:

$$F(x,t) = EA_r\left(\varepsilon_d(x - c_r t) + \varepsilon_r(x + c_r t)\right) \quad \textbf{eq. 2-16}$$

It is also possible to express the force as a function of the velocity, if it is considered that this can be expressed as a function of the unit strains. Then, the equation can be expressed as follows:

$$F(x,t) = \frac{EA_r}{c_r}\left(v_d(x - c_r t) + v_r(x + c_r t)\right) \quad \textbf{eq. 2-17}$$

If the acceleration measurements a are available, it is possible to obtain the velocity and strain by integrating it in the time domain. This is of interest if one considers the possibility of obtaining the particular strain measurement at a point x on the penetrometer. The velocity $v(x,t)$ and strain $s(x,t)$ can be obtained as follows:

$$v(x,t) = \int_{t_0}^{\infty} a(x,t)dt \quad \textbf{eq. 2-18}$$

$$s(x,t) = \int_{t_0}^{\infty} v(x,t)dt \quad \textbf{eq. 2-19}$$

2.2.4.4 Wave propagation within the soil-penetrometer system

The propagation of waves in a dynamic penetrometer of variable energy is a dynamic and cyclic phenomenon characterized by the magnitude of the energy used in the driving. However,

independently of the level of energy transmitted to the penetrometer, the mechanics of the wave-penetrometer-soil interaction is constant. If the characteristics of the penetrometer are varied, the inertial effects associated with the weight of the equipment begin to take on greater importance in the interaction.

The following is a general description of the wave propagation phenomena in the soil penetrometer system.

c. Wave generation in the penetrometer

At the infinitesimal instant of time, just when the hammer-penetrometer contact begins as a result of the collision (Figure 2-8), two compression waves are generated that will transport energy through both the hammer and the penetrometer body.

The waves start displacing both through the hammer and the penetrometer body. In the case of the hammer, the waves will be displaced to the opposite end where they will be reflected back to the point of origin, at which point part of the wave will be transmitted to the penetrometer body and part will be reflected back to the opposite end (Figure 2-8). The wave generated in the body of the penetrometer will be displaced downwards until it reaches the conical tip, where a part of the wave will be transmitted to the soil and another part will be reflected upwards to the point of origin where it will give rise to a cutoff phenomenon (Figure 2-8).

d. Wave Propagation in the penetrometer

The wavefront traveling through the penetrometer body eventually reaches the strain sensors and accelerometer, at which point the signal will show a maximum value that gradually decreases (Figure 2-8a). As it continues to descend, the wavefront reaches the cone-soil interface, at which point part of the energy is transferred to the soil as potential strain energy (Figure 2-8b). Due to the boundary conditions imposed on the cone, the wave is reflected as a tension wave (Figure 2-8c), which, upon arriving at the point of origin generates a shortening by traction of the material (Figure 2-8d), cutting the energy transfer from the hammer, this phenomenon is called cutoff. After the cutoff, the wave in the penetrometer is again reflected back to the cone-soil interface and the hammer begins to fall by gravity (Figure 2-8e). After this first impact, the process is repeated each time with a smaller amount of energy, until it is dissipated and the soil-penetrometer system reaches rest.

In the case of the PANDA 3 penetrometer, an elastic response phenomenon is produced with the capacity to restore energy to the system by generating a vertical pushing of the equipment. This vertical movement implies that the penetrometer gains potential energy capable of generating a new

force on the soil producing a "vibratory" phenomenon between the equipment and the soil characterized by new measurements of new peaks of maximum resistance, but of lesser magnitude.

When displacing through the penetrometer body, the waves suffer energy losses due to the interaction with the material and the morphological characteristics of the equipment. At impedance change points such as connections or section dimension variations, there will be energy losses associated to the reflection of part of the wave or to energy dissipating phenomena such as possible plastic and elastic strains.

Reflection and/or dissipation phenomena require attention if factors such as rod length are considered, since the longer the length of the rods, the greater the possibility of energy dissipation phenomena occurring. These effects have been studied previously and the effects of rod length on the magnitude of the dynamic driving energy have been proven. (Aoki and Cintra 2000; Lukiantchuki 2012; Odebrecht 2003; Odebrecht et al. 2005; Schmertmann 1978; Schmertmann and Palacios 1979; Schnaid, Odebrecht, and Rocha 2007)

e. Energy transfer to the soil

After a theoretical time of l_r/c_r since the collision between hammer and penetrometer occurred, the wave front reaches the cone-soil interface. At this point the magnitude of the net force is positive and cone extension occurs within the soil structure, which generates a resistant response.

When penetration work is performed on the soil, part of the energy contained in the wave will be converted to potential deformation energy and the remainder will be reflected back to the origin. The strains generated in the soil during the first loading cycle will be mostly plastic and to a lesser proportion elastic. The proportion of the type of strain will depend on factors such as density index, state and type of soil.

The mechanism of energy transfer to the soil will be repeated as long as there are internal reflections of the wave and the phenomenon of vibratory response, however, the strains produced by the secondary cycles may not generate the complete mobilization of the shear strength and produce strain phenomena associated with the compressibility and/or elasticity of the soil.

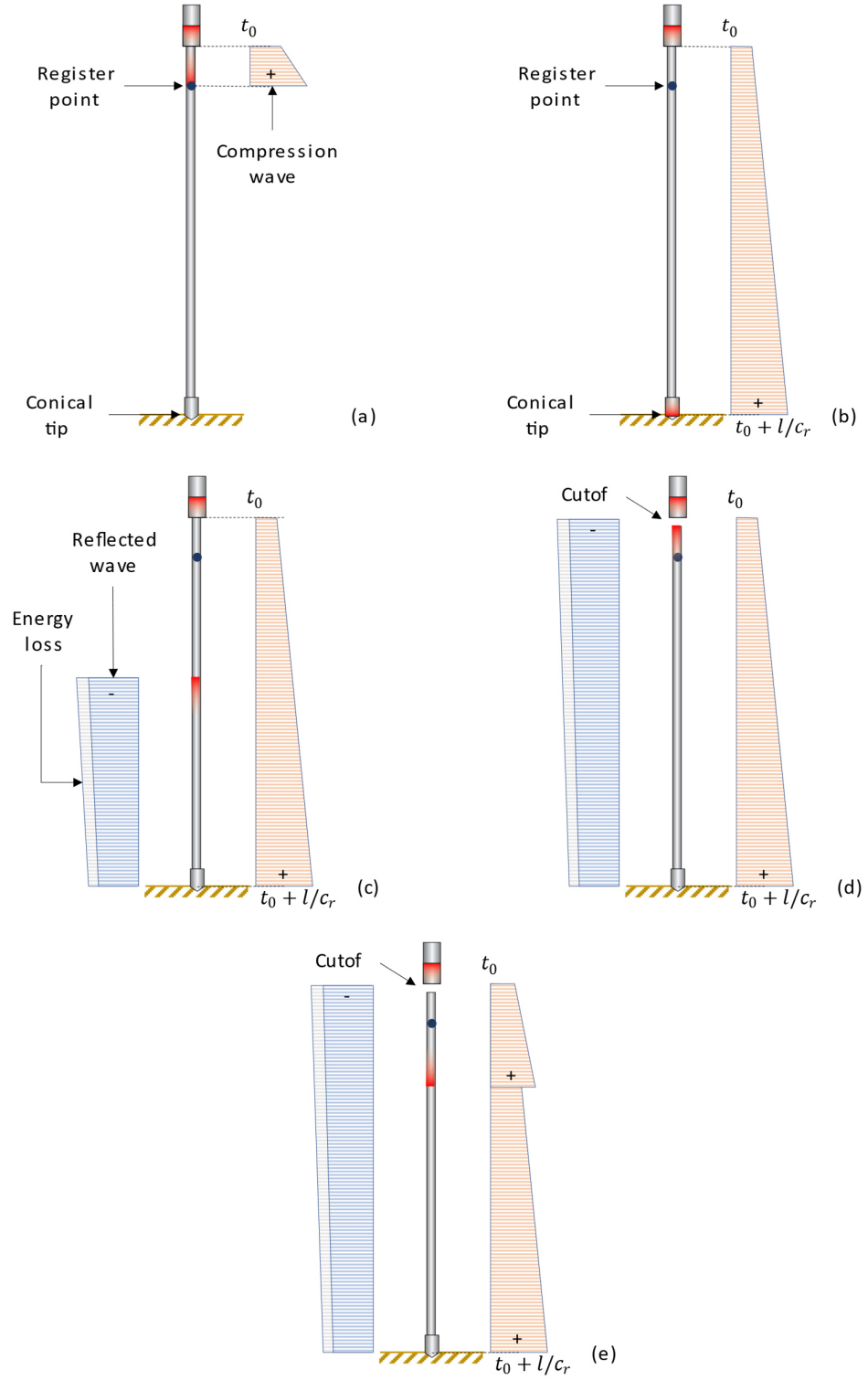

Figure 2-8 - Displacement of the wave through the penetrometer: (a) impact and wave generation; (b) energy transfer to the soil; (c) wave reflected; (d) cutof phenomena; (e) wave reflection.

2.2.4.5 Wave decoupling

Due to the nature of the dynamic driving phenomenon, the waves are superimposed during the occurrence of wave reflections in the penetrometer, so it is necessary to decouple them.

Multiple techniques can be applied to perform waves decoupling (Casem et al. 2003; Jung et al. 2006; Lundberg and Henchoz 1977). In the case of the PANDA 3 penetrometer, used in this research, the method presented by Casem et al. (2003) is used. This method allows decoupling the waves at a point x_A of the penetrometer using strain $\varepsilon_A(t)$ and velocity $v_A(t)$. Casem (2001) method has already been applied on a PANDA 3 penetrometer (Benz 2009a).

The decoupling method allows to obtain the upward and downward wave by applying the following equations:

$$\varepsilon_d(t) = \frac{1}{2}\left[\varepsilon_A(t) - \frac{v_A(t)}{2}\right] \quad \textbf{eq. 2-20}$$

$$\varepsilon_r(t) = \frac{1}{2}\left[\varepsilon_A(t) + \frac{v_A(t)}{2}\right] \quad \textbf{eq. 2-21}$$

If the force and strain relationships expressed in eq. 2-15 are considered, it is possible to present the decoupling of the wave as decoupling of downward and upward force measurements (eq. 2-22 and eq. 2-23). For this, it is necessary to consider that the mechanical impedance corresponds to the ratio of the force and the velocity of the wave ($z_r = F_A/v_A$), and that this is also a function of the characteristics of the penetrometer body ($z_r = A_r\rho_r c$); then it is possible to deduce that the mechanical impedance is a ratio of the section of the material, its elasticity and the velocity of wave propagation ($z_r = A_r E/c$).

$$F_d(t) = \frac{1}{2}[F_A(t) + z_r v_A(t)] \quad \textbf{eq. 2-22}$$

$$F_r(t) = \frac{1}{2}[F_A(t) - z_r v_A(t)] \quad \textbf{eq. 2-23}$$

Then, using the force and velocity measurements obtained at a known point A of the penetrometer, it is possible to decouple the incident and reflected waves (Figure 2-9).

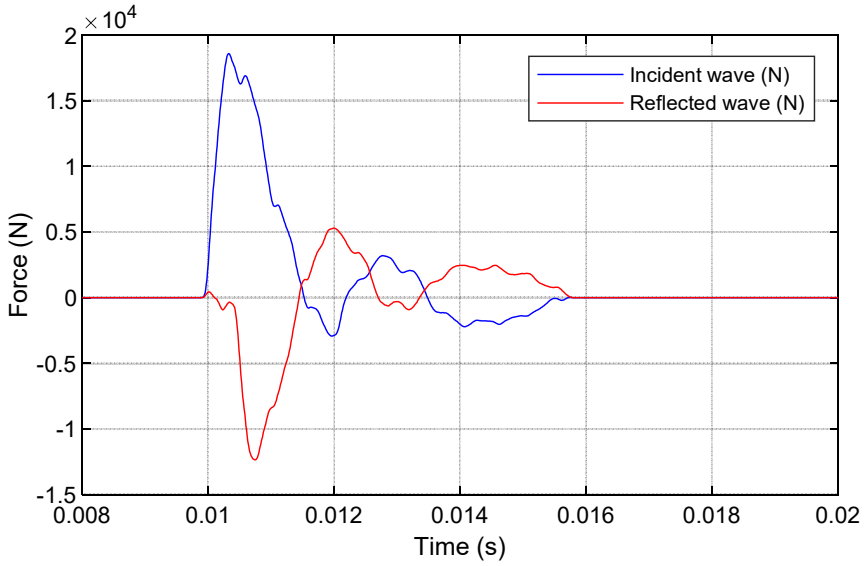

Figure 2-9 – Incident and reflected wave decoupling.

2.2.4.6 Wave reconstruction at the cone-soil interface

If the strain and acceleration measurements are available at a known point of the penetrometer, the geometrical characteristics of the rod and the material are homogeneous and the effects of lateral friction on the rods are considered negligible, the application of decoupling and reconstruction of the dynamic signals at any point N of the penetrometer is possible using and eq. 2-24 and eq. 2-25 (Carlsson, Sundin, and Lundberg 1990; Karlsson, Lundberg, and Sundin 1989).

$$F_N(t) = \frac{1}{2}\left[F_{N-1}\left(t + \Delta t_{n-(n-1)}\right) + F_{N-1}\left(t - \Delta t_{n-(n-1)}\right)\right] + \frac{Z_n}{2}\left[v_{N-1}\left(t + \Delta t_{n-(n-1)}\right) - v_{N-1}\left(t - \Delta t_{n-(n-1)}\right)\right] \quad \textbf{eq. 2-24}$$

$$v_N(t) = \frac{1}{2}\left[v_{N-1}\left(t + \Delta t_{n-(n-1)}\right) + v_{N-1}\left(t - \Delta t_{n-(n-1)}\right)\right] + \frac{1}{2Z_n}\left[F_{N-1}\left(t + \Delta t_{n-(n-1)}\right) - F_{N-1}\left(t - \Delta t_{n-(n-1)}\right)\right] \quad \textbf{eq. 2-25}$$

with:

$$\Delta t_{n-(n-1)} = \frac{(x_{n-1} - x_n)}{c_n}$$

If the configuration of the PANDA 3 dynamic penetrometer is considered, it is possible to note the existence of joints and a tip of different dimensions than the rods, which contradicts the condition of homogeneity of the propagation medium. In the case of the joints, it can be considered that the effects of the joints on the wave are negligible if they are installed correctly. For the geometrical variation of the conical tip, it is possible to apply an iterative calculation procedure that consists of

reconstructing the signals at each point of impedance change, that is, reconstructing first the signal at point B and then at point C (Figure 2-10).

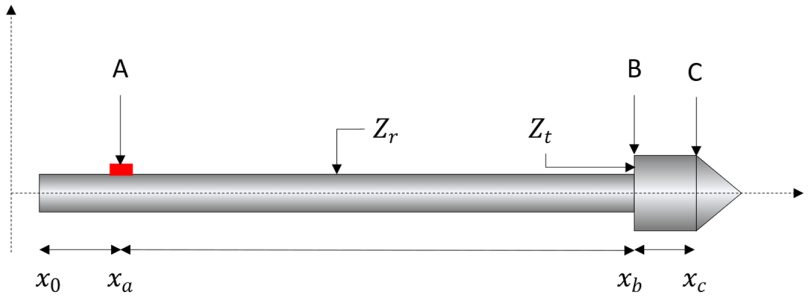

Figure 2-10 – Generalized Scheme of a penetrometer and conical tip configuration.

The application of the dynamic signal reconstruction equations allows obtaining force and velocity measurements at the cone-soil interface (Figure 2-11).

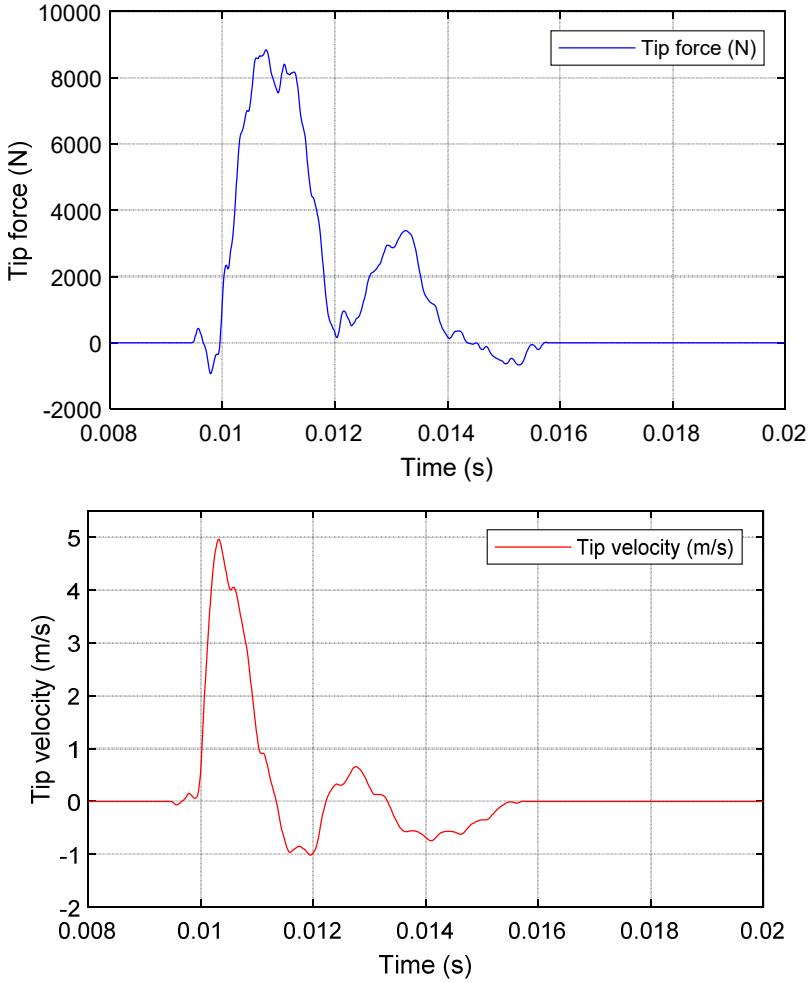

Figure 2-11 – Measurements reconstructed at soil-cone interface: (a) force and (b) velocity.

If the velocity measurement at the soil-cone interface is available, it is possible to obtain the displacements on the cone by applying time domain integration (Figure 2-12).

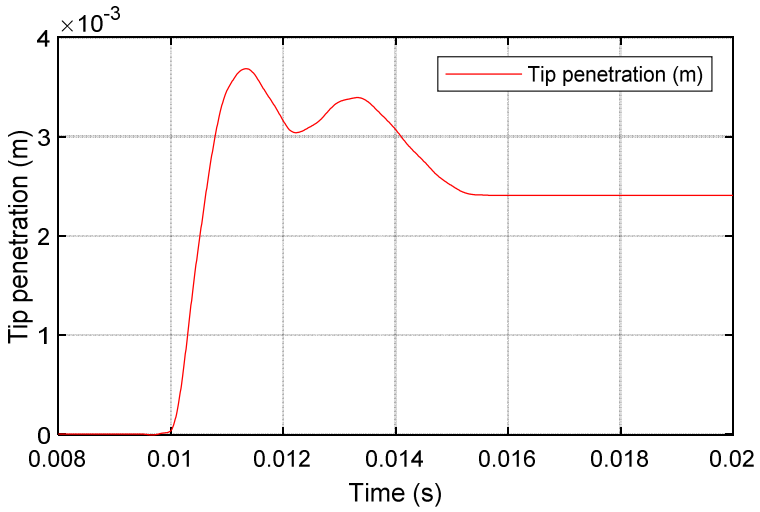

Figure 2-12 – Displacement measurement at cone-soil interface.

2.2.4.7 Dynamic cone load-penetration curve (DCLT curve)

The dynamic cone load-penetration curve or DCLT curve represents the response of the soil subjected to the dynamic load generated by the driving of a dynamic penetrometer. This curve is generated using the dynamic signals reconstructed at the cone-soil interface.

If the force and displacement signals at the soil-cone interface are available, it is possible to generate the dynamic response curve of the soil. To normalize the results, the curve is presented as a relationship between resistance (MPa) and penetration (m) (Figure 2-13).

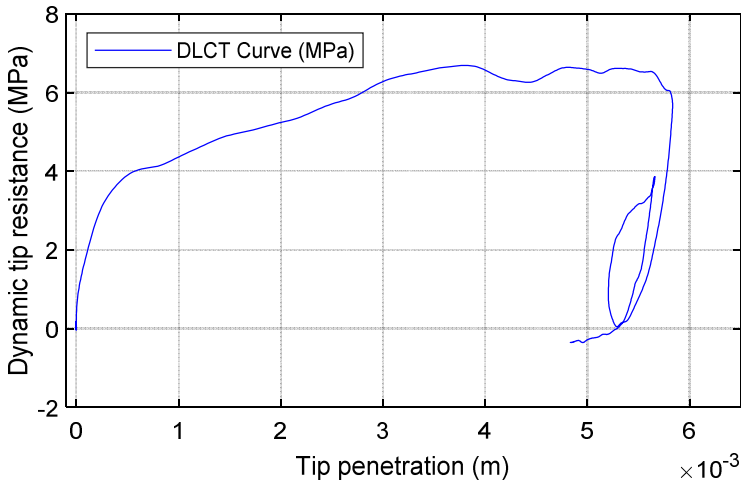

Figure 2-13 – Resistance-penetration curve at cone-soil interface.

2.3 Analysis of dynamic variable energy penetrometer results

2.3.1 Determination of the dynamic driving energy

2.3.1.1 Energy evaluation methods

During dynamic driving, the elastic waves propagating in the body of the penetrometer contain the energy transferred in the impact of the hammer, which has the capacity to perturb and produce displacements producing work. For the case of a moving body or particle, the increment of work used to perform the motion is given by the product of the applied force and the displacement dx produced (eq. 2-26).

$$dW = F(x,t)\,dx \qquad \textbf{eq. 2-26}$$

Then, the total work done in the system is obtained by integrating:

$$W = \int F(x,t)\,dx \qquad \textbf{eq. 2-27}$$

Due to the variability of the energy transmitted to the penetrometer elements, it is convenient to express the work done as a function of time, then, if it is considered that the particular velocity can be described as the displacement per unit time ($v = dx/dt$), it is possible to rewrite the equation for work done or energy (eq. 2-27), as follow:

$$W = \int F(x,t)v(x,t)dt = E(x,t) \qquad \textbf{eq. 2-28}$$

Note that with the above equation is also called EFV method (Energy-Force-Velocity method) and with this it is possible to obtain the energy transferred to the penetration equipment by variable dynamic driving, using a time domain measurement of force and velocity, which can be obtained by means of strain sensors and accelerometers. The integration in the time domain will result in an energy trajectory, in which the maximum energy value represents the maximum energy transferred to the rod.

If the mechanical impedance of the rod is considered, which relates the force and particle velocity on the rod ($Z_t = F(x,t)/v(x,t)$) , and that the impedance is a function of the rod characteristics ($Z_t = A_t\rho_t c_t$), it is possible to obtain the energy as a function of the parameters associated with the penetrometer. By subtracting the rod density from the simplified wave displacement velocity equation, the following is obtained:

$$\rho = \frac{E}{c_r^2} \qquad \textbf{eq. 2-29}$$

Then, replacing it in the impedance calculation equation, it is possible to obtain:

$$Z_r = \frac{A_r E_r}{c_r} \quad \textbf{eq. 2-30}$$

Therefore, the relationship between force and velocity can be rewritten as follows:

$$F(x,t) = \frac{A_r E_r}{c_r} v(x,t) \quad \textbf{eq. 2-31}$$

and equivalently,

$$v(x,t) = \frac{c_r}{A_r E_r} F(x,t) \quad \textbf{eq. 2-32}$$

These force-velocity relationships remain valid as long as the force-velocity relationship remains linear over the time interval in which the impact is generated and the arrival of the reflected wave from the conical tip to the initial measurement point ($2l/c_r$) and the maintenance of a uniform section is also necessary (Sy and Campanella 1991). Note that employing the above relationship allows the energy to be obtained only with a particular force and/or velocity measurement (eq. 2-33 and eq. 2-34). This method is called the force integration method (Sy and Campanella 1991).

$$E(x,t) = \frac{c_r}{A_r E_r} \int \big(F(x,t)\big)^2 \, dt \quad \textbf{eq. 2-33}$$

$$E(x,t) = \frac{A_r E_r}{c_r} \int \big(v(x,t)\big)^2 \, dt \quad \textbf{eq. 2-34}$$

Based on the above, the method that best suits the configuration of the variable dynamic energy penetration equipment is the force-velocity integration method also called EFV method since it is able to capture the entire energy trajectory during the driving phenomenon, considering the multiple cycles of internal reflection of waves and the effects of this on the mechanics of cone-soil interaction.

2.3.1.2 Dynamic curve integration method

Another method of energy evaluation is based on the force-displacement relationship at the cone-soil interface. If energy is considered equal to the total work done (eq. 2-26, eq. 2-27 and eq. 2-28), it is possible to use the force, velocity and displacement measurements for the evaluation of the penetration energy at the soil-cone interface, using the principle of energy conservation (Clough and Penzien 2003).

The load-displacement relationship is composed of multiple loading and unloading cycles, in which restitutive energies not used in the generation of cone penetration are measured. This is why for the application of this methodology it is necessary to differentiate those energies that generate a penetration work from those restitutive energies.

When the cone reaches its maximum penetration and stops, the elastic response of both the equipment and the soil can restore energy to the system (Figure 2-14). These energies can induce the vibrational behavior associated with the new lower energy load cycles which can also generate strain in the soil so they must be considered in the evaluation of the penetration energy. These energies are associated with the elastic behavior of both the soil and the penetrometer. Then, the potential deformation energy used in the penetration is expressed as the difference of the potential deformation energy transferred to the soil and the energies associated with the elastic response of the system and the soil, as follows:

$$W_{nc} = E_{pd} - E_{pds} - E_{pes} \qquad \textbf{eq. 2-35}$$

with:

W_{nc}: total work done by non-conservative forces.
E_{pd}: maximum deformation potential energy.
E_{pds}: potential elastic deformation energy of the system.
E_{pes}: restitutive elastic potential energy of the soil.

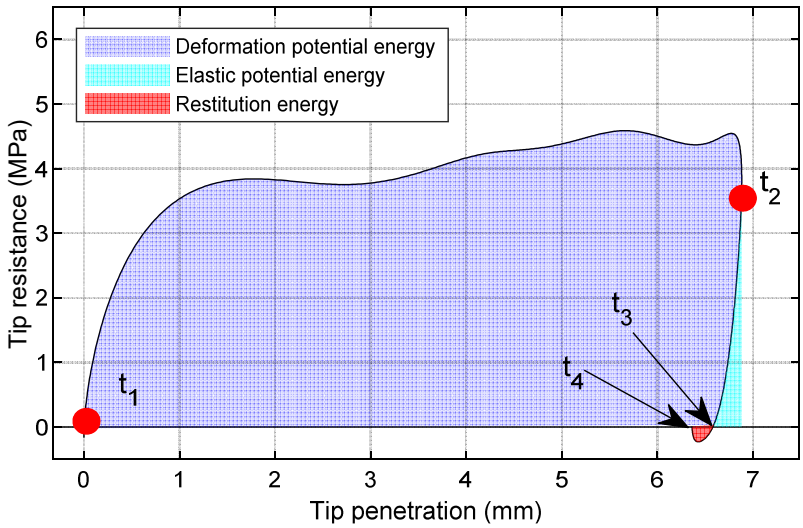

Figure 2-14 – Energy balance analysis in load-displacement trajectories.

If the energy is the resultant of the applied force with respect to the displacements generated, the total non-conservative work is calculated as follows:

$$W_{nc} = \int_{t_1}^{t_2} F(x,t)\,dx - \int_{t_2}^{t_3} F(x,t)\,dx - \int_{t_3}^{t_4} F(x,t)\,dx \qquad \textbf{eq. 2-36}$$

eq. 2-36 allows the calculation of the penetration energy during a dynamic loading cycle. However, in a dynamic penetration test, multiple loading cycles on the soil are possible when considering the elastic response of the soil. Secondary loading cycles can generate residual cone penetrations depending on the state of the soil and the magnitude of the energy carried by the wave. In this case, it is necessary to generalize eq. 2-36 for the calculation of energy in consideration of the occurrence of multiple loading cycles.

If the principle of energy conservation is considered, the total non-conservative work (W_{nc}), will be equivalent to the differences of potential deformation energies and elastic energies, resulting in the total energy used in cone penetration. Then, the general equation of penetration energy calculation is expressed as follows:

$$\Delta E_{nc} = \sum_{1}^{n} \left(\int_{t_n}^{t_{(n+1)}} F(x,t)\,dx - \int_{t_{(n+1)}}^{t_{(n+2)}} F(x,t)\,dx - \int_{t_{(n+2)}}^{t_{(n+3)}} F(x,t)\,dx \right) \qquad \textbf{eq. 2-37}$$

2.3.2 Dynamic penetration resistance determination

2.3.2.1 Dynamic penetration resistance based on load-displacement response

The load-displacement curve or DCLT curve represents the response of a soil subjected to a dynamic load generated at the cone-soil interface (Figure 2-15). Analogous to the strain-stress curves of other static and dynamic tests, the analysis of this curve allows the parametric exploitation of the mechanical response of the soil.

The use of this load-displacement relationship allows a rational evaluation of the soil response, by considering the behavior of the soil subjected to various internal and boundary conditions. However, it is necessary to consider some characteristics associated with dynamic driving for the correct analysis and understanding of the results, especially the factors that affect the repeatability of these, such as the cyclic-dynamic nature of the load generated by the wave reflected several times in the penetrometer, and the effects associated with the vibratory response of the system. These factors are discussed in following chapters.

Based on the dynamic curves, the use of the maximum resistance value measured is based on the principle of ultimate resistance of the soil to dynamic stress. The value of this resistance does not occur at the same penetration level due to the cyclic-dynamic nature of the stress generated by the wave front and the energy variability associated with the dynamic driving process (Figure 2-15).

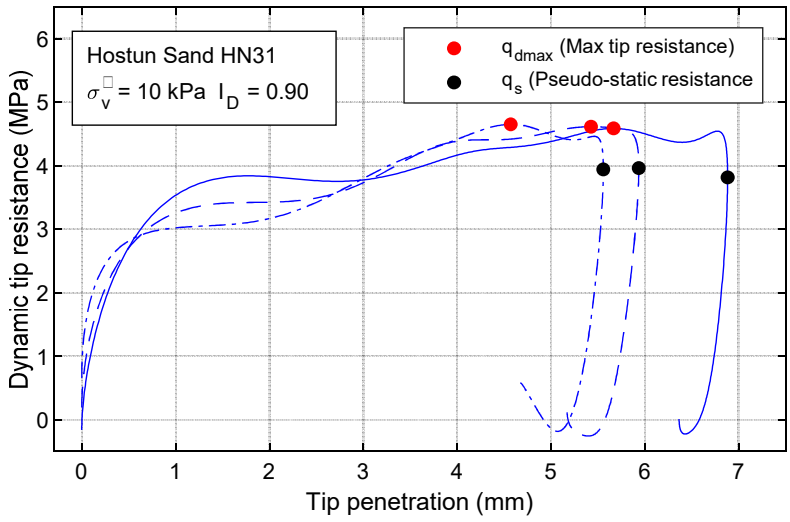

Figure 2-15 – Load-displacement relationships for different dynamic impacts.

2.3.2.2 Pseudo-static penetration resistance

Assuming that in a plastic flow phase during penetration, the total resistance is the result of a static and a dynamic component (Goble et al. 1975; Smith 1960), and that the dynamic part is related to the penetration velocity, the decrease in velocity would be related to a decrease in the dynamic component until its dissipation when the conical tip stops (Boguslavskii et al. 1996). At this point (Figure 2-15), the resistance generated by the soil would be associated only with a static component, thus defining a pseudo-static penetration resistance (q_s).

The establishment of this pseudo-static resistance allows the application of methods of analysis of results based on rheological models like the Smith (1960), allowing an extension in the analysis of the soil response under dynamic penetration.

2.3.2.3 Energy conservation method

An alternative to the direct evaluation of the resistance in the DCLT curve is based on the analysis of energy conservation during cone penetration by applying Hamilton's principle (Clough and Penzien 2003), which states that the sum of the variations of kinetic (E_k) and potential (E_p) energy with the non-conservative work (W_{nc}) of the system is equal to zero for any interval in the time domain (eq. 2-38).

$$\int_{t_i}^{t_f} \delta\left[E_k(t) + E_p(t)\right] dt + \int_{t_i}^{t_f} \delta W_{nc}(t)\, dt = 0 \qquad \textbf{eq. 2-38}$$

If the energies associated with the elastic response of the soil in the system can be calculated from the DCLT curve (E_{pes}, E_{per}) (Figure 2-16), the work done by the non-conservative forces in the

system can be expressed as the difference between the maximum potential deformation energy (E_{pd}) and the elastic potential deformation energies (eq. 2-35, eq. 2-36 and eq. 2-37).

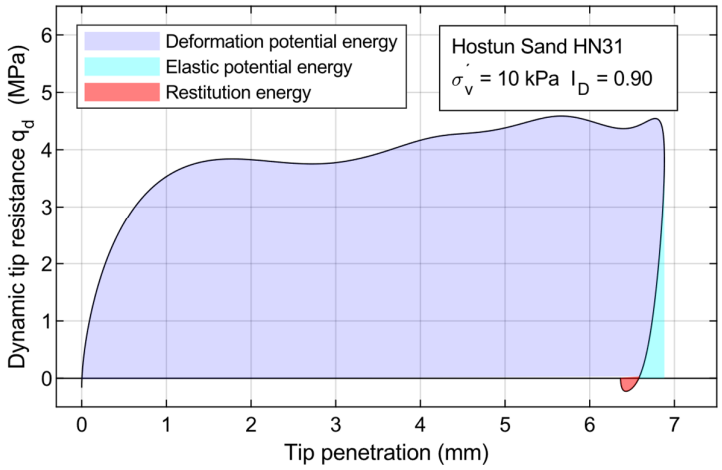

Figure 2-16 – Energy balance during cone penetration.

On the other hand, if the work done on a body is considered to be the resultant of the product of the force applied on it and the displacement generated, it is possible to establish a relationship between the work and the dynamic force applied, as follows:

$$\Delta W_{nc} = F_d \Delta S \qquad \textbf{eq. 2-39}$$

Where:

F_d = Applied dynamic force.
ΔS = Permanent displacement.

Then, it is possible to obtain the dynamic force used in the generation of a non-conservative work, combining equations eq. 2-37 and eq. 2-40, as follow:

$$F_d = \frac{\sum_1^n \left(\int_{t_n}^{t_{(n+1)}} F(x,t)\,dx - \int_{t_{(n+1)}}^{t_{(n+2)}} F(x,t)\,dx - \int_{t_{(n+2)}}^{t_{(n+3)}} F(x,t)\,dx \right)}{\Delta s} \qquad \textbf{eq. 2-40}$$

2.3.2.4 Benz (2009) method

For the calculation of the total dynamic resistance, Benz (2009a) applies a simple elastoplastic model of Smith (1960) to the DCLT curve (Figure 2-17). Based on this model the dynamic resistance ($q_d(t)$) is modeled as a function of a pseudo-static component (q_s) and another resistance associated with the viscous dynamics of the material (q_{dyn}) (eq. 2-41).

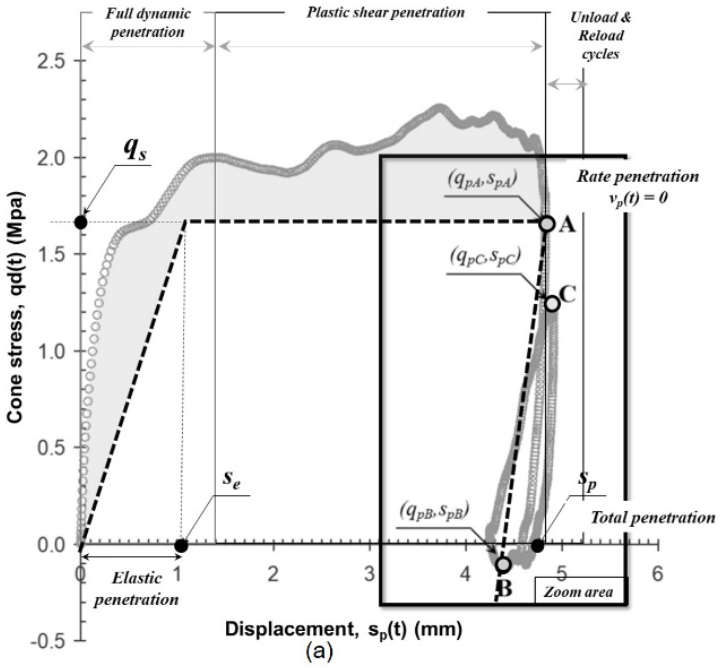

Figure 2-17 – Application of simple elastoplastic model to dynamic resistance analysis of soils (Benz Navarrete et al. 2022)**.**

$$q_d(t) = q_{dyn} + q_s \qquad \textbf{eq. 2-41}$$

The pseudo-static resistance is obtained when the penetration resistance is zero and the dynamic components are considered dissipated (see chapter 2.3.2.2), then, the dynamic component can be obtained by applying the principle of conservation of energy for the case of the dynamic component of resistance (eq. 2-44), in the range of the plastic strains of the curve (Figure 2-17)

$$q_{dyn} = \frac{1}{s_p - s_e} \int_{s_e}^{s_p} (q_d(t) - q_s) ds \qquad \textbf{eq. 2-42}$$

Then, if the static and dynamic components of the curve are known, it is possible to obtain the dynamic resistance of the soil by the sum of the components (eq. 2-41).

2.3.2.5 Dynamic driving equations

The first version of the PANDA dynamic energy penetration equipment used the Dutch equation for the calculation of dynamic resistance. For this, it based the calculation on the characteristics of the equipment and measurements of maximum energy obtained in the penetrometer head. To obtain the permanent penetration, the equipment has an extension sensor implemented by

means of a belt that allows obtaining the penetration measurement during dynamic driving (Figure 2-18).

$$q_d = \frac{1}{A_t}\frac{E_h}{e}\frac{1}{1+\frac{P}{M}} \qquad \textbf{eq. 2-43}$$

with:

e: tip penetration.
A_t: tip section.
M: hammer mass.
P: driving assembly mass (penetrometer : tip, rod and head).
E_h: dynamic driving energy.

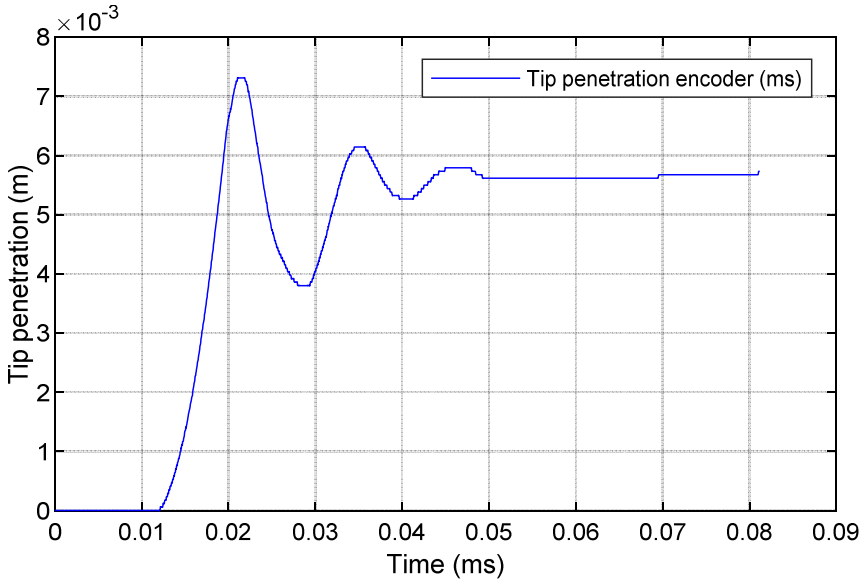

Figure 2-18 – Displacement measurement obtained by encoder.

Several dynamic driving equations can be applied to the results of the variable energy penetrometer using the energy and final penetration measurements, however, their application is limited to the hypotheses established in their development, since some have been created explicitly for some penetrometers such as the SPT. Some of the most common dynamic driving equations are presented in Table 1-1.

2.3.3 Elastic response of soil

The load generated by the penetrometer on the soil has cyclic and dynamic characteristics, so the occurrence of multiple loading cycles is to be expected. These characteristics are visible in the dynamic curves during the vibratory phase (Figure 2-19b), in which multiple dynamic load loops

associated with the soil-penetrometer interaction and the elastic response mechanism of the soil can occur.

When the main load cycle stop (point A) (Figure 2-19a)., and the penetration velocity is zero, the soil generates an elastic response capable of pushing the penetrometer upwards, restoring part of the energy transferred by the wave, then the penetrometer again generates a lower energy load on the soil associated to the inertial effect of self-weight and remaining energy and producing loading and reloading loops that will deform the soil mostly in the elastic domain.

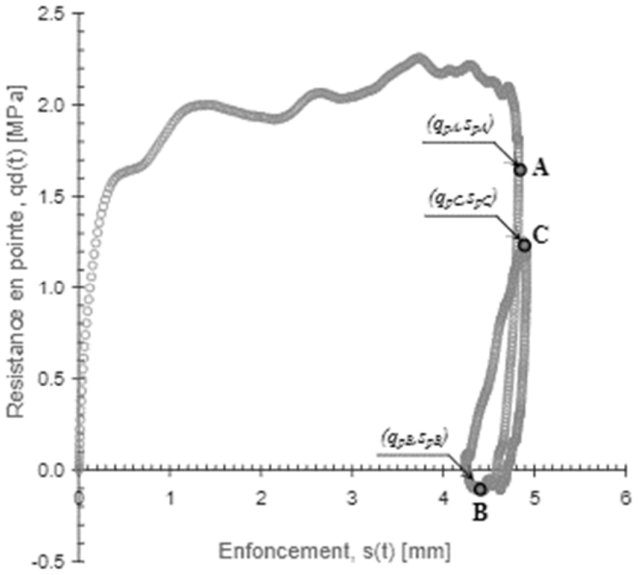

Figure 2-19 – Dynamic load-penetration curve at soil-cone interface (Benz 2009a)**.**

Research by Zhou (1997) and Arbaoui et al. (2006) showed that the unloading-reloading cycle obtained from a penetration loading test is mainly constant and therefore the unloading elastic moduli are constant and independent of the unloading velocity, in the case of the reloading modulus the constant response is obtained from the third loading cycle. This characteristic allows inferring that the value of this modulus represents an intrinsic characteristic of the material.

For the determination of the elastic modulus of unloading and reloading, the approach presented by Arbaoui et al. (2006) is used, in which the cone is considered a rigid circular plate embedded in the soil at a depth z under a semi-infinite elastic soil mass, then, by applying the Boussinesq equation (eq. 2-44) and considering a Mindlin coefficient k_M equal to 2 (Arbaoui et al. 2006):

$$E = (1 - \nu^2)\frac{\Delta q_p}{\Delta s_p}\frac{\pi d_p^2}{4}\frac{1}{k_M} \quad \textbf{eq. 2-44}$$

with:

Δq_p: applied stress.
d_p: plate diameter (cone).
Δs_p: displacement.
k_M: Mindlin Coefficient.

Since after reaching zero velocity ($v_p = 0\ m/s$) and maximum cone penetration during the first loading cycle, an elastic response of the soil is obtained, the first modulus defined is the unloading secant elastic modulus E_{p3}^d (eq. 2-45). This module is defined by the points A where the elastic unloading begins and B where a new loading cycle begins.

$$E_{p3}^d = (1 - \nu^2)\left(\frac{q_{pA} - q_{pB}}{s_{pA} - s_{pB}}\right)\frac{\pi d_p^2}{4}\frac{1}{k_M} \quad \textbf{eq. 2-45}$$

After the elastic discharge, a reloading phase occurs between B and C, allowing the definition of the reloading secant modulus E_{p3}^r (eq. 2-46).

$$E_{p3}^r = (1 - \nu^2)\left(\frac{q_{pC} - q_{pB}}{s_{pC} - s_{pB}}\right)\frac{\pi d_p^2}{4}\frac{1}{k_M} \quad \textbf{eq. 2-46}$$

Depending on test and soil conditions, new cycles of unloading and reloading may occur, however, the evaluation of these is complex and the results may be unrealistic due to perturbations in the signals not associated with soil response.

2.3.4 Polar shock method

The polar shock method allows obtaining parameters such as mechanical impedance, particle velocity and deformation, both in the rod and in the soil. (Anh Tran et al., 2019; Aussedat, 1970; Azzedine, 1989; Benz, 2009; Benz Navarrete et al., 2022; Iskander et al., 2015; Lodygowski and Rusinek, 2014; Meunier, 1974; Omidvar et al., 2014; Oularbi and Levacher, 2009).

The application of the polar shock method on a material evaluates the relationship between the velocity and the particular force associated with the passage of a plane elastic shock wave. The

application of this method allows the analysis of waves propagating from a medium A to another medium B (penetrometer and soil respectively), i.e. when changes of impedance (Z) occur.

To establish a relationship between force and particle velocity, a system with two elements at rest (penetrometer and soil) must be considered. When the penetrometer is perturbed by a hammer impact, a compression wave $u_d(t)$ is generated (incident wave) and propagates downwards in the direction of the cone-soil interface. The relationship between the force and velocity of this incident wave can be expressed as a function of the mechanical impedance of the material (Z_r) (eq. 2-47).

$$\sigma_d = \frac{E_r}{c} v_d = \rho_r c v_d = Z_r v_d \qquad \textbf{eq. 2-47}$$

Once the wave arrives at the cone-ground interface, a part of it will be transmitted to the ground $u_T(t)$ and another part will be reflected back to the origin $u_r(t)$. Like the incident wave, the relationship between the force and the particular velocity of the reflected wave can be expressed as a function of the mechanical impedance (Z_r) (eq. 2-48).

$$\sigma_r = \frac{E_r}{c} v_r = \rho_r c v_r = Z_r v_r \qquad \textbf{eq. 2-48}$$

The Figure 2-20 is a representation of the shock polar of a material and construction of the ground shock polar from the incident and reflected signals. Points A and C are inscribed in the shock polar of the rod, where the slope of these curves is represented by the mechanical impedance of the rod ($\pm Z_r$).

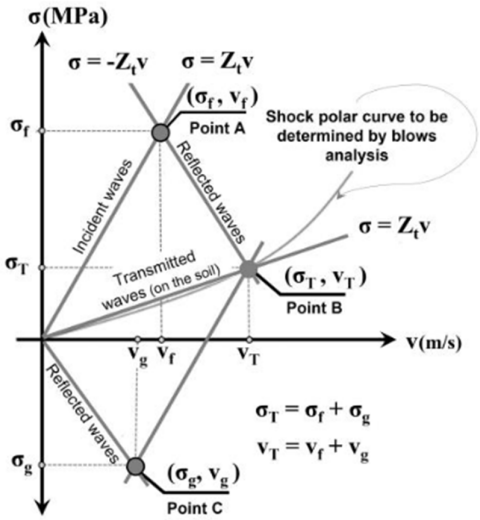

Figure 2-20 – Scheme of a Shock Polar and representation of the construction of the soil shock polar (Benz Navarrete et al. 2022)**.**

After the reflection of the incident wave at the cone-soil interface, the reflected wave will have been affected with a decrease in its energy content due to a transfer of energy to the ground, and therefore its strength and velocity will be modified. The energy differences contained in the reflected wave correspond to the energy transferred to the ground, and therefore a perturbation will be produced in the ground, whose particular strength and velocity correspond to the differences of the incident and reflected measurement (eq. 2-49 y eq. 2-50).

$$\sigma_T = \sigma_d - \sigma_r \qquad \textbf{eq. 2-49}$$

$$v_T = v_d + v_r \qquad \textbf{eq. 2-50}$$

If the force and velocity measurements transmitted to the soil (σ_T y v_T) are available, it is possible to construct the shock polar in the time interval of the first reflection of the wave front ($t_0 + 2\,l_r/c_r$), for this, first of all, the incident and reflected waves must be decoupled and the force and velocity measurements transmitted to the soil must be calculated (eq. 2-49 y eq. 2-50), which when plotted and fitted by linear regression describe a relationship between force and velocity given by the mechanical impedance of the soil ($\sigma_T = Z_s v_T$) (Figure 2-21). Note that it is also possible to obtain the mechanical impedance of the rod through the force and velocity signals recorded in the penetrometer in the time interval ($t_0 + 2\,l_r/c_r$), an interval in which force and velocity are proportional.

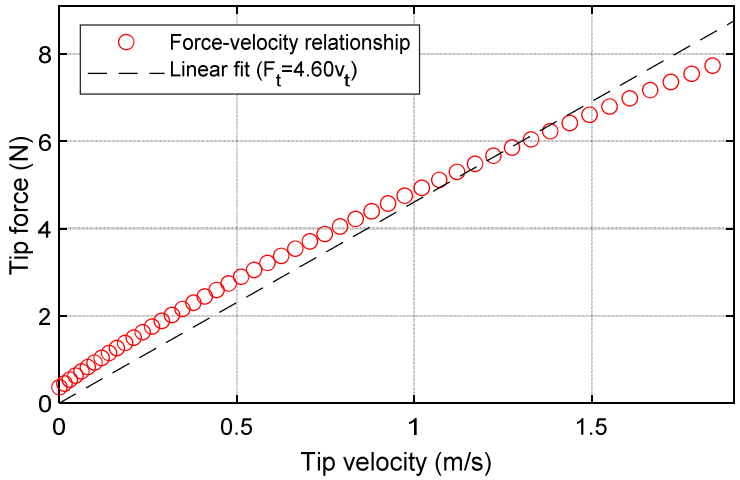

Figure 2-21 – $F = Zv$ ratio for a granular soil.

Another way of presenting the relationship between force and velocity is presented by Oularbi & Levacher (2009). This method is based on the evaluation of the relationship between the maximum velocity and the force generated at that velocity, in a series of dynamic impacts. In the case of the

dynamic variable energy penetrometer, this is applied to the reconstructed signals at the cone-soil interface to obtain the velocity-force relationship of the soil (Figure 2-22). The points generated by the relationship can be fitted by linear regression to obtain the value of the mechanical impedance of the soil as the slope of this relationship.

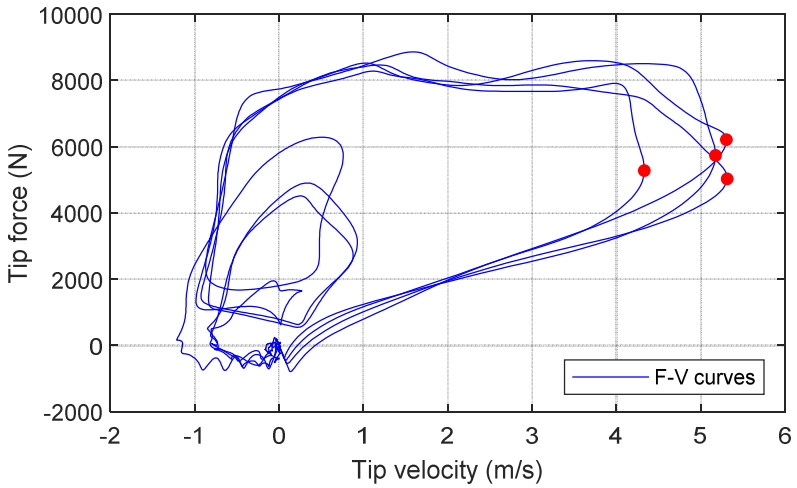

Figure 2-22 – Evaluation of the mechanical impedance of the soil by means of a maximum velocity-resistance relationship.

2.3.5 Analysis of soil response in the frequency domain

Based on the work presented by Paquet (1968) for pile monitoring, it is possible to analyze the effect of the wave generated by the impact of the hammer using an approach based on the frequency analysis of dynamic signals. Based on this approach the shock wave caused by the impact of the mass on the penetrometer and the vibrations in the soil-penetrometer system can be described by means of the impedance, which can be obtained by applying the Fourier transform method (eq. 2-51 and eq. 2-52), from which it is possible to establish the transfer functions.

$$F(t) \leftrightarrow F(f) = FFT[F(t)] \qquad \textbf{eq. 2-51}$$

$$v(t) \leftrightarrow v(f) = FFT[v(t)] \qquad \textbf{eq. 2-52}$$

Frequency domain transfer functions allow to analyze the spectral response of the reconstructed signals in the penetrometer cone as a function of an imposed force and thus determine system properties and how the penetrometer-soil system responds to the impact of the hammer.

2.3.5.1 Dynamic module E_{kd}

If the dynamic signals for an impact are available, it is possible to obtain the dynamic stiffness (k_d) both in the penetrometer and at the cone-soil interface, and through an approach based on the equations proposed by Boussinesq considering the tip as a rigid plate embedded in the soil, it is

possible to calculate the dynamic strain modulus E_{kd} (eq. 2-53 and eq. 2-54), establishing a limiting frequency range in the E_{kd} spectra.

$$k_d = 2\pi \frac{\Delta\omega}{\Delta M} \quad \textbf{eq. 2-53}$$

$$E_{kd} = \frac{(1-\mu^2)}{d_p} k_d \quad \textbf{eq. 2-54}$$

With k_d is the dynamic stiffness, ΔM the mobility ($M(f) = v(f)/F(f)$), μ is the Poisson coefficient (set to 0.33) and d_p the cone diameter.

To analyze the dynamic modulus through the curves, the limit is established as the section in which a linear regime is maintained between frequency and modulus (Figure 2-23). To establish the lower limit f_{min} the characteristics of the acquisition system are considered (24 Hz). To establish the upper limit, the dynamic modulus spectrum at the penetrometer head (measurement point) is plotted and the upper limit is established as the value at which the curves diverge in the linear range (f_{max}). The frequency range in which linearity is maintained will depend on the density and nature of the soil, consequently, the higher the stiffness of the soil the greater the extent of the linear proportionality range (Tran et al., 2018; Tran et al., 2019).

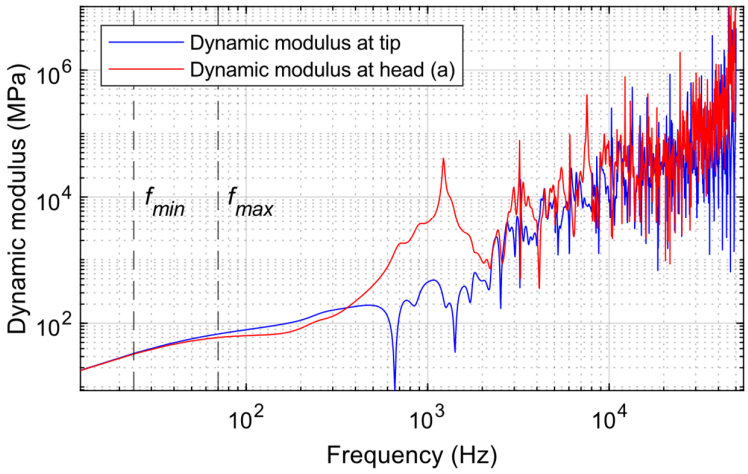

Figure 2-23 - Dynamic modulus spectra E_{kd} at the cone level and at the measurement point.

Once the maximum and minimum limits are set at f_{max} and f_{min} respectively, two dynamic moduli are defined. A minimum dynamic modulus ($E_{kd(min)}$) associated to the minimum frequency and a maximum modulus ($E_{kd(max)}$) associated to the maximum frequency. Then, a third modulus is

defined as the one associated to the average of the maximum and minimum frequencies or mean dynamic modulus (E_{kd}).

2.4 K_0 Calibration chamber

A K_0 calibration chamber developed in the geotechnical team of Navier laboratory (Le 2014), is used for the dynamic penetration tests (Figure 2-24). The design of the calibration chamber allows the generation of a sealed and hermetic space for the reconstitution of soil specimens of different characteristics. The existing setup has been modified to perform PANDA3® test on dry and saturated sand.

Figure 2-24 – View of the K_0 calibration chamber of Navier laboratory.

2.4.1 Description and operating principle

The calibration chamber is an equipment that allows the reconstitution of soil specimens, the application of dry and saturated conditions, the reproduction of specific boundary conditions and the application of vertical effective stresses up to a maximum value of 600 kPa. The system consists of the specimen reconstitution mold, a water snubbing reservoir, a vertical loading system and a pore pressure application system. These systems are driven by vacuum pumps and hydraulic pressure systems. With these elements, the system is able to control vertical loading and saturation conditions (Figure 2-25).

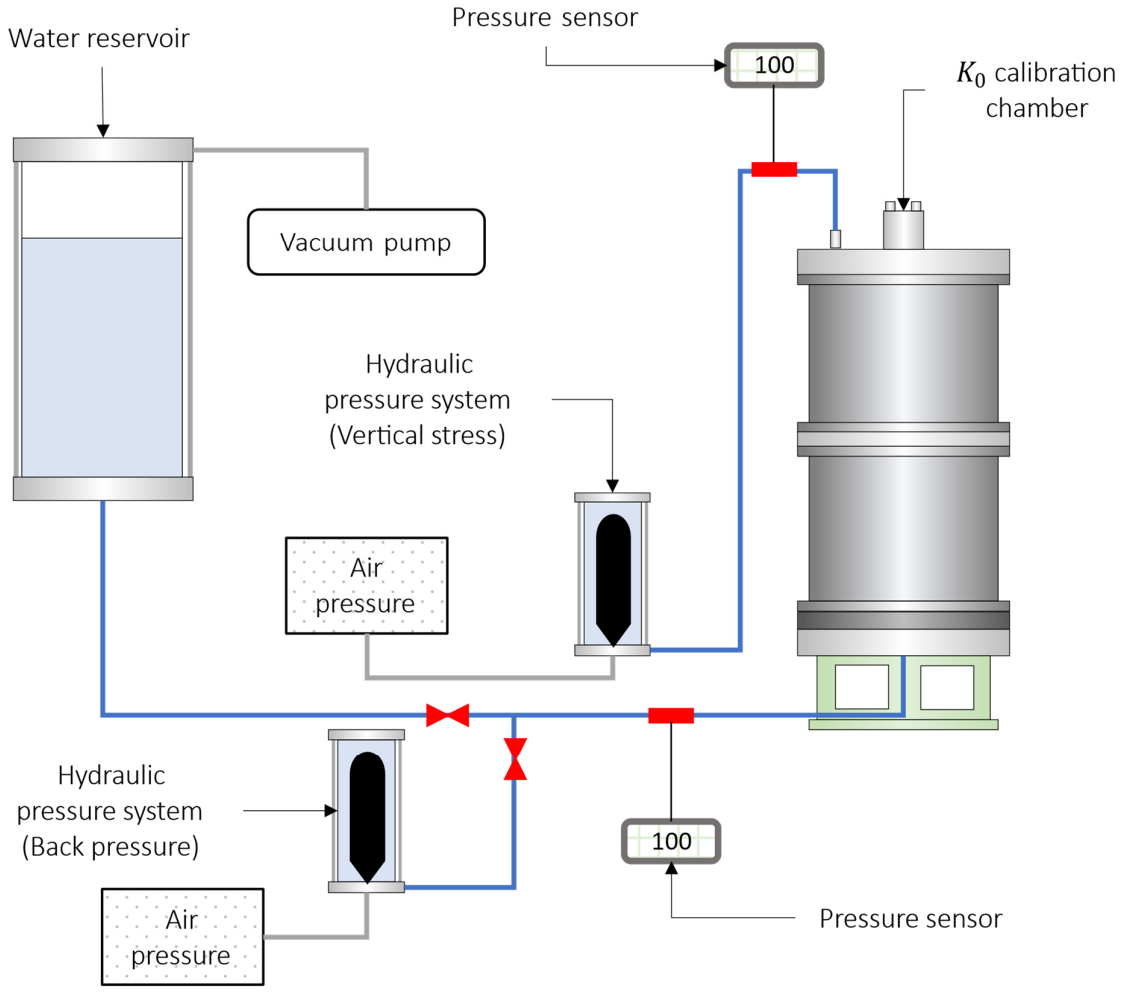

Figure 2-25 – K_0 calibration chamber system.

The cylindrical mold allows the reconstitution of the specimen at the target density index in an hermetic environment, which allows the installation of the penetrometer rods by means of a system that ensures the sealing of the specimen. The specimen is consolidated and depending on the test conditions, dry and saturated conditions can be reproduced. Once the specimen is finished, a dynamic penetration test is performed at different levels of vertical effective stress.

The main elements that compose the calibration chamber system are described below:

a. Cylindrical mold

The mold is composed by two metallic cylinders and a metallic ring that, together, allow the construction of a specimen up to 73 centimeters high and 55 centimeters in diameter (Figure 2-26). The ring is installed between the two cylinders and allows sealing by installing o-rings. The three elements are fixed by means of bolts that allow a unique configuration and ensure the sealing.

Figure 2-26 – Cylindrical mold of K_0 calibration chamber.

b. Base plate

The base of the K_0 calibration chamber is composed of two disks. A base disk with a perforation in the center that allows the passage of ducts inside the specimen (Figure 2-27a), and a plate that allows the correct distribution of water from the base to saturate the specimen by means of a porous disk (Figure 2-27b). The plates are hermetically adapted to the mold and allow for the installation of the rods that seal the system.

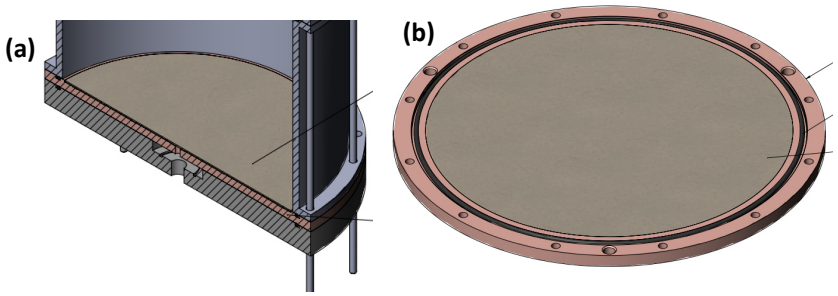

Figure 2-27 – K_0 Calibration chamber base.

c. Vertical loading system

For uniform application of the vertical stress, a circular load plate is provided on which a passage system for the penetrometer rod is installed (Figure 2-28a). The passage system is composed of a sealing system based on o-rings that ensure the sealing between the rod and the load plate. Due to the size of the cone, it is necessary to place the plate with the cone-rod assembly previously installed.

For the generation of the vertical stress there is a rubber membrane driven by hydraulic water pressure coming from the hydraulic pressure chamber, which is transmitted to the inside of the membrane by means of a conduit that ensures the sealing when passing through the upper cover by means of o-rings. This membrane is installed between the loading plate and the top cover, so the pressure is exerted by extending the membrane.

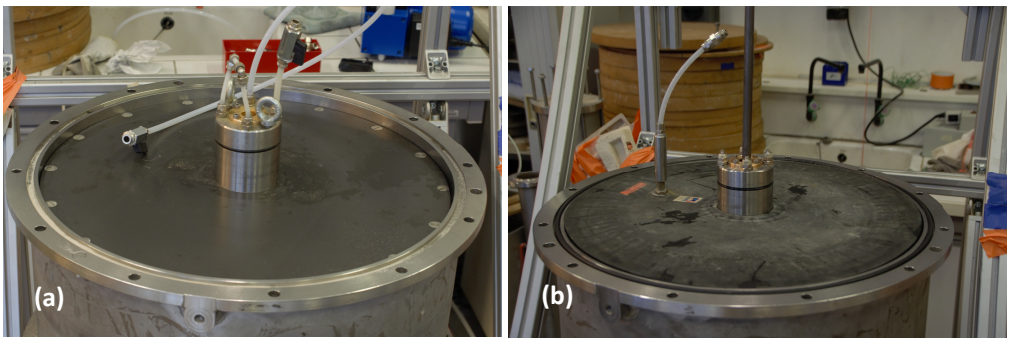

Figure 2-28 – Vertical loading system of the K_0 calibration chamber.

d. Calibration chamber top cover

The top cover of the calibration chamber is composed of a steel cover, a central sealing system and a circular sealing plate for the passage of the conduit that transmits the pressure to the rubber membrane. The upper steel cover is installed on the upper cylinder of the chamber and its sealing is ensured by an o-ring installed in the cylinder (Figure 2-29a). The central sealing system provides sealing between the steel cover and the penetrometer rod passage system installed in the loading plate (Figure 2-29b). The circular sealing system for the passage of the pressure pipe to the rubber membrane ensures the sealing between the duct and the steel cover (Figure 2-29c).

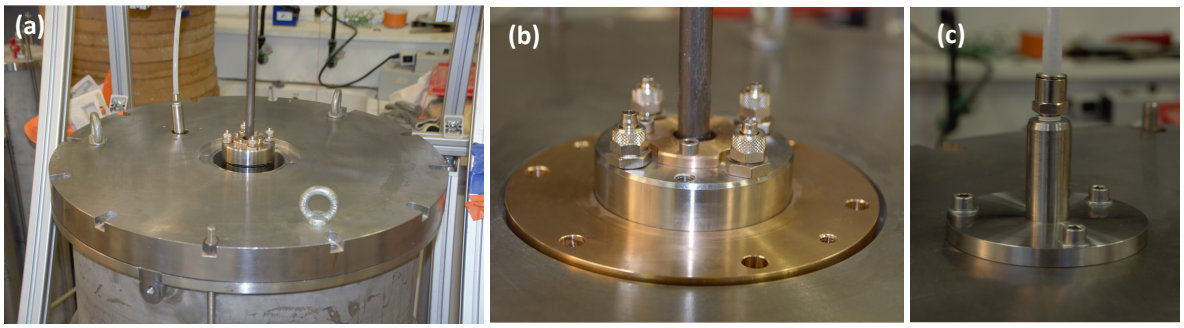

Figure 2-29 – K_0 calibration chamber top cover system.

e. Saturation system

To apply saturated conditions to the specimen inside, a system consisting of a hermetic water reservoir with inlet and outlet ducts at the bottom and at the top is available. The upper connection can be used to apply vacuum by means of pumps in order to apply a water deaeration process. The

lower duct is normally used as a connection to the calibration chamber to produce the saturation of the specimen.

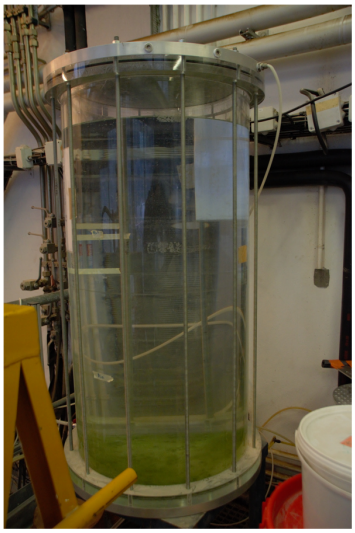

Figure 2-30 – Water reservoir for specimen saturation and water de-aeration.

2.5 Experimental procedure

The experimental work includes the execution of dynamic penetration tests of variable energy on specimens of Hostun HN31 and Fontainebleau NE34 sand, reconstituted at different density index levels and in dry and saturated conditions. Each specimen is subjected to different levels of effective vertical stress.

Before each test, the equipment is checked and put in conditions for the safe performance of the procedure and to avoid possible negative effects on the signals recorded by the dynamic penetrometer, associated to the boundary conditions.

2.5.1 Specimen reconstitution

The reconstitution of specimens at density indices from 0.30 to 0.90 was considered, in order to cover densities associated with loose and very dense soils. These specimens were subjected to dynamic penetration tests in dry and saturated state.

For specimen reconstitution, dry deposition was used with controlled layers until reaching the pre-established dimensions for the K_0 calibration chamber mold, and in the case of low density specimens, wet deposition was used to maintain the stability of the loose specimens (Figure 2-31a).

Figure 2-31 – Reconstituted sand specimen.

Once the specimen has been reconstituted, the vertical stress system is installed. The first step is the installation of a drainage system composed of a granular layer separated by geomembranes. A geomembrane is installed over the specimen (Figure 2-32a) and a 2 cm granular layer is placed on top of it to establish a separation and drainage space between the specimen and the bearing plate (Figure 2-32b). Another layer of geomembrane is installed on top of the granular layer to establish a barrier between the granular elements and the bearing plate (Figure 2-32c).

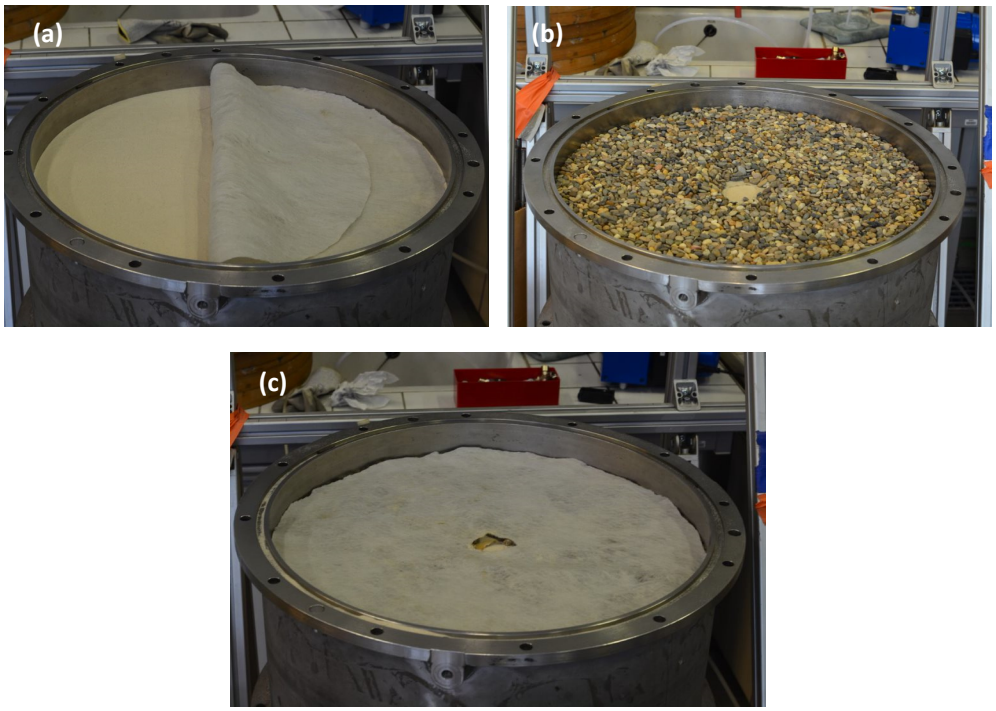

Figure 2-32 – Installation of drainage layer over sand specimen: (a) geomembrane; (b) granular layer; (c) geomembrane layer over granular layer.

After the drainage layer is installed, the load plate is installed with the rod-cone assembly pre-installed in the rod duct (Figure 2-33a). This rod installation procedure is necessary to maintain the sealing of the system. The pressure membrane is installed over the plate (Figure 2-33b), ensuring a level surface to allow the correct installation of the top cover of the chamber. The top cover is installed

to ensure the passage of the ducts that connect the pressure membrane to the external pressure cell system (Figure 2-33c). To seal the system, the central sealing piece (Figure 2-33d), is installed, generating the sealing of the system by means of o-rings. It is also necessary to seal the conduit that transmits the pressure to the membrane installed inside the specimen, for this purpose a screwed plate is installed that seals the system by means of o-rings (Figure 2-33e).

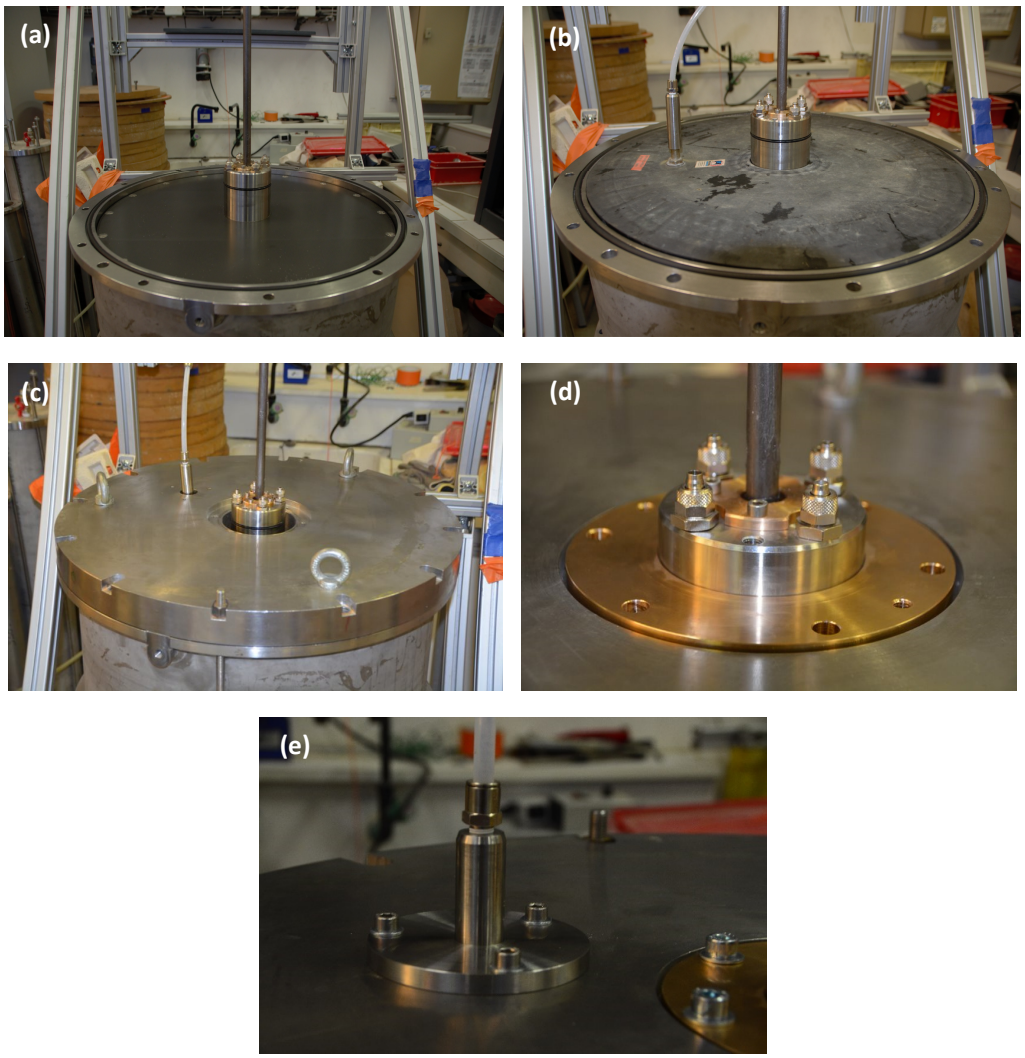

Figure 2-33 – Installation of vertical loading system: (a) granular layer; (b) loading plate; (c) loading membrane; (d) central cover closure piece; (e) vertical loading system sealing plate.

The system is sealed by installing threaded rods, which are fastened to both the upper and lower plates by means of nuts, generating the pressure necessary to ensure the sealing of the joints in the system.

2.5.2 Specimen saturation

The saturation process begins with the application of vacuum by means of vacuum pumps. This process is necessary to extract the air in the interstitial spaces of the granular structure and thus

achieve effective saturation. On the other hand, the water used in the saturation of the specimen must be de-aerated by applying negative pressure by means of a vacuum pump to the water reservoir (Figure 2-34a). This process is maintained for at least 4 hours.

Once the specimen has been treated with negative pressure and the water has been de-aerated, the specimen is saturated by connecting the reservoir to the calibration chamber through ducts in the lower base plate (Figure 2-34b) During the saturation process, negative pressure is maintained inside the calibration chamber to prevent the entry of air and facilitate the saturation of the specimen.

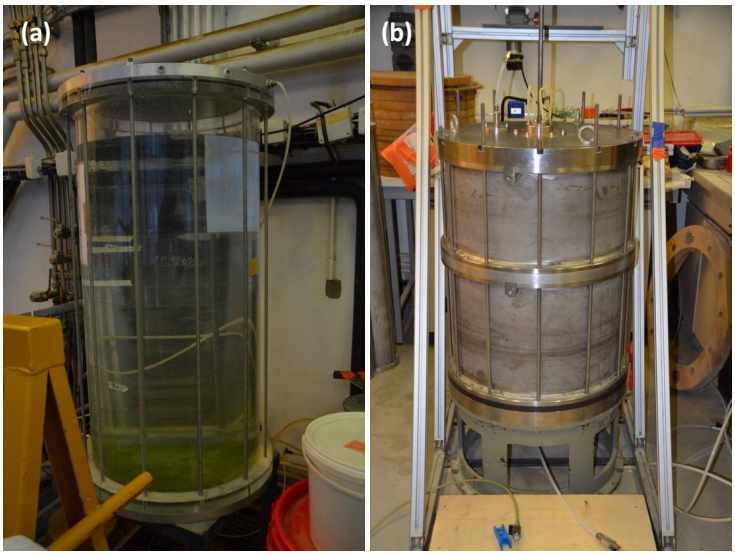

Figure 2-34 – (a) Water de-airing reservoir; (b) water supply ducts.

The saturation process is completed once the water begins to flow out of the upper duct of the calibration chamber. At this moment the water flow is maintained to eliminate possible remaining air bubbles inside the specimen. With the saturation process completed, the vertical pressure is raised to 200 kPa and a pore pressure of 200 kPa.

2.5.3 Dynamic Penetration Test

With the specimen reconstituted, either in dry or saturated condition, the dynamic penetration test is performed, for which the rod train and the conical tip (4 cm^2) have been previously installed (Figure 2-35a), so the striking head is installed and connected to the UCA (Figure 2-35b). With the connections made, the inhalambric link with the controlled mobile device is generated and the test configurations are set (conical tip surface, rod length, device type…).

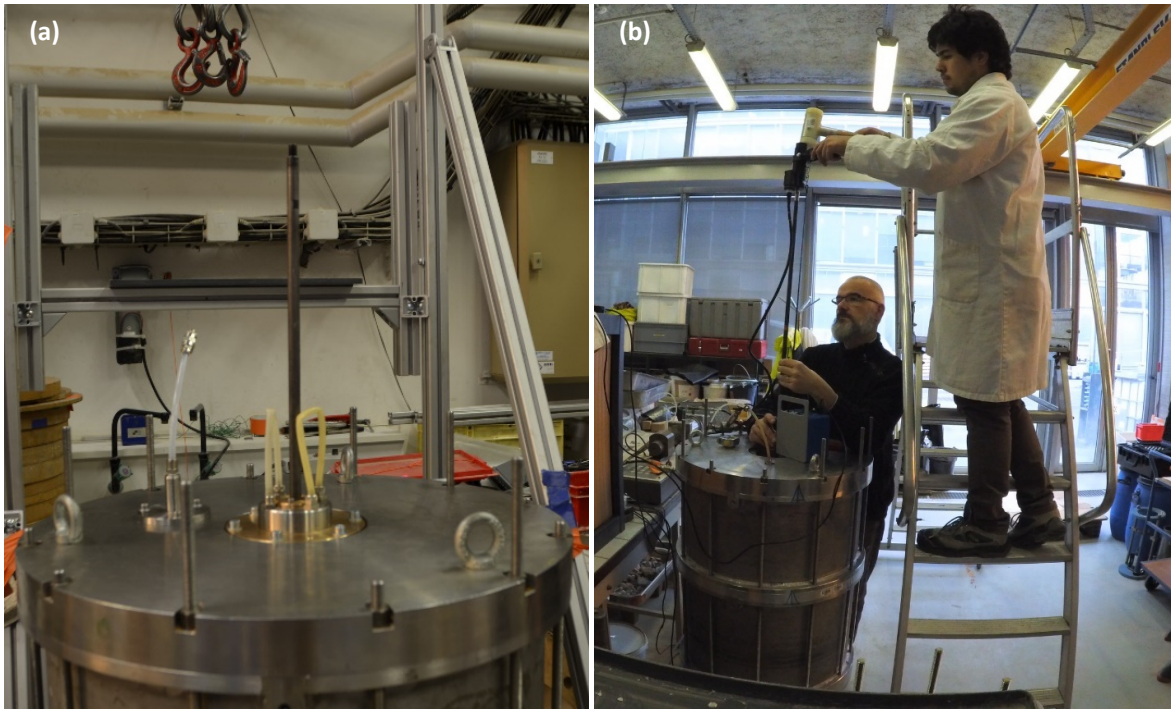

Figure 2-35 – Dynamic penetration test: (a) penetrometer rod train installation; (b) penetrometer installed and dynamic driving.

When the configuration of the penetration equipment is complete, it is possible to start the dynamic driving of the penetrometer. The specimen will be subjected to dynamic driving at vertical effective stress intervals of 10, 25, 50, 75, 100, 200, 300 and 400 kPa, ensuring a minimum penetration of 5 centimeters at each interval to obtain a minimum number of impacts for analysis (Figure 2-36).

To avoid boundary effects, impacts performed in the first 10 centimeters of the specimen depth and the last 10 centimeters before reaching the base plate of the calibration chamber are excluded from the analysis (Figure 2-36). This consideration excludes impacts made before the critical penetration depth is reached, especially in dry tests.

The mobile application allows the visualization of basic penetration test results (depth, dynamic resistance, penetrograms), so at the end of the test it is necessary to import the measurements from the UCA for later processing. The imported results can be processed and exploited for parametric evaluation of the soil.

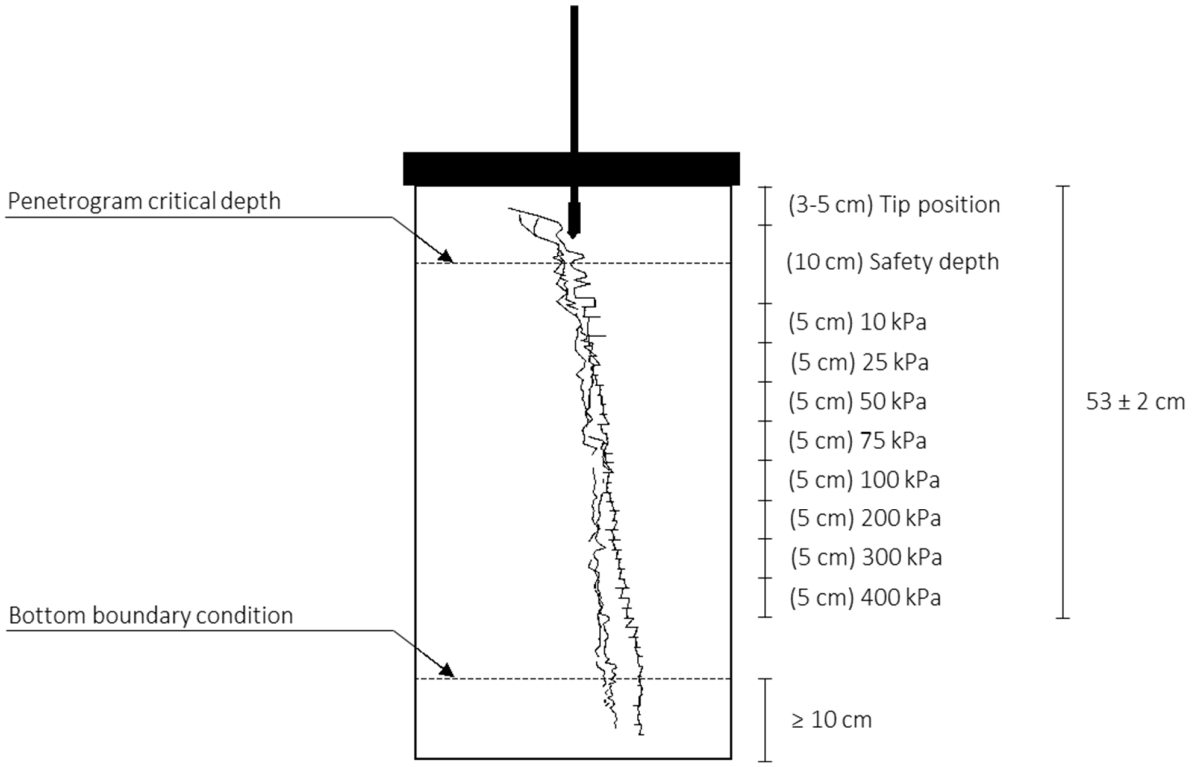

Figure 2-36 – Dynamic driving scheme on reconstituted specimens.

2.6 Conclusions

The main features of the variable energy light dynamic penetrometer have been presented. These characteristics allow this equipment to perform dynamic tests in the field under a wide range of operating conditions that other penetrometers are not able to provide, where its portability and speed in the test performance are remarked as one of the most important conditions.

The ability to perform rapid tests under adverse soil conditions gives it great capability in soil analysis, since it allows the acquisition of a large number of data which can be processed in the field to obtain an initial characterization and later, through specific analysis of the signals, parameters that require greater computational power. These characteristics also allow the possibility of performing a multiparametric evaluation of the soil response.

In the case of liquefaction potential analysis of soils, methods based on correlations have been developed for application with the PANDA 3 dynamic penetrometer, however, the possibility of performing a characterization based on a multiparametric approach allows the creation of a method based on the test results themselves, and a data base that can be exploited and adjusted to new theories and hypotheses that are applied to the analysis of the test results.

For a first analysis of the penetrometer capabilities, dynamic tests have been performed in a K_0 calibration chamber, for which an experimental procedure has been developed in order to reproduce in a better way the conditions of a reconstituted soil under variable stress and saturation conditions.

The calibration chamber allows the reconstitution of soil specimens under controlled conditions and the performance of dynamic penetration tests in the laboratory. An experimental procedure has been designed to ensure a uniform reconstitution of the specimens at different density levels, and a correct sealing to reproduce both dry and saturated conditions inside the chamber. The design of the chamber and the procedure make sure that the boundary conditions are controlled and their effect on the test results are correctly treated and excluded.

3 VARIABLE ENERGY DYNAMIC PENETRATION TESTS IN A CALIBRATION CHAMBER

This chapter presents the results of variable energy dynamic penetration tests performed in the K_0 calibration chamber, with the objective of analyzing the response of the soils considered in this investigation. The dynamic cone load test curve or DCLR curve obtained for the different conditions of effective stress state and density index for dry and saturated sands are presented. An analysis of the most important parameters obtained from the analysis of the dynamic signals is also presented.

Special emphasis has been placed on the analysis of the dynamic penetration resistance because it is the most representative parameter of the soil response and the state in which it is found, establishing a framework for its evaluation based on the effects of the density index, vertical effective stress applied to the sand specimen and saturation conditions. In the same way, the dynamic modulus E_{kd} is analyzed as a second characteristic parameter of the soil as an element of differentiation of the response of both soils. Other parameters are also analyzed in a general way to introduce them as possible geotechnical parameters of soil response to dynamic penetration, for an extension of the liquefaction potential evaluation method.

Due to the dynamic nature of the dynamic penetration test, an analysis of the effects of dynamic driving energy and cone velocity during penetration on maximum strength and curve shape is also presented.

The results obtained allow the creation of a reference framework for the establishment of liquefaction potential evaluation method based on the identification and differentiation of the two types of sands tested during this research.

3.1 Presentation and analysis of dynamic penetration test results in the calibration chamber

3.1.1 Experimental program

An experimental program was defined with the objective of obtaining the dynamic signals under different levels of density index, and different levels of effective vertical stress applied to the sand specimen, for both dry and saturated conditions, in two types of sands (Hostun HN31 and Fontainebleau NE34). The experimental program carried out is presented in the Table 3-1.

Table 3-1 – Program of test carried out.

Test number	Sand	Density index	State of sand
DPT1	Hostun HN31	0.30	Dry
DPT2	Hostun HN31	0.30	Dry
DPT3	Hostun HN31	0.30	Dry
DPT4	Hostun HN31	0.40	Dry
DPT5	Hostun HN31	0.50	Dry
DPT6	Hostun HN31	0.60	Dry
DPT7	Hostun HN31	0.70	Dry
DPT8	Hostun HN31	0.70	Dry
DPT9	Hostun HN31	0.70	Dry
DPT10	Hostun HN31	0.70	Dry
DPT11	Hostun HN31	0.80	Dry
DPT12	Hostun HN31	0.90	Dry
DPT13	Hostun HN31	0.90	Dry
DPT14	Fontainebleau NE34	0.10	Dry
DPT15	Fontainebleau NE34	0.30	Dry
DPT16	Fontainebleau NE34	0.30	Dry
DPT17	Fontainebleau NE34	0.30	Dry
DPT18	Fontainebleau NE34	0.40	Dry
DPT19	Fontainebleau NE34	0.40	Dry
DPT20	Fontainebleau NE34	0.50	Dry
DPT21	Fontainebleau NE34	0.50	Dry
DPT22	Fontainebleau NE34	0.50	Dry
DPT23	Fontainebleau NE34	0.50	Dry
DPT24	Fontainebleau NE34	0.50	Dry
DPT25	Fontainebleau NE34	0.60	Dry
DPT26	Fontainebleau NE34	0.60	Dry
DPT27	Fontainebleau NE34	0.70	Dry
DPT28	Fontainebleau NE34	0.70	Dry
DPT29	Fontainebleau NE34	0.80	Dry
DPT30	Fontainebleau NE34	0.90	Dry
DPT31	Fontainebleau NE34	0.90	Dry
DPT32	Hostun HN31	0.30	Saturated
DPT33	Hostun HN31	0.30	Saturated
DPT34	Hostun HN31	0.50	Saturated
DPT35	Hostun HN31	0.50	Saturated
DPT36	Hostun HN31	0.70	Saturated
DPT37	Hostun HN31	0.90	Saturated
DPT38	Fontainebleau NE34	0.30	Saturated
DPT39	Fontainebleau NE34	0.30	Saturated
DPT40	Fontainebleau NE34	0.50	Saturated
DPT41	Fontainebleau NE34	0.70	Saturated
DPT42	Fontainebleau NE34	0.90	Saturated
DPT43	Fontainebleau NE34	0.90	Saturated

3.1.2 Typical dynamic penetration test results

3.1.2.1 Typical dynamic signals

The signals obtained during dynamic driving show a typical shape and trajectory in all cases, characterized by the occurrence of maximum peaks associated with the passage of the incident and reflected wave front (Figure 3-1). It has been observed that the force and velocity signals are proportional in the reflection time lapse of the first wave front and diverge when the reflected wave arrives from the cone-soil interface. This divergence is produced by the vector sum of the force magnitudes (Figure 3-1).

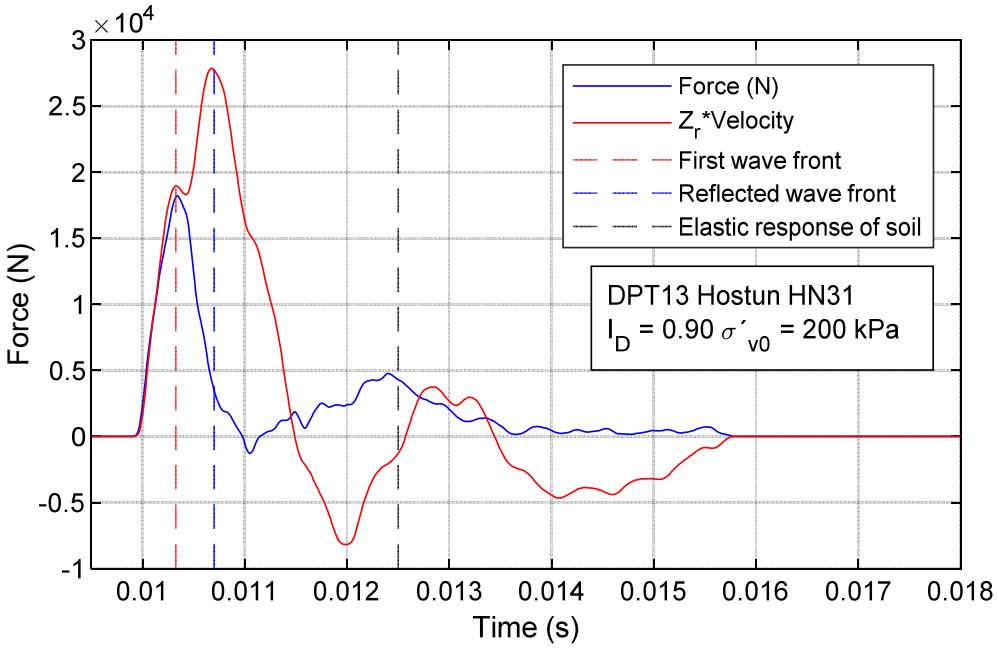

Figure 3-1 - Measurement of dynamic signals at the penetrometer head.

After the point of maximum value of parameters measured, a phase of lower energy reflections was observed, culminating with the occurrence of an intermediate energy peak associated with the elastic response of the soil acting on the penetrometer, to give place to a gradual decrease in the magnitude of the energies until their convergence to zero. Due to these characteristics, the wave front traveling through the penetrometer can be characterized as a cyclic and dynamic behavior.

Figure 3-2 shows the decoupling results of incident and reflected waves typically found in dynamic penetration tests. In these, the occurrence of the force peaks associated with the measurement of the wave fronts was observed. At the beginning of the reflected wave measurements and at a time of l_r/c_r, the measurements should be zero, however, small force peaks associated with the occurrence of reflections during the displacement of the wave front are

observed, mainly to the inside of the striking head and at the impedance change points of the penetrometer. The measurements during this time can be considered negligible.

The reconstructed resistance and velocity signal at the cone-soil interface (Figure 3-3a and Figure 3-3b) show the response of the soil to dynamic cone penetration. In general, an abrupt increase in resistance is observed followed by a relatively stable resistance state around a maximum value due to the mobilization of the maximum dynamic shear resistance of the soil, after which there is a rapid decrease in resistance due to the stopping of the cone. In the case of velocity, the response is similar, however, the maximum velocity peaks are transient due to their relationship with the displacement of the cone.

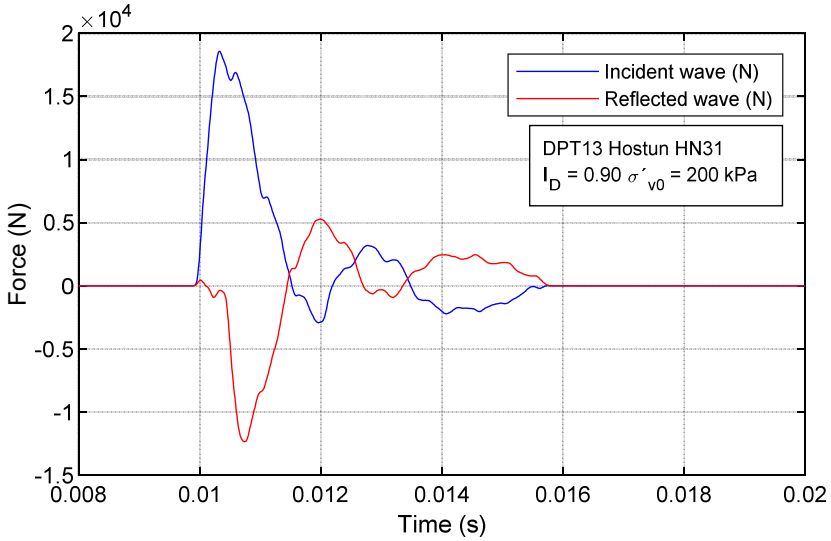

Figure 3-2 - Incident and reflected waves decoupling.

A second peak of resistance and velocity, of medium energy is observed. This peak of maximum resistance is associated with the restitutive response of the soil, which reintroduces significant amounts of energy into the system from the elastic response of the soil and the upward thrust generated on the penetrometer. This energy can produce an inertial response of the penetrometer and press the soil again.

The displacement of the cone penetrating the soil obtained from the reconstructed velocity signal is shown in Figure 3-4. The displacement trajectory of the cone over the soil shows a cyclic displacement associated to the wavefront reflections. In addition, the occurrence of an elastic response of the soil characterized by a partial recovery of the maximum displacements at the as-soil interface is observed.

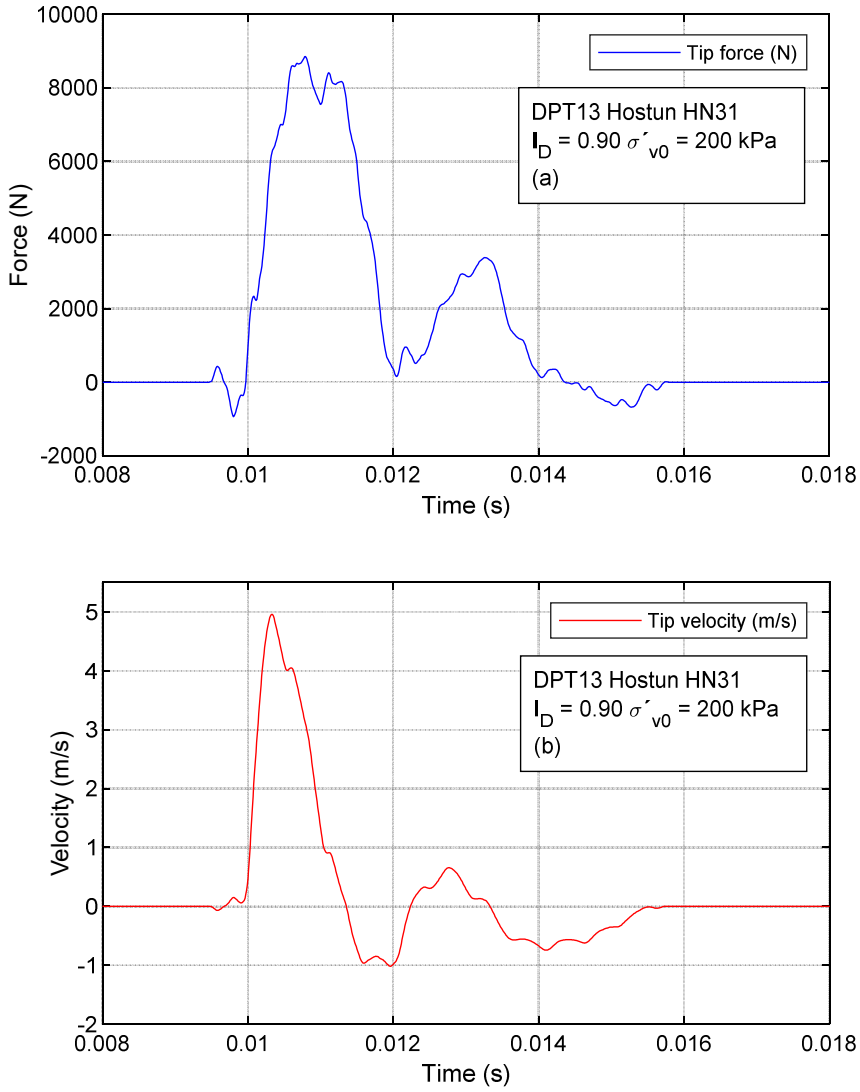

Figure 3-3 – Reconstructed dynamic signals at cone-soil interface: (a) tip force; (b) tip velocity.

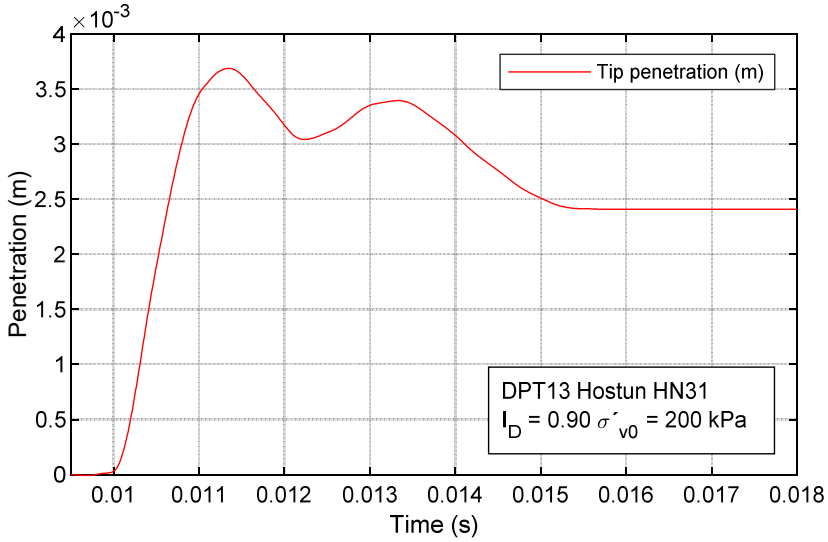

Figure 3-4 - Dynamic penetration measurement reconstructed at cone-soil interface.

3.1.2.2 Dynamic load-displacement curves

With the strength and displacement measurements at the soil-cone interface, the construction of the load-displacement curve, or DLCT curve, is possible by relating the strength and penetration signals (Figure 3-5). The DLCT curves show general elements of the dynamic response of the soil, characterized by an initial stiff-elastic response, a yield phase, a stage of maximum stable resistance and/or plastic flow phase and a vibratory or elastic response phase of the soil. These phases have been observed in all the specimens tested and in both types of sand; however, a different behavior has been observed for lower density in saturated sands (see chapter 3.1.2.3).

The stress-strain responses obtained from the penetration tests show a characteristic shape in all ranges of applied conditions, showing variations with respect to the type of soil, its state and applied boundary conditions. This shape allows the identification of some typical elements of the soil response that can be described individually, in addition to the analysis for the parameterization of the soil.

In general, the dynamic load-displacement curves show four successive phases: an initial elastic-rigid phase (1), a yield phase (2), a plastic flow phase (3) and an elastic vibratory response phase (4) (Figure 3-5). These four general phases are each characterized by a specific type of response behavior of the soil subjected to dynamic penetration loading.

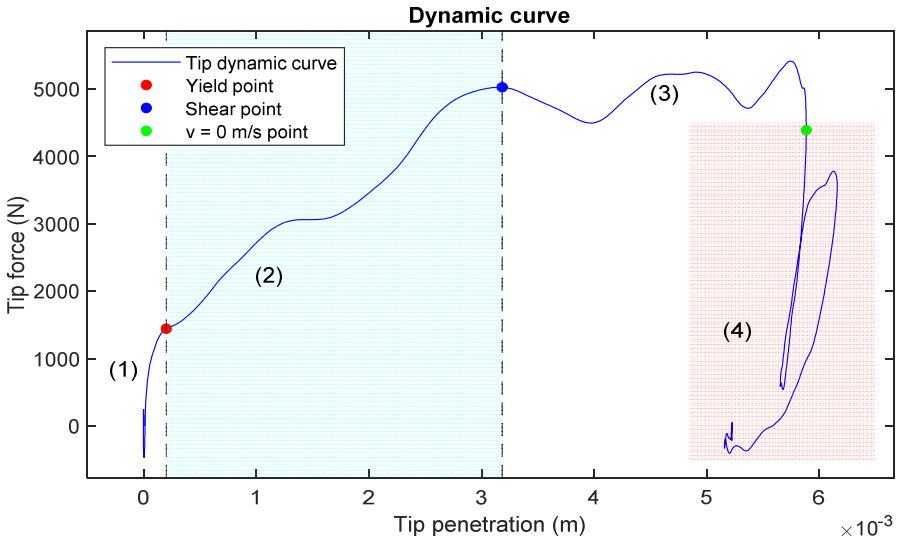

Figure 3-5 - Load-displacement relationship at cone-soil interface.

f. Elastic-rigid phase (1)

The elasto-rigid phase represents the initial response of the soil to dynamic penetration. This phase is characterized by high stiffness against conical tip penetration, which is produced by the dynamic interaction between the particles of the sand packing. The wave front arriving at the cone-soil interface generates a dynamic load that produces a rapid strain in a short period of time. This

loading favors the generation of force chains between the particles; However, the short duration of the loading and the high strengths of individual grains prevent grain breakage failure and the deformation will be governed mainly by elastic response phenomena of the grains, resulting in an abrupt increase in strength (Iskander et al. 2015; Karimpour and Lade 2010; Lee et al. 1969). This initial elastic-rigid response is terminated as grains begin to displace and rearrange and to a lesser extent to rupture.

g. Yield phase (2)

This phase corresponds to the process by which significant soil strains develop. At this point, there is a process by which the resistance in the contacts between particles begins to be exceeded by the dynamic load transmitted to the soil and sliding and rearrangement mechanisms are generated. This phase is characterized by a gradual increase in dynamic resistance until reaching a maximum resistance mobilized between particles in a plastic flow regime.

h. Plastic flow phase (3)

The phase of maximum resistance or plastic flow is the phase in which the maximum dynamic resistance of the soil is mobilized and the measured values will oscillate around an average constant value. During this phase, the soil is not able to assume a higher load and the conical tip will penetrate until the energy contained in the wave is not sufficient to generate work. At this point the strains generated are mostly plastic, and associated with sliding, rearrangement and particle breakage. The possibility of particle breakage is multifactorial, however, the higher the confining pressure and density index, the higher the probability of its occurrence (Iskander et al. 2015; Karimpour and Lade 2010; Lee et al. 1969). This phase ends when the conical tip stops ($v = 0\ m/s$), and an abrupt decrease in the resistance measurement occurs.

The length of this phase depends on the amount of driving energy contained in the wavefront, for which a higher amount of energy is able to generate more penetration work and therefore a longer extension of this phase. On the contrary, a lower energy will be able to mobilize the shear resistance, however, it will generate less penetration work. If other parameters such as the density index and the vertical effective stress are considered, the extension of this plastic phase will also vary at the same driving energy level, since the higher the density and/or effective vertical stress, the greater the resistance opposed by the soil and the same amount of energy will be able to produce a lower amount of penetration work.

i. Elastic vibratory response phase (4)

The vibratory phase corresponds to the phase in which a series of discharge and recharge cycles associated with the reflected wave fronts and the restitutive response of the soil occur. When

the conical tip stops, a rapid elastic response of the soil begins, which is able to push the penetrometer upwards and reinject energy into the penetrometer (Benz 2009a). This can be observed on the curve as a recovery of the penetration and as resistance values with negative sign.

During this phase, multiple dynamic loading cycles may occur on the soil, which are capable of producing additional penetration; However, it is not possible to ensure that the shear strength is mobilized in these cycles, since the strains or sliding may be associated with the compressibility of the soil. The penetrations associated with the loading cycles in the vibratory phase are a function of the level of remaining energy included in the cycles, the state of density of the granular aggregate, physical composition of the granular medium, particle morphology, among others.

3.1.2.3 Load-displacement relationships in saturated sand

In the case of saturated specimens, it has been observed that the DCLT curves follow the same pattern as for the dry tests, differing in the magnitude of the maximum strengths developed and in a phenomenon of abrupt reduction of the initial strength observed in loose, saturated specimens subjected to low levels of effective vertical stress. This phenomenon proved to be repetitive under the mentioned conditions (Figure 3-6).

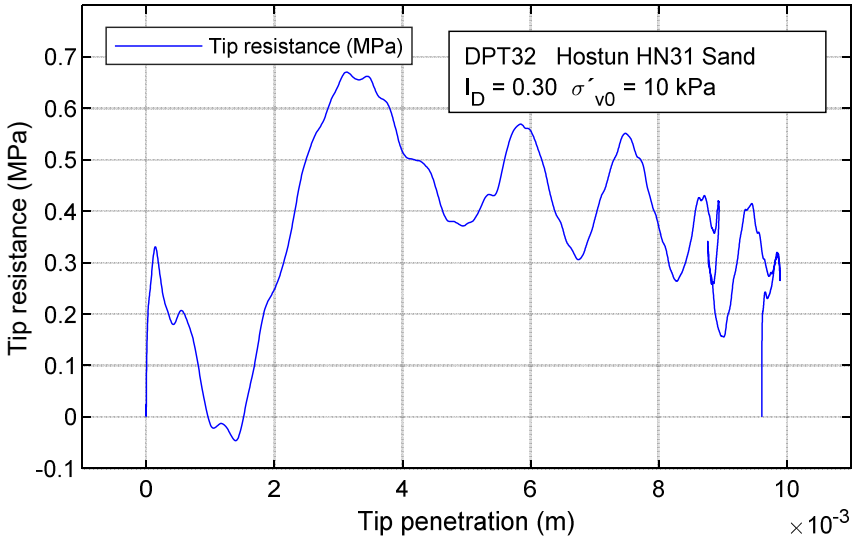

Figure 3-6 – DCLT curve for saturated loose soil.

An abrupt decrease of the penetration resistance measurement was observed in the range of about 15% of the maximum penetration and around the maximum velocity reached by the cone (Figure 3-7a). At this point, the decrease in strength can reach a value around zero. This reduction is followed by a rapid reincrease in resistance until reaching a maximum value after which the soil response shows a behavior similar to the drained case (Figure 3-7b).

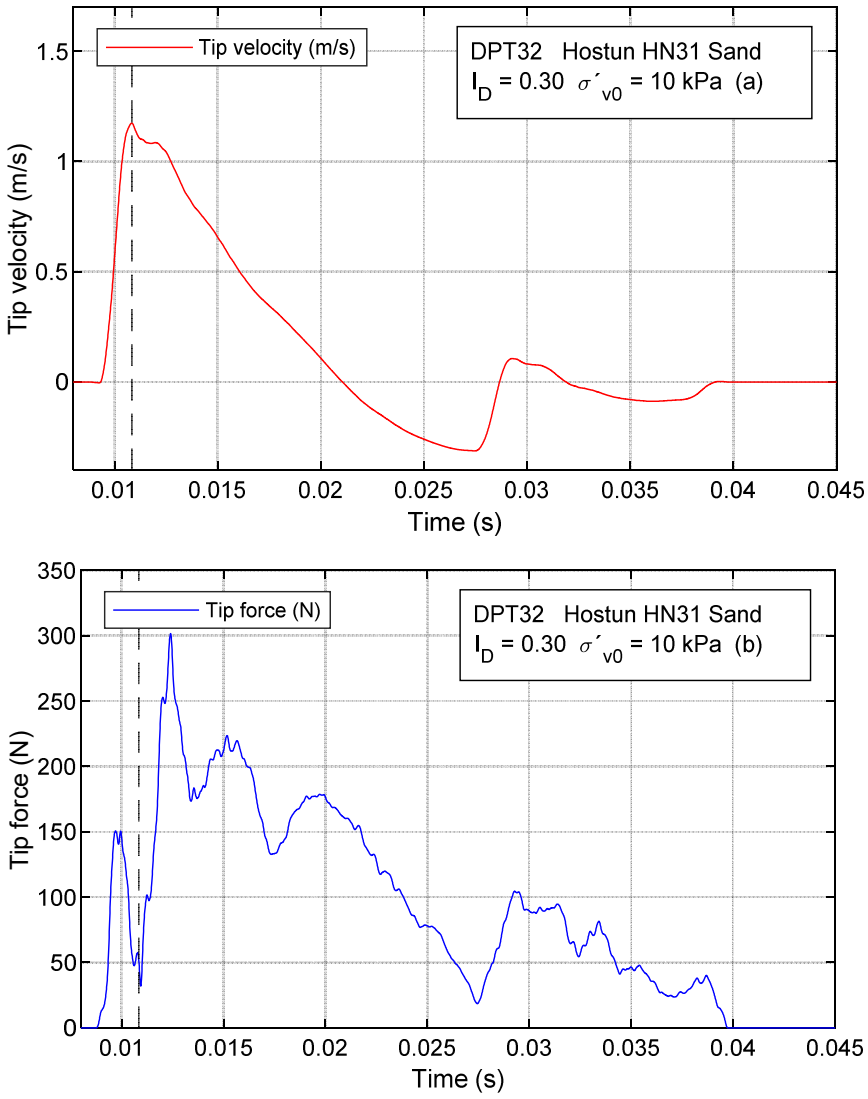

Figure 3-7 – Signals measured in saturated loose soils: (a) tip velocity; (b) tip force.

The rapid decrease in resistance can be explained by a temporary liquefaction phenomenon located around the soil-cone interface. When the wave front reaches the cone-soil interface, displacement begins on the soil applying a dynamic load of ascending velocity that will be initially assumed by the granular structure, which is observed in the initial rigid response; then, due to the loading velocity, the drainage of the water through the granular structure is not possible and undrained conditions are produced, which, added to the continuous increase of the cone pressure, initiates a process of load transfer to the fluid producing a rapid increase of the pore pressure and a decrease of the effective resistance of the soil until the localized liquefaction phenomenon occurs. This phenomenon is observed in low density specimens subjected to low levels of vertical effective stress.

The decrease in resistance will reach its minimum value around the maximum penetration velocity, after which there will be an increase in resistance associated with the decrease in the

kinetic energy of the cone and therefore the force generated on the soil, which allows the soil to recover its stability and resistance.

This phenomenon can also be observed in the signals measured by the sensors located at the penetrometer head. In a normal test performed on dry soil, at the arrival of the wave front at the cone-soil interface, the soil generates a resistant response involving energy consumption, which would continue until the maximum resistance mobilized by the soil is reached and will be reflected in a gradually decreasing velocity measurement, However, if the energy transfer decreases abruptly, as in the case of a rapid decrease in soil resistance, the reflected wave will contain a greater amount of unconsumed energy showing maximum velocity peaks after the arrival of the first reflected wave front at the measurement point (Figure 3-8).

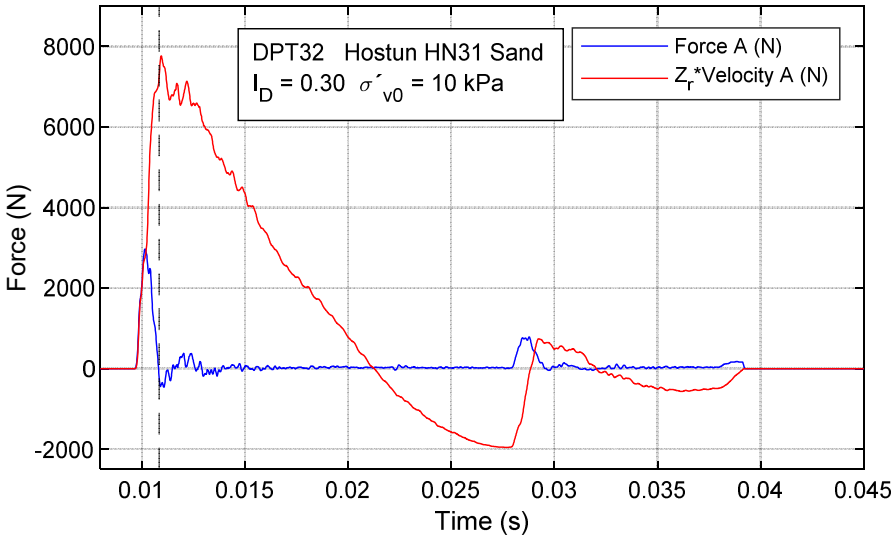

Figure 3-8 – Dynamic signals recorded at the penetrometer head: (a) force; (b) velocity.

3.1.3 Repeatability of dynamic stress-strain paths

It is important to evaluate the repeatability of the tests to establish the validity of the results. In the case of dynamic penetration tests, the variable nature of the driving energy implies that repeatability must be examined from two points of view: between two equally reconstituted specimens and between different impacts within the same specimen under the same boundary conditions.

To establish a comparison between two dynamic driving results, it is necessary to consider the cyclic nature of the load generated in the wave reflections, in addition to the variability of the energy, which can generate variable penetration work (Figure 3-9). This characteristic implies that two curves will never be identical, however, it has been proven that the maximum dynamic penetration resistance is an intrinsic property and independent of the energy level transmitted to

the penetrometer, within the operating range normally expected for the equipment used in this research.

Figure 3-9 shows two dynamic curves obtained from a penetration test performed on a saturated specimen ($I_D = 0.50$ and $\sigma'_v = 50\ kPa$). The shape of the curves shows a different load-displacement response in each case; Moreover, although the maximum strength value presents a difference of approximately 4% (0.082 MPa), the location of the strength peaks does not occur at the same penetration depth.

Another appreciable difference is the maximum cone penetration. At impact 39 there is an 18% greater penetration which is consistent with the 13% (0.35 J) greater energy generated in dynamic driving (Figure 3-9). This energy differential is converted to more work producing a greater displacement of the cone and not an increase in tip resistance.

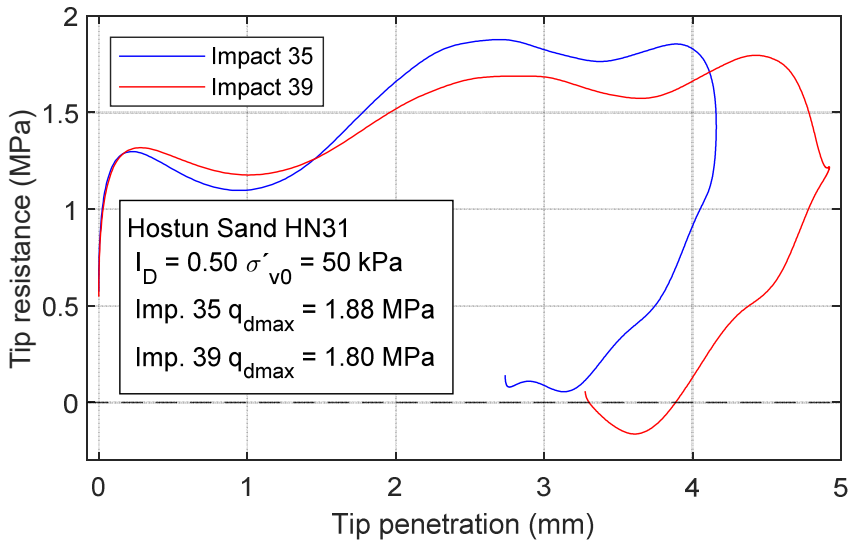

Figure 3-9 – Load-displacement curve for Hostun HN31 sands ($\sigma'_v = 50\ kPa$).

Considering the characteristics of the DCLT curves, a comparison can be made by taking into account the maximum value of the tip resistance and excluding the shape of the loading curve, because if the strength is an intrinsic characteristic of the soil, its value should not vary considerably if the applied load is sufficient to mobilize the maximum shear strength.

Two specimens of Hostun HN31 sands were reconstituted at a density index of 0.50 and saturated. To perform the dynamic penetration test, the specimen was subjected to values of σ'_v equal to10, 25, 50, 75, 100, 200 and 400 kPa. During the application of the vertical loads a variable number of impacts were applied. Figure 3-10 shows DCLT curves resulting from dynamic driving on the specimens subjected to effective vertical stresses of 50, 100 and 200 kPa. At each load level, 3 representative curves obtained from each specimen are shown.

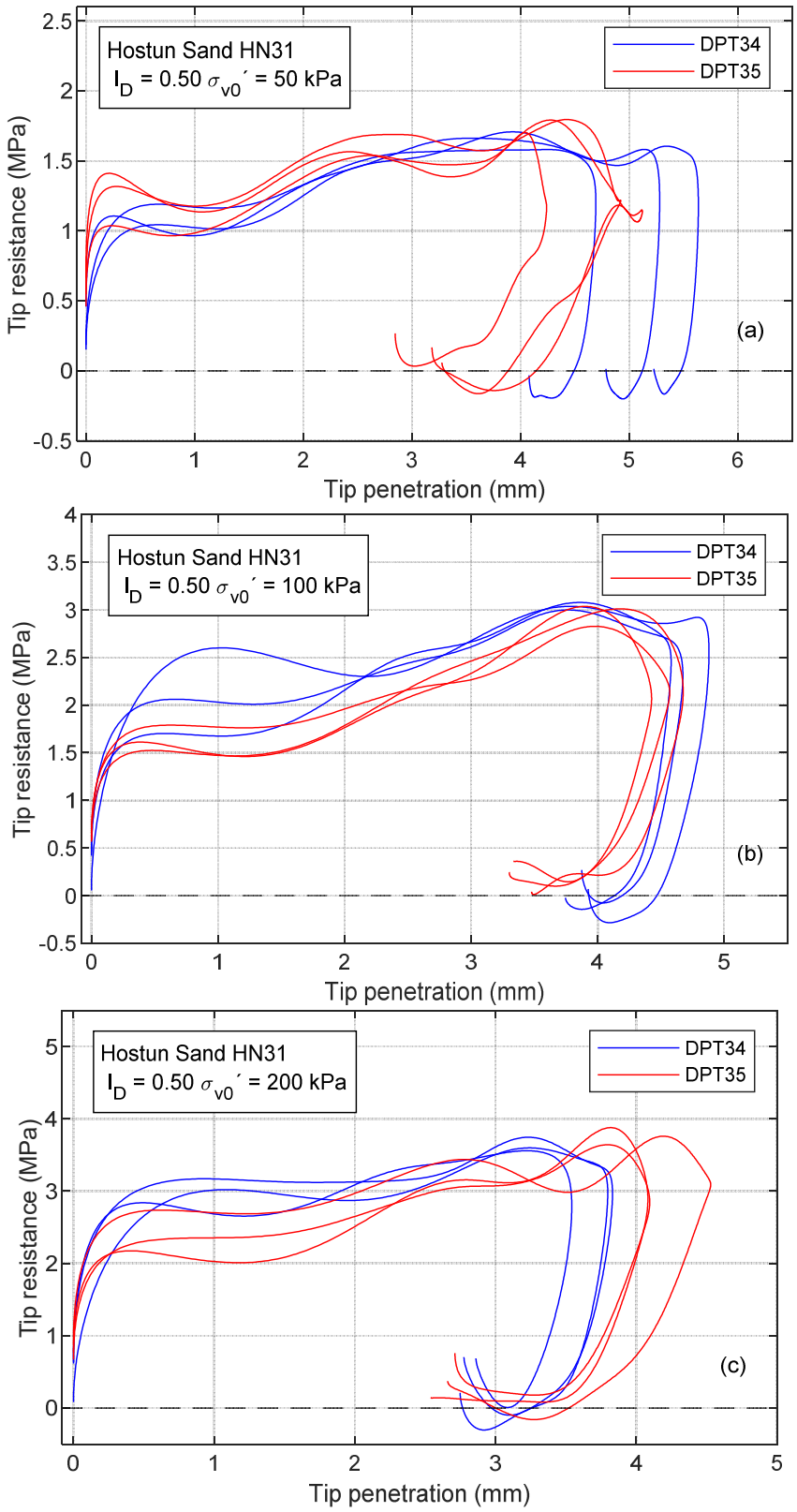

Figure 3-10 – Repeatability of DCLT curves in Hostun HN31 saturated sand: (a) $\sigma'_v = 50\ kPa$; (b) $\sigma'_v = 100\ kPa$; (c) $\sigma'_v = 200\ kPa$.

The observed responses shows agreement between the two specimens and differences in the magnitude of the maximum penetration. Similarly, the shape of the trajectories shows differences associated with the cyclic nature of the loading, however, the maximum strength results agree with each other. For the curves obtained applying a σ'_v of 50 kPa, a difference of 0.16% (0.0035 MPa) was observed, under a σ'_v of 100 kPa a difference of 4.8% (0.14 MPa) and under a σ'_v de 200 kPa a difference of 4.58% (0.17 MPa). Considering the comparative results, the repeatability of the tests is considered satisfactory.

3.1.4 Penetration velocity effects

If the movement of the cone on soil is considered, a damping component related to the velocity magnitude must be considered. This viscous component implies that at a higher velocity, the resistance to cone penetration will be higher. (Bazhenov et al. 2003; Iskander et al. 2015; Omidvar et al. 2014; Schreyer and Ehiu 1991).

In the case of the dynamic penetrometer driven by variable energy, the impact velocity of the hammer on the anvil will be variable and the effects of viscosity on the cone penetration resistance should be variable. In the PANDA 3 dynamic penetrometer, the penetration velocities measured are in the range of 1 m/s to 8 m/s.

To show the relationship between penetration velocity and penetration resistance, Figure 3-11 shows the results obtained for test DPT23 in terms of cone penetration velocity, resistance and penetration signal versus time for an impact made on a specimen of Fontainebleau NE34 sands, reconstituted at a density index of 0.50 and subjected to an effective vertical stress of 200 kPa.

The results show that the maximum penetration rate occurs before and out of phase with respect to the maximum dynamic resistance of the soil (Figure 3-11a and Figure 3-11b). On the other hand, it is observed that the maximum resistance occurs during the decrease of the penetration velocity. This implies that the mobilization of the maximum dynamic shear resistance in the soil is independent of the magnitude of the penetration velocity as long as the stress on the soil is sufficient to generate shear failure of the soil.

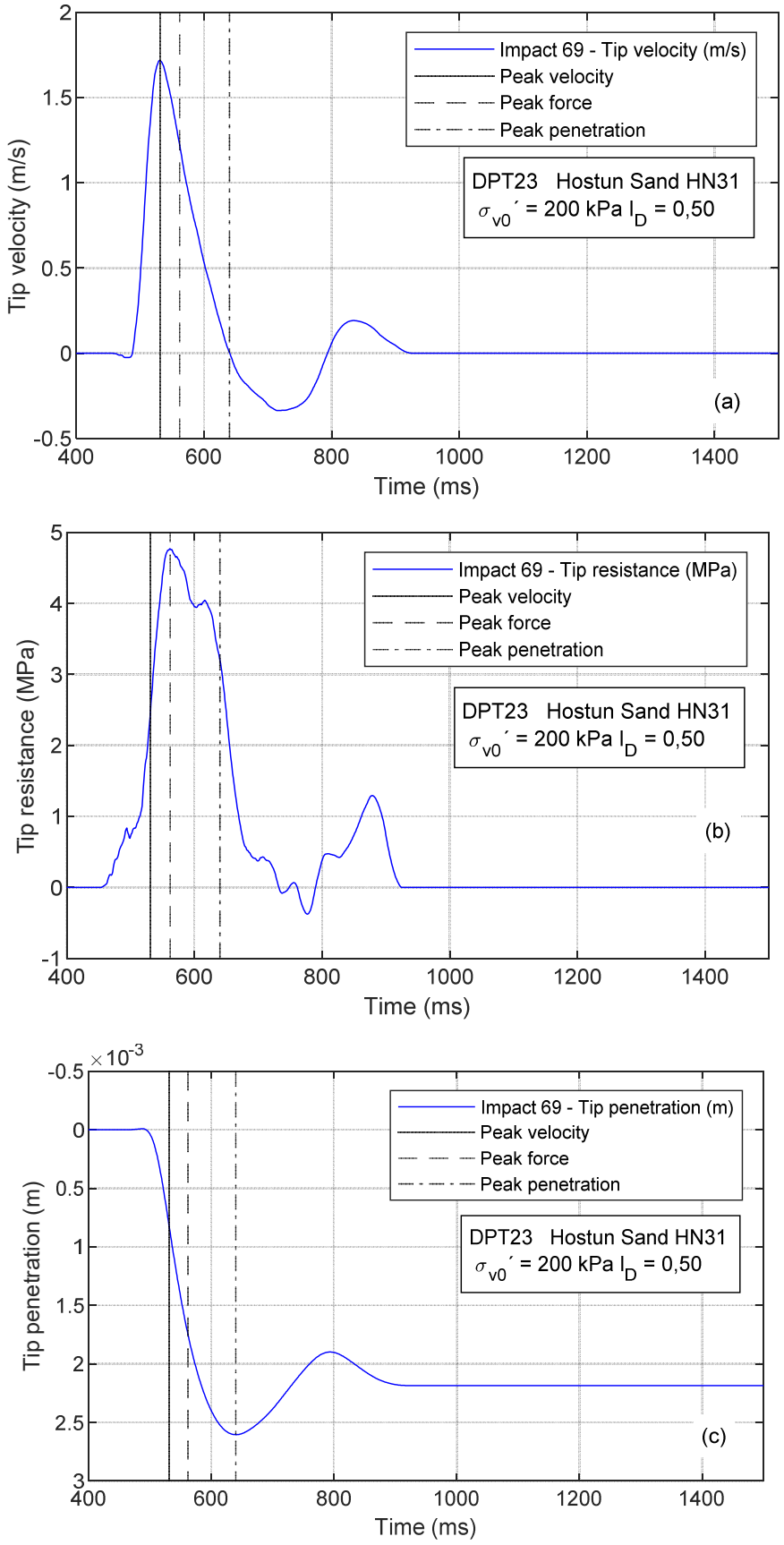

Figure 3-11 – Reconstructed signals at tip: (a) penetration velocity; (b) penetration resistance; (c) cone penetration.

The maximum velocity of the cone is reached in the initial phase of the penetration, so the response of the soil will initially be rigid, not producing the mobilization of the maximum resistance of the soil, however, by continuing to move, the transfer of energy to the soil and the generation of penetration work is maintained, which, after a yield phase, reaches a phase of plastic flow with stable resistance.

The failure of the soil occurs when the cone velocity is in a decreasing stage, which is possible because it continues moving and generating a penetration work on the soil. This work will continue to apply a stress on the soil so it continues to transmit energy in the form of potential deformation energy into the soil, until the cone stops at the maximum penetration depth of this loading cycle (Figure 3-11c) and there is a measurement decrease of mobilized resistance in the soil (Figure 3-11b).

After reaching zero velocity, the potential energy transferred to the soil will be converted mostly into non-conservative work; However, in the soil there is an elastic restoring response that pushes the penetrometer particles upwards, which is perceived as negative velocity. This upward pressure on the penetrometer activates the inertial effects associated with the penetrometer's own weight, generating a new load cycle of lower energy and therefore lower velocity (Figure 3-11a)

Figure 3-12 shows measurements of maximum resistance and penetration velocity at which it occurs for dynamic impacts performed on a Hostun HN31 sand specimen reconstituted at an I_D of 0.50 and subjected to an effective vertical stress of 100 kPa. In the case of the maximum penetration resistance, an average value of 2.2 MPa was observed (Figure 3-12a), however, the establishment of an average velocity associated with the average resistance is complex due to the high dispersion of the penetration velocity values at the time of maximum resistance (Figure 3-12b).

By observing Figure 3-12b it could be established that there is no relationship between the maximum resistance of a soil and the penetration velocity at which it occurs, contradicting the results presented in the literature (Bazhenov et al. 2003; Iskander et al. 2015; Omidvar et al. 2014; Schreyer and Ehiu 1991). On the other hand, the mentioned works have shown results of resistance-velocity relationship at high velocities in which an exponential relationship between resistance and impact velocity is presented, which is out of the range of impact-penetration velocity recorded in the equipment used in this research (1 a 8 m/s).

Under the above considerations, the high dispersion in the relationship between resistance and penetration velocity can be attributed to the low influence of the viscous response of the soil subjected to penetration, based on this, it is possible to consider that the viscosity effects are

negligible in the operating range of the PANDA 3 dynamic variable energy penetrometer (from 1 to 8 m/s)

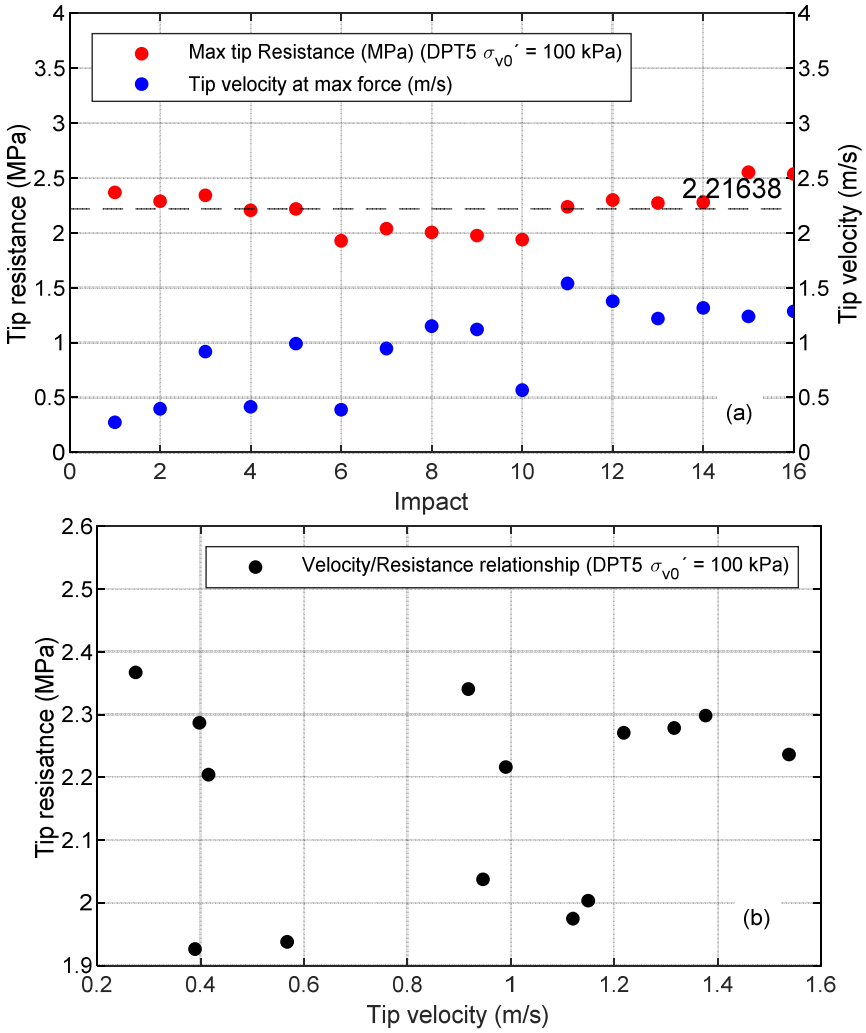

Figure 3-12 – Penetration velocity-resistance ratios: (a) maximum resistance measurements and (b) penetration velocity - maximum resistance ratio.

The relationship between maximum resistance and penetration velocity shows a high degree of dispersion under different levels of applied stress and, in all cases, the variation of resistance from one impact to another remains low.

In the opposite case, when the cone reaches the maximum penetration velocity (Figure 3-13a), the penetration resistance is variable and dispersed with respect to the velocity. This implies that in the range of penetration velocities reached by the cone during the test, it is not possible to establish a correlation (Figure 3-13b).

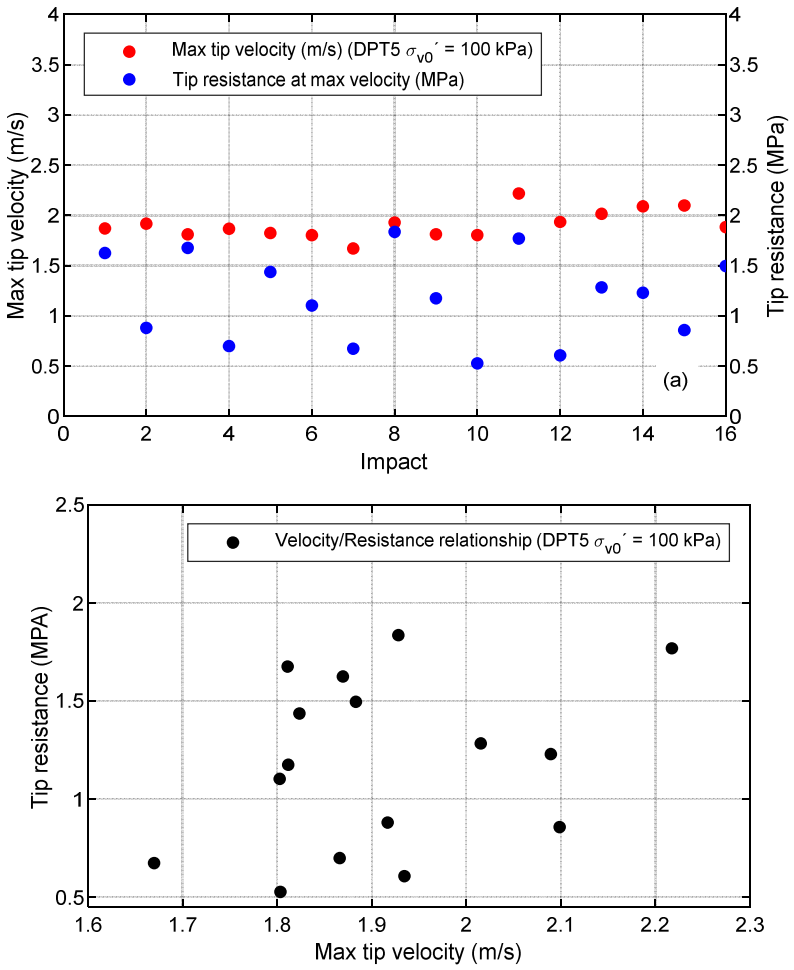

Figure 3-13 - Maximum velocity and penetration resistance relationship: (a) Maximum velocity registers; (b) penetration velocity - maximum resistance relationship.

3.1.5 Penetration energy

If the principle of energy conservation is considered in the analysis of the dynamic driving of the penetrometer, the penetration work done by the cone will be directly related to the amount of energy that reaches the cone-soil interface. Considering this relationship, the description of the interaction between the energy contained in the compression wave produced by the impact of the hammer and the penetrometer-soil system can be modeled by means of the Hamilton principle (Clough and Penzien 2003), by which it is possible to explain that the greater the energy applied to the system, the greater the non-conservative work. In the case of the dynamic penetrometer this is related to a higher level of penetration of the cone.

With PANDA 3® it is possible to obtain the dynamic driving energy at the penetrometer head by applying the EFV method directly at the cone-soil interface using the reconstructed force and velocity signals. It is also possible to apply the energy conservation principle to the DCLT curve relationship to obtain the total energy used in the penetration. Depending on the measurement point of the wave, the magnitude of the energy will vary due to the interaction of the

wave with the penetrometer and the boundary, where one of the most critical aspects of this interaction is the lateral friction.

Figure 3-14 shows the relationship between the dynamic driving energies recorded at the penetrometer head and the calculated energy at the soil-cone interface obtained from the reconstructed cone signals. The measurements were obtained from impacts on a reconstituted Fontainebleau NE34 sand specimen at an I_D de 0.90 subjected to a range of effective vertical stresses varying from 10 kPa to 400 kPa. The results obtained show a linear relationship with a slight tendency to higher energy values at the head of the penetrometer (4%), this difference may be multifactorial and cannot be attributed to a single mechanism (lateral friction, signal treatment, reconstruction process, among others). However, the difference in energy obtained at both points can be considered negligible for purposes of analysis of the dynamic driving phenomenon and the setup of the experimental apparatus used in this research.

The low energy loss shown by the measurements evaluated at both points is related to the controlled conditions of the test, in addition, the length of the rods (1 meter), favors a lower energy loss due to the lateral interaction of the penetrometer.

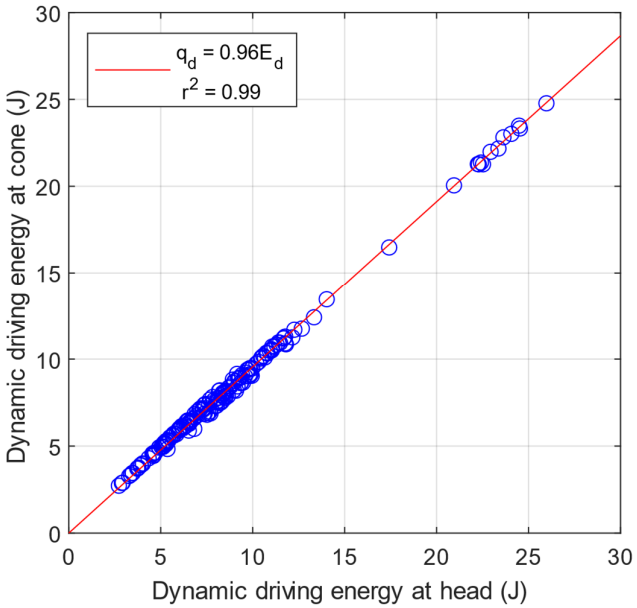

Figure 3-14 – Ratio of energies evaluated at penetrometer head and cone-soil interface.

For failure of the soil to occur, it is necessary to reach a stress limit capable of mobilizing the shear strength of the soil. The magnitude of the stress is multifactorial and in the case of the dynamic penetrometer, the type of stress generated by the cone is associated with a kinetic energy.

However, if it is considered that the effects associated with the velocity are negligible (Chapter 3.1.4), and the resistance is an intrinsic property of the soil, a greater magnitude of driving energy results in the generation of a non-conservative work of greater magnitude under a maximum resistance limit.

Due to the anisotropic characteristics of the soil, and the cyclic-dynamic nature of the stress generated in the cone, the DCLT curves will never be identical to each other, but the maximum value obtained should be fairly independent of the level of driving energy. An example of this fact is presented in Figure 3-15, which shows different impacts performed on a Hostun HN31 sand specimen reconstituted to an I_D of 0.30 and subjected to an effective vertical stress of 200 kPa (test DPT1). The DCLT curves (Figure 3-15a) which is reached in the range of minimum and maximum driving energies between 1.03 J and 1.92 J, respectively. When comparing the DCLT curves, it can be observed that the higher the driving energy, the higher the penetration, which is associated with non-conservative work (Figure 3-15c).

DCLT curves, energy paths and energy-penetration relationships are presented in Figure 3-16 and Figure 3-17 for impacts performed on specimens reconstituted to an I_D of 0.30, subjected to vertical effective stresses of 200 kPa and 400 kPa, respectively. The average tip resistance for the specimen consolidated at 200 kPa of vertical effective stress was 2.29 MPa (Figure 3-16a) and the range of driving energies from 1.44 J to 2.26 J (Figure 3-16b). For the specimen consolidated at 400 kPa, the average maximum strength was 5.88 MPa (Figure 3-17a) and the driving energies ranged from 5.11 J to 14.1 J (Figure 3-17b).

In the three cases presented, it was observed that the driving energy is directly related to the level of penetration (non-conservative work) performed by the cone (Figure 3-15c, Figure 3-16c and Figure 3-17c). This implies that in the range of energies and penetration velocities in which the variable energy dynamic penetrometer operates, a higher driving energy level will generate a higher penetration work and not an increase of the dynamic resistance.

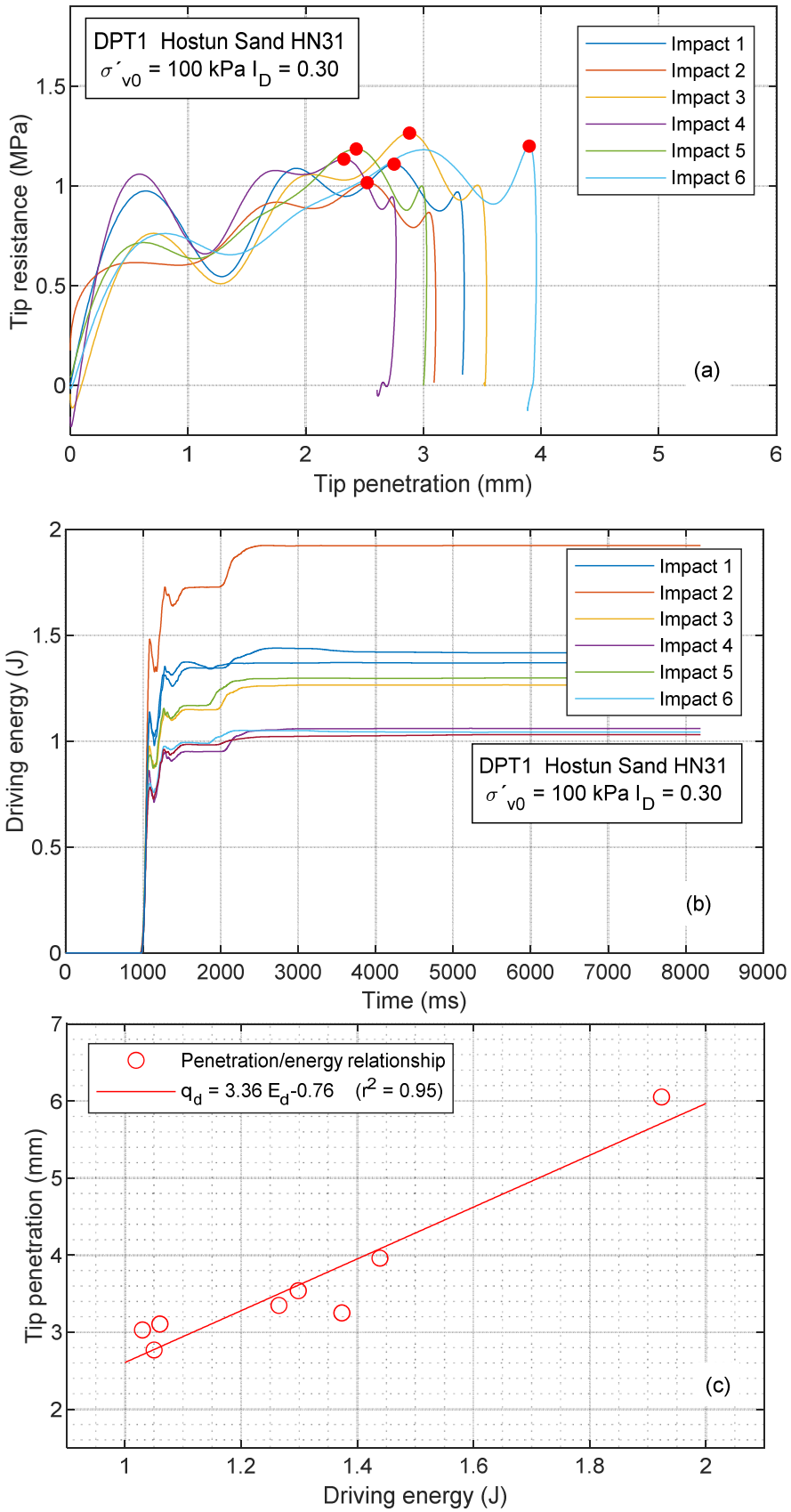

Figure 3-15 – (a) DCLT curves for different impacts on the same specimen; (b) dynamic energy paths during penetrometer driving; (c) relationship between dynamic driving energy and penetration ($\sigma'_v = 100\ kPa$).

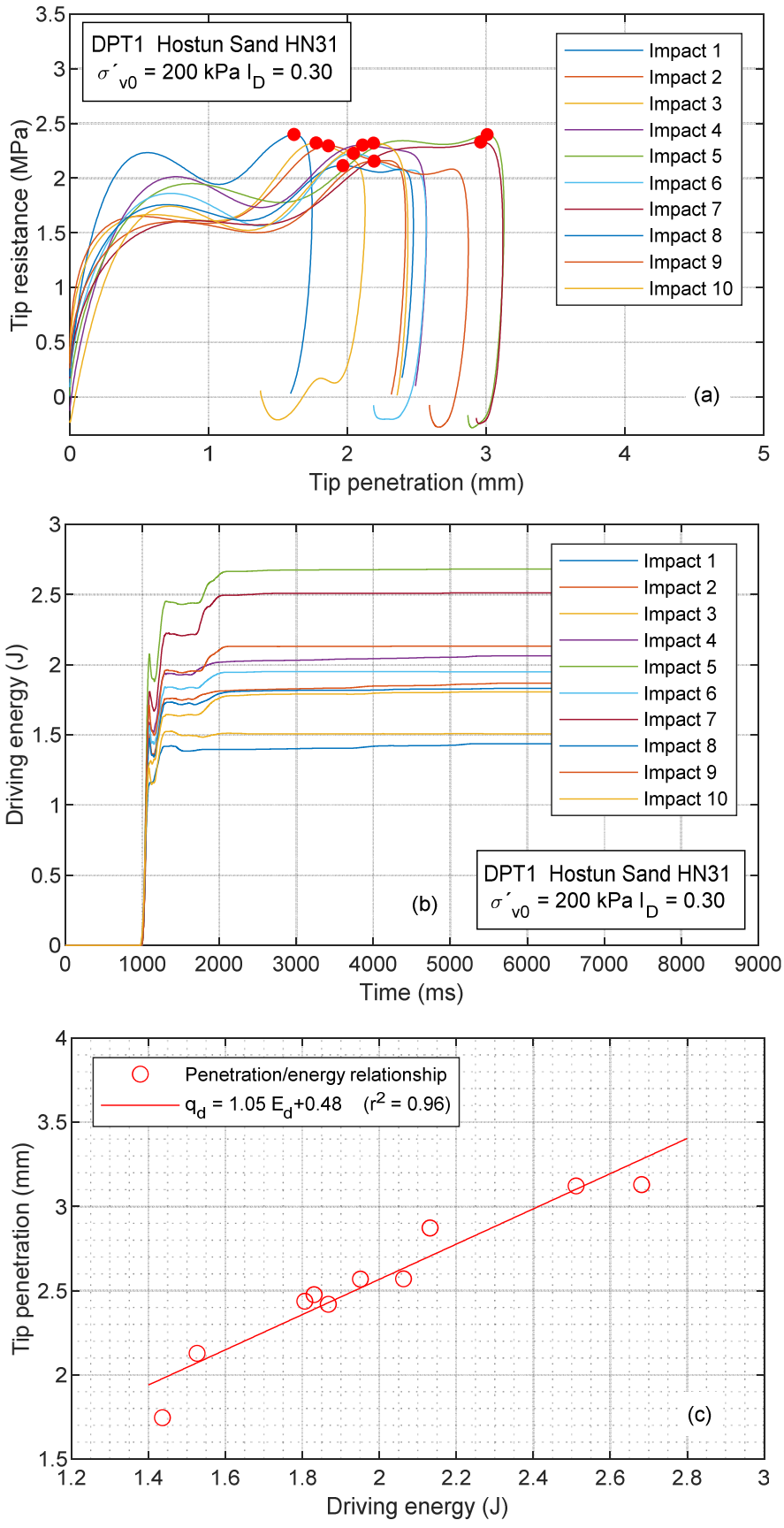

Figure 3-16 – (a) DCLT curves for different impacts on the same specimen; (b) dynamic energy paths during penetrometer driving; (c) relationship between dynamic driving energy and penetration ($\sigma'_v = 200\ kPa$).

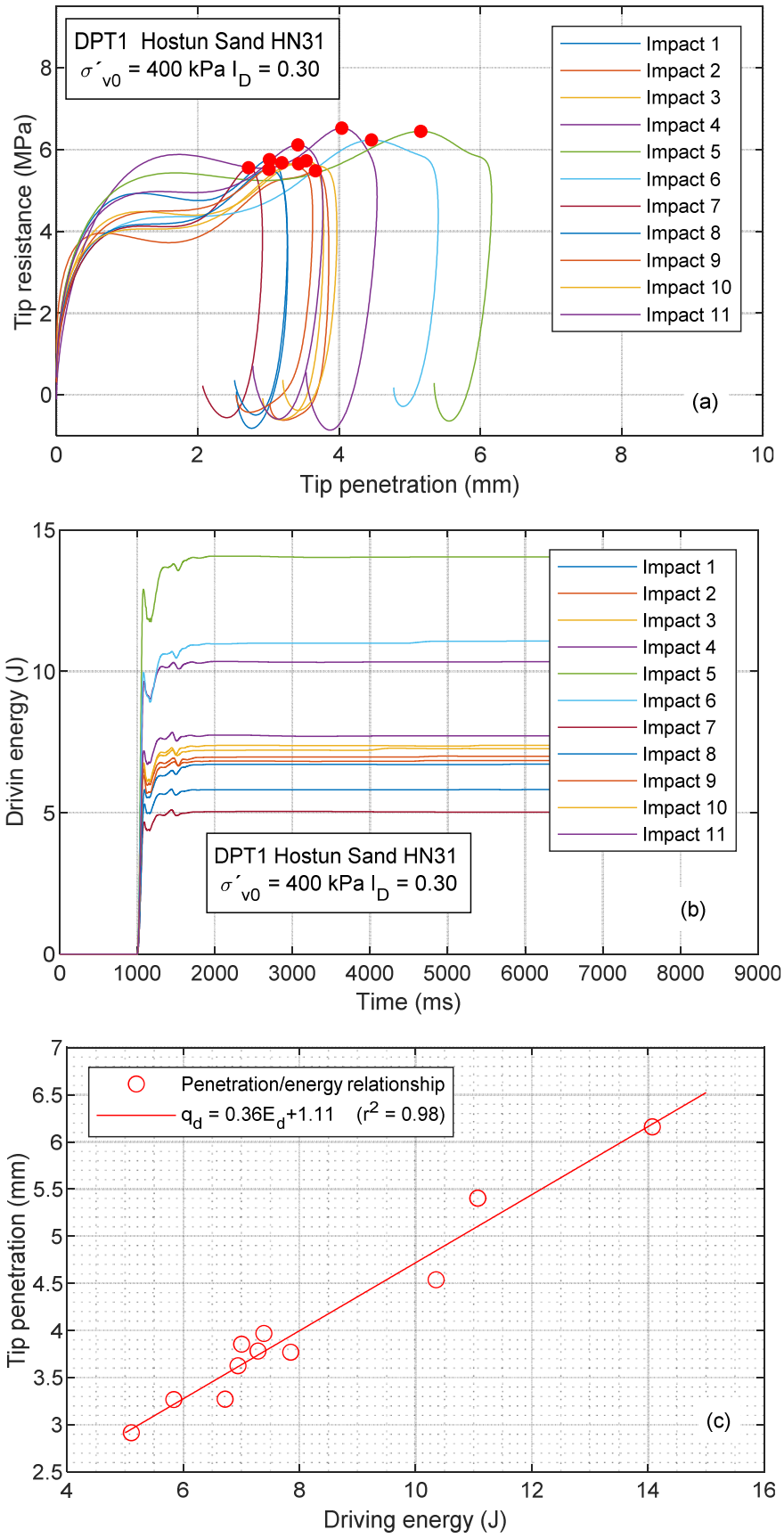

Figure 3-17 – (a) DCLT curves for different impacts on the same specimen; (b) dynamic energy paths during penetrometer driving; (c) relationship between dynamic driving energy and penetration ($\sigma'_v = 400\ kPa$).

Figure 3-18 shows the relationship between the dynamic driving energy and the maximum resistance generated in the first loading cycle, under different levels of vertical effective stress. In general, the relationship shows maximum resistance values around a constant value for impacts on soils subjected to the same vertical effective stresses and with the application of different energy levels.

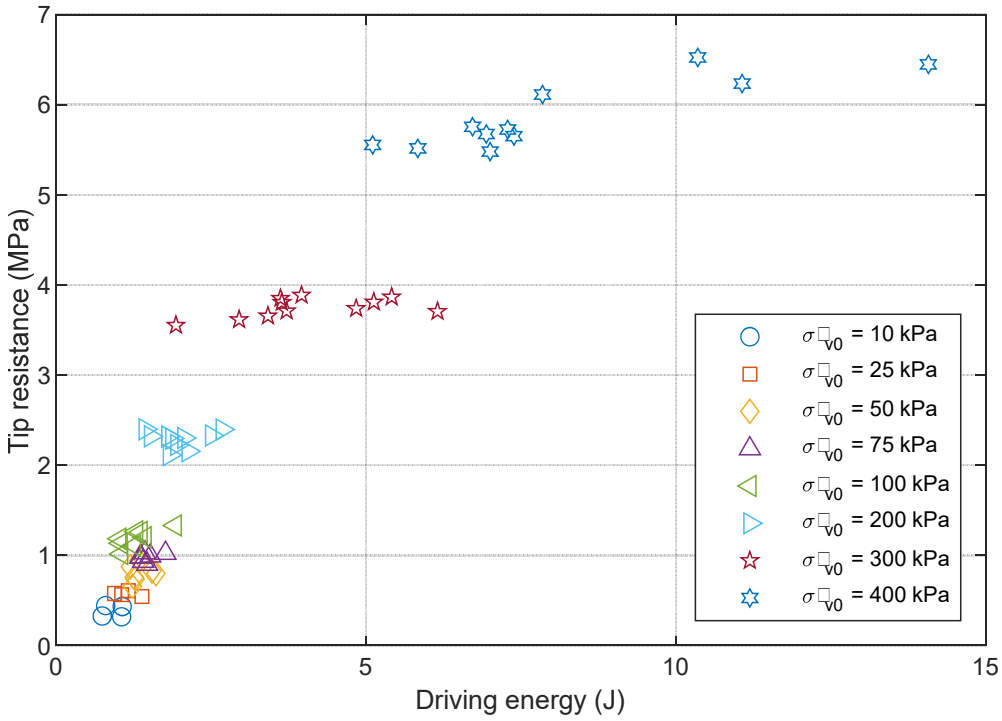

Figure 3-18 – Penetration resistance - dynamic driving energy relationship.

Another visible aspect in Figure 3-18 is the relationship between the driving energy level and the magnitude of the vertical stress applied. Although the energy applied at each impact is variable, in general there is a tendency for higher energy levels to be applied the greater the vertical stress. This is consistent with the need to apply greater kinetic energy during the hammer impact in order to penetrate the soil.

3.1.6 Typical results obtained on dry test study

3.1.6.1 Influence of the vertical effective stress σ'_v

To analyze the effect of vertical effective stress on the DCLT curves, dynamic penetration tests were performed on specimens subjected to staggered vertical stresses, following an application program of 10, 25, 50, 75, 100, 200, 300 and 400 kPa. The same vertical loading and testing procedure was applied to all specimens.

Figure 3-19 and Figure 3-20 show DCLT curves obtained from impacts on reconstituted specimens of Fontainebleau NE34 and Hostun HN31 sands at densities index values of 0.30 and 0.70 subjected to different levels of vertical effective stress σ'_v. The results show that the higher the vertical effective stress, the greater the amplitude of the DCLT curve. Above 50 kPa of effective vertical stress, the amplitude differences are notorious, however, below this limit the curves show maximum amplitudes within a more limited range.

Although the penetration test involves different energies at each impact, a tendency to a greater penetration distance can be observed in those DCLT curves obtained from specimens of low density and low vertical effective stress applied. This is due to the fact that under these specimen conditions, the same energy level is capable of producing a higher non-conservative penetration work, associated to a lower resistance developed by the soil.

As for as the shape of the loading curves is concerned, an ondulatory behavior can be noted in the plastic flow phase. This behavior is related to the cyclic-dynamic nature of the stress applied by the cone on the soil; however, at low levels of vertical effective stress this behavior is more marked and extended due to the greater work generated during penetration. On the other hand, it can also be observed that, independently of the extension of the plastic phase, at low levels of effective stress, the maximum values of the curve oscillate around a maximum limit characterized as the maximum dynamic shear resistance mobilized by the soil. In the case of specimens subjected to high vertical effective stresses, the plastic flow phase occurs during a smaller extension. This phenomenon occurs because the driving energy is not sufficient to perform a higher penetration work due to a higher soil resistance associated with the confining conditions.

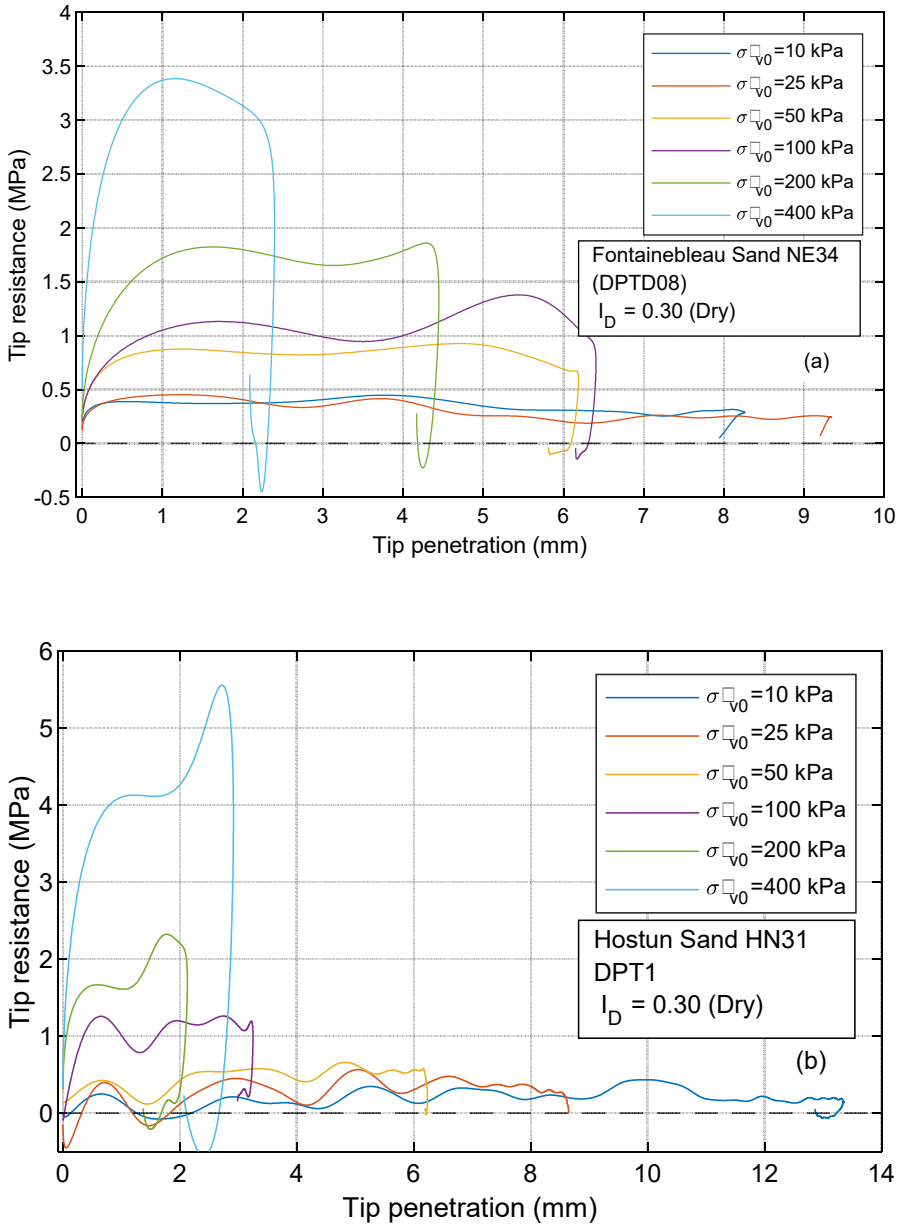

Figure 3-19 – DCLT curves for specimen of dry sand ($I_D = 0.30$) for different vertical effective stress σ'_v; (a) Fontainebleau Sand NE34; (b) Hostun Sand HN31.

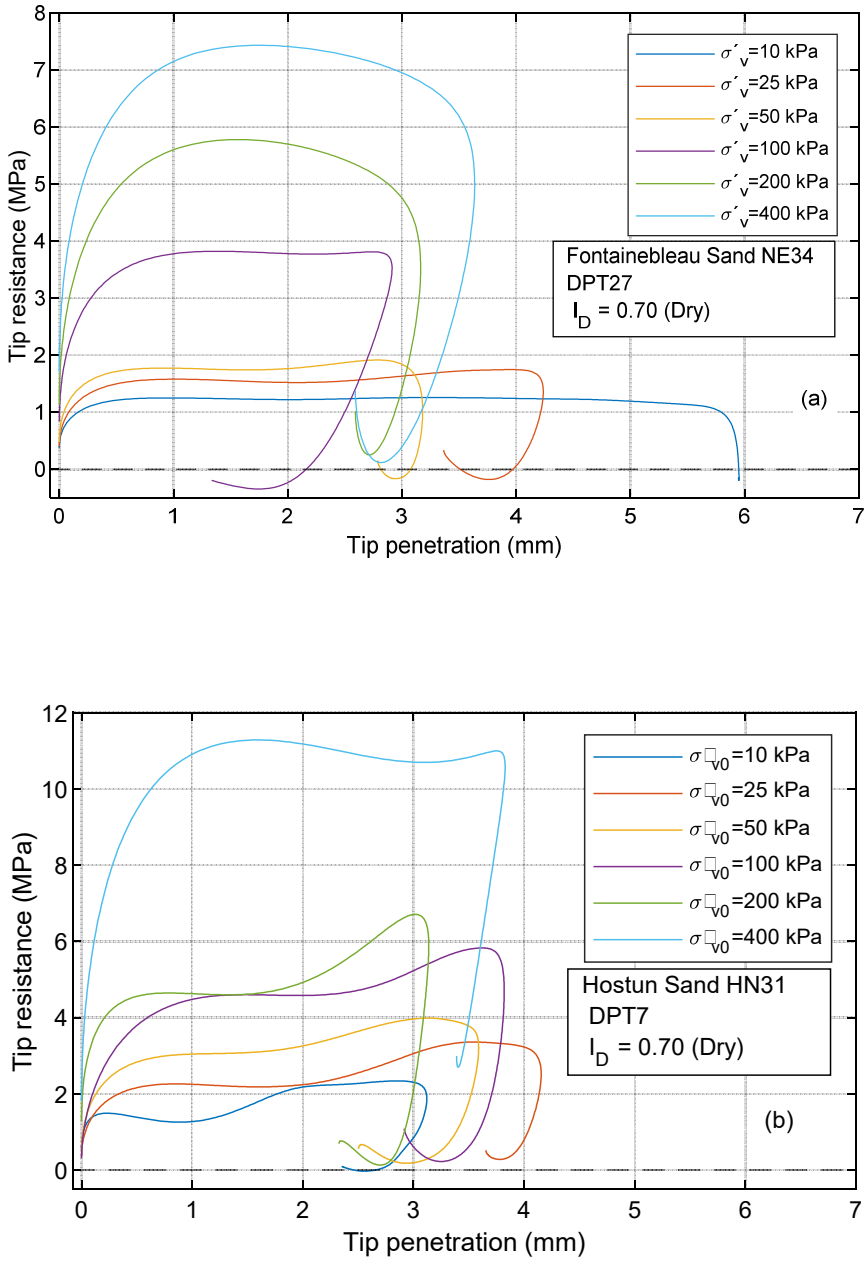

Figure 3-20- DCLT curves for specimen of dry sand ($I_D = 0.70$) for different vertical effective stress σ'_v; (a) Fontainebleau Sand NE34; (b) Hostun Sand HN31.

The load-displacement relationship, shown in the DCLT curves shows the same shape in both types of sands, however, higher maximum tip resistance are appreciated in Hostun HN31 sands (test DPT7) under the same level of vertical effective stress and in dry state. In the case of $\sigma'_v = 10\ kPa$, and under density index level of $I_D = 0.30$, a difference of 0.043 MPa (~10%) was obtained, and for an $I_D = 0.70$, a difference of 1.05 MPa. These tip resistance differences may not be noticeable between both types of sands due to the low average magnitude of the maximum strengths under these conditions, however, if the vertical effective stress is increased these

differences are accentuated. Under a vertical stress of 400 kPa, the average difference obtained for both sands were 2.01 MPa (~50%), and 2.48 MPa (~31%), for I_D specimens of 0.30 and 0.70 respectively.

According to the curves obtained for the different vertical effective stress conditions, an effect on the amplitude of the DCLT curves has been observed. The higher the vertical effective stress, the greater the amplitude (maximum resistance) of the curve. On the other hand, the effect of the type of soil under the same loading conditions was also observed, where Hostun sands show a greater amplitude in the range of applied loads, obtaining a greater difference when the applied vertical stress is higher.

The extension of the plastic phase was also noted to be dependent on the effective vertical stress, especially in low density specimens, however, it is not possible to establish a relationship between the extension of the plastic flow and the vertical stress directly, since the latter depends on the level of dynamic driving energy applied, which is variable in all cases. However, the observed tendency may be due to the fact that the range of applied energies is small, producing dependence on the confinement conditions.

3.1.6.2 Density index (I_D) effect

Figure 3-21 and Figure 3-22 present DCLT curves obtained for Hostun HN31 sand specimens, for density index conditions of 0.30, 0.50, 0.70 0.90, under effective vertical stresses of 10, 25, 50, 100, 200 and 400 kPa. The resulting curves show that the maximum value obtained on the DCLT curves (maximum resistance) is higher the higher the density index of the specimen. This characteristic establishes a relationship between the dynamic penetration resistance and the density index of a sand and allows the establishment of predictive models of the density state of the soil. (Chaigneau 2001; Gansonré et al. 2019; López Retamales et al. 2021; López Retamales et al. 2020). This relationship is observed in all the cases studied.

It has been observed that the strength is higher when the density index of the soil is higher, and also the strength will increase when the effective vertical stress is higher. In specimens of Hostun HN31 sand reconstituted at an I_D of 0.30, there is an increase of 5.49 MPa between vertical stresses from 10 kPa to 400 kPa and for an I_D of 0.90 a difference of 14.88 MPa. a difference of 14.88 MPa. In the case of Fontainebleau NE34 sands with I_D of 0.30 the difference is 3.43 MPa and at an I_D of 0.90 of 12.19 MPa for the same change in vertical effective stresses. This observation implies that the maximum strength observed in the DCLT curve increases more when the density index and the effective stress are higher.

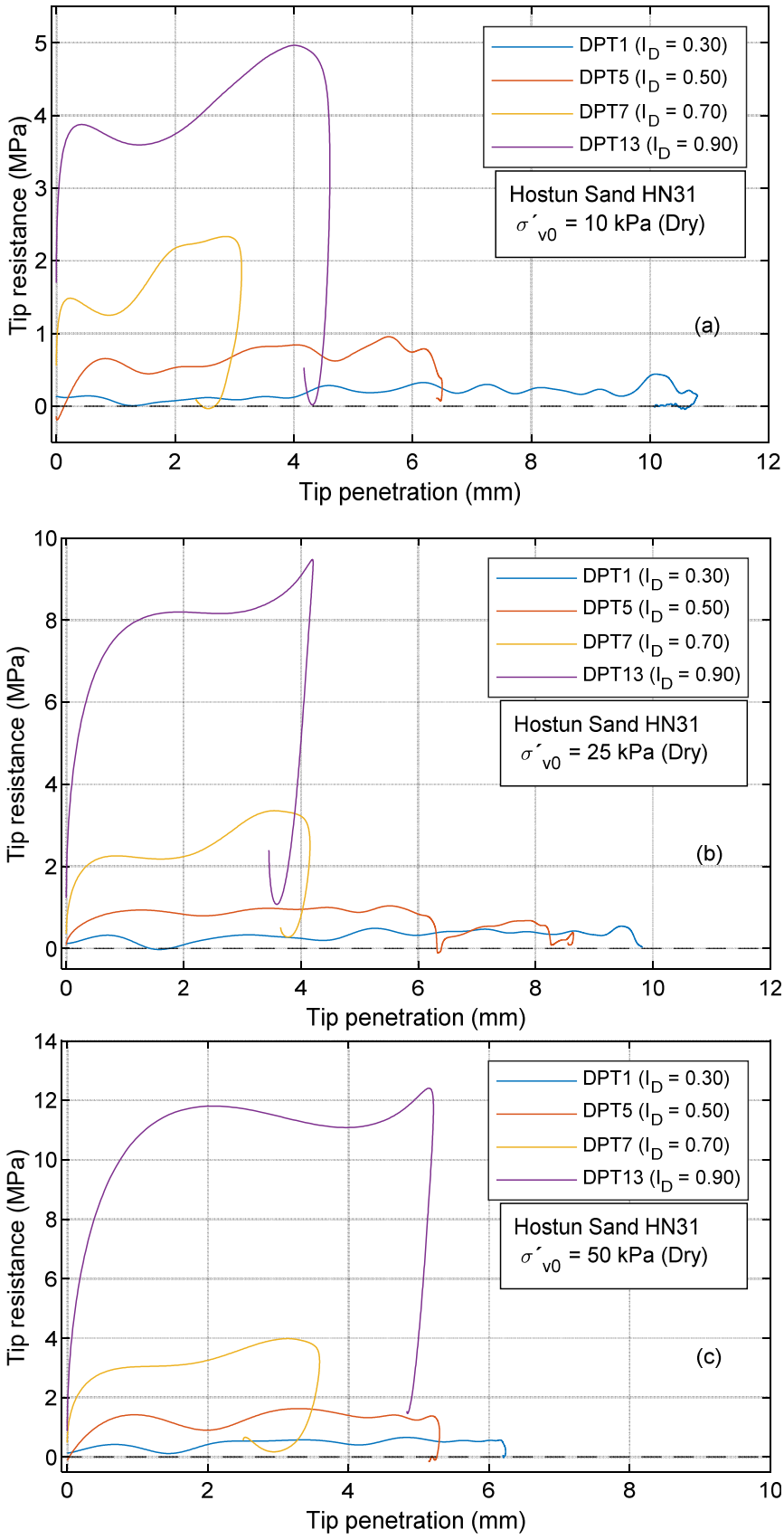

Figure 3-21 – DCLT curves obtained for dry Hostun HN31 sands: combined influence of density index I_D and vertical consolidation stress σ'_v.

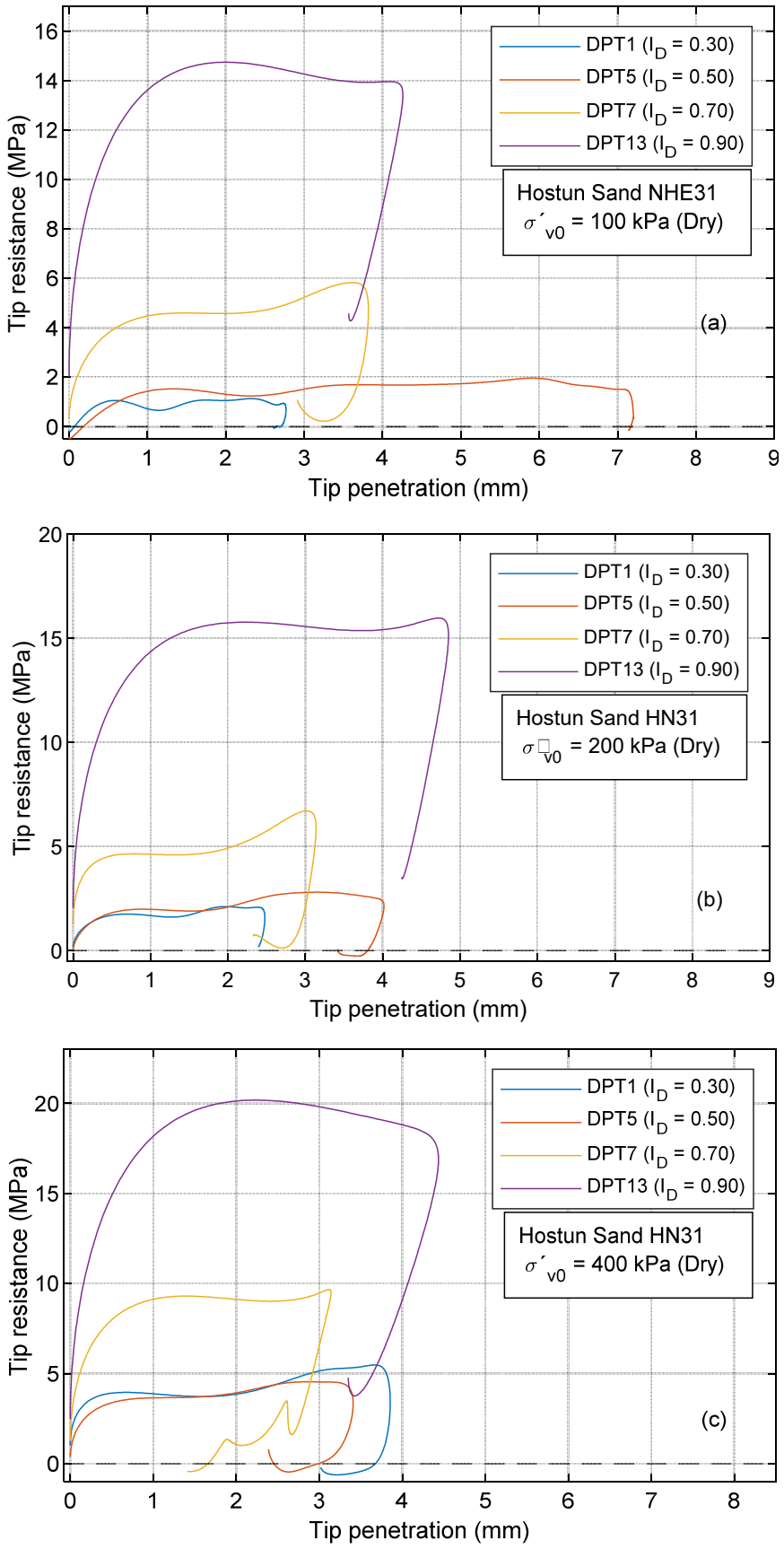

Figure 3-22 – DCLT curves obtained for dry Hostun HN31 sands: combined influence of density index I_D and vertical consolidation stress σ'_v.

Similar to the analysis of the effect of vertical effective stresses, in the case of the density index there is a tendency for the occurrence of more extended plastic flow phases when the soil density is lower, being this phenomenon more significant at low levels of vertical effective stress (Figure 3-21), however, although the relationship is proven under the same energy level, the variable character of the penetrometer does not allow attributing this extension only to the soil density without considering the magnitude of the driving energy.

In the case of specimens under higher effective vertical stresses (Figure 3-22), the differences in the plastic flow phase for the different density indices do not present a marked tendency, and may even be greater in specimens with a density indexes of 0.90. The reason for this is the fact that in order to produce the driving of the penetrometer a higher level of energies is required, which are not controlled by the operator, but measured by the equipment.

The curves analyzed allow the description of a relationship between the soil density index and the maximum amplitude of the DCLT curve. This relationship allows the establishment of correlations between the state of the soil and its resistance through a logarithmic regression analysis, which added to the difference in the variation of resistance according to the type of soil and the effective vertical stresses, allows the generation of unique $q_d - I_D$ relationships for each type of soil.

3.1.7 Typical results obtained for saturated sand

Concerning the DCLT curves, the results show the same behavioral trend with respect to the vertical effective stress conditions; however, a behavior associated with a decrease in resistance was observed after a peak of resistance in the rigid response phase. This decrease was observed in specimens under low vertical effective stresses and reconstituted at low density indexes ($I_D = 0.30$) (Figure 3-23a), however, and as demonstrated in previous chapters, there is an increase in resistance until a plastic flow phase is produced. This behavior has been attributed to a localized liquefaction phenomenon at the tip contour, resulting from the rapid loading of the penetrometer and the generation of undrained conditions.

The curves obtained from dense specimens (Figure 3-23b), did not show a sudden initial decrease and the trajectory was similar to that of the dry case, however, the results show that the differences in strength between the two types of sands disappear, and the strength magnitudes are similar throughout the range of effective vertical stresses and density index.

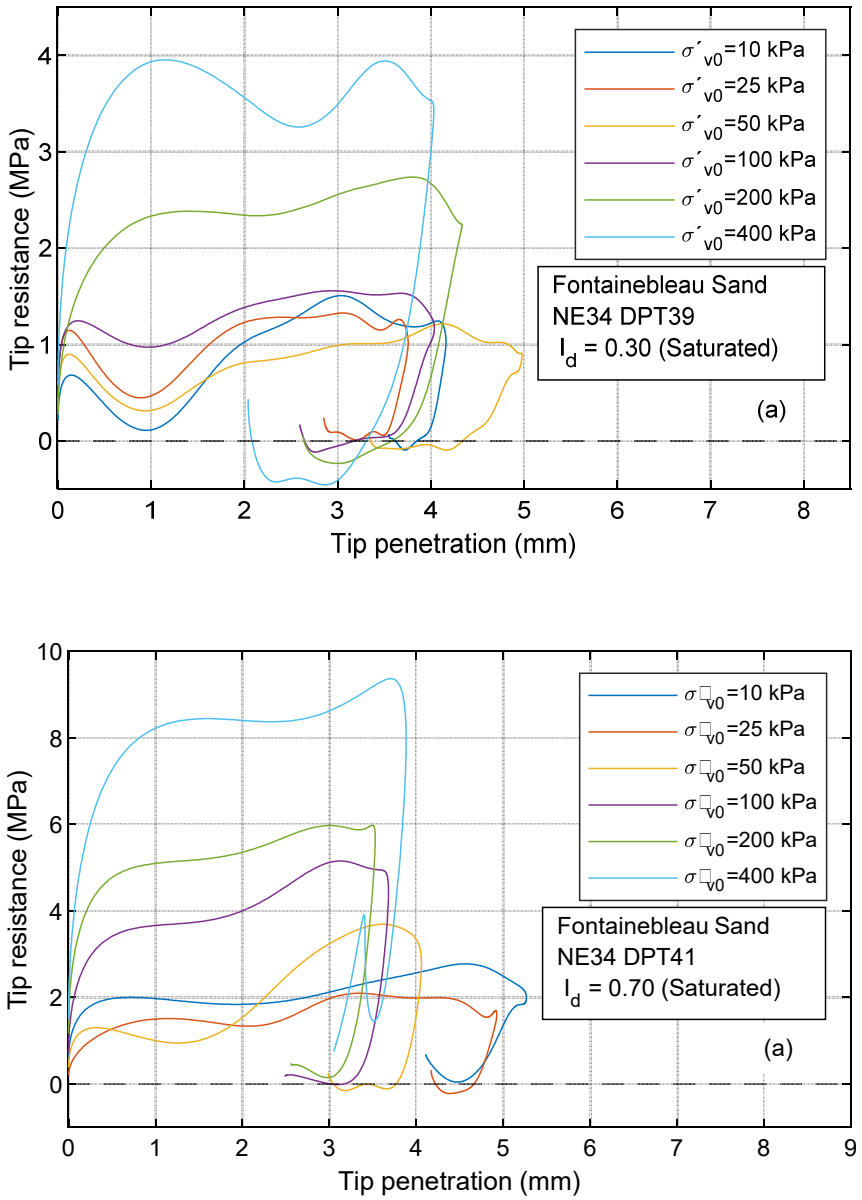

Figure 3-23 – DCLT curves obtained for dry Hostun HN31 sands: combined influence of density index I_D and vertical consolidation stress σ'_v.

The effects on the shapes of the DCLT curves associated with the density index are shown to be similar to those observed in dry specimens (Figure 3-24), except in the case of low density (local liquefaction phenomena), and as mentioned above, no significant difference was observed in the magnitudes of maximum strengths in different sands for the same level of density index.

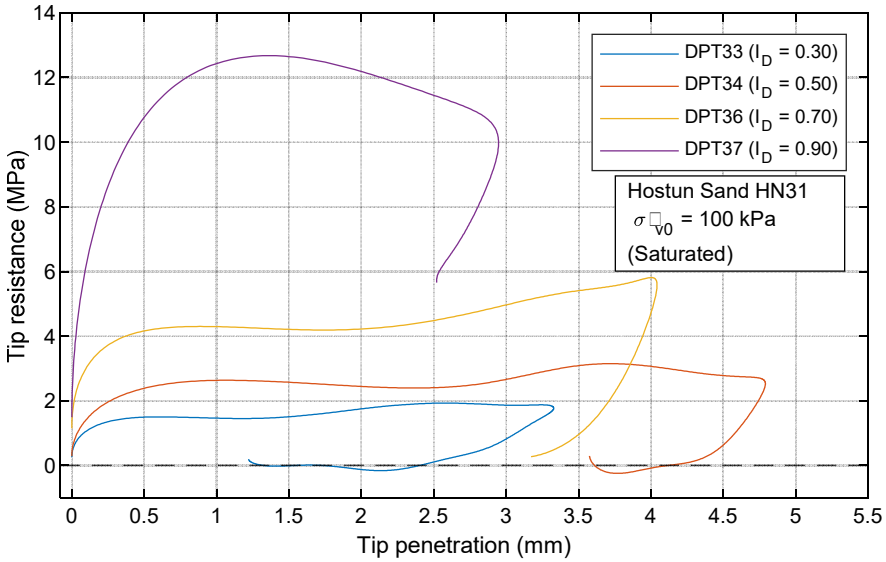

Figure 3-24 – DCLT curves for specimens in saturated Hostun HN31 sands $\sigma'_v = 100\ kPa$.

3.2 Dynamic penetration resistance

Dynamic penetration resistance can be obtained by several methods. Depending on the one selected, the conditions of the analysis may be different and the evaluation will have to take into account the type of soil and the test conditions. For this research, an approach based on the DCLT curve has been chosen because it represents the response of the soil and its behavior under dynamic loading.

To calculate the resistance, the maximum resistance value of the DCLT curve (Figure 3-25) is used, assuming that this resistance corresponds to the maximum shear resistance mobilized in the soil when it is penetrated by the cone.

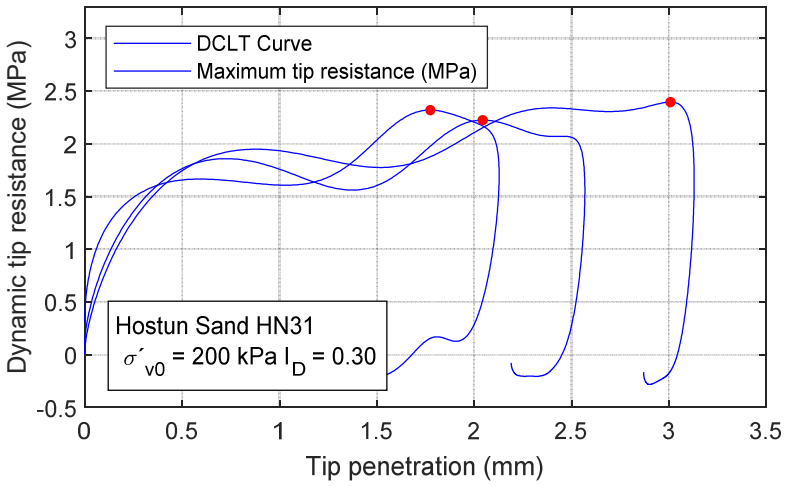

Figure 3-25 – DCLT curve with maximum dynamic resistance.

Due to the cyclic and dynamic nature of the load generated by the penetrometer on the soil and the energetic variability, the location of the maximum resistance in the DCLT curve will not

be constant, however, it has been possible to establish that the magnitude of the maximum resistance is located around a constant value during the plastic flow phase for impacts performed on a soil under the same conditions. Taking this into account, it is considered acceptable to use the average value of the dynamic resistance obtained for the set of dynamic impacts performed on a specimen under the same internal and boundary conditions as a representative value.

Obtaining the maximum strength values allows the construction of penetrograms of dynamic strength versus effective vertical stress. Figure 3-26 shows maximum strength penetrograms from variable energy dynamic penetration tests performed on Hostun HN31 sand specimens reconstituted at densities index of 0.30, 0.50, 0.70 and 0.90. Impacts were performed on specimens subjected to a range of vertical effective stress from 10 kPa and up to 400 kPa.

From the penetrograms, it can be observed that the resistance value of the soil is sensitive to the vertical effective stresses, where the resistance transitions are more prominent for tests on sands with an I_D of less than 0.70 between each vertical effective stress scale. In the case of tests on specimens with I_D of 0.90, the strength transitions from one vertical stress to another are smoother, however, it is possible to observe an increase in the dynamic resistance. In all cases it is possible to establish an increase of the penetration resistance as a function of the increase of the vertical effective stress.

On the penetrograms, it is possible to observe some atypical resistance values that do not follow the average trend of the values (red circles). In the case of laboratory tests, these values are not associated with the real response of the soil and their occurrence is related to errors in the measured signals. These errors occur when the dynamic signals are perturbed by boundary elements such as the rigid bottom of the calibration chamber or non-concentric hammer impacts on the penetrometer head. The occurrence of these points is not recurrent and does not represent the real behavior of the soil, so they can be excluded from the analysis of the results.

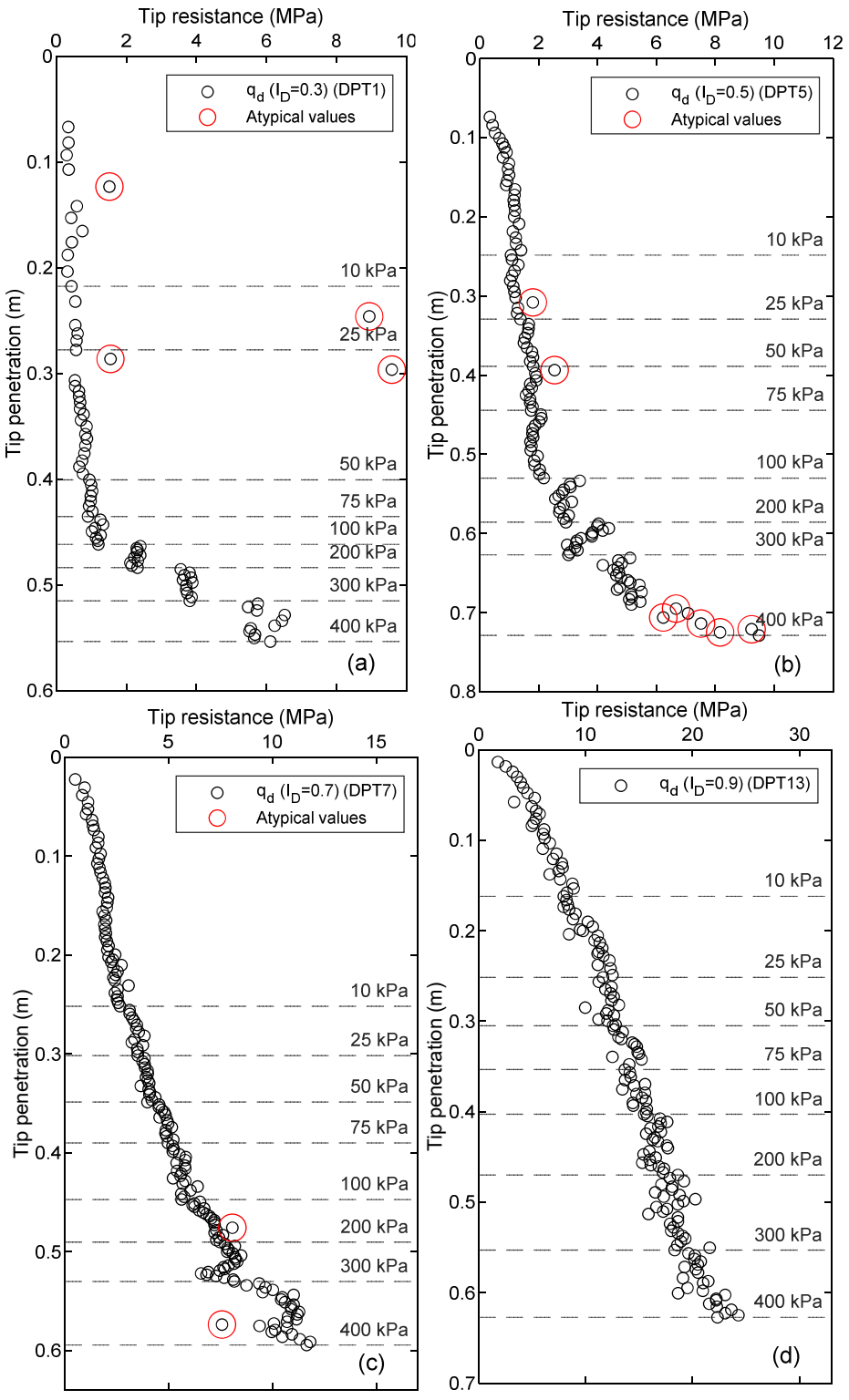

Figure 3-26 – Penetrograms of dynamic penetration tests in k_0 calibration chamber.

Table 3-2 and Table 3-3 present the average dynamic penetration resistance results for each level of effective vertical stress applied to the reconstituted specimens at different density levels, in the dry state. Table 3-4 and Table 3-5 present penetration resistance results for saturated specimens of Fontainebleau NE34 and Hostun HN31 sands, respectively.

Table 3-2 – Average dynamic penetration resistance in dry specimens of Fontainebleau NE34 sands.

σ'_{v0}/I_D	q_d						
	0.30	0.40	0.50	0.60	0.70	0.80	0.90
10	0.423	0.719	0.893	1.193	1.424	1.935	2.959
25	0.441	0.914	1.106	1.419	1.651	2.411	3.593
50	0.866	1.165	1.460	1.803	2.128	3.382	5.957
75	1.119	1.620	1.721	1.922	2.692	4.343	7.067
100	1.349	1.822	1.843	2.445	3.692	5.085	8.289
200	1.945	2.695	2.581	3.503	5.665	7.472	10.483
300	2.471	4.127	4.047	4.927	6.805	9.440	11.339
400	3.861	4.991	5.321	6.491	7.939	11.063	15.158

Table 3-3 – Average dynamic penetration resistance in dry specimens of Hostun HN31 sand.

σ'_{v0}/I_D	q_d						
	0.30	0.40	0.50	0.60	0.70	0.80	0.90
10	0.462	0.792	0.978	2.060	2.481	4.479	5.431
25	0.573	1.238	1.249	2.821	3.426	7.215	7.945
50	0.799	1.517	1.667	3.057	3.977	9.050	11.986
75	0.979	1.513	1.826	3.616	4.843	10.186	13.061
100	1.188	1.609	1.910	4.596	5.622	11.891	13.433
200	2.196	2.982	2.901	5.466	6.991	14.989	17.728
300	3.745	3.805	3.575	6.604	7.778	17.405	21.598
400	5.289	4.993	5.666	7.141	10.420	18.639	27.100

Table 3-4 – Average dynamic penetration resistance in saturated Fontainebleau NE34 sand specimens.

σ'_{v0}/I_D	q_d			
	0.30	0.50	0.70	0.90
10	1.154	1.674	2.337	5.796
25	1.260	1.692	2.433	6.991
50	1.215	2.056	3.830	9.682
75	1.516	2.018	4.812	12.712
100	1.955	2.496	5.244	13.767
200	2.840	3.651	6.236	18.041
300	3.615	3.992	7.766	21.997
400	4.041	5.769	8.978	23.325

Table 3-5 – Average dynamic penetration resistance in saturated Hostun HN31 sand specimens.

σ'_{v0}/I_D	q_d			
	0.30	0.50	0.70	0.90
10	0.805	1.352	2.012	5.629
25	1.207	1.602	2.885	7.337
50	1.468	1.768	3.952	8.855
75	1.569	2.431	5.279	10.611
100	1.920	2.970	6.058	13.324
200	2.910	3.820	6.980	15.772
300	3.362	4.945	7.742	21.862
400	4.462	6.256	10.312	23.316

3.2.1 Vertical effective stress influence

The results allow establishing a relationship between the resistance to dynamic penetration and the vertical effective stress, which can be represented by a potential function defined by two correlations factors A and B (eq. 3-1). The relationship will be unique for each density index level, and it can be observed that when the vertical effective stress is higher, the resistance will be higher at each density increment. Figure 3-27 presents the average resistance results for density indices

of 0.30, 0.50, 0.70 and 0.90 in the different scales of effective vertical stress, for the two types of sands and in dry and saturated conditions.

$$\sigma'_{vc} = A \cdot (q_d)^B \qquad \textbf{eq. 3-1}$$

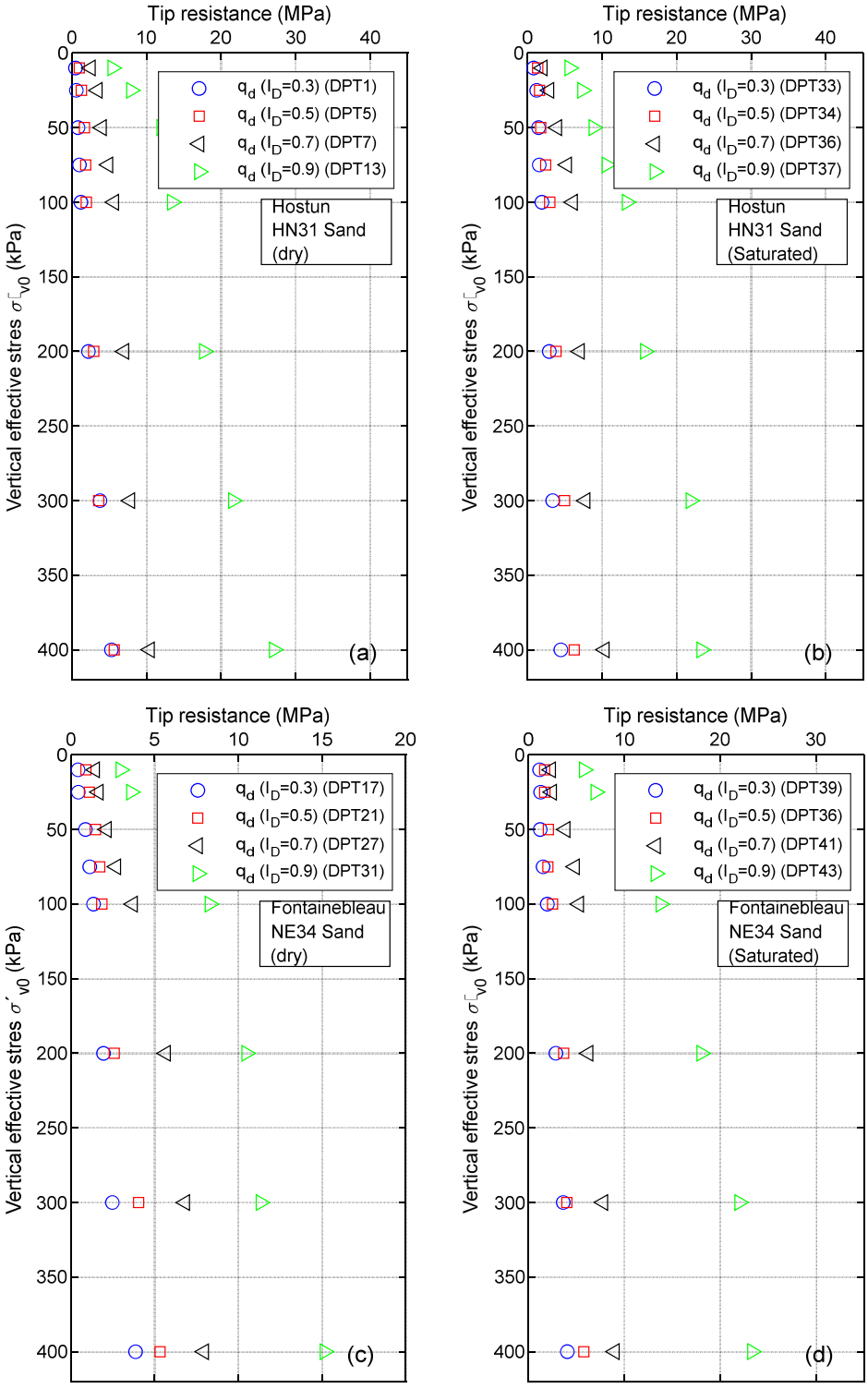

Figure 3-27 - Relations $q_d - \sigma'_{vc}$ for test results performed on reconstituted specimens: (a) dry Hostun HN31 sands; (b) saturated Hostun HN31 sands; (c) dry Fontainebleau NE34 sand; (d) saturated Fontainebleau NE34 sands.

3.2.2 Influence of density index on dynamic penetration resistance

When the density index of a sand is higher, particles will be in a more compact state and the contact number between them will be higher. This results in an increase of the inter-particle friction and a better redistribution of the dynamic stresses by means of force chains developed in granular assembly. Considering this, it is to be expected that when the density of a soil is higher, its resistance will be higher.

Previous research using a dynamic variable energy penetrometer has demonstrated the existence of a correlation between the density index I_D and the dynamic penetration resistance q_d based on a logarithmic equation (eq. 3-2) (Chaigneau 2001; Gansonré et al. 2019; López Retamales et al. 2021; López Retamales et al. 2020)

$$I_D = A \ln(q_d) + B \qquad \textbf{eq. 3-2}$$

Figure 3-28a and Figure 3-28b present $q_d - I_d$ relationship of reconstituted specimens of dry Fontainebleau NE34 and Hostun HN31 sands under effective vertical stresses of 25, 50 and 100 kPa. The results show that the relationship presented in eq. 3-2, correctly models the relationship between dynamic strength and specimen density index. The good fit of the model is demonstrated by the high value of the correlation coefficient obtained in all cases. The correlation also shows the sensitivity of the resistance to the vertical effective stress, whose relationship implies that the higher the vertical stress, the higher the resistance.

The fit of the models to the results obtained implies that the correlation factors A and B are related to the specific effective vertical stress conditions under which they were obtained, generating a unique soil strength model for each condition. Table 3-6 and Table 3-7 present the values of correlation factors for use with eq. 3-2 in the calculation of the density index for a known effective vertical stress in Fontainebleau NE34 and Hostun HN31 sands.

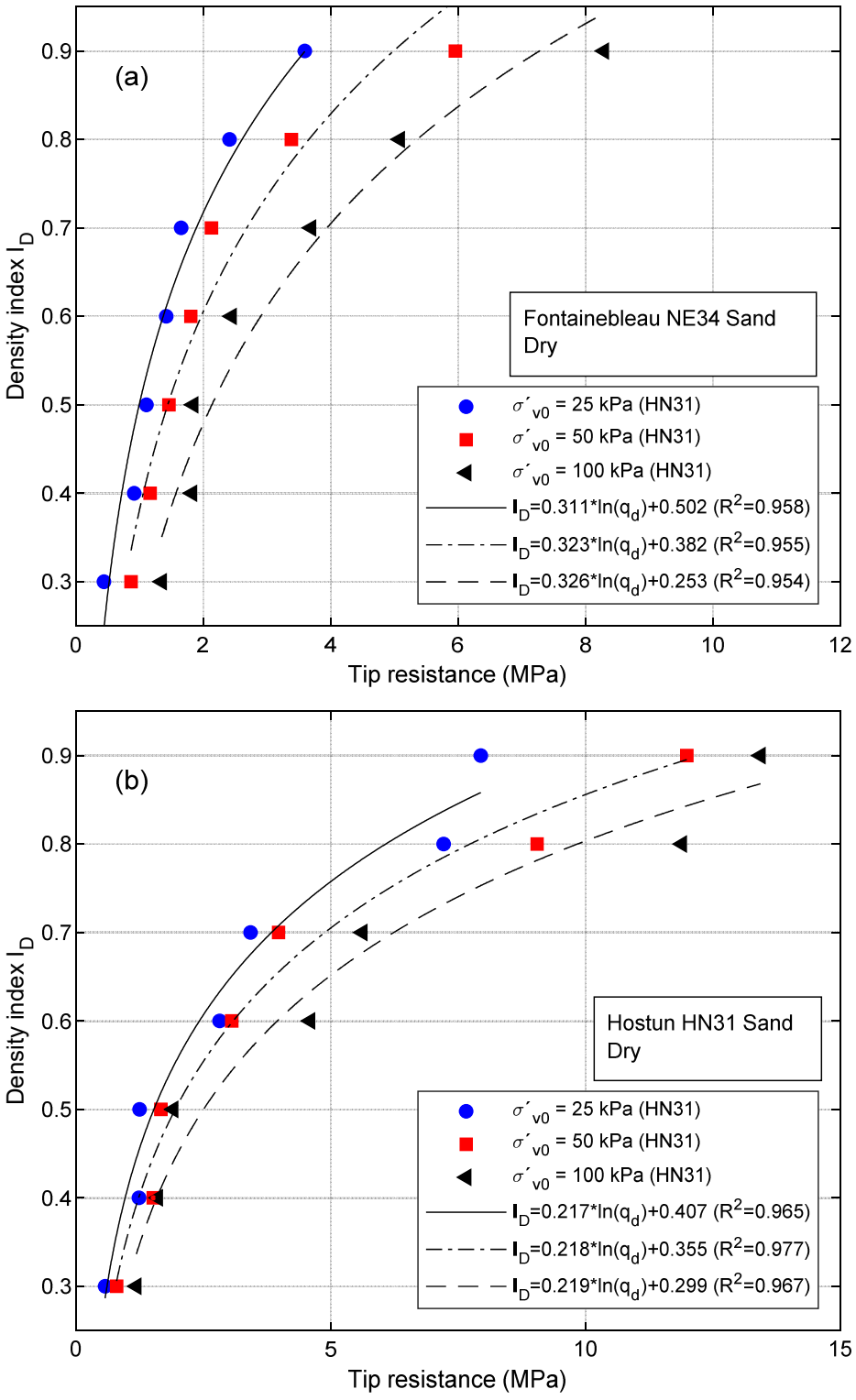

Figure 3-28 - $q_d - I_d$ relationship under different vertical stress conditions in dry condition (a) Fontainebleau NE34 sand and (b) Hostun HN31 sand.

Table 3-6 – Correlation factors for dry specimens of Fontainebleau NE34 sands.

σ'_{v0}	A	B	R^2
10	0.332	0.554	0.982
25	0.311	0.502	0.958
50	0.323	0.382	0.955
75	0.328	0.310	0.930
100	0.326	0.253	0.954
200	0.340	0.116	0.957
300	0.399	-0.079	0.962
400	0.445	-0.270	0.968

Table 3-7 – Correlation factors for Hostun HN31 dry sand specimens.

σ'_{v0}	A	B	R^2
10	0.233	0.474	0.982
25	0.217	0.407	0.965
50	0.218	0.355	0.977
75	0.219	0.326	0.983
100	0.219	0.299	0.967
200	0.256	0.155	0.949
300	0.273	0.062	0.885
400	0.306	-0.080	0.891

Similarly, in the case of saturated specimens the relationship between strength and density and effective stress can be represented by a general logarithmic equation (eq. 3-2) (Figure 3-29a and Figure 3-29b), defined for each level of effective stress by a correlation factor A and B. The correlation factors for dynamic penetration tests performed on saturated specimens are presented in Table 3-8 and Table 3-9, or Fontainebleau NE34 and Hostun HN31 sands respectively.

Table 3-8 – Correlation factors for saturated NE34 Fontainebleau sands specimens.

σ'_{v0}	A	B	R^2
10	0.362	0.305	0.937
25	0.328	0.306	0.902
50	0.287	0.275	0.982
75	0.263	0.256	0.953
100	0.286	0.181	0.942
200	0.302	0.068	0.917
300	0.293	0.027	0.892
400	0.331	-0.102	0.943

Table 3-9 – Correlation factors for saturated Hostun HN31 sand specimens.

σ'_{v0}	A	B	R^2
10	0.306	0.408	0.954
25	0.315	0.308	0.945
50	0.304	0.257	0.943
75	0.304	0.193	0.988
100	0.302	0.137	0.985
200	0.337	0.001	0.956
300	0.310	-0.015	0.939
400	0.352	-0.177	0.962

3.2.3 Influence of sand type on results obtained

When comparing the strengths obtained for both types of sands under the same conditions of vertical effective stress, differences were observed between the dry and saturated specimens. In the case of the strengths obtained in dry specimens (Figure 3-30a), it was observed that the higher the magnitude of the vertical effective stress, the Hostun HN31 sand specimens present higher strengths. In the case of low strength magnitudes, the differences decrease and the strength can be considered equivalent for both types of sands.

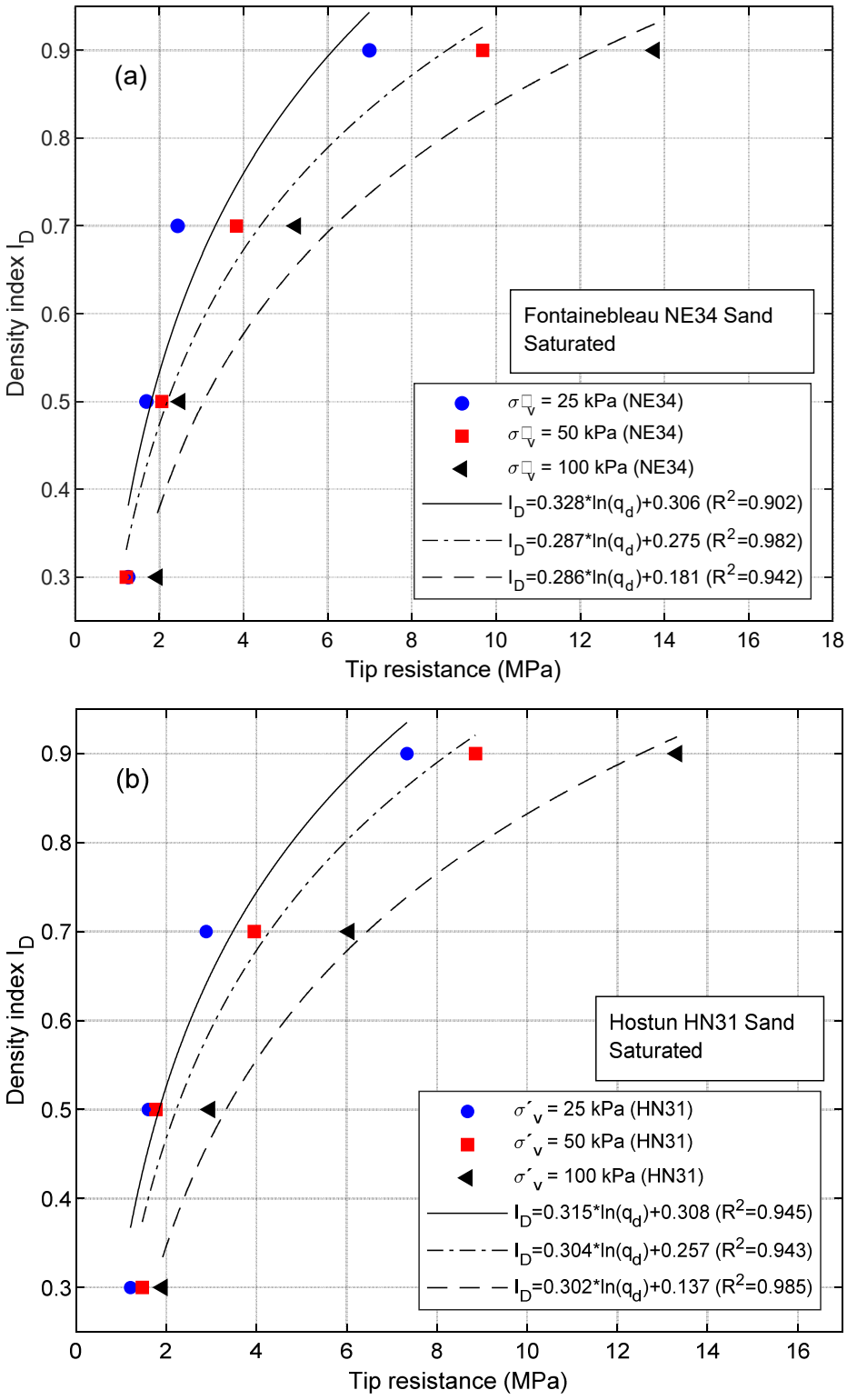

Figure 3-29 - $q_d - I_d$ relationship under different vertical stress conditions in saturated condition (a) Fontainebleau NE34 sand and (b) Hostun HN31 sand.

For the saturated specimens, it was observed that the strengths are linearly related to each other under the same vertical effective stress conditions (Figure 3-30b), so the strength can be

considered equivalent for both types of sands and in the range of densities considered (0.30 to 0.90).

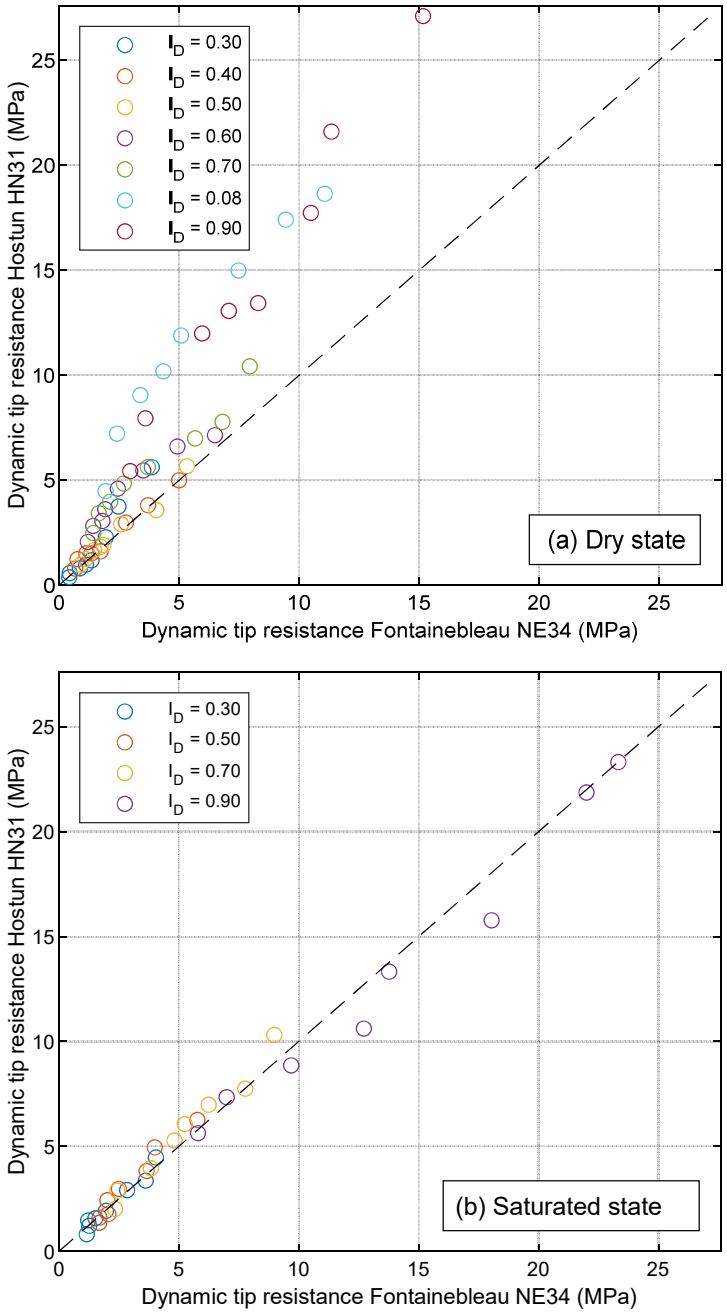

Figure 3-30 – Dynamic penetration resistance comparison between Fontainebleau NE34 and Hostun HN31 sands: (a) dry state; (b) saturated state.

In general, it is not possible to establish a difference between both types of sands considering only the penetration resistance, however, in the dry case it is observed that Hostun HN31 sands present a higher penetration resistance in dry specimen, these differences disappear when the specimens are saturated. However, it is possible to state that it is not possible to identify a soil only

considering the dynamic penetration resistance because this parameter is influenced by other factors such as saturation state.

3.2.4 Penetration resistance normalization

In order to establish a common point of analysis and comparison, normalization is applied considering a reference effective vertical pressure. In this research it has been chosen to use a normalization approach based on that presented by Villavicencio (2009), applying a normalization factor C_{p3}. (eq. 3-3 and eq. 3-4)

During the application of the correction factor, it was noticed that the results did not show a good adjustment for the resistances associated with low levels of density index and low effective vertical stress, therefore, a modification to the correction factor was applied through an iterative process of non-linear regressions by applying the Levenberg Marquardt iteration algorithm until the best possible adjustment was reached.

The results of the adjustment to the normalization factor allowed the setting of a maximum limit equal to or less than 2.5 and a potential factor n equal to 0.5.

$$q_{dN} = q_d C_{p3} \quad \textbf{eq. 3-3}$$

$$C_{p3} = \left(\frac{P_a}{\sigma'_v}\right)^{0.5} \quad \textbf{eq. 3-4}$$

with:

$$C_{p3} \leq 2.5$$

With q_{dN} the normalized penetration resistance, C_{p3} the normalization factor, P_a the atmospheric pressure and σ'_v the effective vertical stress. Both the vertical pressure and the effective vertical stress should be expressed in the same units.

The normalization results are presented in Figure 3-31a and Figure 3-31b and the relationships between density index and normalized strength for Fontainebleau NE34 and Hostun HN31 sands are presented in eq. 3-5 and eq. 3-6 respectively.

$$I_D = 0.335 \ln(q_{dN}) + 0.237 \quad \textbf{eq. 3-5}$$

$$R^2 = 0.928$$

$$I_D = 0.234 \ln(q_{dN}) + 0.260 \quad \textbf{eq. 3-6}$$

$$R^2 = 0.931$$

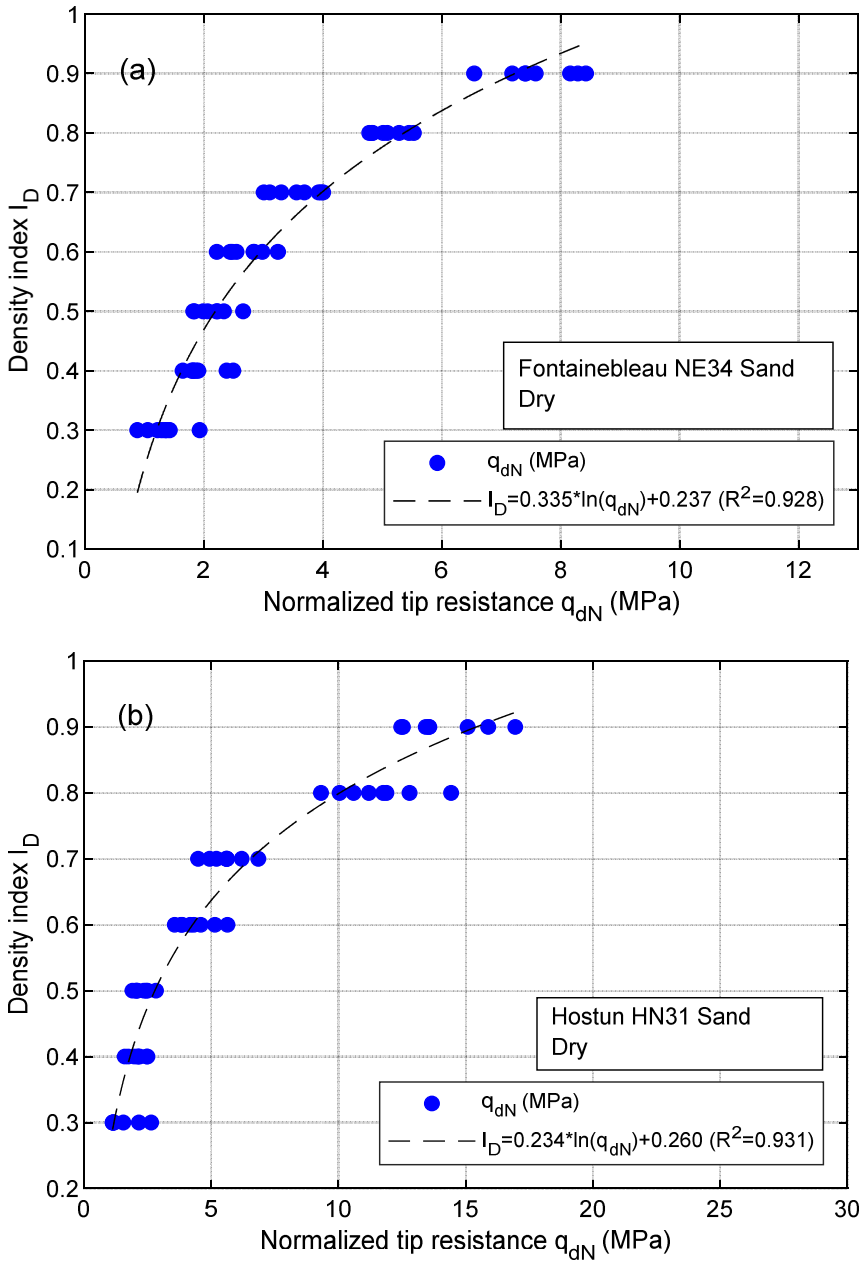

Figure 3-31 – Normalized penetration resistanceq_{dN} in dry specimens: (a) Fontainebleau NE34; (b) Hostun HN31 sand.

The same normalization process is applied to the results of tests for saturated sand (eq. 3-7 and eq. 3-8, or Fontainebleau NE34 and Hostun HN34 sands, respectively). The normalization results are presented in Figure 3-33a and Figure 3-33b.

$$I_D = 0.294 \ln(q_{dN}) + 0.159 \qquad \textbf{eq. 3-7}$$

$$R^2 = 0.903$$

$$I_D = 0.312 \ln(q_{dN}) + 0.130 \qquad \textbf{eq. 3-8}$$

$$R^2 = 0.948$$

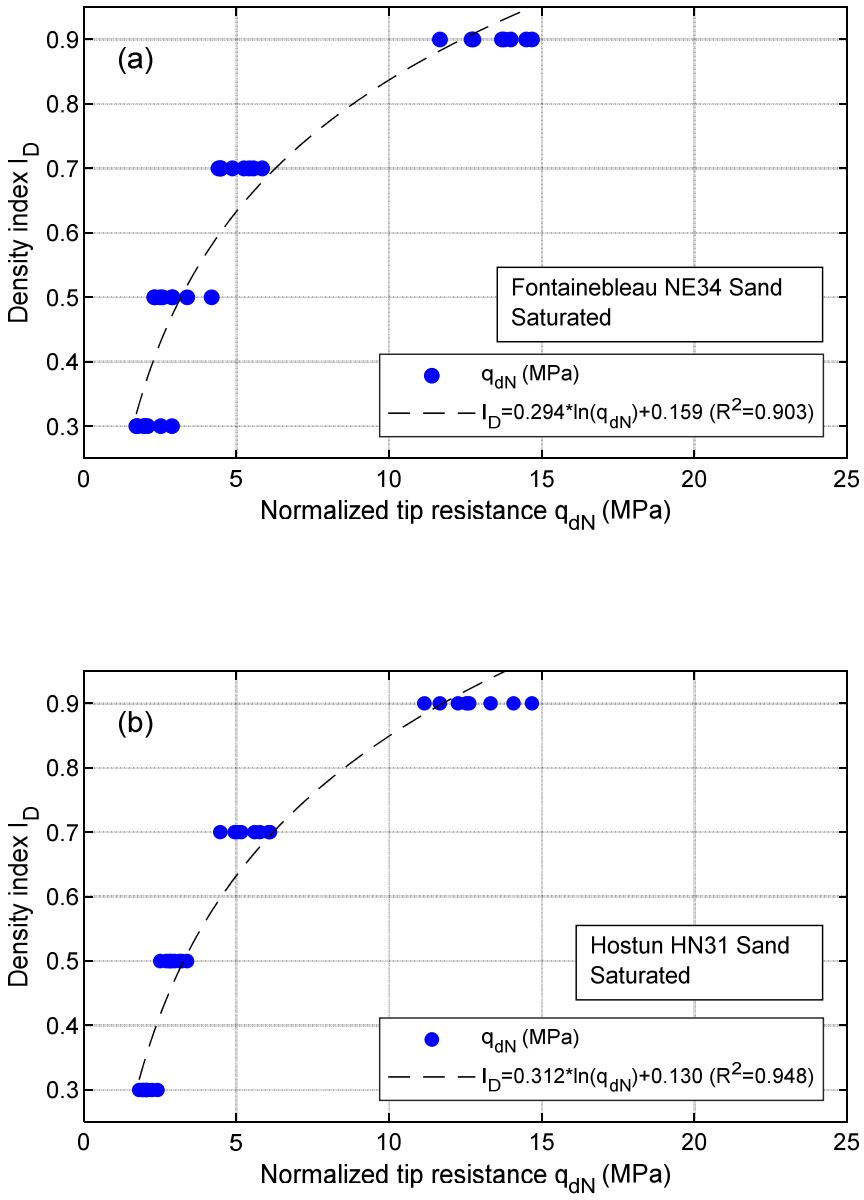

Figure 3-32 – Normalized penetration resistance q_{dN} in saturated specimens: (a) Fontainebleau NE34 sand; (b) Hostun HN31 sand.

3.2.5 Dynamic module E_{kd}

The dynamic modulus is a soil parameter based on the analysis of the dynamic signals measured in the penetrometer and reconstructed at the cone-soil interface and is not dependent on

the application of frequency filters for its evaluation. This is the reason why the evaluation of this parameter allows to evaluate the response of the soil independent of the treatment given to the signals and to establish a relationship between the magnitude of the parameter and the internal and boundary conditions of the tested specimen..

Figure 3-33 and Figure 3-34 show the dynamic modulus spectra E_{kd} for different density index levels and for effective vertical stresses of 50, 100 and 200 kPa. As previously indicated (Chapter 2.3.1.9), the evaluation of the modulus $E_{kd\,(min)}$ is set at a minimum frequency f_{min} defined by the limitations of the data acquisition system and its configuration, so in all cases the lower limit is 24 Hz, and a maximum frequency f_{max} limited by the linearity limit between the dynamic modulus and the frequency vector.

The maximum frequency limits depend on the density index level and the magnitude of the effective vertical stress. In Figure 3-33a, it can be observed that for a density index of 0.30, the limit of the E_{kd} modulus proportionality range is an average of 100 Hz, for I_D of 0.50, 0.70 and 0.90, the identified frequencies are 180, 280 and 450 Hz, respectively. This trend verifies the results presented by Tran et al. (2018) and Tran et al. (2019) where a relationship between soil density and the extent of the linear range of E_{kd} is established.

The same behavior has been observed at higher effective vertical stress levels in both Hostun HN31 and Fontainebleau NE34 sands. In tests carried out on Hostun HN31 sands under 100 kPa effective vertical stresses, average maximum frequencies of 130, 190, 280 and 490 Hz were observed for I_D of 0.30, 0.50, 0.70 and 0.90 respectively. At 200 kPa of vertical stress the average maximum frequencies are 140, 210, 300 and 545 Hz for I_D of 0.30, 0.50, 0.70 and 0.90. The same trend was observed in specimens of Fontainebleau NE34 sands (Figure 3-34)

From the same charts, a relationship between the effective vertical stress and the maximum limit frequency can be observed. For I_D of 0.30, the f_{max} values obtained were 170, 200 and 250 Hz for effective vertical stresses of 50, 100 and 200 kPa. For I_D of 0.50, frequencies of 250, 300 and 420 Hz were obtained for I_D of 0.70 maximum frequencies of 430, 500 and 650 and for I_D of 0.90 maximum frequency limits of 800, 1100 and 1300 Hz for 50, 100 and 200 kPa in all cases.

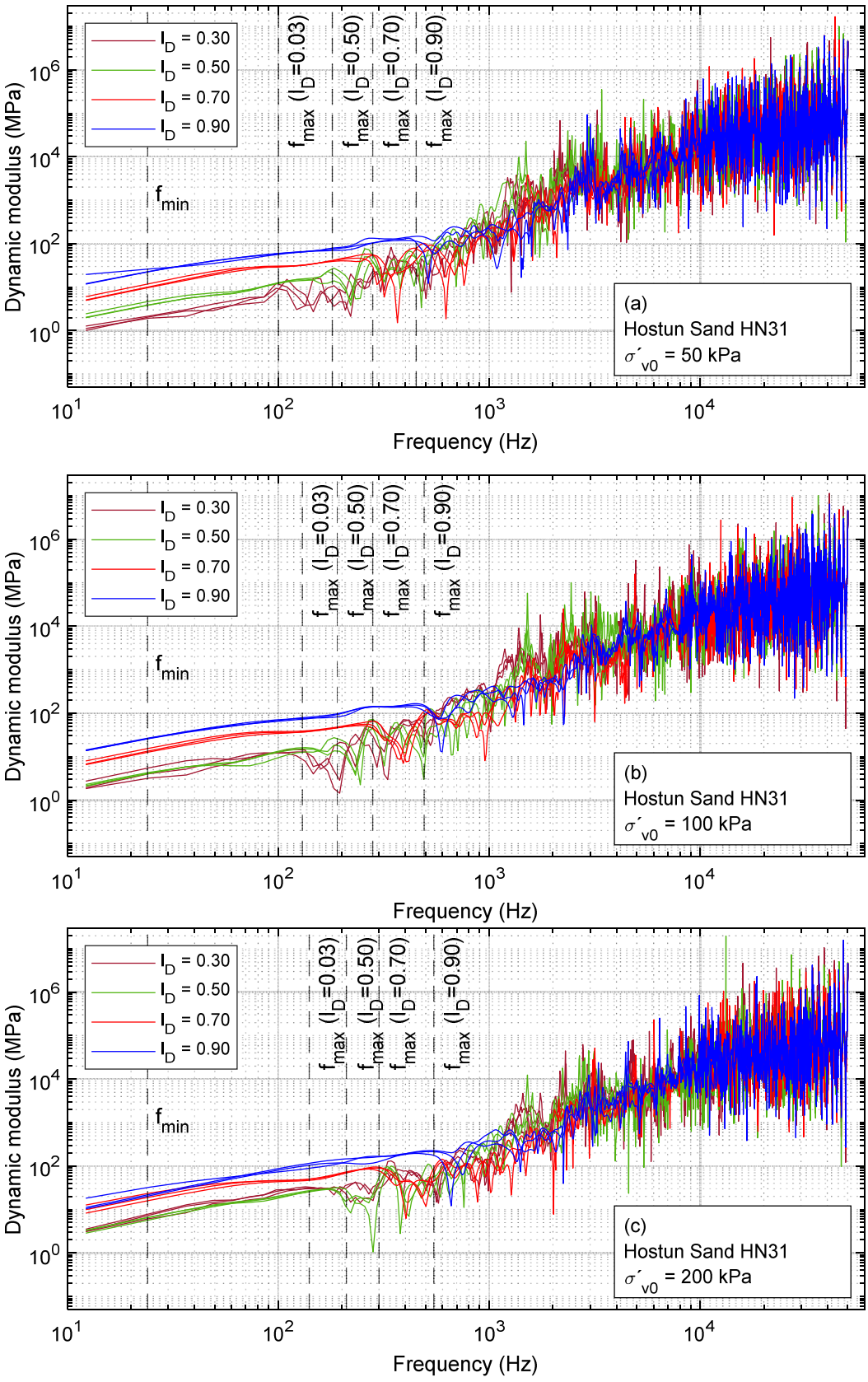

Figure 3-33 – Influence of density index on dynamic modulus E_{kd} under different levels of vertical effective stress in Hostun HN31 sands: (a) 50 kPa; (b) 100 kPa; (c) 200 kPa.

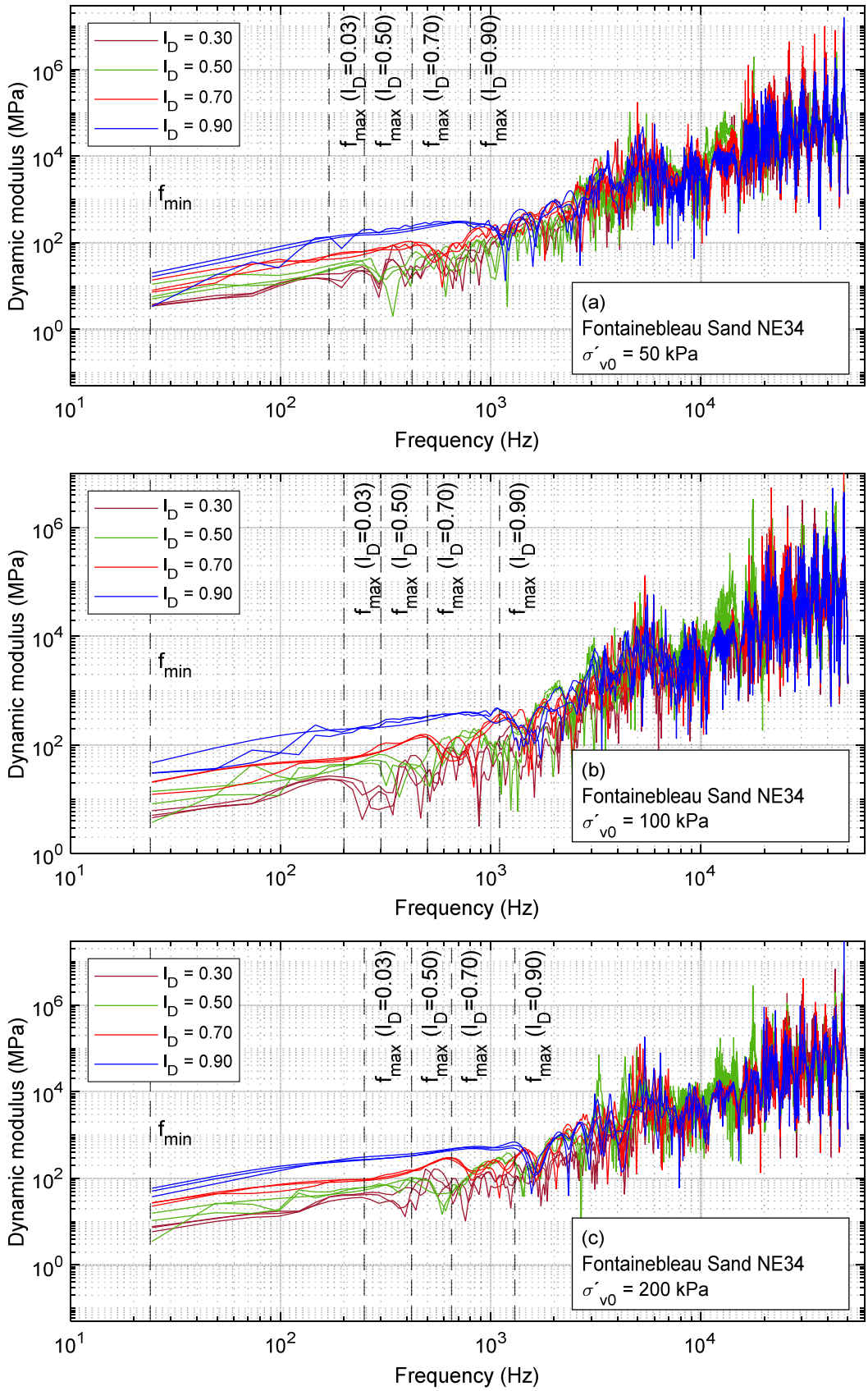

Figure 3-34 – Influence of density index on dynamic modulus E_{kd} under different levels of vertical effective stress in Fontainebleau NE34 sands: (a) 50 kPa; (b) 100 kPa; (c) 200 kPa.

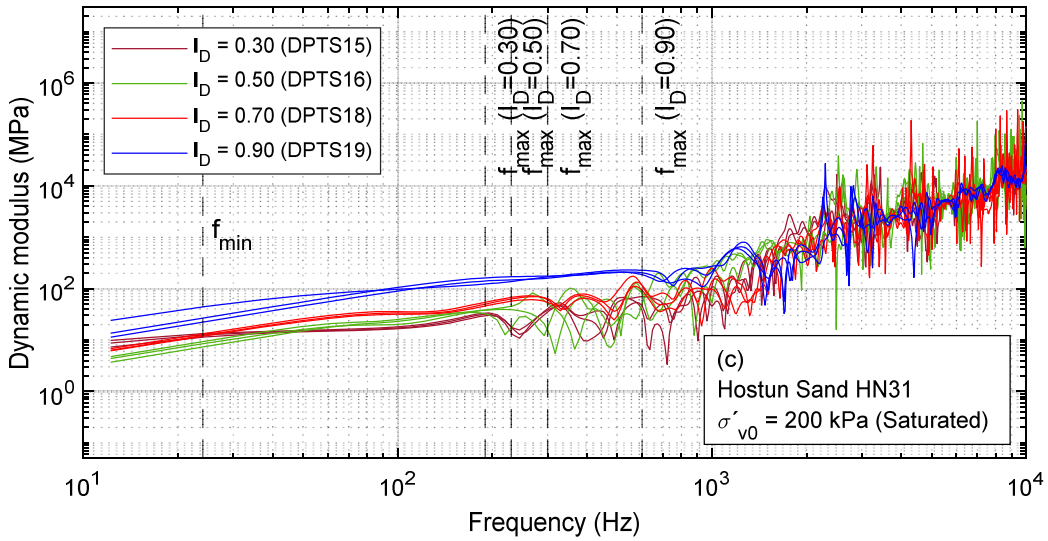

Figure 3-35 - Influence of density index on dynamic modulus E_{kd} under different levels of vertical effective stress in Hostun HN31 saturated sands: (a) 50 kPa; (b) 100 kPa; (c) 200 kPa.

and Figure 3-36 show the dynamic modulus spectra E_{kd} for different density index levels and for vertical effective stresses of 50, 100 and 200 kPa, obtained from saturated specimens of Hostun HN31 and Fontainebleau NE34 sands. As in the dry case, it has been observed that the extension of the linearity ranges of the spectrum are proportional to the density index under the range of effective stresses presented.

In Figure 3-35a, it can be observed that for a density index of 0.30, the upper limit f_{max} of the E_{kd} modulus proportionality range is an average of 150 Hz, for I_D od 0.50, 0.70 and 0.90, the maximum average frequencies at which linearity is maintained identified are 200, 270 and 450 Hz, respectively. The same has been observed in saturated specimens subjected to higher magnitude effective vertical stresses in both Hostun HN31 and Fontainebleau NE34 sands. In tests performed in Hostun HN31 sands under effective vertical stresses of 100 kPa (Figure 3-35b), average maximum frequencies of 145, 215, 280 and 470 Hz were observed, with 200 kPa of vertical effective stress (Figure 3-35b), the average maximum frequencies are 190, 230, 300 and 600 Hz for I_D of 0.30, 0.50, 0.70 and 0.90 in all cases. The same trend in the spectra was observed in specimens of saturated Fontainebleau NE34 sands (Figure 3-36)

The effect of the vertical effective stress on the upper limit of linearity f_{max} of the spectra was also observed. From the E_{kd} spectra for Fontainebleau NE34 sands (Figure 3-36), at an I_D of 0.30 maximum limiting frequency f_{max} values of 105, 150 and 180 Hz were obtained for vertical effective stresses of 50, 100 and 200 kPa. For I_D of 0.50 frequencies of 155, 190 and 240 Hz were

obtained for, for I_D of 0.70 maximum frequencies of 270, 260 and 300 and for I_D of 0.90 maximum frequency limits of 410, 500 and 590 Hz for 50, 100 and 200 kPa in all cases.

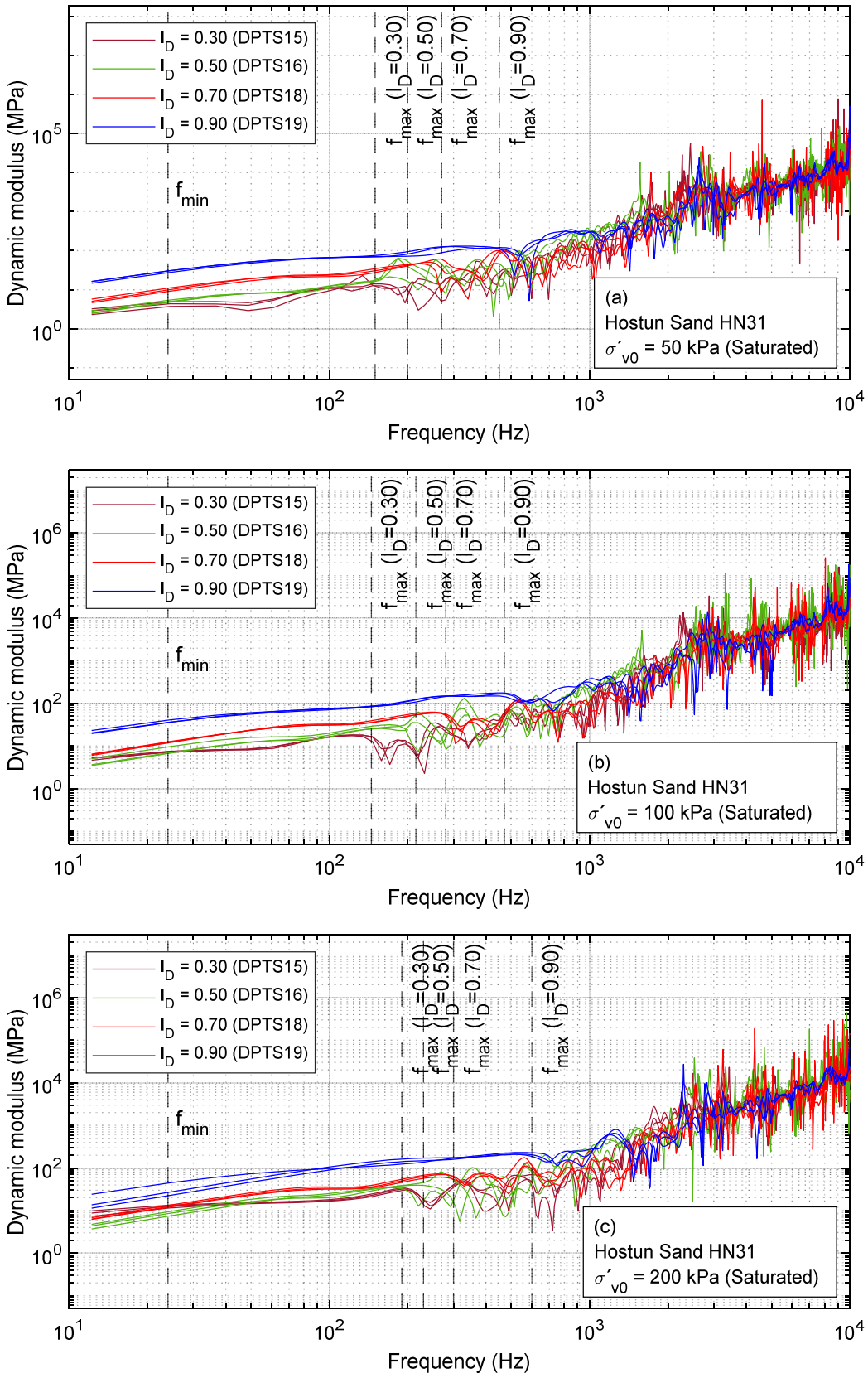

Figure 3-35 - Influence of density index on dynamic modulus E_{kd} under different levels of vertical effective stress in Hostun HN31 saturated sands: (a) 50 kPa; (b) 100 kPa; (c) 200 kPa.

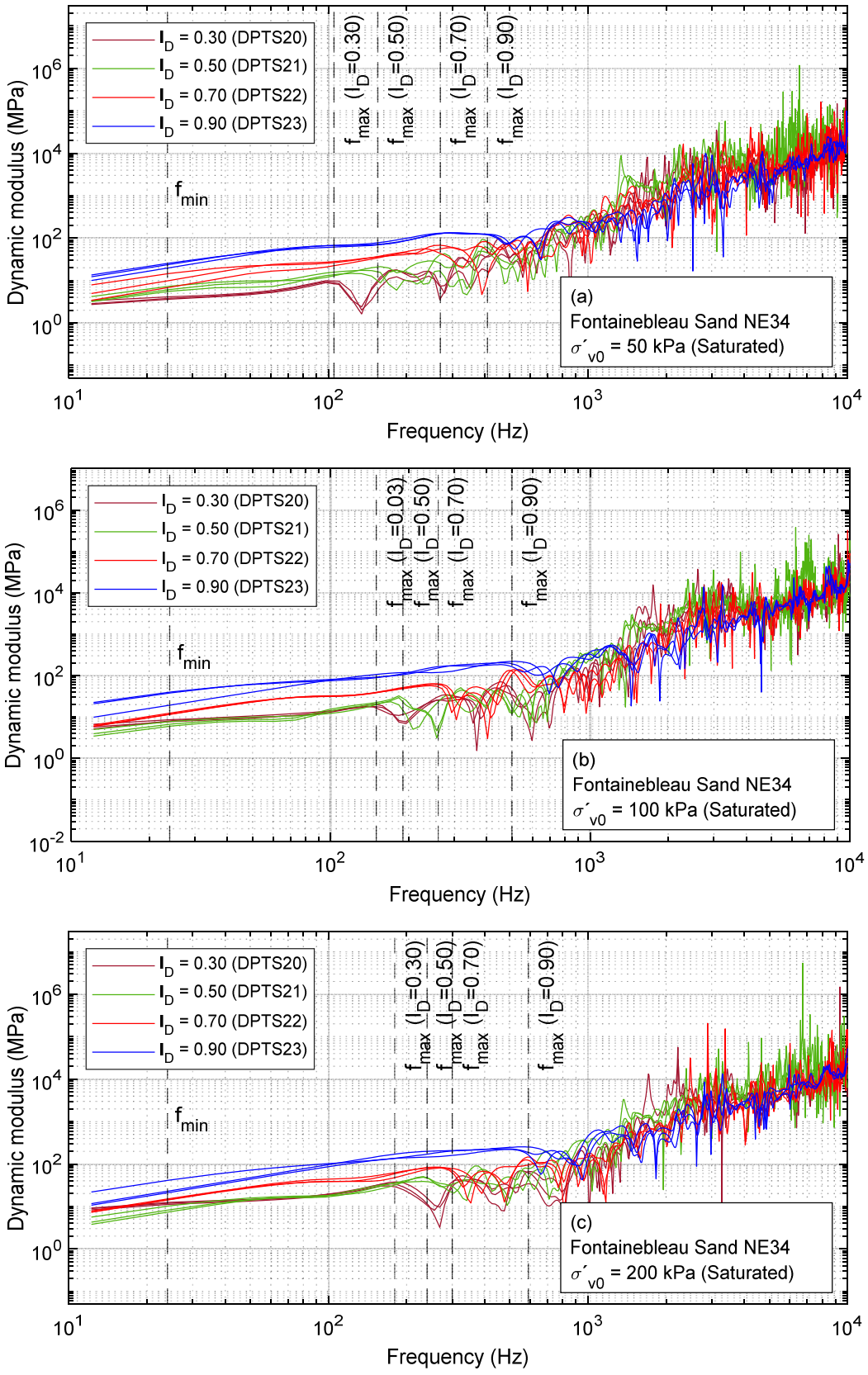

Figure 3-36 – Influence of density index on dynamic modulus E_{kd} under different levels of vertical effective stress in Fontainebleau NE34 saturated sands: (a) 50 kPa; (b) 100 kPa; (c) 200 kPa.

As with the maximum penetration resistance of the soil, the three established dynamic modulus are influenced by the effects of the density index and the effective vertical stress, however, the average dynamic modulus E_{kdm} has been selected as the reference for the analysis of the soil.

The results of the E_{kd} evaluation present the sensitivity to the effective vertical stress. Figure 3-37a shows a penetrogram of dynamic modulus E_{kd} for a specimen of Fontainebleau NE34 sands reconstituted to a density index of 0.70. In this one, it is observed that when the vertical effective stress is higher, the higher is the magnitude of the dynamic modulus E_{kd}. When observing the relationship of the average modulus values as a function of the vertical effective stress, a relationship described by potential function similar to that observed in the penetration resistance (Figure 3-37b).

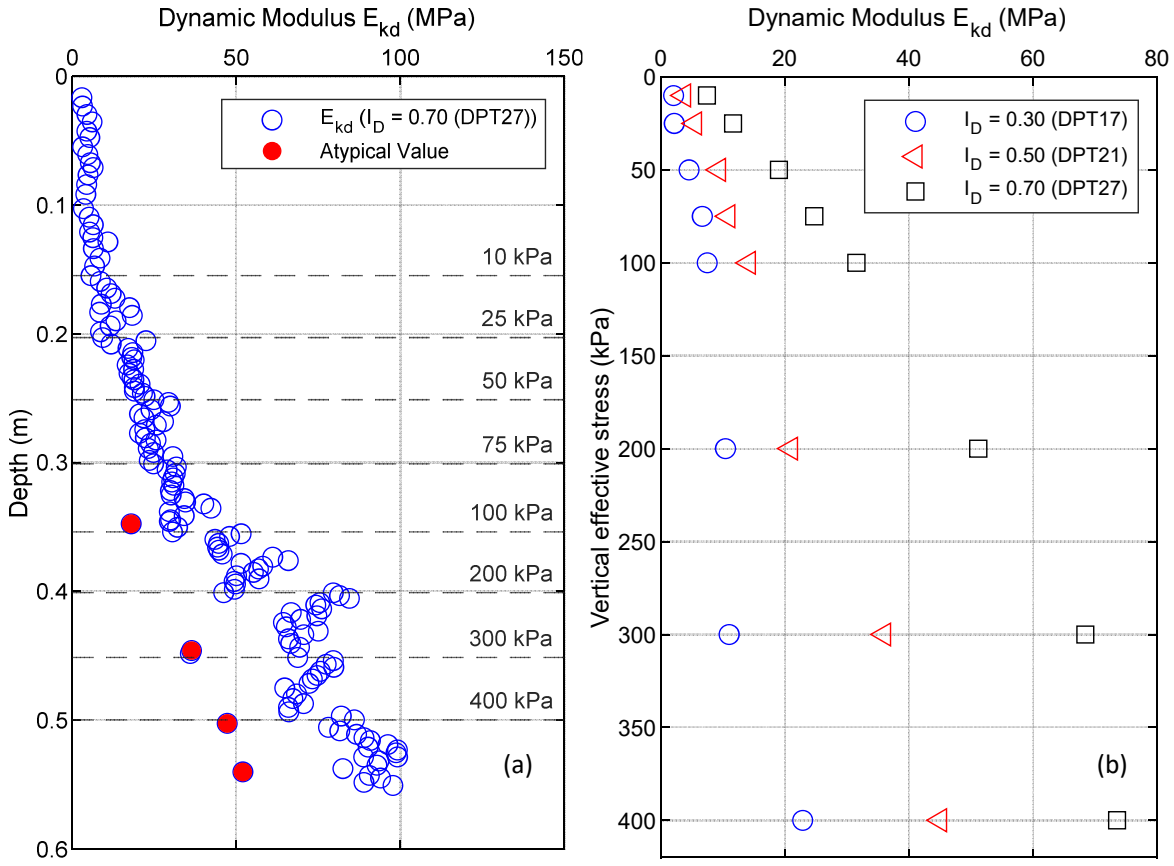

Figure 3-37 – Dynamic modulus E_{kd} penetrogram: (a) E_{kd} penetrogram for Fontainebleau NE34 sand at an $I_D = 0.70$; (b) E_{kd} - σ'_{v0} relationships for Fontainebleau NE34 sands.

Table 3-10, Table 3-11, Table 3-12 and Table 3-13 present the results of the evaluation of the dynamic modulus E_{kd} for the different dynamic penetration tests carried out on Hostun HN31 and Fontainebleau NE34 sand specimens for the different reconstitution density index and in all the range of applied vertical effective stresses.

Table 3-10 – Average dynamic modulus in dry specimens of Fontainebleau NE34 sands.

σ'_{v0}/I_D	E_{kd}						
	0.30	0.40	0.50	0.60	0.70	0.80	0.90
10	2.033	4.756	3.683	5.106	7.412	22.094	31.171
25	2.142	5.664	5.481	6.495	11.613	23.656	39.975
50	4.527	6.778	9.322	8.569	19.011	39.953	61.294
75	6.659	8.364	10.843	10.477	24.697	48.012	87.953
100	7.456	12.304	14.143	14.057	31.514	63.147	99.839
200	10.403	20.956	20.918	28.345	51.158	88.754	155.275
300	10.995	26.464	35.948	36.069	68.410	121.475	182.787
400	22.848	27.026	44.969	47.734	73.516	178.149	215.515

Table 3-11 – Average dynamic modulus in dry specimens of Hostun HN31 sand.

σ'_{v0}/I_D	E_{kd}						
	0.30	0.40	0.50	0.60	0.70	0.80	0.90
10	1.457	2.428	3.373	6.500	11.442	17.454	23.761
25	3.144	4.250	4.767	11.256	16.007	25.332	35.663
50	4.696	5.807	6.013	14.077	23.192	38.866	53.897
75	6.482	6.418	8.422	18.412	27.017	46.217	58.332
100	9.234	7.782	9.958	21.304	33.996	50.104	73.268
200	12.767	13.897	13.582	29.470	49.028	65.331	87.452
300	16.660	13.922	17.147	35.144	65.430	68.998	105.161
400	30.636	16.978	20.192	37.479	69.798	99.173	131.207

Table 3-12 – Average dynamic modulus in saturated Fontainebleau NE34 sand specimens.

σ'_{v0}/I_D	E_{kd}			
	0.30	0.50	0.70	0.90
10	3.907	4.128	9.264	33.500
25	4.273	6.043	11.750	59.600
50	5.524	9.240	25.217	81.676
75	8.182	9.954	34.809	101.848
100	10.052	11.564	37.776	100.959
200	13.598	16.007	55.154	131.902
300	18.843	23.964	54.635	190.378
400	21.171	40.035	66.811	222.582

Table 3-13 – Average dynamic modulus in saturated Hostun HN31 sand specimens.

σ'_{v0}/I_D	E_{kd}			
	0.30	0.50	0.70	0.90
10	1.702	5.209	7.871	28.281
25	2.639	6.244	12.802	53.066
50	4.092	6.753	22.128	70.196
75	4.852	10.290	23.902	78.341
100	9.939	11.745	26.947	97.770
200	14.017	20.009	29.964	126.235
300	20.004	26.454	36.047	131.538
400	25.609	26.781	39.011	148.311

Similar to the findings in some dynamic resistance penetrograms, some outliers of E_{kdm} were observed under an effective vertical pressure of 100, 300 and 400 kPa (Figure 3-37a). The occurrence of these anomalies is associated with problems recorded in the signals, which may be associated with perturbations external to the soil. The inclusion of these values in the analysis requires the operator's judgment, however, their occurrence is not frequent and the effects of their exclusion from the analysis are considered negligible.

The results of the evaluation of this modulus have allowed establishing that the relationship between the dynamic modulus E_{kdm} and the density index for each loading state can be represented by a logarithmic relationship (eq. 3-9). Figure 3-38a and Figure 3-38b, show the above relationships for test results on Hostun HN31 and Fontainebleau NE34, respectively. It is possible to observe how the curves are displaced to the right when the effective vertical stress is higher, proving the relationship between effective vertical stress and the increase of the dynamic modulus for both sands.

$$I_D = A \ln(E_{dm}) + B \qquad \textbf{eq. 3-9}$$

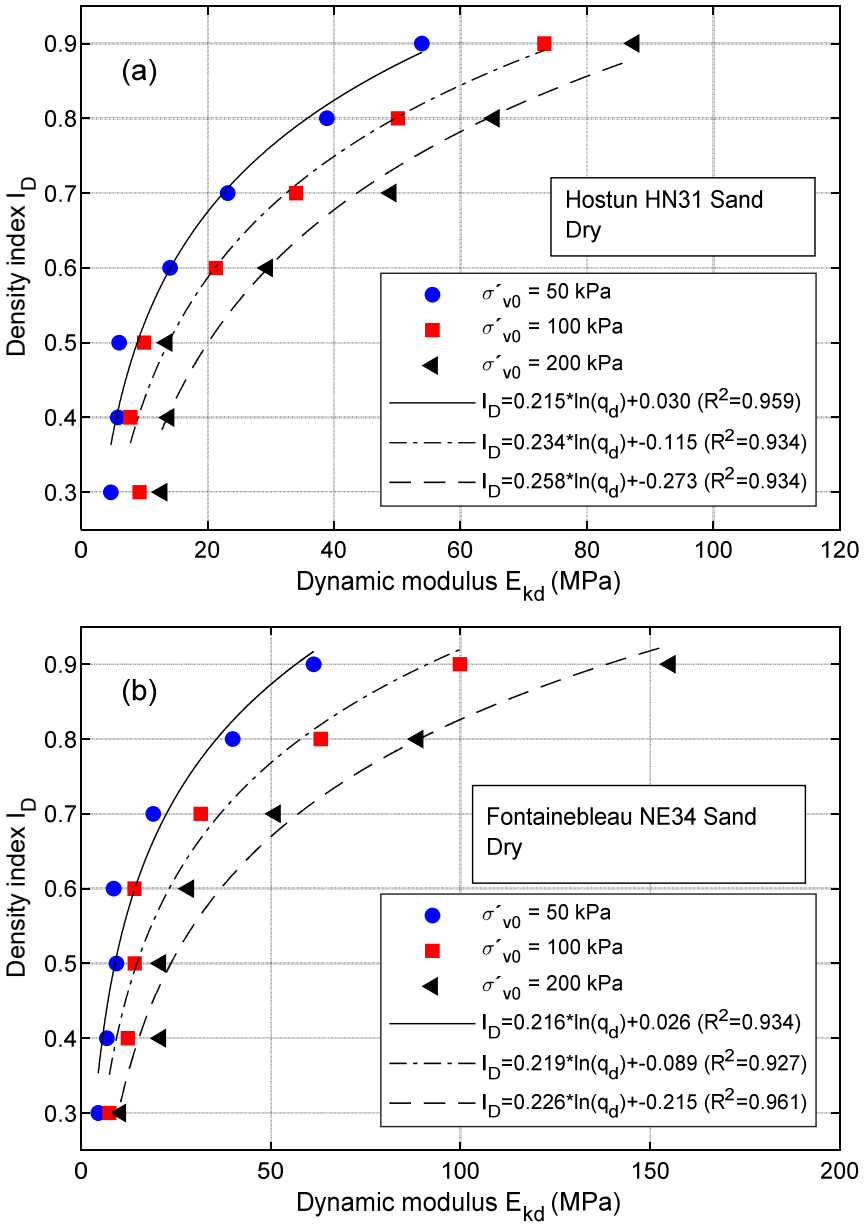

Figure 3-38 - $E_{kdm} - I_d$ relationship under different vertical effective stress in dry condition: (a) Hostun HN31 sand and (b) Fontainebleau NE34 sand.

In the case of saturated sands, the effects of density and effective vertical stress are the same as those observed in the case of dry sand. Figure 3-39a and Figure 3-39b present the $E_{kdm} - I_d$ relationships for both saturated sands under an effective vertical load of 50, 100 and 200 kPa. Similar to the dry case, the curves are displaced to the right with increasing vertical effective stress. The dynamic modulus increase is also observed with the increase of the density index.

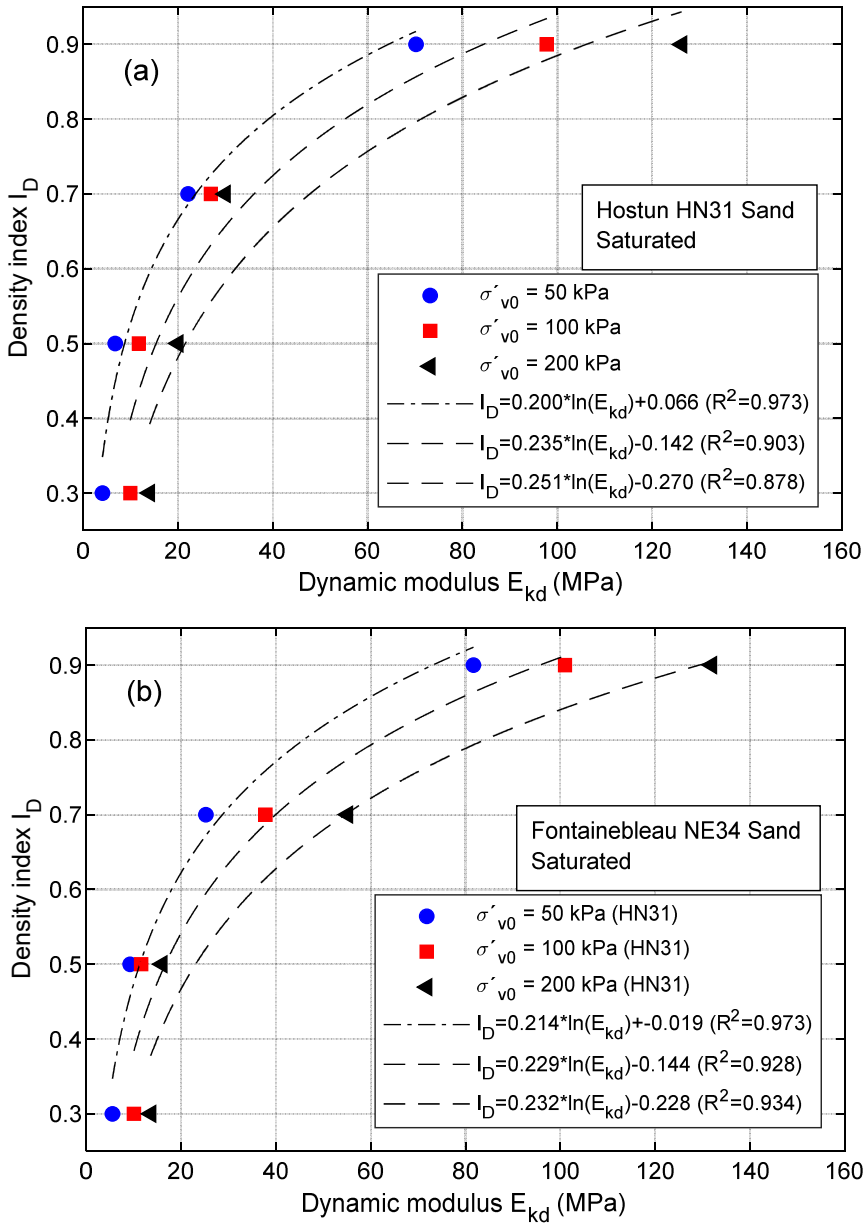

Figure 3-39 - $E_{kdm} - I_d$ relationship under different vertical effective stress in saturated condition: (a) Hostun HN31 sand and (b) Fontainebleau NE34 sand.

Table 3-14 and Table 3-15 how the correlation factors A and B for the establishment of the relationships between density index and dynamic modulus for Hostun HN31 and Fontainebleau

NE34 dry sands, respectively. Table 3-16 and Table 3-17 show the list of correlation factors for the saturated cases of both sands. These correlation factors can be used for the estimation of the density and dynamic modulus parameters in the vertical effective stress ranges, however, it is possible to normalize the results to establish a unique relationship between the density index and the dynamic modulus independent of the level of vertical effective stresses applied.

Table 3-14 – $E_{kdm} - I_d$ Relationship correlation factors of dry Hostun HN31 sands

σ'_{v0}	A	B	R^2
10	0.205	0.224	0.992
25	0.226	0.078	0.975
50	0.215	0.030	0.959
75	0.229	-0.053	0.958
100	0.234	-0.115	0.934
200	0.258	-0.273	0.934
300	0.253	-0.302	0.911
400	0.245	-0.329	0.798

Table 3-15 – $E_{kdm} - I_d$ Relationship correlation factors of dry Fontainebleau NE34 sand

σ'_{v0}	A	B	R^2
10	0.208	0.191	0.890
25	0.212	0.135	0.937
50	0.216	0.026	0.934
75	0.211	-0.013	0.911
100	0.219	-0.089	0.927
200	0.226	-0.215	0.961
300	0.222	-0.258	0.960
400	0.242	-0.399	0.949

Table 3-16 – $E_{kdm} - I_d$ Relationship correlation factors of saturated Hostun HN31 sands

σ'_{v0}	A	B	R^2
10	0.219	0.185	0.968
25	0.201	0.132	0.976
50	0.200	0.066	0.973
75	0.215	-0.015	0.988
100	0.235	-0.142	0.903
200	0.251	-0.270	0.878
300	0.287	-0.456	0.854
400	0.278	-0.456	0.785

Table 3-17 – $E_{kdm} - I_d$ Relationship correlation factors of saturated Fontainebleau NE34 sand

σ'_{v0}	A	B	R^2
10	0.241	0.087	0.873
25	0.209	0.088	0.896
50	0.214	-0.019	0.973
75	0.212	-0.067	0.935
100	0.229	-0.144	0.928
200	0.232	-0.228	0.934
300	0.238	-0.312	0.922
400	0.254	-0.439	0.962

3.2.5.1 Dynamic modulus normalization

Similar behavior to that observed in the relationship between penetration resistance and effective stress was observed, so a similar approach was chosen to establish a normalization factor C_{kd} based on the use of a reference vertical effective pressure and an exponential factor n.

For the vertical effective stress, a pressure of 100 kPa was set as references, and the exponential factor n was obtained through an iterative nonlinear regression process until the best fit of the data was reached. Under this process, the n factor that produced the best results was 0.50. To limit oversizing to low vertical effective stress magnitudes, the normalization factor was limited to a maximum of 3. This value was established by considering a process of iterative analysis until the best fit was achieved at low magnitude dynamic modulus values.

$$E_{kdN} = E_{kd} C_{p3} \quad \textbf{eq. 3-10}$$

$$C_{kd} = \left(\frac{P_a}{\sigma'_v}\right)^{0.50} \quad \textbf{eq. 3-11}$$

With:

$$C_{kd} \leq 3$$

The normalization results allowed obtaining unique relationships between the soil density index and the normalized dynamic modulus by applying a nonlinear regression through the application of the Levenberg Marquardt iteration algorithm. eq. 3-12 and eq. 3-13 represent the relationship between the density index and the normalized dynamic modulus for Hostun HN31 and Fontainebleau NE34 dry sands, respectively.

$$I_D = -0.313 + 0.281 \ln(E_{kmN} - 4.207) \quad \textbf{eq. 3-12}$$

$$R^2 = 0.924$$

$$I_D = -0.011 + 0.195 \ln(E_{kmN} - 1.130) \quad \textbf{eq. 3-13}$$

$$R^2 = 0.90$$

For the case of saturated specimens, the relationships are established by eq. 3-14 and eq. 3-15, or Hostun HN31 and Fontainebleau NE34 sands, respectively.

$$I_D = -0.026 + 0.210 \ln(E_{kmN} - 1.254) \quad \textbf{eq. 3-14}$$

$$R^2 = 0.89$$

$$I_D = 0.142 + 0.165 \ln(E_{kmN} - 6.029) \quad \textbf{eq. 3-15}$$

$$R^2 = 0.94$$

The results of the normalization of the dynamic modulus showed a good degree of fit at low to medium density indices, showing a greater dispersion of the results at high densities in the case of dry specimens of both sands (Figure 3-40a and Figure 3-40b). he same effects are observed in the case of saturated specimens (Figure 3-41), however, at medium to low density levels, the results show a good fit.

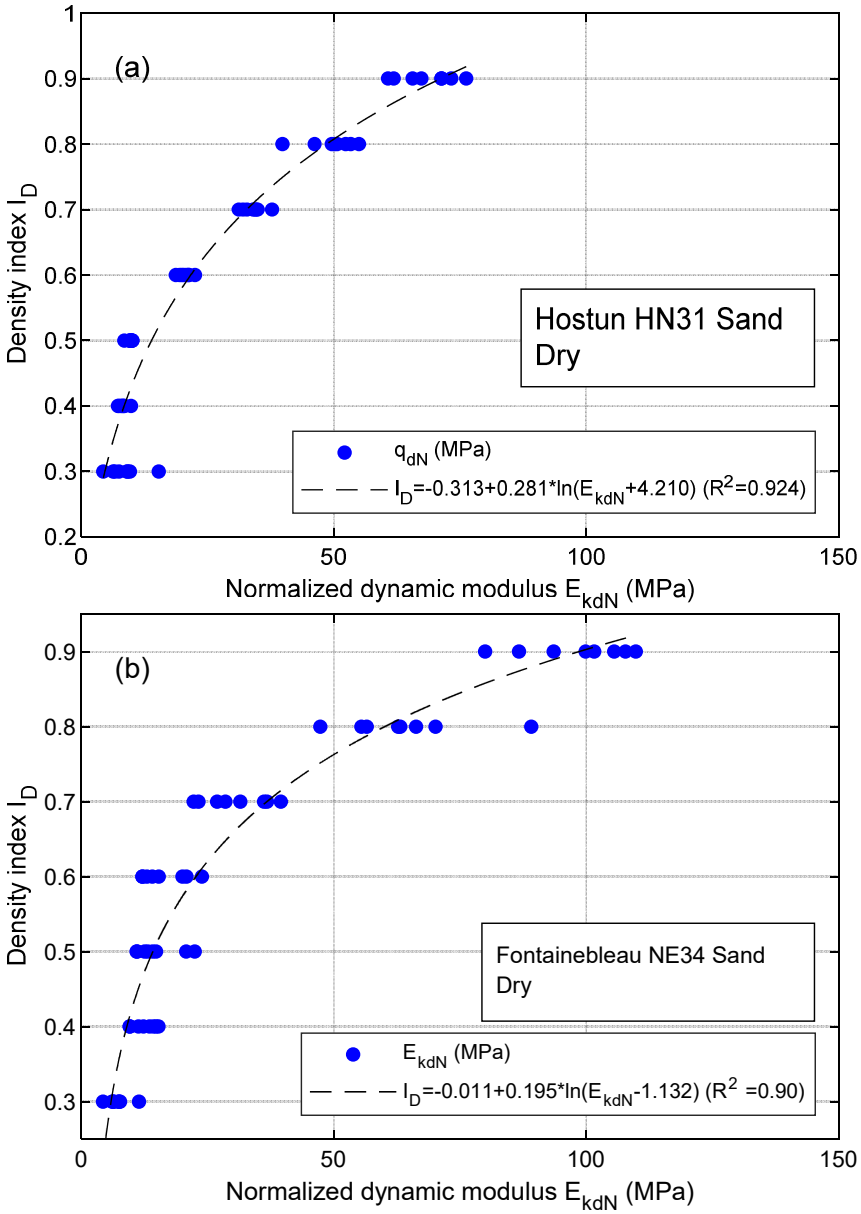

Figure 3-40 - Normalized dynamic modulus E_{kmN} in dry specimens: (a) Hostun HN31 sand and (b) Fontainebleau NE34 sand.

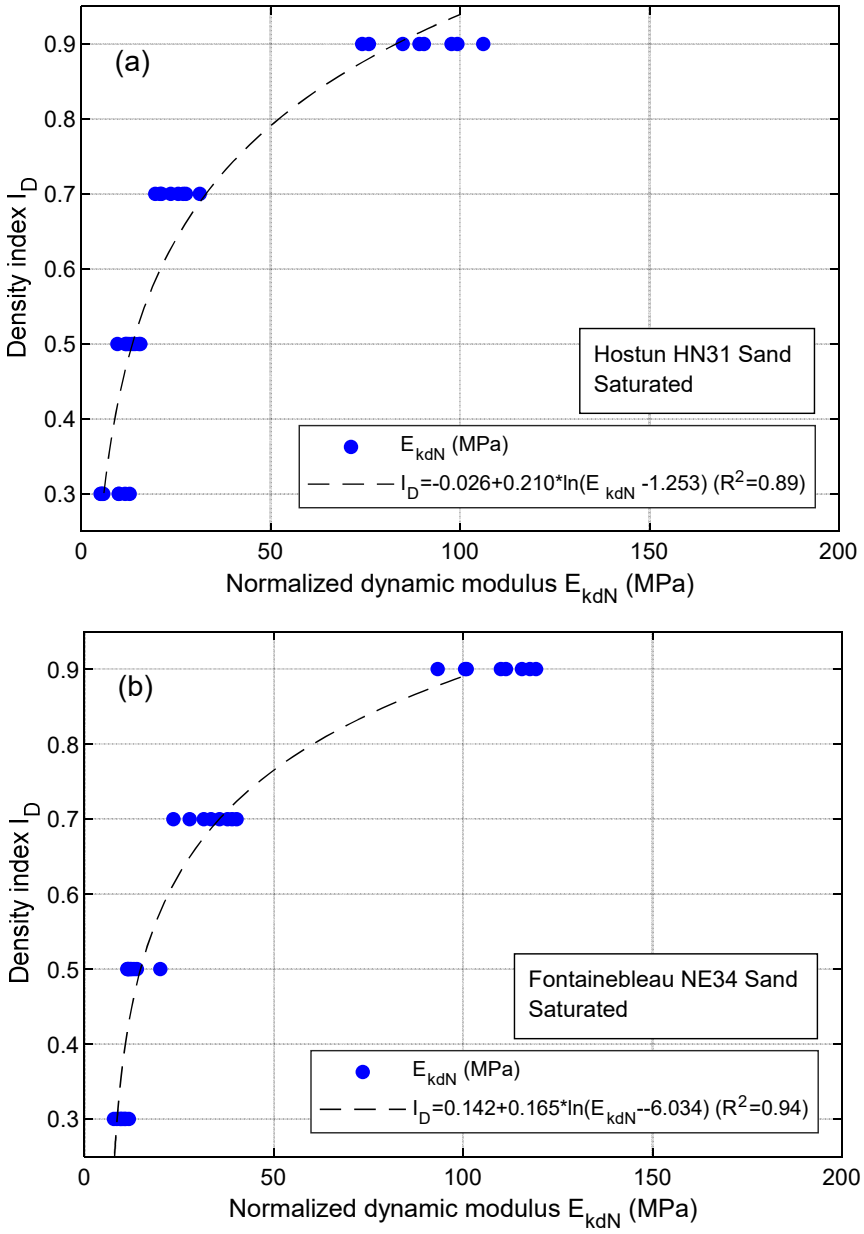

Figure 3-41 – Normalized dynamic modulus E_{kmN} in saturated specimens: (a) Hostun HN31 sand and (b) Fontainebleau NE34 sand.

3.3 Other parameters analyzed

To extend the analysis to other parameters obtained from the analysis of the dynamic signals, a general analysis of the secant elastic modulus of discharge E_{p3}^{d} (chapter 2.3.3) and the mechanical impedance of the soil Z_s (chapter 2.3.4) calculated through the reconstructed signals at the cone-soil interface was performed. The mention of these parameters is interesting in this research because of the potential future inclusion in the method for the evaluation of liquefaction potential.

3.3.1 Elastic modulus E_{p3}^{d}

Figure 3-42 presents a box plot that allows the comparison of the results of the unloading elastic modulus E_{p3}^{d} calculation for Fontainebleau NE34 sand specimen in dry state. The results show a high dispersion, which is more significant at a density index of 0.90. At low densities the dispersion is lower, however, the amplitude presented does not allow to establish a relationship between the characteristics of the soil and the magnitude of the elastic modulus.

The magnitude of this modulus was shown to be highly dependent on the treatment of the dynamic signals and the signal cut times. Therefore further research is required to evaluate this elastic modulus.

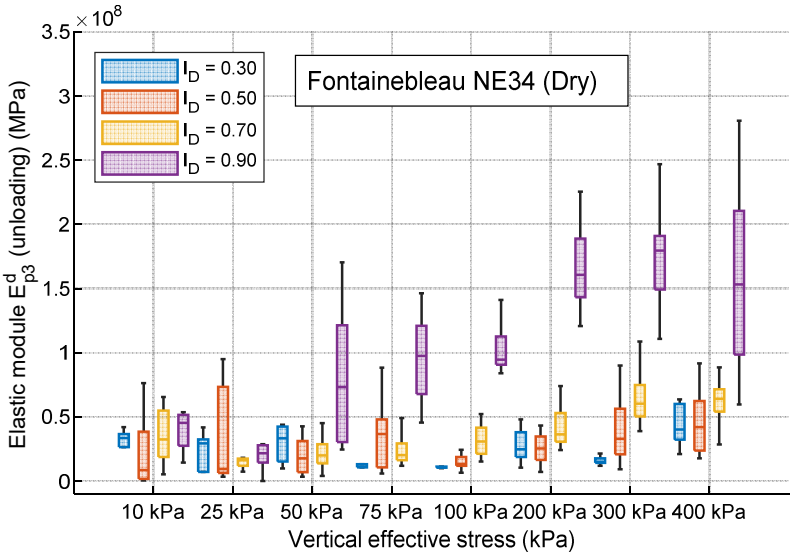

Figure 3-42 - E_{p3}^{d} Elastic modulus of unloading in Fontainebleau NE34 sands in dry state.

3.3.1.1 Soil mechanical impedance Z_s

Figure 3-43a and Figure 3-43b show the box plots comparing the results of the soil mechanical impedance analysis obtained from the analysis of the reconstructed signals at the soil-soil interface in Fontainebleau NE34 and Hostun HN31 sands.

In general, a high dispersion of values and a non-existent relationship between the impedance value and the state of the soil were observed; this characteristic prevents the use of this parameter as a characteristic value of the soil. However, there is strong theoretical evidence that relates this parameter to the resistance of the soil, so it is recommended to continue with the research on the evaluation of this parameter in dynamic penetration tests of variable energy.

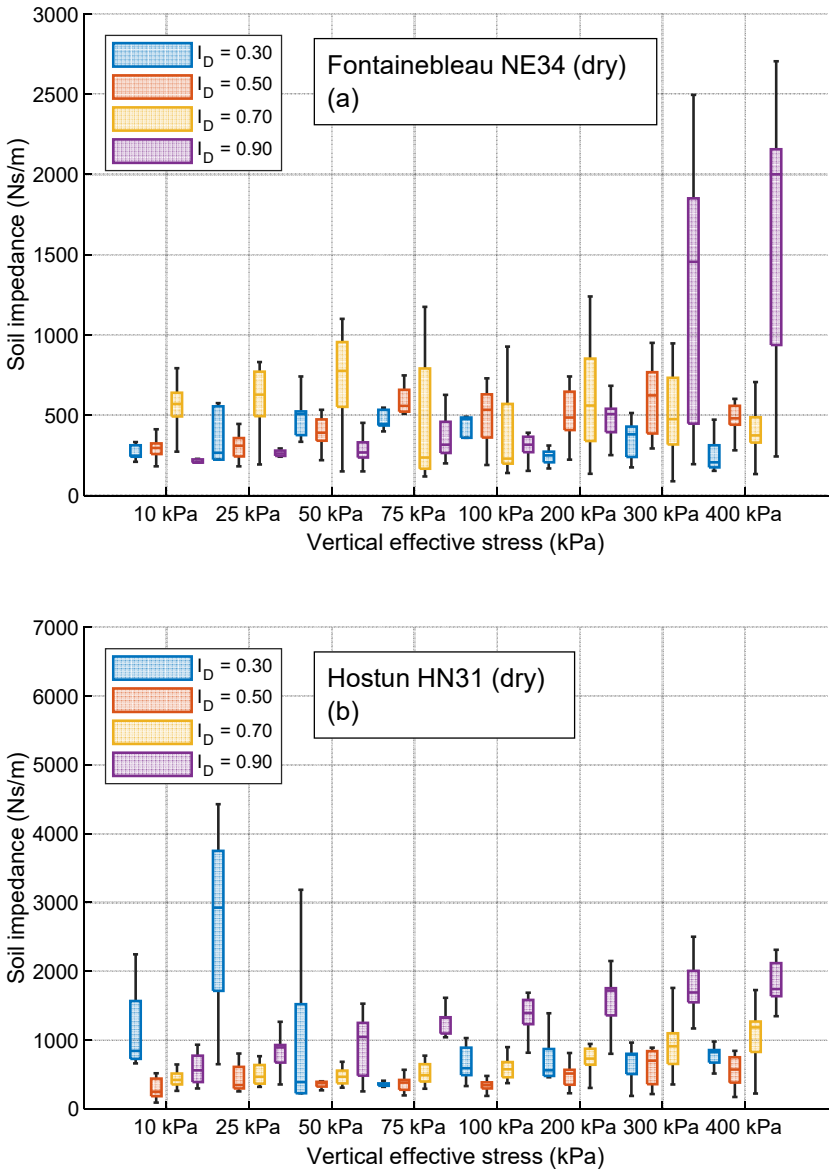

Figure 3-43 – Soil mechanical impedance in dry condition: (a) Fontainebleau NE34 sand; (b) Hostun HN31 sand.

3.4 Conclusions on dynamic variable energy penetration tests

The main results of the dynamic penetration tests performed on reconstituted species in a K_0, calibration chamber have been presented, which show the ability of the DPT to evaluate and characterize the response of a soil to dynamic penetration of variable energy.

The DCLT curves are proved to be sensitive to the variation of the effective vertical stresses, to the density index and to the saturation conditions of the specimen, so it is possible to perform an analysis of the soil condition by performing a parameter analysis of these curves. Taking this into account, the use of the maximum resistance value of the curve is considered as representative

of the maximum shear resistance mobilized by the soil when it is penetrated by the conical tip of the equipment.

The use of the maximum resistance of the DCLT curve has been demonstrated to be effective in the evaluation of the soil response because it has been shown to be independent of the magnitude of the driving energy and the maximum velocities reached in each hammer impact. This is validated in the range of speeds in which the penetrometer used in this research operates (1 a 8 m/s).

The independence of the dynamic resistance with respect to the driving energy of each impact, allows the consideration of q_d as an intrinsic parameter related to the conditions and state of the soil. Under this conclusion, the use of this parameter as a reference in a liquefaction potential evaluation method is proved.

The evaluation of the parameters resulting from the analysis of the curves and dynamic signals has demonstrated that the dynamic modulus E_{kd} is sensitive to both the density index and the vertical effective stress. This has logical support if it is considered that the signals associated with the waves generated by the impact of the hammer are affected in the process of penetrometer-soil interaction, especially at the cone-soil interface. The results of the evolution of this parameter indicate that it is an intrinsic property of each soil, which allows the differentiation between two different types of soils.

The elastic modulus E_{p3}^{d} show a high dispersion of the results avoiding the establishment of a relationship between the magnitude of the parameter and the state of the soil, this is because it is not currently considered as a characteristic parameter of the soil, however, its evaluation has shown to be sensitive to the conditions of treatment of the dynamic signals. In the case of the mechanical impedance Z_s, the results are also scattered. Although the mentioned parameters cannot be used at present, it is possible that improvements in the treatment of dynamic signals will allow in the future to include these parameters in the analysis and characterization of the soil, extending the possibilities of characterization of the materials.

Regarding to the normalization, the results allows establishing a comparison between two different tests and parameters, a necessary feature in a liquefaction potential evaluation method and in the establishment of databases for its application. However, a continuous revision of the correction factor based on new data from dynamic penetration tests is recommended.

Finally, it must be concluded that it is not possible to differentiate between two types of soils through the analysis of a single geotechnical parameter extracted from the exploitation of dynamic

signals, however, it is possible to establish a framework for the use of two or more characteristic soil parameters for their identification.

4 LIQUEFACTION PROPERTIES OF THE TESTED SANDS

In order to study the liquefaction properties of Hostun HN31 and Fontainebleau NE34 sands, a program of cyclic triaxial tests has been carried out. These tests have allowed to determine the cyclic shear resistance with the purpose of developing correlations with the results of dynamic penetration tests of variable energy.

This chapter presents the characteristics of the cyclic triaxial equipment used in this research, the test procedure used and the predefined experimental program. The main results of cyclic triaxial tests for both types of sands tested and the cyclic resistance curves are then presented.

4.1 Cyclic triaxial equipment

A prototype cyclic triaxial equipment (Figure 4-1), developed in the geotechnical team of Navier laboratory, was used to perform the cyclic triaxial test. This is basically a servohydraulic system, the deviatoric force being applied thanks to a servohydraulic 50 kN actuator. The test control and data acquisition is done through a digital controlling system (MTS system), which allow to select testing characteristic (shape, amplitude and frequency of loading signal, etc.)

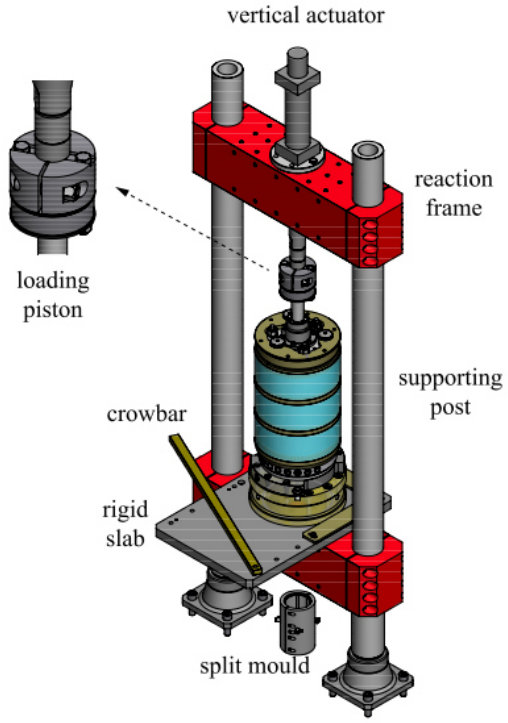

Figure 4-1 – Drawing showing the complete servohydraulic triaxial setup (Jradi 2018).

Figure 4-2 present the triaxial cell, which is composed of a waterproof guide system that allows the movement of the cyclic loading piston and which is supported on three rods with threaded termination to fix by means of nuts, a base on which both specimen and confinement

container are supported. The specimen is reconstituted on a lower base, which is connected to the outside by means of pipes through which the exchange of fluids with the outside of the chamber takes place. An upper base is installed on top of the specimen with the capacity to exchange fluids with the exterior by means of pipes (Figure 4-2).

The measurement of displacement data is performed by means of a linear variable differential transformer (LVDT) with an accuracy of 0.01 mm and a force sensor with an accuracy of 0.001 kN. The force sensor is installed under the base of the specimen to avoid parasite friction due to the loading piston (Figure 4-2).

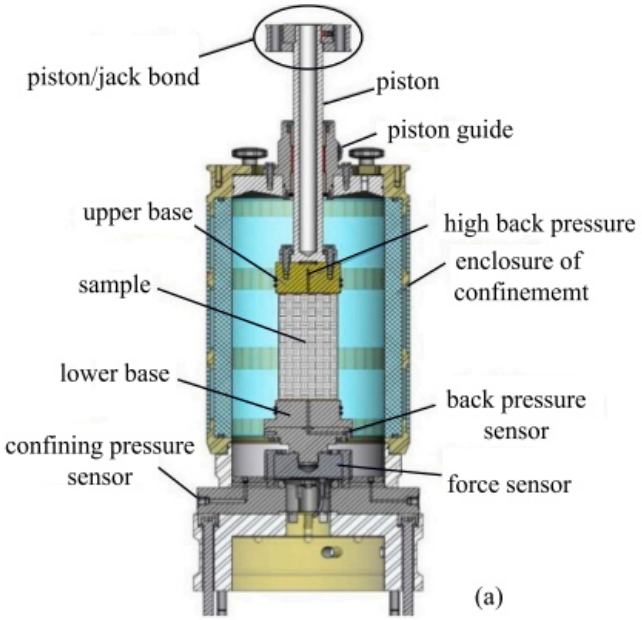

Figure 4-2 – Schematic diagram of the triaxial cell (Jradi 2018)**.**

4.1.1 Experimental procedure

To perform a cyclic triaxial test, a series of steps are required to ensure the correct reconstitution of the specimen and an adequate saturation for simulating proper soil conditions. In this test, four successive steps should be performed:

1. System and specimen preparation.
2. Saturation of specimen.
3. Consolidation of specimen.
4. Cyclic shear.

The above are described below.

1.1.1.1 System and specimen preparation

The preparation of the system and specimen corresponds to the reconstitution of the specimen inside the confinement chamber, by means of appropriate techniques according to the type and characteristics of the soil tested. In the case of this research, clean granular soils are tested at density indexes of 0.30 and 0.70. In the case of denser specimens, reconstitution was carried out by dry deposition in layers.

The looser specimen requires more care due to the sensitivity of the granular structure. In these specimens the wet deposition method has been used, which has been described by Castro (1969). This reconstitution methodology has been systematically employed in subsequent studies (Sladen et al., 1985, Been and Jefferies, 1985, Been et al., 1992, Kramer and Seed, 1988; Canou, 1987; 1989, Canou et al., 1990, 1994; Konrad, 1990; Konrad et al., 1991; Zlatović et Ishihara, 1997; Vaid et al., 1999).

The wet deposition method consists of adding water at a ratio of 1% and 5%, mixing until homogeneity is achieved and reconstituting a specimen in layers according to the density index required. This method is based on the generation of capillary bonds between the sand grains due to the presence of water, generating an increase of resistance in the contacts. This increase in resistance allows the reconstruction of specimens at very low density, including densities less than zero (Jradi 2018).

For the preparation of the specimen, in a first step, a porous plate is installed on the lower base in order to facilitate and improve the drainage of the specimen (Figure 4-3a), then, a latex membrane is installed covering the lower base. This membrane will be fixed by means of an o-ring (Figure 4-3b), which will also serve to ensure the sealing of the specimen in the bottom section.

To perform the deposition of the layers inside the latex membrane, a split mold with the dimensions of the specimen (100 mm in diameter and 200 mm high) is installed on the lower base. The latex membrane is stretched and fitted to the mold (Figure 4-3c). To ensure that the membrane fits the mold and allows the construction of a more homogeneous specimen, vacuum is applied at the membrane-mold interface.

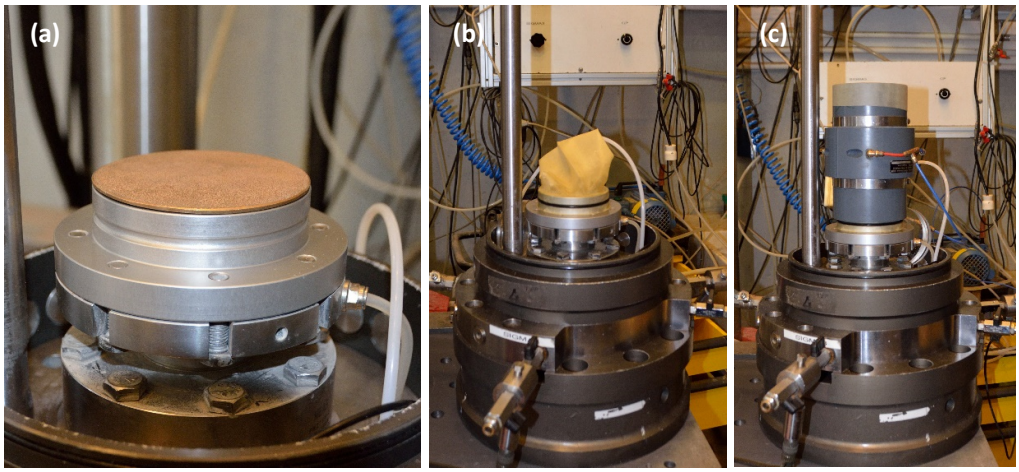

Figure 4-3- Reconstitution of specimen: (a) porous disk installation; (b) latex membrane installation; (c) mold installation.

To prepare the soil used in the loose specimen, the sample was prepared by mixing the sand with water in a mixer for at least 5 minutes to ensure homogeneity. Once the sample was homogeneous, it was deposited in 20 mm layers until reaching a height of 200 mm. Each layer was compacted until the required density index was reached.

Once the reconstitution of the specimen has been completed (Figure 4-4a), a porous disk is installed on top of it, and then the upper base cylinder, in which the latex membrane will be fitted and fixed by installing an o'ring. Then, in order to remove the mold and maintain the stability of the specimen, a vacuum pressure is applied to the inside of the specimen (Figure 4-4b).

With the specimen stabilized by vacuum, a sealing membrane is installed on the upper base cylinder to generate sealing during contact with the loading piston and then the upper cover containing the loading piston (Figure 4-4c). This cover is fixed by nuts to the vertical rods. With the loading system secured by nuts, the loading piston is placed in position so as to avoid perturbations on the specimen.

With the loading system installed, it is possible to install the hermetic confining cylinder (Figure 4-5), which is fixed to the loading system by means of bolts on the upper cover. Once the assembly is completed and its sealing is complete, it is displaced and adjusted in position to be connected with the hydraulic loading system and the chamber is filled with the water that will generate the confining pressure on the specimen.

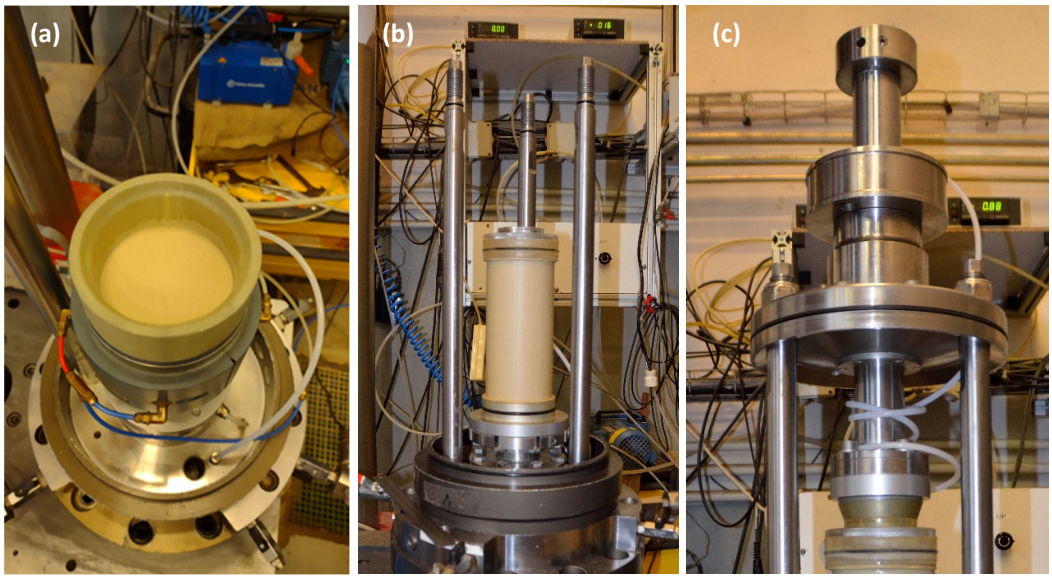

Figure 4-4- Reconstitution of specimen and preparation of loading system: (a) reconstituted specimen; (b) Top sealing of specimen; (c) installation of loading piston.

Figure 4-5 – Adjustment of the lateral confinement chamber.

4.1.1.1 Saturation stage

The objective of saturation is to fill the void space with water. This process comprises three successive stages: replacement of air by carbon dioxide CO_2, circulation of de-aerated water and application of back pressure.

The application of carbon dioxide is intended for air replacement, and this is performed by applying a flow of CO_2 at a pressure of about 15 kPa for a period of about 10 minutes to ensure complete replacement of air. The use of carbon dioxide is due to its high solubility with water.

To saturate the specimen, de-aerated water is used. Water deaeration is necessary to eliminate the air bubbles inside the fluid. These are capable of affecting the volumetric variations of the specimen subjected to shearing. Once the specimen is connected to the de-aerated water reservoir, the valves are opened to allow the flow through the specimen.

Once the specimen has been saturated, a back pressure is applied inside the specimen. At this stage, the correct saturation of the specimen is verified by using the Skempton's B coefficient. for the tests carried out within this research, it was ensured that B values higher than 0.98 were obtained.

4.1.1.2 Consolidation stage

The objective the consolidation stage, is to bring the specimen to the preselected effective stress conditions before shear. In this procedure, the pressure in the confinement chamber is raised, maintaining the pore pressure at a constant value. In the case of the tests carried out in this research, a effective consolidation pressure of 200 kPa has been set (260 kPa of total consolidation stress and 60 kPa of back pressure).

4.1.1.3 Shear stage

The shear stage consists in the application of the cyclic deviatoric stress specified for each test. In the first stage, it is necessary to make contact between the loading piston and the upper cylindrical base of the specimen. This operation must be carried out with caution so as not to generate perturbations in the specimen. Once contact has been achieved, the self-compensation system is started to ensure complete contact between the loading piston and the specimen by applying vacuum pressure. The point of contact is isolated from the chamber contour by means of a sealing membrane (Figure 4-6).

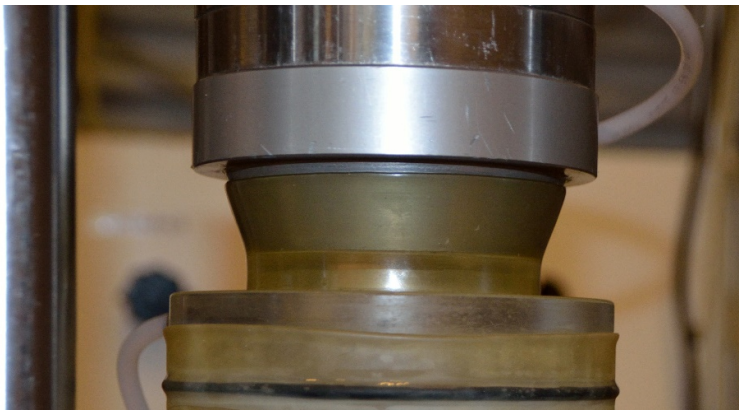

Figure 4-6 – Sealing membrane in piston-specimen contact.

The test characteristic are loaded into the controller software ("MTS FlexTest 60"). For the tests performed in this research, the set of parameters includes the application of a sinusoidal

shaped load of frequency 0.1 Hertz. The magnitude of the applied deviatoric stress Δq_{cyc} is configured according to the magnitude of the target cyclic resistance.

After completion of the configuration of the loading system, the cyclic shear program is started, which will stop when the preconfigured safety conditions have been reached. For this research, controlled force tests are performed, and the load cycles will stop after the occurrence of the cyclic instability phenomenon.

4.2 Undrained behavior of saturated sands under cyclic shearing

4.2.1 Experimental program

An experimental program was defined with the objective to obtain cyclic shear resistance curves for two different sands with different liquefaction properties (Hostun HN31 and Fontainebleau NE34), and for two density levels (loose and dense). The corresponding experimental program carried out is presented in Table 4-1.

Table 4-1 - Cyclic triaxial testing program

Test Reference	I_D	σ'_c (kPa)	Sand	R_{cyc}	Δq_{cyc} (kPa)
TCC1	0.70	200	Fontainebleau NE34	0.20	80
TCC2	0.70	200	Fontainebleau NE34	0.18	72
TCC3	0.70	200	Fontainebleau NE34	0.16	64
TCC4	0.70	200	Fontainebleau NE34	0.14	56
TCC5	0.30	200	Fontainebleau NE34	0.16	64
TCC6	0.30	200	Fontainebleau NE34	0.14	56
TCC7	0.30	200	Fontainebleau NE34	0.12	48
TCC8	0.30	200	Fontainebleau NE34	0.10	40
TCC9	0.70	200	Hostun HN31	0.24	96
TCC10	0.70	200	Hostun HN31	0.22	88
TCC11	0.70	200	Hostun HN31	0.20	80
TCC12	0.70	200	Hostun HN31	0.18	72
TCC13	0.30	200	Hostun HN31	0.16	64
TCC14	0.30	200	Hostun HN31	0.14	56
TCC15	0.30	200	Hostun HN31	0.12	48
TCC16	0.30	200	Hostun HN31	0.10	40

4.2.2 Typical cyclic triaxial test results

In cyclic triaxial tests, two different phenomena may be observed upon cyclic undrained shear: true liquefaction and cyclic mobility. Both phenomena are related to the loss of shear

resistance of the material due to a progressive decrease of effective stress σ'_v resulting from progressive increase of excess pore water pressure Δu. However, in the case of true liquefaction, there is a total loss associated with large strains and on the contrary, in the phenomenon of cyclic mobility, the observed behavior correspond to an accumulation of strains associated with a loop of increase and loss of the effective resistance associated with the application of load circles (ratchet phenomenon).

Both cyclic instability phenomena are associated with a progressive increase in excess pore water pressure (EPWP), which growth is associated with an increase in pressure when cyclic loading occurs and a decrease in the unloading phase, after which a cumulative increase in residual EPWP is obtained after each cycle.

In order to establish a criterion allowing the identification of cyclic instability phenomenon, a value of 5% of the maximum axial strain from peak to peak was defined as a limit and the cycle number at which these conditions occur is called critical cycle, N_{liq}.

A description of the typical cyclic instability phenomena occurring in sands is presented below. Then, the main results of the cyclic triaxial tests performed and an analysis of the effects associated with the different parameters controlled during the tests are presented.

4.2.2.1 True liquefaction

Figure 4-7a shows the sinusoidal cyclic loading signal applied on a reconstituted Hostun sand specimen at a density index of 0.00. This specimen was consolidated under an effective stress σ'_v of 200 kPa and alternated cycles with an amplitude of 36 kPa was applied. Figure 4-7b shows the evolution of EPWP with the number of cycles applied. The shape of the curve shows that the increase occurs gradually and in a relatively linear shape until reaching the critical load cycle for which there is an abrupt increase in EPWP, which reaches a value equal to the initial consolidation stress. At this point it is possible to say that the soil is in a state of complete liquefaction ($\sigma' = 0$).

Figure 4-7c shows the accumulation of axial strains produced during the test. On the graph it can be seen that the axial strains remain small during the mayor part of the test; however, when the critical cycle is reached, there is a sudden increase in axial strain. This is a typical characteristic of the true liquefaction phenomenon, in which the loss of shear resistance produces a sudden collapse of the granular structure.

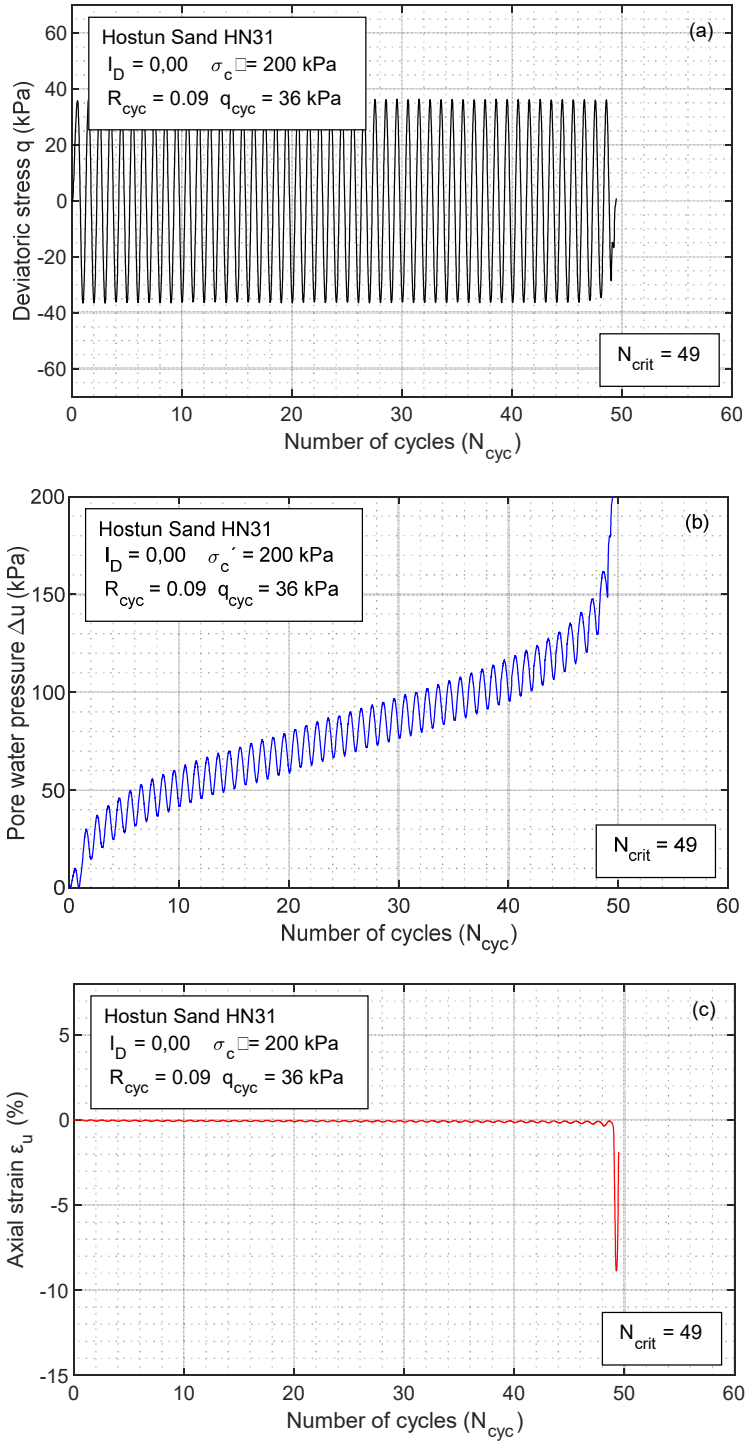

Figure 4-7 – True liquefaction phenomenon in Fontainebleau sand NE34: (a) Cyclic loading signal; (b) excess pore water pressure generation; (c) $\varepsilon_a - N_{cyc}$ curve.

The relationship between axial strain and EPWP is presented in Figure 4-8a. The graph shows how at very low increase in axial strain there is a gradual and cumulative increase in excess pore water pressure, until reaching a critical point where the EPWP migrates rapidly to a state in which the initial consolidation stress is reached. The evolution of the axial strains can also be observed in Figure 4-8b, in which the relationship between the deviatoric stress and axial strains

is presented. In the chart it can be observed how a small and limited accumulation occurs during the greater part of the extension of the deviatoric stress cycles; however, once liquefaction begins, large strains occur, a typical characteristic of liquefied soils.

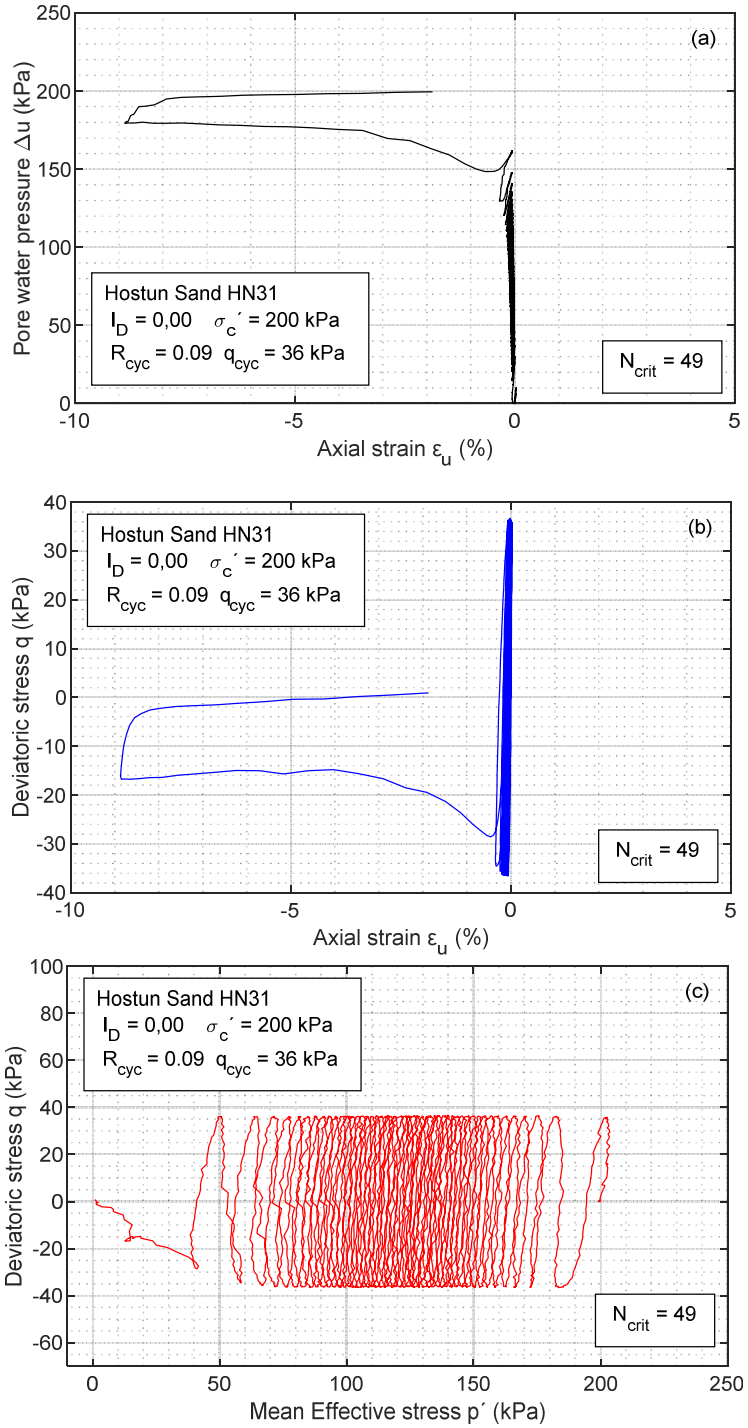

Figure 4-8 - True liquefaction phenomenon in Fontainebleau sands NE34: (a) Δu versus ε_a curve; (b) q versus ε_a curve; (c) effective stress path in the $(q - p')$ plane.

Figure 4-8c presents the relationship between the corresponding effective stress pathin the $(q - p')$ plane. It can be observed how the effective stress path migrates gradually toward the left, approaching the origin. Once the critical load cycle is reached, an abrupt decrease of the effective stress is observed, characterized by the displacement of the effective stress path towards the origin point, showing a total loss of strength of the specimen.

4.2.2.2 Cyclic mobility

Figure 4-9 and Figure 4-10 show the results of a cyclic triaxial test carried out on a Fontainebleau sand for a medium dense specimen ($I_D = 0.70$). Consolidation pressure of 200 kPa and alternated cyclic with an amplitude of 72 kPa are applied until the cyclic mobility phenomenon is reached (Figure 4-9a).

Figure 4-9b shows the evolution of EPWP with the number of cycles. It can be seen that the curve presents two well defined steps. A first step of gradual increase of the EPWP and a second step in which the EPWP reaches a magnitude equal to the initial consolidation stress. In the last step, a double peak mechanism can be observed in the EPWP generation, which is accompanied by a rapid accumulation of strain (Figure 4-9c)

Figure 4-10a shows the relationship between EPWP and axial strains. In this graph, one of the main differences with the real liquefaction phenomenon can be observed. Although limited axial strains are observed at the beginning of the cyclic loading process, when the cyclic mobility phenomenon is reached, a loop of increasing and decreasing EPWP is initiated with the cumulative increase of axial strains.

The evolution of the deviatoric stress as a function of axial strains is presented in Figure 4-10b. The effective stress decreases with each applied load cycle until cyclic mobility takes place. In the graph it can be observed how at the beginning of the cyclic loading the axial strains remain close to zero until reaching the critical load cycle, at this moment a process of accumulation of axial strains begins, which increase in each cycle of deviatoric stress. This cyclic loop behavior is also observed in the relationship between the deviatoric stress and the effective stress (Figure 4-10c). The effective stress decreases with each applied load cycle until cyclic mobility occurs, at this point the effective stress reaches a value of zero followed by a recovery associated with the reversal load. This looping behavior is characteristic of the cyclic mobility phenomenon.

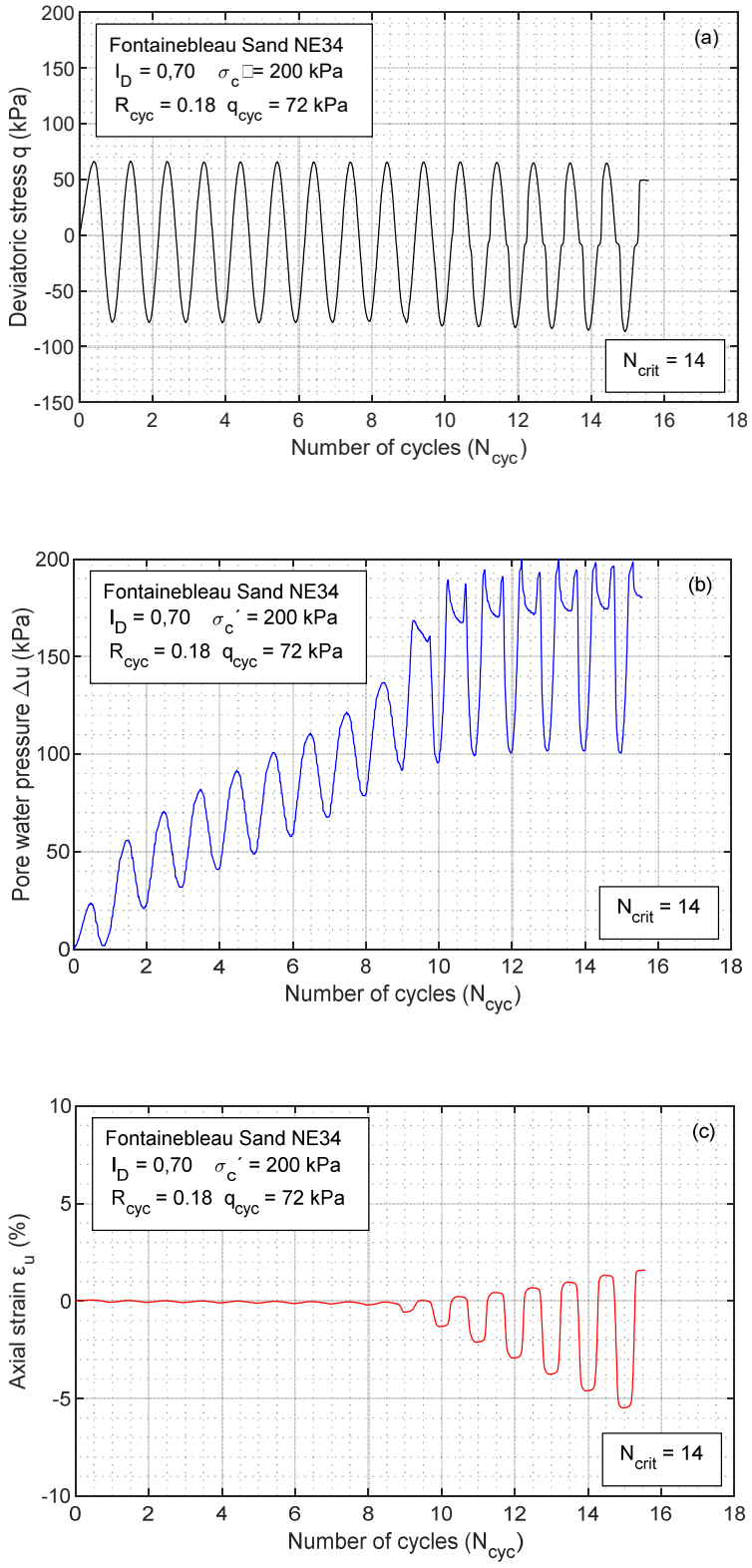

Figure 4-9 - Cyclic mobility phenomena in Fontainebleau NE34 sands: (a) Cyclic loading signal; (b) excess pore water pressure generation; (c) $\varepsilon_a - N_{cyc}$ curve.

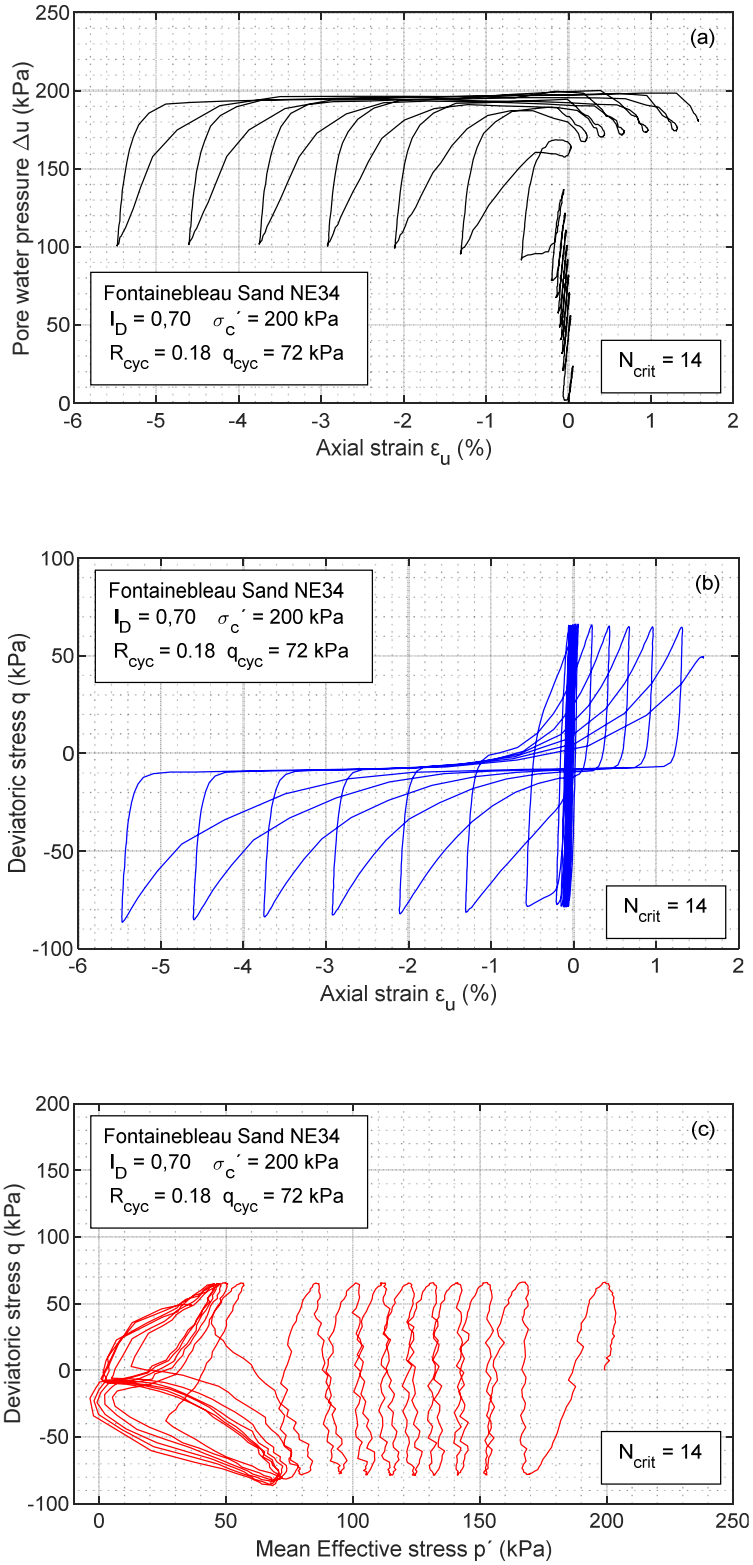

Figure 4-10 - Cyclic mobility phenomena in Fontainebleau NE34 sands: (a) Δu versus ε_a curve; (b) q versus ε_a curve; (c) effective stress path in the $(q - p')$ plane.

4.2.3 Parametric study

4.2.3.1 Influence of the density index

To analyze the effects of the density index on the cyclic response of the soil, cyclic triaxial tests were performed on specimens reconstituted at two different density indices (0.30 and 0.70) while maintaining the boundary conditions. Both specimens were consolidated under a consolidation pressure of 200 kPa and a cyclic deviator amplitude Δq_{cyc} of 64 kPa was applied, in order to observe the differences in the response of the soil (Figure 4-11).

For the specimen reconstituted at an I_D of 0.30, cyclic instability was reached for $N_{crit} = 27$, and in the specimen with an I_D of 0.70, cyclic mobility is reached at 42 cycles. This demonstrates the effect of relative density on cyclic strength, which implies that value of I_D the density, the higher the cyclic strength.

For of both specimens, the observed response corresponds to cyclic mobility phenomenon characterized by the occurrence of double peaks of EPWP when it reaches the value of the consolidation pressure (Figure 4-11a), in addition to the accumulation of axial strains without a critical loss of stability of the specimen (Figure 4-11b), and the occurrence of a dilatancy and contraction loop (Figure 4-11c).

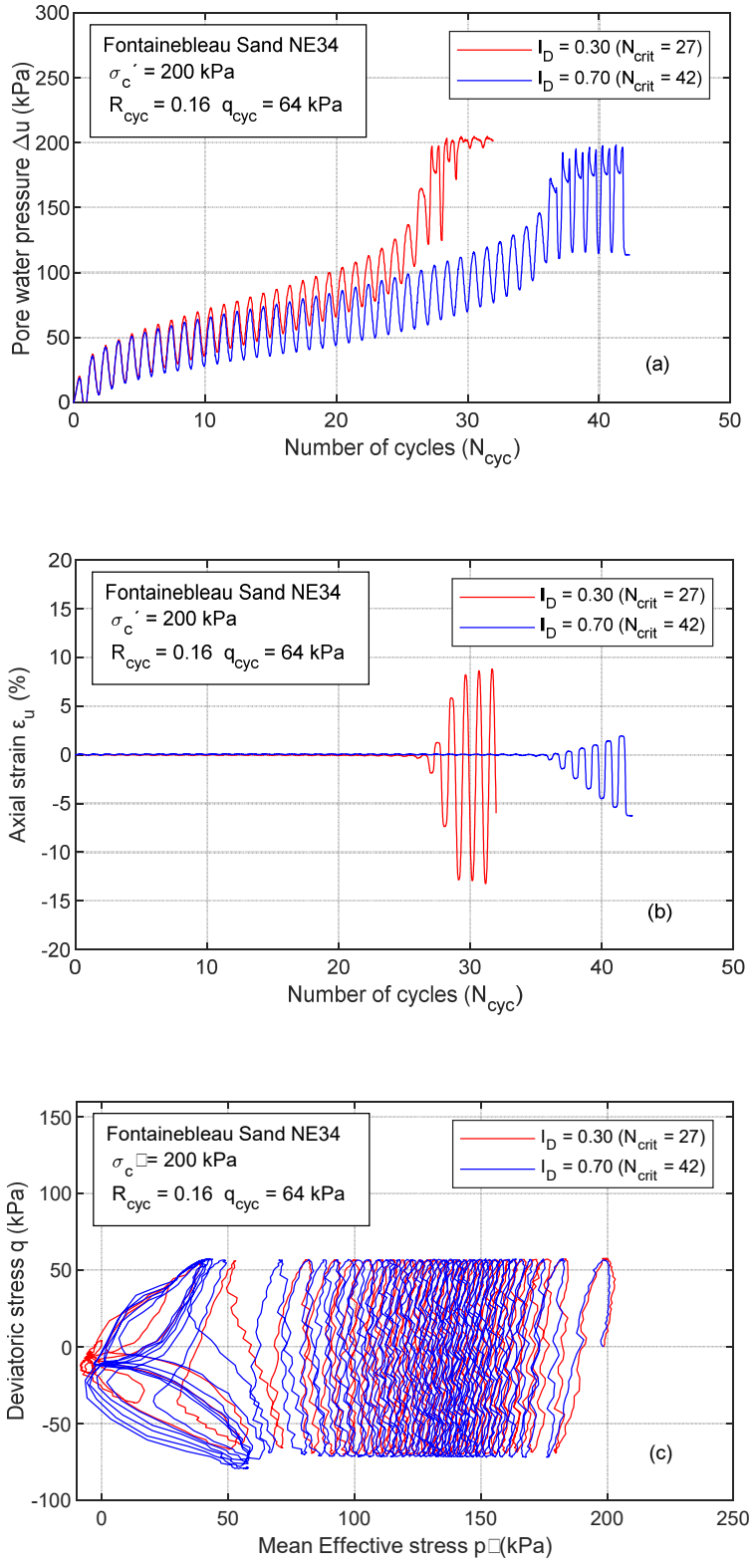

Figure 4-11 – Influence of density index on the cyclic response of Fontainebleau NE34 sand: (a) excess pore water pressure generation; (b) $\varepsilon_a - N_{cyc}$curve; (c) effective stress path in the ($q - p'$) plane.

4.2.3.2 Influence of the cyclic stress ratio

Cyclic stress and density index are the most important parameters for characterizing the response of soil subjected to cyclic loading. In the case of cyclic stress, it represents the stress applied on the soil necessary to produce a true liquefaction or cyclic mobility phenomenon.

The results of a comparative analysis of tests performed by setting density conditions to establish the effects of cyclic stress variation on sand specimens are presented below.

a. Case of loose sand ($I_D = 0.30$)

In order to establish the effects of the cyclic stress ratio on the cyclic behavior of the sand, three reconstituted specimens were compared at a density index of 0.30 and the cyclic loading was varied by 0.16, 0.14 and 0.12. The three specimens were consolidated at an effective stress of 200 kPa. Figure 4-12a shows the variation of pore pressure for the three tests performed, Figure 4-12b he axial strain and Figure 4-12c the variation of the effective stresses in the specimen.

The EPWP curves (Figure 4-12a), show that the rate of EPWP generation increases with increasing amplitude of the R_{cyc}, so the number of cycles required to reach an instability phenomenon will be higher when the cyclic load decreases. Figure 4-12 shows that, for Hostun sand HN31, cyclic mobility phenomenon is observed in all cases. The specimen subjected to a cyclic stress of 0.16 reaches instability at 96 cycles, and those subjected to 0.14 and 0.12 at 171 and 402 cycles, respectively.

The plot of axial strains (Figure 4-12a), shows small initial strains in the three cases, followed by a development of rapidly increasing strain associated with the instability of the soil are reached after a different number of critical cycles.

b. Case of dense sand ($I_D = 0.70$)

In Figure 4-13a, Figure 4-13b and Figure 4-13c, the results of cyclic triaxial tests performed on dense specimens ($I_D = 0.70$) subjected to a cyclic stress ratio of 0.20, 0.18 and 0.16 and consolidated at an effective stress of 200 kPa are presented. The results show that the EPWP generation presents a evolution as the one observed in loose specimens, characterized by an increase in pressure rate when the cyclic loading is increased (Figure 4-13a).

An important feature observed in the EPWP curves (Figure 4-13a), is that the evolution shows the occurrence of two phases. A primary phase in which there is a gradual increase in pore pressure with sinusoidal shaped cycles, in which the increase in pressure can be related to the number of cycles, and a secondary phase characterized by the occurrence of a double peak of pore

pressure when it reaches the consolidation pressure. This behavior was similarly reported by Jradi (2018)

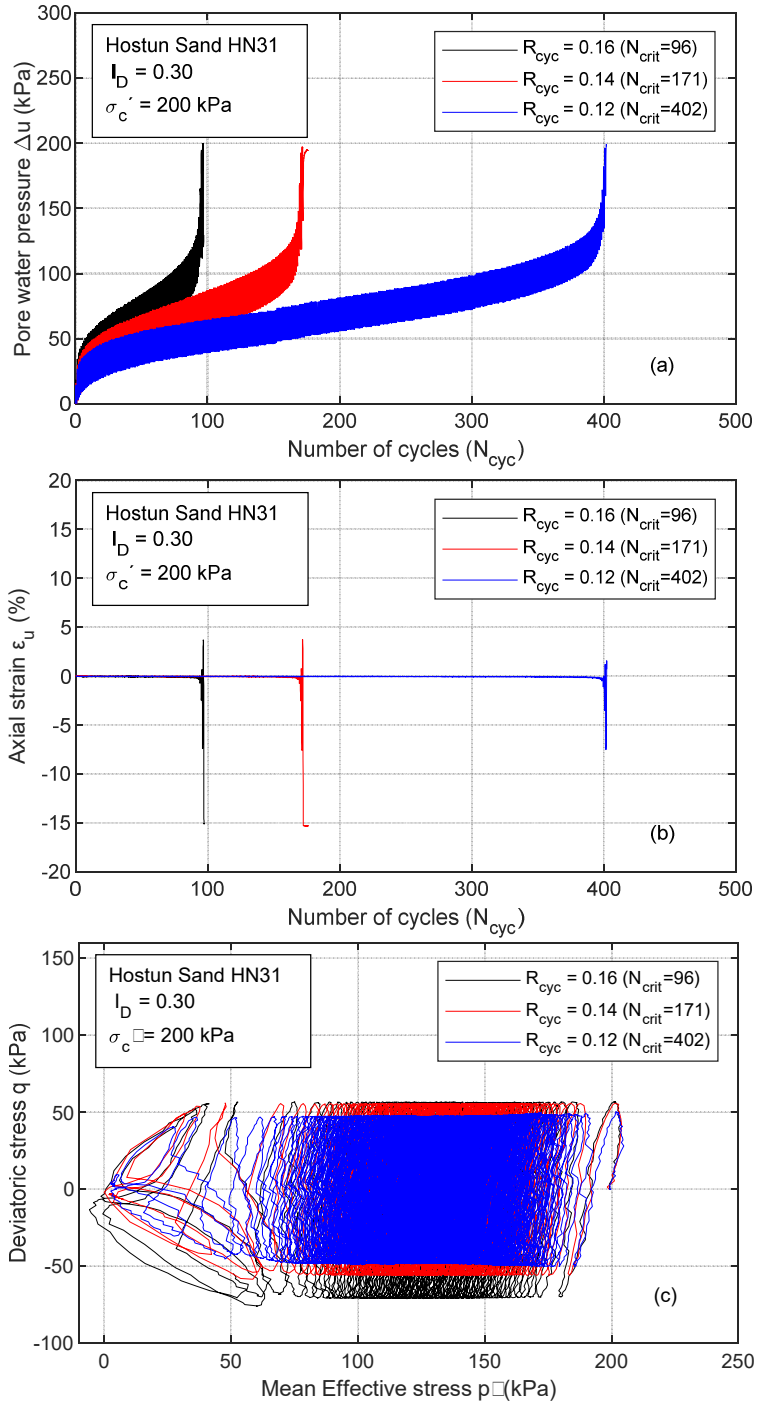

Figure 4-12 – Cyclic stress ratio influence on loose Fontainebleau NE34 sands: (a) excess pore water pressure generation; (b) $\varepsilon_a - N_{cyc}$curve; (c) effective stress path in the ($q - p'$) plane.

Figure 4-13b presents the cyclic axial strain evolution during the test. The results show that in the three cases there is an initial phase of very small axial strains, however, when reaching cyclic mobility, a behavior of accumulation of increasing axial strains is observed.

According to Figure 4-13c, it is possible to determine that the instability phenomenon reached in the specimen is cyclic mobility, due to the loop behavior observed when the EPWR reaches the initial effective consolidation stress of the specimen. In the case of the specimen subjected to a cyclic stress of 0.20, cyclic mobility was reached at cycle number 7; for cyclic stresses of 0.18 and 0.16, instability was reached at 14 and 42 cycles, respectively.

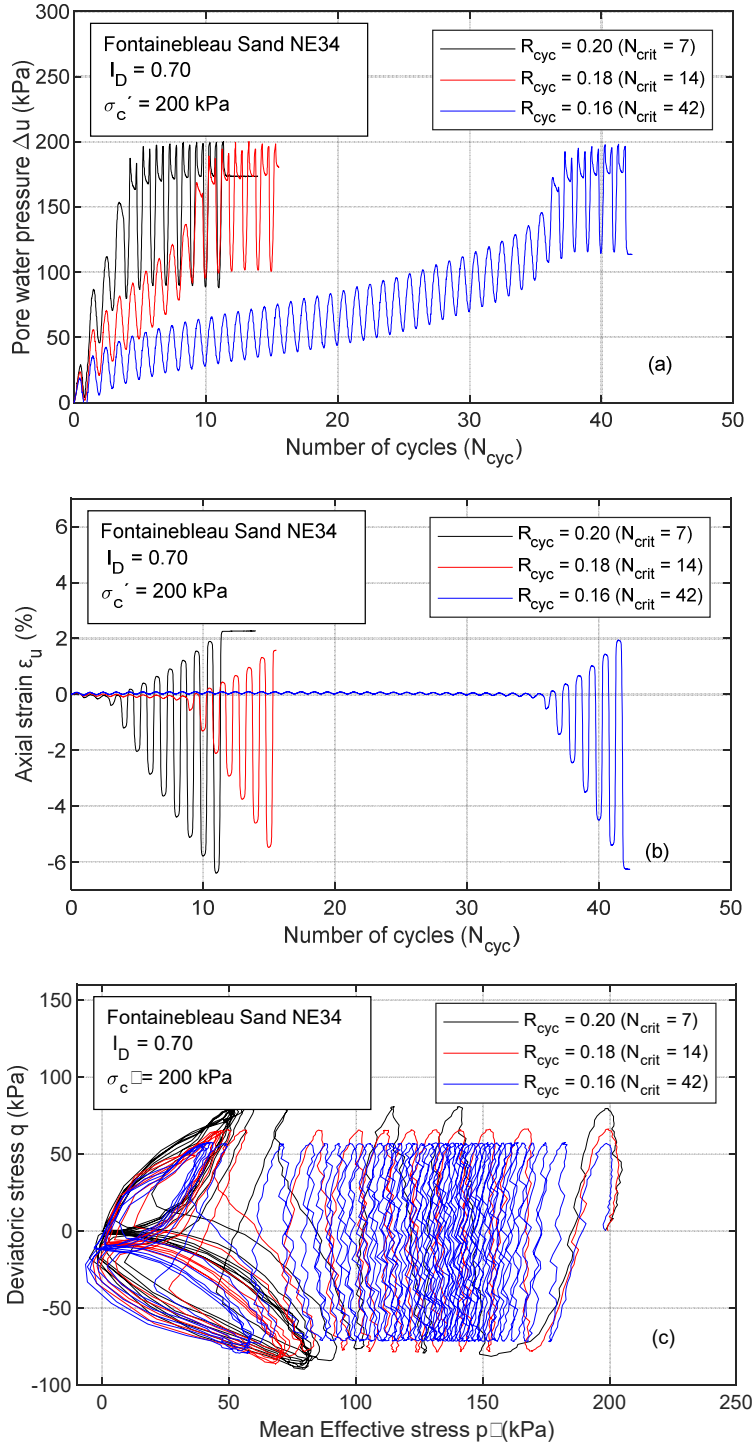

Figure 4-13 – Cyclic stress ratio influence on dense Fontainebleau NE34 sands: (a) excess pore water pressure generation; (b) $\varepsilon_a - N_{cyc}$curve; (c) effective stress path in the ($q - p'$) plane.

4.2.4 Cyclic resistance curves

The relationship between the cyclic stress ratio (CSR) applied on the specimen $\tau_{cyc}/2\sigma'_c$ and the number of cycles required to reach true liquefaction or cyclic mobility N_{crit}, allows the construction of cyclic resistance ratio (CRR) curves. This relationship is represented in a semilogarithmic plane to facilitate its interpretation and it is constructed as a function of a fixed density index.

The establishment of these curves makes it possible to predict the behavior of the soil by dividing the CSR-N_{crit} plane into two domain. A first domain below the adjusted cyclic resistance curve, where the behavior of the soil is stable and cyclic instability phenomena do not occur, and a second domain above the curve, where the relationships established in theory are not possible, because they exceed the cyclic resistance limit of the soil and the soil has already failed. This subdivision of spaces implies that the CRR represents the stability limit of the soil under cyclic loading for a given density state.

Since the CRR curve represents the limiting resistance of the soil to the occurrence of liquefaction or cyclic mobility phenomena, its use allows the analysis of the liquefaction potential of a soil by comparing its results with the seismic stress likely to occur at a given location or CSR. For this, it is necessary to establish a comparison framework based on the normalization of the stress and the cyclic resistance of the soil. A number of cycles equivalent to an earthquake of magnitude M_w of 7.5, which in the case of triaxial tests is equivalent to 15 load cycles, has been commonly considered as a normalization standard. Normally it is not possible to pre-fix the occurrence of failure in soil in load cycle 15, however, it is possible to apply a non-linear regression process on the CRR-N_{cyc} points and calculate the equivalent resistance by means of the fitted curve equation.

The results of the CRR curves obtained for the tests performed on loose sands at an I_D of 0.30 and on dense sands at an I_D of 0.70 and for both types of sands tested are presented below.

4.2.4.1 CRR curves in loose sands

Cyclic resistance curves obtained for Hostun HN31 and Fontainebleau NE34 sand specimens reconstituted at a density index of 0.30 are presented in Figure 4-14. All specimens were consolidated at an effective stress of 200 kPa and subjected to different cyclic loading amplitudes to capture the variation of cyclic strength with respect to the number of cycles applied.

The CRR curves show that Hostun HN31 sand specimens require a higher number of cycles to produce cyclic instability under the same level of cyclic stress ratio. This implies that

Fontainebleau NE34 sand has a lower resistance to cyclic shear and is more liquefiable than Hostun sand HN31. These results are consistent with other results reported in the available bibliography, in which similar soils were analyzed (Benahmed 2001; Jradi 2018).

Through the evaluation of the nonlinear regression applied to the points to obtain the cyclic resistance curve, the CRR value was obtained for the number of cycles equivalent to an earthquake of magnitude M_w of 7.5 (15 cycles). For Hostun HN31 sands $CRR_{7.5}$ is 0.22, and for Fontainebleau NE34 sands it is 0.16.

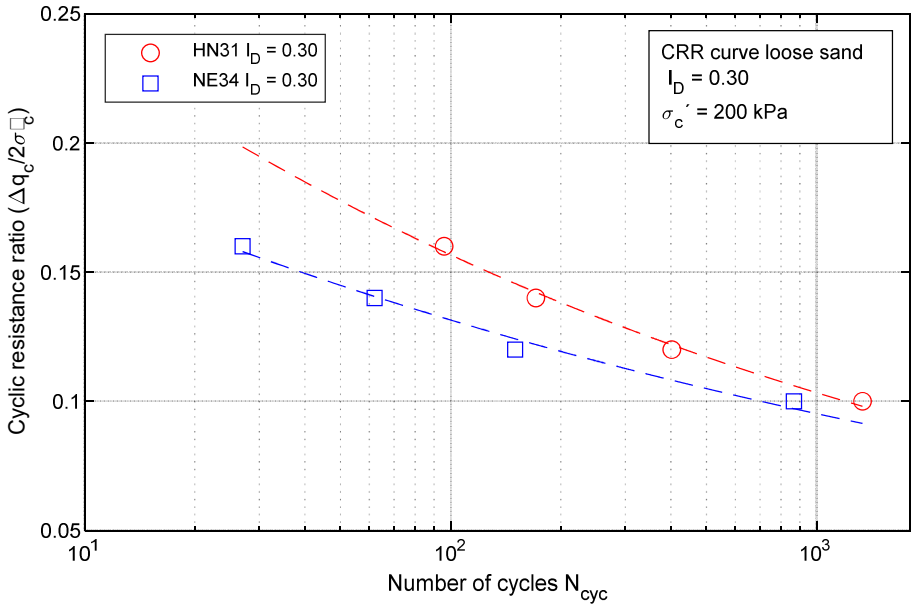

Figure 4-14 – Cyclic shear resistance curves for loose sand specimens ($I_D = 0.30$).

1.1.1.2 CRR curves for dense sands

Figure 4-15 shows the resistance curves from cyclic triaxial tests performed on Hostun HN31 and Fontainebleau NE34 sands, on specimens reconstituted at an I_D of 0.70. As for the case of loose sand specimens, the curves show that Hostun HN31 sand are more resistent than Fontainebleau NE34 sands to liquefaction.

In tests performed on specimens with this density index, the cyclic instability phenomenon was described as cyclic mobility, which is consistent with results in cyclic triaxial tests performed on sands under similar conditions (Benahmed 2001; Jradi 2018; Zhu et al. 2021).

The values of cyclic resistance equivalent to an earthquake of magnitude M_w of 7.5 (15 cycles) were calculated with the same procedure as in the case of loose sands, obtaining values of $CRR_{7.5}$ of 0.25 and 0.18 for Hostun HN31 and Fontainebleau NE34 sands, respectively.

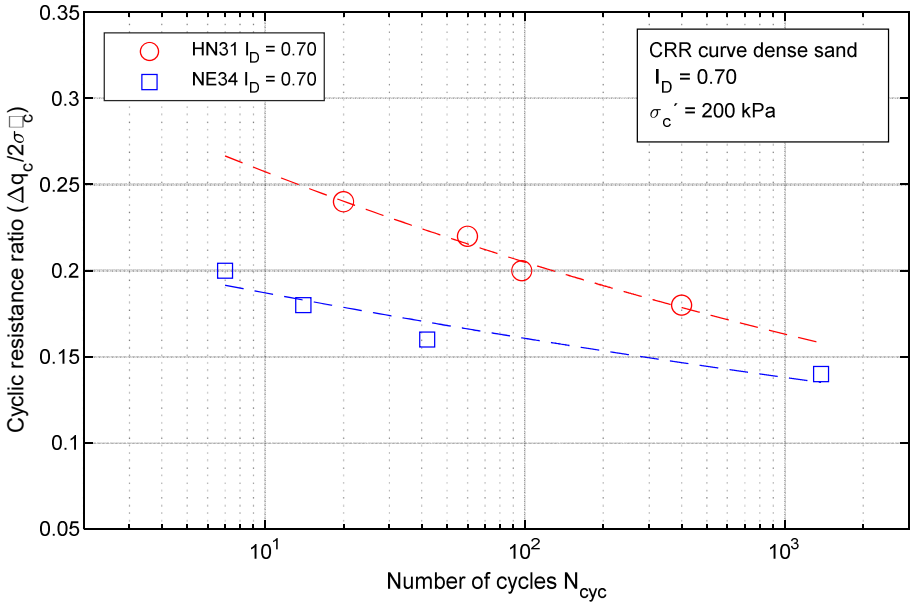

Figure 4-15– Cyclic shear resistance curves for dense sand specimens ($I_D = 0.70$).

4.2.5 Conclusion

The results of cyclic undrained triaxial tests carried out on Hostun HN31 and Fontainebleau NE34 sands with two density indices (0.30 and 0.70) have been presented to establish the liquefaction properties of both sands and the value of the equivalent cyclic resistance to an earthquake of magnitude M_w of 7.5 or 15 load cycles. The cyclic behavior observed in the two sands shows the predominance of the cyclic mobility phenomenon. This behavior is related to the magnitude of the cyclic stress applied on the specimens and the density indices considered.

The test results showed that for both density index levels Hostun HN31 sands present higher resistance to undrained cyclic shear, which is consistent with the results of cyclic resistance analysis presented in the available bibliography considering the same or similar sands (Benahmed 2001; Jradi 2018; Zhu et al. 2021). It was also found that the higher the magnitude of the cyclic stress ratio applied to the specimen, the lower the number of cycles required to produce the cyclic mobility phenomenon.

Finally, the results of the cyclic tests allowed obtaining the values of cyclic resistance CRR corresponding to an earthquake of magnitude M_w de 7.5. The values obtained for a density index of 0.70 were 0.25 and 0.18 for Hostun HN31 and Fontainebleau NE34 sands, respectively. For a density index of 0.30, the values were 0.22 and 0.16 for Hostun HN31 and Fontainebleau NE34 sands, respectively.

5 PREPOSITION OF A METHOD FOR THE EVALUATION OF LIQUEFACTION POTENTIAL OF SANDS

The preceding chapters have made it possible to study and analyze the response of the soil to the dynamic penetration of a variable energy equipment in two types of sands, in specimens reconstituted at different density index levels and under different levels of effective vertical stress. This chapter presents a soil type characterization methodology based on the results of dynamic tests performed on the two types of sands and establishes an initial methodology for the differentiation of the two soil types based on a multiparametric approach.

The results obtained from the dynamic tests (chapter 3) have allowed establishing a reference framework for the creation of a liquefaction potential evaluation method based on the characterization of the soil type and the use of a database with previously established relationships between the cyclic resistance of the soil and a combination of dynamic parameters associated to the penetration test.

The method can be summarized in five main steps (Figure 5-1). The first step is the conduct of the dynamic penetration test at the place where there is a possibility of occurrence of the liquefaction phenomenon. The second step consists of the evaluation of the dynamic signals and the evaluation of the soil response parameters based on these measurements. The third step involves the normalization of the results in terms of an Effective Vertical Stress of reference in order to make the results comparable with other tests, the fourth step consists in the identification of the type of soil based on relationships between the parameters analyzed and finally, the obtaining of the cyclic resistance based on the information contained in the database.

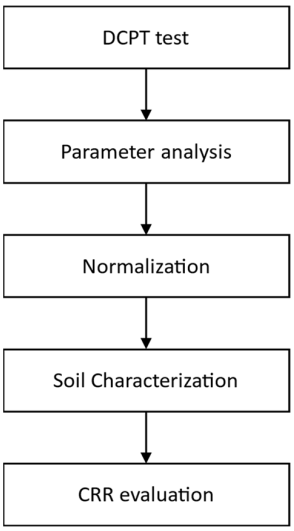

Figure 5-1 - General scheme of the method for evaluating the liquefaction potential of soils.

The application of the penetration test is carried out in a place where the liquefaction phenomenon is likely to occur, this means that the minimum necessary requirements can be found, such as: existence of a granular material, existence of a water table and the possibility of a monotonic or cyclic stress capable of producing an increase in pore pressure

The parameters obtained from the analysis of the dynamic signals are associated with a specific state of the soil, so in order to make the results comparable with other tests and/or with the cyclic stresses applied to the soil, it is necessary to normalize them to a reference effective consolidation stress. This normalization makes it possible to compare two different soils both parametrically and with respect to their liquefaction properties.

Soil type characterization is carried out by establishing relationships between the normalized penetration resistance and the normalized dynamic modulus in a q_{dN}-E_{kdN}, plane, which when plotted generate subspaces associated with soil types of similar characteristics, thus, the coordinates generated by the pair of normalized parameters are located in a subspace that groups each soil type. The identification of the soil type allows obtaining the density index by means of pre-established relationships and the cyclic resistance from records stored in a database.

With the soil type identified it is possible to use a database to obtain the cyclic resistance from previous records or by establishing relationships between $CRR_{7.5;1atm}$ and q_{dN} or I_D, then the value of the $CRR_{7.5;1atm}$ is compared with the value of cyclic stress ratio $CSR_{7.5;1atm}$ possible to occur at the evaluation location, establishing a safety factor against liquefaction occurrence.

The database is composed of cyclic resistance values obtained from cyclic laboratory tests and normalized parameter values obtained from dynamic penetration tests. Estos parámetros permiten obtener de forma directa la resistencia cíclica para un valor de resistencia a la penetración especifico o índice de densidad o mediante el establecimiento de relaciones entre $CRR_{7.5;1atm}$y q_{dN} o I_D. Esta base de datos puede ser extendida de manera similar a aquellas basados en ensayos realizados en ubicaciones la licuefacción ocurrió o no, sin embargo (Boulanger, Wilson, and Idriss 2012; Idriss and Boulanger 2010; Seed and Idriss 1971), los datos agregados se basan en ensayos de laboratorio.

In the following chapters, the soil type identification procedure, the cyclic strength evaluation method and the application to the results of the tests carried out on the sands used in this research are presented in detail.

5.1 Soil type characterization

To characterize the soil type penetrated by the cone, a methodology based on a multi-parameter approach using normalized penetration resistance and normalized dynamic modulus values has been established. The procedure involves the location of the parameter pair q_{dN}-E_{kdN} in a space subdivided into spaces delimiting groups of similar soil types.

The procedure for establishing soil type subspaces and the methodology for soil type identification is presented below.

5.1.1 Soil Type definition

Identification of the soil and its characteristics is required in order to establish the necessary parameters in the liquefaction potential evaluation. For this purpose, a multiparametric approach has been developed to establish unique relationships between the dynamic penetration resistance and a characteristic parameter of the soil obtained from the dynamic strain and acceleration signals measured in the DPT test.

Early methodologies for evaluating liquefaction potential using dynamic penetrometers employed a combination of parameters to establish the state of the soil and evaluate its cyclic resistance (Seed and Idriss 1971). The use of this approach is based on the application of correlations, since there is no framework for a direct evaluation of liquefaction potential based on the mechanical response of the soil when it is subjected to dynamic penetration.

In the initial work directed to the evaluation of liquefaction potential by means of the SPT penetrometer, the value of the density index was used to establish a value of the cyclic resistance by means of correlations (Seed and Idriss 1971). Concerning the CPT static penetrometer, the value of the tip resistance and the lateral friction are used to identify soil types by means of a behavioral index and then obtain the value of the cyclic resistance by correlation (Robertson and Campanella, 1985; Robertson and Fear, 1995; Youd et al., 1997).

In the PANDA3® penetrometer, it is possible to evaluate different parameters (tip resistance, dynamic modulus, compression wave velocity, mechanical impedance, secant elastic modulus of unloading and reloading). However, the dynamic modulus has been identified as the most sensitive to the soil type. The analysis of the normalized penetration resistance values and dynamic modulus has allowed the establishment of unique relationships for both sand used in this study (Figure 5-2).

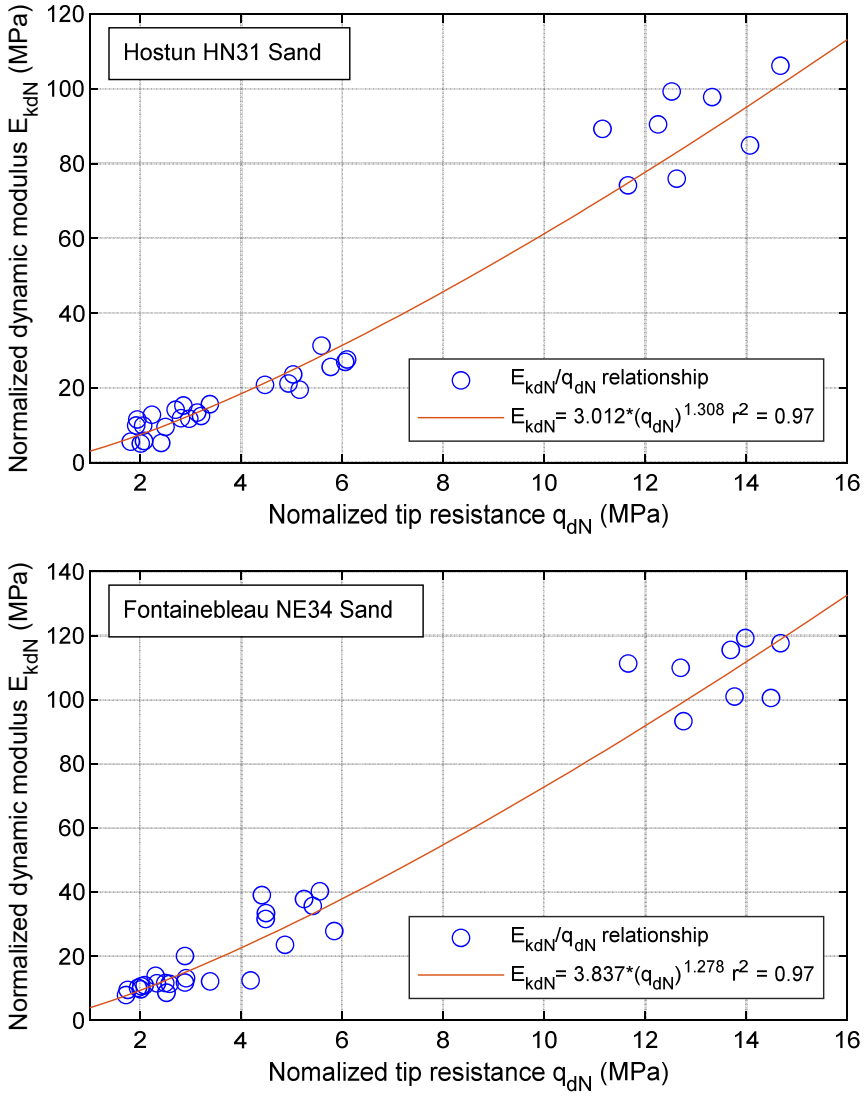

Figure 5-2 - Relaciones -: (a) Arenas Hostun HN31; (b) Arenas Fontainebleau NE34.

The relationships between normalized dynamic modulus and normalized penetration resistance, can be modeled by a potential equation based on two factors. A multiplicative factor *A* and a exponent factor n. The eq. 5-1 and eq. 5-2 represent the relationships between normalized dynamic modulus and normalized dynamic penetration resistance for Fontainebleau NE34 and Hostun HN31 sands, respectively.

$$E_{kdN} = 3.837 {q_{dN}}^{1.278} \qquad \textbf{eq. 5-1}$$

$$R^2 = 0.97$$

$$E_{kdN} = 3.012 {q_{dN}}^{1.308} \qquad \textbf{eq. 5-2}$$

$$R^2 = 0.97$$

The plotting of these relationships allows the division of the q_{dN}-E_{kdN} plane into subplanes associated with the soil type (Figure 5-3). In order to establish a division between the spaces, a boundary line is established corresponding to the midpoint of the relationships associated with the soil types. This boundary represents the passage from one soil type to another.

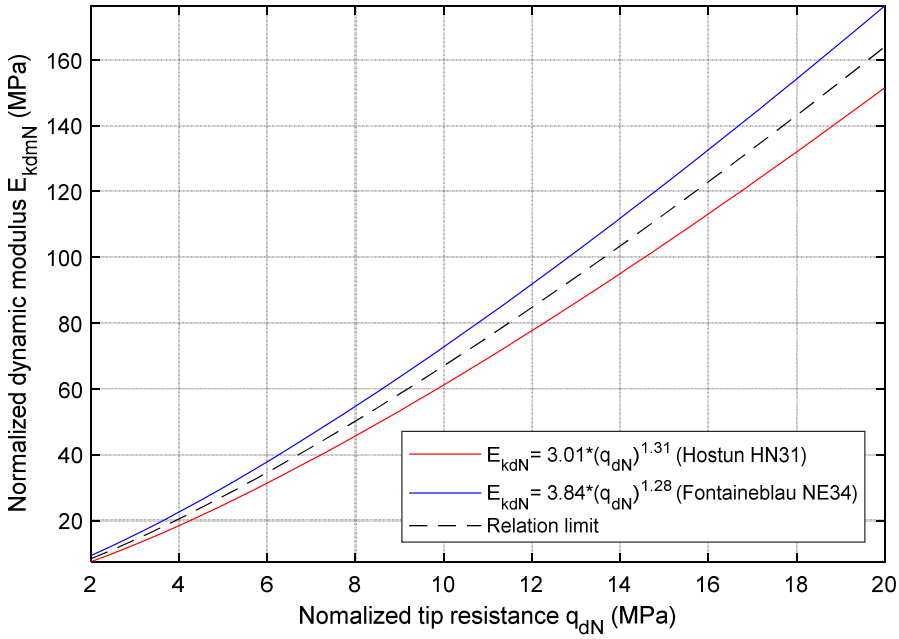

Figure 5-3 – Relationships for Hostun HN31 and Fontainebleau NE34 sands.

Figure 5-3 resents the graph showing the subspaces generated for Hostun HN31 and Fontainebleau NE34 sands. relationships of different soils must be added. This extension of defined soil types will allow a more accurate classification and a more accurate liquefaction potential evaluation.

5.1.2 Soil Type Identification

To identify the type of soil tested, the normalized values of q_d and E_{kd} are obtained. The value of these parameters represents the coordinate within the q_{dN}-E_{kdN} space and its location within one or the other subspace implies that it can be classified within the limits of the corresponding soil type. In the case of the sands tested, the differences are larger when the normalized penetration resistance is higher and more closed when the resistance is low..

If the dynamic penetration test results do not allow an accurate identification, for example if the relation q_{dN}-E_{kdN} is in the limit of the subspaces, the identification of the soil type should be made using a safety criterion, i.e. preferring to classify the soil as the lower resistant to cyclic stresses. This recommendation is based on the fact that low penetration resistances are associated with a low density index and with a higher potential to reach some cyclic failure.

Figure 5-3 represents the first effort in the development of a method for soil type identification by means of dynamic penetration of variable energy test results, applying a parametric analysis that considers at least two characteristic parameters of the soil type sensitive to the state of the soil and boundary conditions, therefore, its differentiating potential is limited to the two sands tested or to soils with similar characteristics. The latter implies that with a larger number of q_{dN}-E_{kdN}, relationships, a larger number of soil types could be defined and more specific subspaces could be established, in a similar way as presented the soil type prediction methods based on the CPT penetrometer charts (Olsen and Koester, 1995; Olsen and Mitchell, 1995; Robertson, 2009, 2010; Robertson and Campanella, 1983; Youd et al., 1997).

5.1.3 Density index determination

The density index is directly related to cyclic resistance, therefore the evaluation of this parameter allows to establish the behavior of a soil when it is cyclically loaded. This is the reason why quantifying this parameter and identifying the type of soil would allow to establish the maximum cyclic resistance by means of databases.

If the identification of the soil type is available by establishing the q_{dN}-E_{kdN} relationships, it is possible to use the - relationship of the corresponding soil type to calculate the density index in saturated condition, using eq. 3-7 and eq. 3-8 for Hostun HN31 and Fontainebleau NE34 sands respectively. Initially these equations are valid for a range of density indices from 0.30 to 0.90 due to the range of densities over which they were developed.

$$I_D = 0.312 \ln(q_{dN}) + 0.130 \quad \textbf{eq. 5-3}$$

$$I_D = 0.294 \ln(q_{dN}) + 0.159 \quad \textbf{eq. 5-4}$$

It has been observed that the penetration resistances for both types of sands are similar (Figure 5-4). The similarity of the q_{dN}-I_D relationships in both types of sands has made it possible to establish a unique relationship for both types of sands (eq. 5-5).

$$I_D = 0.303 \ln(q_{dN}) + 0.145 \quad \textbf{eq. 5-5}$$

$$r^2 = 0.93$$

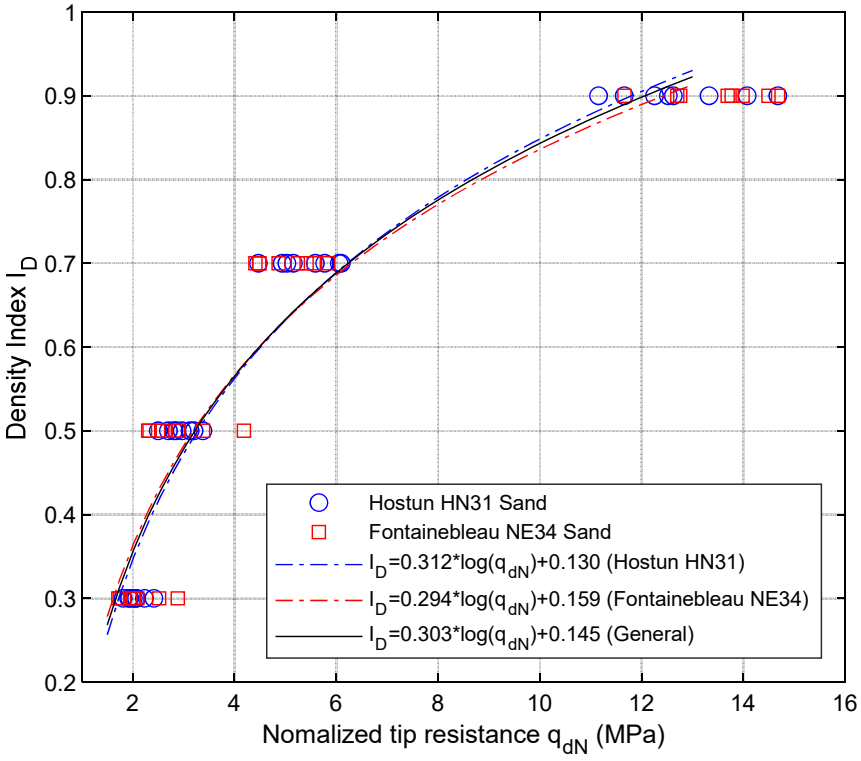

Figure 5-4 – Relationships ($I_D - q_{dN}$) for saturated Hostun HN31 and Fontainebleau NE34 sands.

Although eq. 5-3, eq. 5-4 and eq. 5-5 allow estimating the value of the soil density index, in the case of the soils tested in this research, the use of one or the other is indistinct, since the differences are considered negligible; however, the range of validity of these equations is limited to normalized penetration resistance values between 0.5 and 20 MPa. Values outside these ranges have not been investigated. On the other hand, this methodology is limited to the soils used in this research or to soils with similar characteristics. A generalization may not represent the real density index value of other soil types. Based on this, it is necessary to establish relationships for a major number of soils.

5.2 Dynamic penetration test result database

For the establishment of a liquefaction potential evaluation method based on variable energy dynamic penetration tests, a database has been created with the dynamic signals measured in the variable energy penetration tests and another database with the parameters that allow the characterization of the soil and the calculation of the cyclic resistance ratio.

5.2.1 Dynamic signal database

Obtaining the characteristic parameters of each soil by means of dynamic penetration tests requires the evaluation of dynamic signals. These measurements must be corrected and treated to exclude the effects of the contour not associated with the soil response on the signals.

Concerning the PANDA 3 penetrometer, the correction and processing of dynamic signals has been constantly improved, so the establishment of this database will be by storing the raw measurements, without corrections. For each dynamic impact, the measurement of force, acceleration and displacements obtained by means of the measuring belt is stored.

The objective of storing the raw dynamic signals is the possibility to update the database of parameters for soil characterization taking into account improvements in signal processing or re-evaluation of parameters associated with the dynamic driving of penetrometers.

5.2.2 $q_{dN} - CRR$ parameter data base

For the routine application of the liquefaction potential evaluation method, a database is established for the storage of the minimum parameters required for the calculation of the cyclic resistance CRR as a function of parameters obtained from the dynamic penetration tests. This means that the elements constituting the database allow the construction of the curves relating CRR to q_{dN} or CRR to I_D. Note that it is also possible to establish relationships between CRR and other parameters such as density index and normalized dynamic modulus and average grain size D_{50}.

The values of cyclic resistance CRR are obtained from cyclic laboratory tests so that the CRR - q_{dN} relationship curves represent the limit of liquefaction resistance to cyclic mobility or true liquefaction. This characteristic implies that it is not based on in-situ test results in places where liquefaction phenomena occurred or not but contains accurate cyclic resistance values measured in the laboratory.

Density index values are included because cyclic resistance is highly dependent on this parameter (Benahmed 2001; Idriss and Boulanger 2008; Jradi 2018). On the other hand, it has been possible to establish a dependence of the penetration resistance on the density index, so it is possible to establish relationships between the penetration resistance and the cyclic resistance through density index.

The mean grain size D_{50} are included to obtain the relationships with the CRR because previous research showed the relationship between soil granulometry and cyclic resistance value (Seed and Idriss 1971). Considering this characteristic, D_{50} can be used as a reference parameter to relate soils of different denomination but similar granulometric characteristics. The inclusion of other parameters in the data base is allowed in order to extend the database and improve the accuracy of the analysis.

To establish a cyclic resistance ratio CRR comparable with the cyclic stress ratio CSR, the values must be normalized considering an earthquake of magnitude M_w of 7.5 and at a reference consolidation pressure of 100 kPa (eq. 5-6). Being based on laboratory tests and on obtaining the cyclic resistance curves, the value of the CRR for an earthquake of magnitude M_w de 7.5 can be extracted as the resistance with a function of the occurrence of 15 cycles. To normalize to a reference consolidation pressure, the use of the correction factor k_σ, mentioned by Idriss and Boulanger (2008) (eq. 5-6) is suggested.

$$CRR_{7.5;1atm} = \frac{CRR_{7.5\sigma'_v}}{k_\sigma} \qquad \textbf{eq. 5-6}$$

$$k_\sigma = 1 - C_a \ln\left(\frac{\sigma'_{v0}}{P_a}\right) \qquad \leq 1.1 \qquad \textbf{eq. 5-7}$$

$$C_a = \frac{1}{18.9 - 17.3 I_D} \qquad \leq 0.3 \qquad \textbf{eq. 5-8}$$

Since the database contains values obtained under controlled conditions and there are no static shear stress effects associated with sloping ground surface, no corresponding correction factors are considered.

The initial values of the database are presented in Table 1. This table includes data obtained from tests performed during this research and results of cyclic triaxial tests extracted from the available literature in which the same soils as the ones used in this research, were tested (Benahmed 2001; Jradi 2018).

Table 5-1 – Summary of data for CRR curve generation.

Site	Date	Soil	Soil type	q_{dN} (MPa)	E_{kdN} (MPa)	I_D	$CRR_{7.5}$	σ'_c	K_σ	$CRR_{7.5;1atm}$	D_{50} (mm)	
NAVIER Laboratoty	feb-22	Hostun HN31	1	1.7	5.9	0.30	0.21	200	0.949	0.221	0.35	this research
NAVIER Laboratoty	feb-22	Hostun HN31	1	6.2	33.0	0.70	0.25	200	0.898	0.278	0.35	this research
NAVIER Laboratoty	feb-22	Hostun HN31	1	1.3	4.2	0.20	0.13	200	0.955	0.136	0.35	Benahmed (2001)
NAVIER Laboratoty	feb-22	Hostun HN31	1	0.9	3.0	0.10	0.10	200	0.960	0.104	0.35	Benahmed (2001)
NAVIER Laboratoty	feb-22	Hostun HN31	1	6.2	33.0	0.70	0.25	200	0.898	0.278	0.35	Benahmed (2001)
NAVIER Laboratoty	feb-22	Fontainebleau NE34	2	1.6	8.6	0.30	0.16	200	0.949	0.169	0.21	this research
NAVIER Laboratoty	feb-22	Fontainebleau NE34	2	6.3	35.5	0.70	0.18	200	0.898	0.200	0.21	this research
NAVIER Laboratoty	feb-22	Fontainebleau NE34	2	0.8	6.8	0.10	0.08	200	0.960	0.082	0.21	Jradi (2018)
NAVIER Laboratoty	feb-22	Fontainebleau NE34	2	3.2	14.8	0.50	0.16	400	0.865	0.185	0.21	Jradi (2018)

5.3 Liquefaction potential evaluation method

The liquefaction potential evaluation methodology is based on a multi-parametric approach of geotechnical characterization of the soil and the use of information established in a database that allows obtaining the cyclic resistance of a soil by means of a unique relationship associated to a characteristic parameter of the soil.

The application of this methodology assumes knowledge of the water table position or the possibility of knowing the depth by some auxiliary method. Independently of this, the identification of the water table level can be done through the analysis of the variation of a dynamic parameter associated to the signals measured for each impact, however, the solution to this problem is considered out of the scope of this research.

In general, the method begins with the carrying out of a dynamic penetration test (Figure 5-5), followed by the evaluation of the penetration resistance parameters and the dynamic modulus. Then, based on the soil characteristics obtained in-situ, the effective stresses that will be used in the normalization of the parameters are established. After the normalization, the soil type is identified using the chart in Figure 5-3, which will serve to access a database containing the parameter values necessary for the establishment of the specific CRR-I_D or CRR-q_d relationship. Finally, this relationship being established, it is possible to obtain the normalized cyclic resistance $CRR_{7.5;1atm}$.

Once the normalized cyclic resistance value $CRR_{7.5;1atm}$, has been obtained, evaluation of the liquefaction potential by establishing the safety factor against liquefaction occurrence is possible by comparing with the normalized cyclic shear stress ratio $CSR_{7.5;1atm}$..

The steps associated with the application of the liquefaction potential evaluation method are presented below, applying the results of dynamic penetration tests performed in a K_0 calibration chamber.

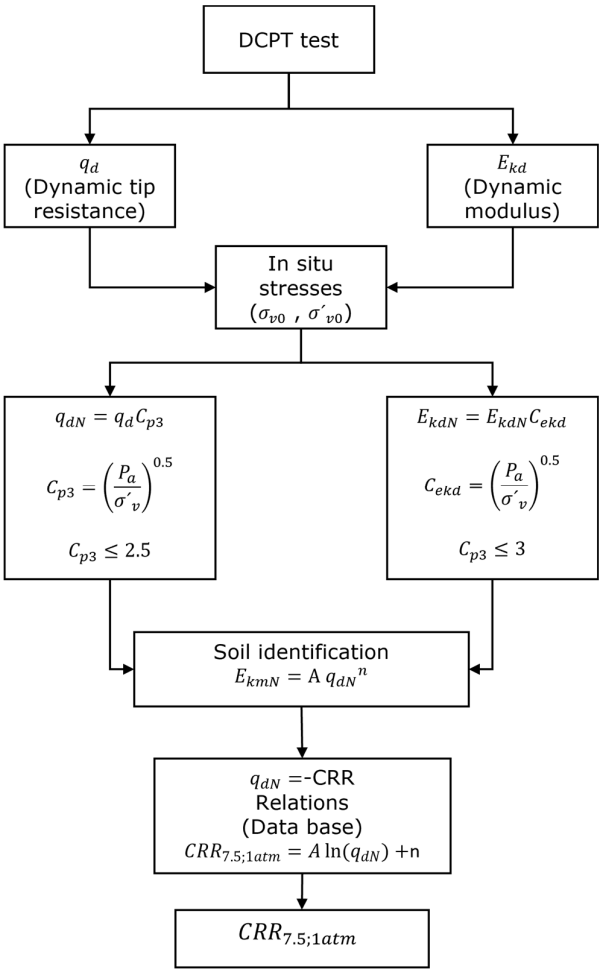

Figure 5-5 – General flow chart of the cyclic resistance ratio evaluation method.

5.3.1 Dynamic penetration test

The DPT test at the site of interest is conducted following the pre-established protocols for the penetration equipment, ensuring the reduction of any factor that may affect the dynamic signals measured by the equipment.

Although the PANDA 3® penetrometer used in this research is driven by variable energy, the nature of the measurements makes them sensitive to boundary and internal soil factors, which can cause atypical signals that result in parameters that are not representative of the soil response. In general, it was observed that the outlier results are minimal and their effect on the analyses performed is negligible, so they can be excluded.

Some of the sources of atypical results in the dynamic signals are related to the presence of rocks that produce resistance magnitudes greater than the trend. Another source of anomalies was observed in the laboratory when eccentric hammer blows occur. This type of blows generates transversal deformations in the rods that make them interact with the contours in the form of normal and non-tangential contact

5.3.2 Establish in situ stress conditions (σ_{v0} and σ'_{v0})

Based on the characteristics of the soil, the stress conditions in the soil must be determined. For this purpose, it is possible to obtain the soil parameters by means of laboratory tests. The identification of these stress states allows the application of the normalization procedure.

5.3.3 Parameter normalization

with the purpose of making the parameters obtained from the dynamic penetration test comparable either with other tests or with other parameters, normalization is applied to the penetration resistance value and the dynamic modulus, considering an effective vertical stress pressure of 100 kPa.

The normalized penetration resistance can be obtained by means of eq. 5-9.

$$q_{dN} = q_{dN} C_{p3} \quad \textbf{eq. 5-9}$$

$$C_{p3} = \left(\frac{P_a}{\sigma'_v}\right)^{0.5} \quad \textbf{eq. 5-10}$$

with:

$$C_{p3} \leq 2.5$$

The normalized mean dynamic modulus can be obtained by eq. 5-11

$$E_{kdN} = E_{kd} C_{p3} \quad \textbf{eq. 5-11}$$

$$C_{kd} = \left(\frac{P_a}{\sigma'_v}\right)^{0.50} \quad \textbf{eq. 5-12}$$

with:

$$C_{kd} \leq 3$$

5.3.4 Soil type identification

To identify the soil type, the relationship between q_{dN} and E_{kdN} is analyzed. The identification can be done by locating the coordinate corresponding to the pair q_{dN} - E_{kmdN} (Figure 5-3) or by establishing the limits numerically using eq. 5-1 and eq. 5-2. Currently only two ratios are available, associated with Hostun HN31 and Fontainebleau NE34 sands, so it is not possible to establish the outer limits of the subspaces for these materials, In addition, it has been observed that at low levels of penetration resistance, the boundary between the two sand is smaller, and the accuracy of identification decreases. If the characterization is not sufficiently accurate to identify the soil type, the recommendation is to select the soil type that is related to a lower cyclic resistance value, establishing a safety criterion.

Figure 5-6 shows the relationships q_{dN} - E_{kdN} for a test conducted on Hostun HN31 sands at a density index of 0.50 and subjected to the range of effective vertical stresses from 10 to 400 kPa. In the graph it can be seen how most of the relationships between the normalized penetration resistance and the normalized dynamic modulus are located in the subspace to the Hostun HN31 sand type. In Figure 5 6 it is also possible to observe two q_{dN} - E_{kdN} ratio values located outside the boundary of the Hostun HN31 sand subspace. This anomaly is related to dynamic pile driving performed on soils subjected to high effective vertical stresses (300 to 400 kPa), where a higher variability of both penetration resistance and dynamic modulus results was observed.

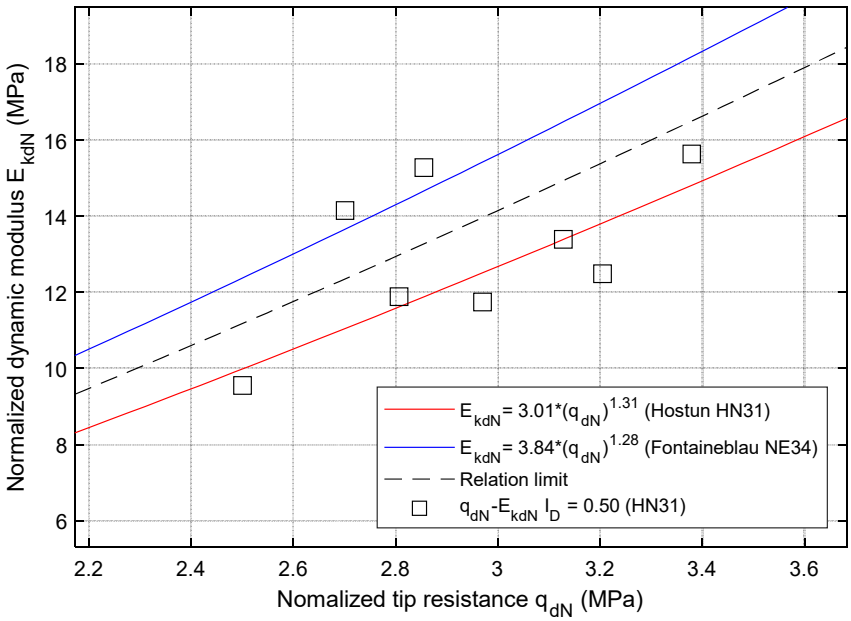

Figure 5-6 – Soil classification in the q_{dN} - E_{kdN} plane.

After identification of the soil it is possible to establish the relationship between the different parameters and the density index by means of the relationship q_{dN} - I_D.

5.3.5 Cyclic resistance $CRR_{7.5;1atm}$ determination

To obtain the value of $CRR_{7.5;1atm}$, the penetration resistance q_{dN} or the density index associated with the identified soil type is used to enter the table until the corresponding value is found. If a penetration resistance and/or density index value is not available in Table 5-1 construction of a relationship $q_{dN}(CRR_{7.5;1atm})$ o I_D $(CRR_{7.5;1atm})$, with the data available for that soil type, is possible. This relationship will allow the generation of a model through the application of nonlinear regression (Figure 5-7 and Figure 5-8).

Figure 5-7a presents the relationship $I_D(CRR_{7.5;1atm})$ and Figure 5-7b presents the relationship between q_{dN} and $CRR_{7.5;1atm}$ for Fontainebleau NE34 sand (eq. 5-13 and eq. 5-14eq. 1-25). These relationships make it possible to calculate the cyclic resistance value for other values

of density index or normalized penetration resistance. Cyclic resistance values were obtained from three different sources (this research, Benahmed (2001) and Jradi (2018)), In all three investigations cyclic triaxial tests were performed for different values of density index. The results show a good fit between both parameters.

$$CRR_{7.5;1atm} = 0.0613\ln(I_D) + 0.2288 \qquad r^2 = 0.97 \qquad \textbf{eq. 5-13}$$

$$CRR_{7.5;1atm} = 0.0546\ln(q_{dN}) + 0.1142 \qquad r^2 = 0.82 \qquad \textbf{eq. 5-14}$$

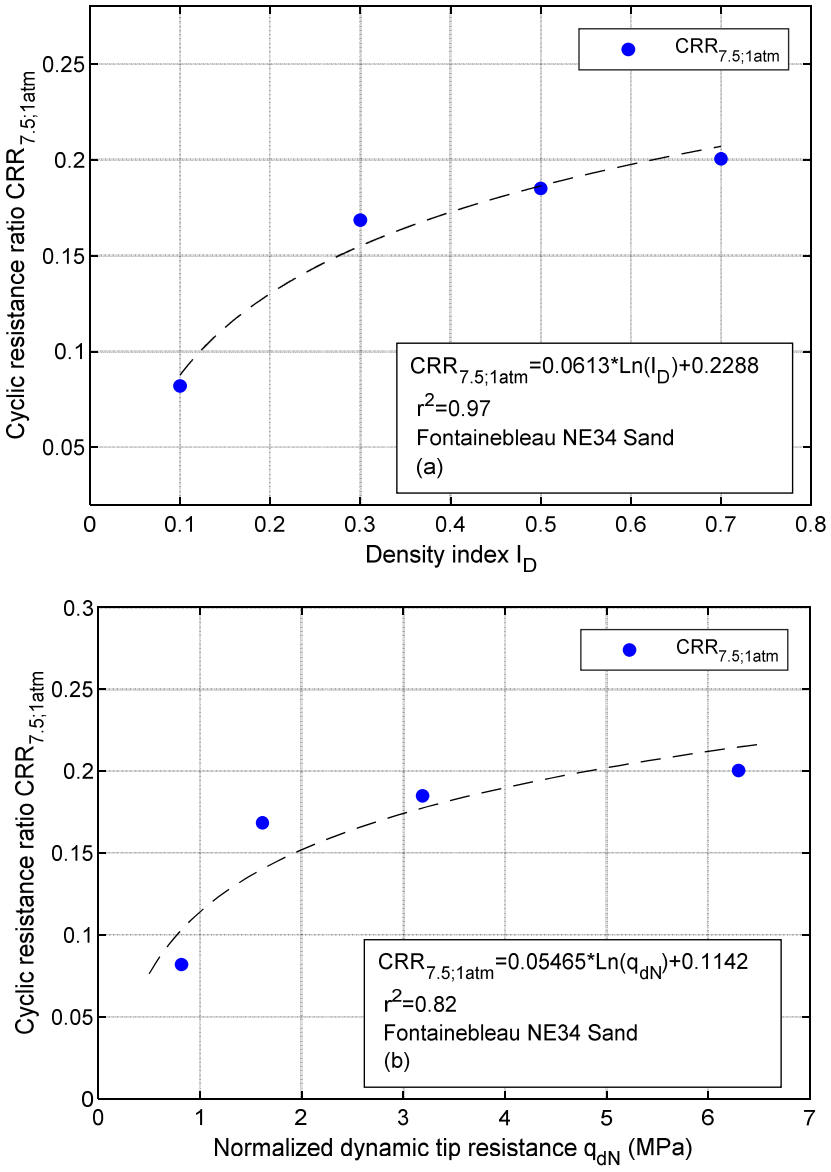

Figure 5-7 – Evaluation of normalized cyclic resistance in Fontainebleau NE34 sands: (a) I_D -$CRR_{7.5;1atm}$ ratio; (b) q_{dN} -$CRR_{7.5;1atm}$ ratio.

Similarly as in the previous case, in Hostun HN31 sands the construction of the relationships I_D -$CRR_{7.5;1atm}$ and q_{dN} -$CRR_{7.5;1atm}$ is also possible (Figure 5-8a and Figure 5-8b respectively).

Cyclic resistance values were obtained from two different sources (this research and Benahmed, (2001)), in both investigations cyclic triaxial tests were performed at different density index levels.

The curves generated by nonlinear regression and relating cyclic resistance and density index or normalized penetration resistance (eq. 5-15 and eq. 5-16) can be improved by integrating new cyclic resistance values into the data base. Considering this, the increase of entries in Table 5-1 will increase the predictive power of the obtained relationship.

$$CRR_{7.5;1atm} = 0.09405\ln(I_D) + 0.3133 \qquad r^2 = 0.96 \qquad \textbf{eq. 5-15}$$

$$CRR_{7.5;1atm} = 0.08492\ln(q_{dN}) + 0.1307 \qquad r^2 = 0.90 \qquad \textbf{eq. 5-16}$$

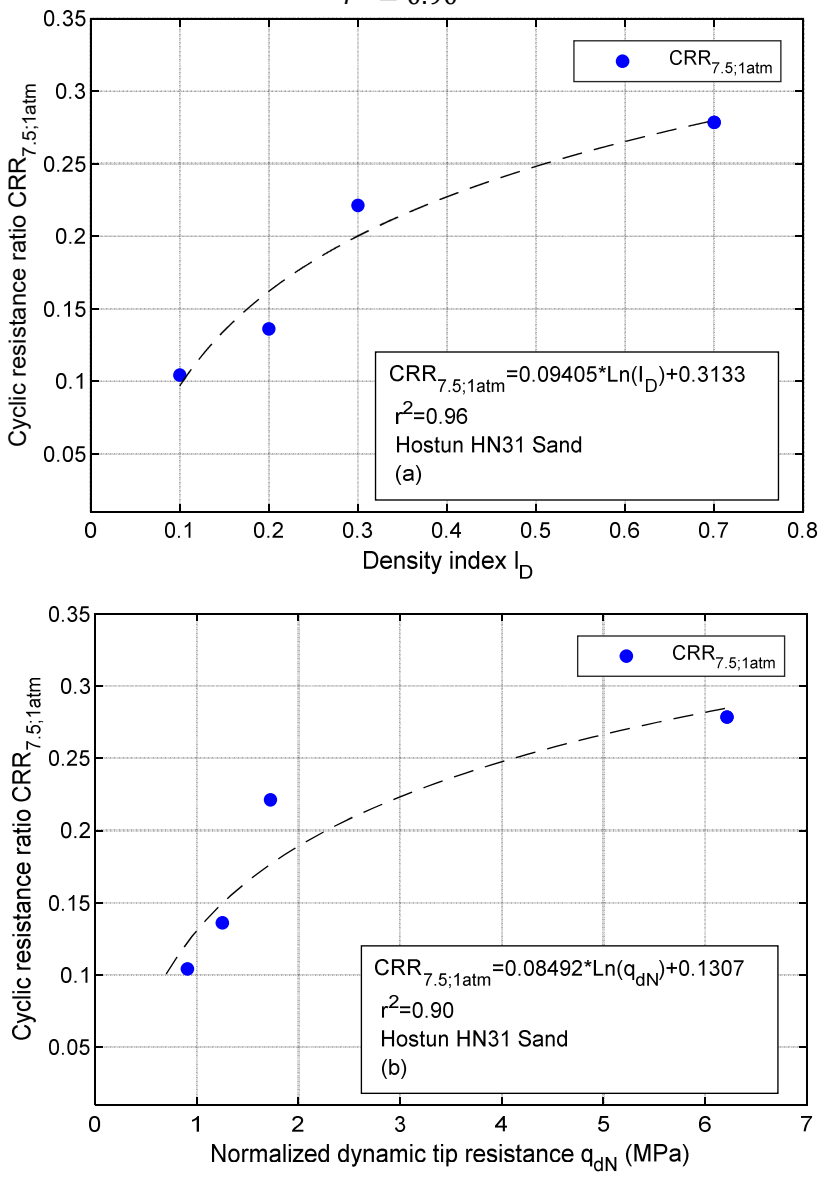

Figure 5-8 – Evaluation of normalized cyclic resistance in Hostun HN31 sand (a) I_D -$CRR_{7.5;1atm}$ ratio; (b) q_{dN} -$CRR_{7.5;1atm}$ ratio.

In cases in which limited data and tests on a specific soil are available, an auxiliary parameter such as the value of the mean grain size D_{50} can be used. The use of this parameter is based on the relationship established between this parameter and cyclic resistance in previous research. (Seed and Idriss, 1971).

5.3.6 Liquefaction Safety Factor calculation

Finally, based on the value of the normalized cyclic resistance $CRR_{7.5;1atm}$, it is possible to calculate the safety factor as the ratio between CRR and CSR. The cyclic stress ratio is calculated by conventional methods available in the literature, which are based on the early work of Seed and Idriss (1971) . The cyclic stress ratio should be normalized to a standard earthquake of magnitude M_w de 7.5 and to an effective consolidation stress in the same way as applied to the cyclic resistance ratio.

The value of the normalized cyclic stress ratio for any reference earthquake and for a given effective overburden stress is calculated as follows:

$$CSR_{7.5;1atm} = \frac{CSR_{M\sigma'_v}}{MSF * k_\sigma} \quad \textbf{eq. 5-17}$$

Finally, the safety factor against liquefaction is obtained as follows:

$$FS_{liq} = \frac{CRR_{7.5;1atm}}{CSR_{7.5;1atm}} \quad \textbf{eq. 5-18}$$

5.4 Example of cyclic resistance evaluation

With the purpose of evaluating the liquefaction potential of a soil deposit it is necessary to establish both the cyclic resistance ratio CRR and the cyclic stress ratio CSR induced on the deposit. As mentioned, the first step is to conduct a variable energy dynamic penetration test at the location where the occurrence of cyclic instability phenomena may occur. In the case of this example, two dynamic penetration tests are used, one carried out on Hostun HN 31 sand (DPT36) and another carried out on Fontainebleau NE34 sands (DPT41) at a density index of 0.70 and with a range of effective vertical stresses from 10 kPa up to 400 kPa in an increasing way.

In the case of the tests used, the effective vertical stress conditions are known and the values of penetration resistance and dynamic modulus are normalized using eq. 5-9 and eq. 5-11 respectively and are presented in Table 5-2.

Table 5-2 – Normalized values of dynamic resistance and dynamic modulus .

	Hostun HN31 (DPT36)		Fontainebleau NE34 (DPT41)	
σ'_v	E_{kdN}	q_{dN}	E_{kdN}	q_{dN}
10	23.613	5.029	27.792	5.841
25	25.604	5.771	23.500	4.867
50	31.294	5.589	35.662	5.416
75	27.600	6.096	40.194	5.557
100	26.947	6.058	37.776	5.244
200	21.188	4.936	39.000	4.409
300	20.812	4.470	31.543	4.483
400	19.505	5.156	33.406	4.489

The normalized parameters are plotted on the q_{dN}-E_{kdN} plane to identify the corresponding soil type (Figure 5-9). The location of the points of the same test shows that they are grouped mostly around a specific subspace, however, in the case of the points associated with Fontainebleau NE34 sands, two points are located outside the subspace. Despite this, 75% of the values are in the range of the Fontainebleau NE34 sands subspace, so the soil can be classified as such.

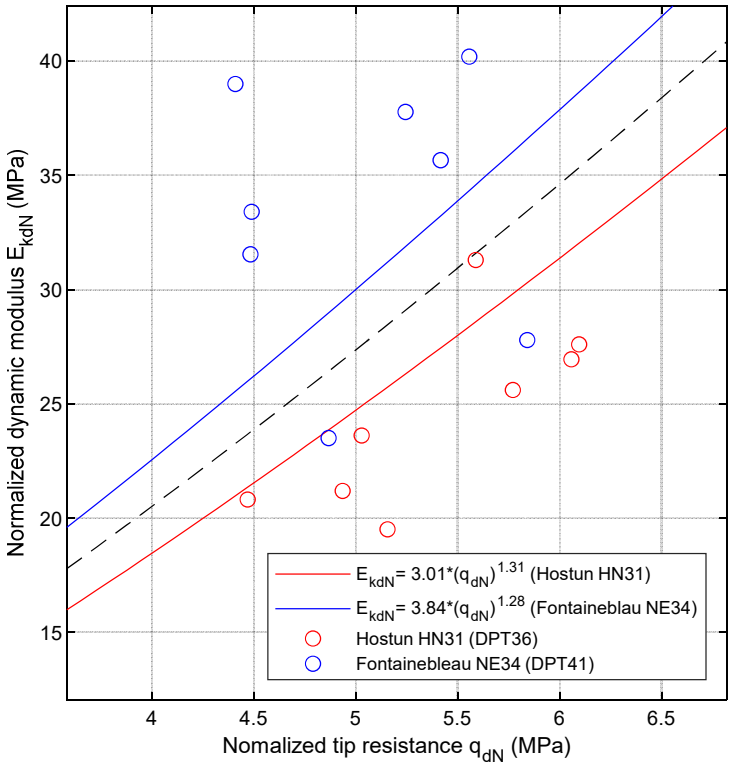

Figure 5-9 – Identification of soil types.

With the identified soils it is possible to use the equations relating the normalized penetration resistance q_{dN} and the value of the normalized cyclic resistance ratio $CRR_{7.5;1atm}$ (eq. 5-14 and eq. 5-16 for Fontainebleau NE34 sand and Hostun HN31 Sand respectively), to calculate the value

of the cyclic resistance in each test. The results of the calculation of the cyclic resistance from the relationships associated to each type of soil are presented in Table 5-3

Table 5-3 – Valores normalizados de resistencia dinámica y modulo dinámico.

	Hostun HN31 (DPT36)	Fontainebleau NE34 (DPT41)
σ'_{v0}	$CRR_{7.5;1atm}$	$CRR_{7.5;1atm}$
10	0.27	0.21
25	0.28	0.20
50	0.28	0.21
75	0.28	0.21
100	0.28	0.20
200	0.27	0.20
300	0.26	0.20
400	0.27	0.20

Figure 5-10 presents the results of the evaluation of the cyclic strength ratio calculated for Hostun HN31 and Fontainebleau NE34 sands at a density index of 0.70. The results show that for the complete range of vertical effective stresses applied on the specimens, the Hostun HN31 sands are more resistant to the occurrence of liquefaction phenomenon.

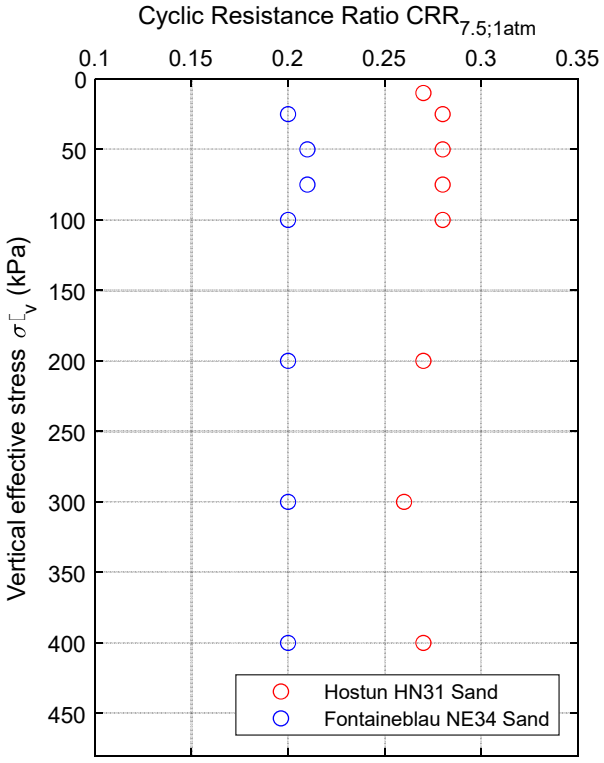

Figure 5-10 – Comparison of normalized cyclic resistance ratios for Hostun HN31 and Fontainebleau NE34 sands.

Figure 5-10 presents the results of the evaluation of the normalized cyclic resistance ratio $CRR_{7.5;1atm}$ for the two sands analyzed in this research. To establish a value of the safety factor against soil liquefaction, it is necessary to compare the value of the cyclic resistances with the magnitude of the normalized cyclic stress ratio $CSR_{7.5;1atm}$ possible to occur at a point of analysis. Although the cyclic strength values are normalized with respect to the effective consolidation stress, they are presented in the form of penetrograms to demonstrate the possibility of presenting the results as a function of test penetration depth to establish a comparison profile between $CRR_{7.5;1atm}$ and $CSR_{7.5;1atm}$.

5.5 Conclusions

A methodological approach has been presented for the evaluation of the liquefaction potential of a sand by means of the results of dynamic penetration tests of variable energy. This method is based on a multiparametric approach that relates at least two parameters obtained from the analysis of the dynamic signals measured with the penetrometer and the characterization by establishing relationships between the dynamic penetration resistance and the dynamic modulus.

The unique relationships between the penetration resistance and the normalized dynamic modulus allow differentiating the two sand types tested by establishing subdomains in a q_{dN}-E_{kdN} plane (Figure 5-3). However, it has been observed that the limits of the subdomains at low penetration resistance are small and the differentiation can be complex. Taking this into account, it has been recommended to apply a safety criterion by adopting the soil type with the lowest cyclic resistance.

The possibility to identify the soil type allows the establishment of more accurate relationships for the evaluation of the density index and cyclic strength of a soil using a database with historical data of cyclic tests performed on known soils, which can be scaled to an increasing number of data and soil types, improving the accuracy of the calculations and allowing the evaluation of the liquefaction potential of soils.

The proposed liquefaction potential evaluation methodology allows the evaluation of the normalized cyclic resistance ratio and from this and the analysis of the normalized cyclic stress ratio obtained from conventional methods it is possible to calculate the value of the liquefaction safety factor

Finally, it should be mentioned that this is the first effort to establish a database with dynamic penetration test cases and cyclic tests. This database is scalable and can be extended to a larger number of parameters such as fines content, which will allow more and more accurate analysis of the soil, especially in the liquefaction potential analysis.

6 GENERAL CONCLUSION AND PERSPECTIVES

Based on the work carried out in this research, conclusions can be formulated and new lines of research associated with this work have been identified that are of interest for further analysis and evaluation of the results of dynamic penetration tests of variable energy and the liquefaction potential evaluation of sands.

The main conclusions and perspectives associated with the results of this research are presented below:

- From the literature review it can be concluded that liquefaction continues to be a problem that requires attention due to the negative externalities associated with its occurrence, especially those associated with safety and human activities.

- There is a need to extend the knowledge and research associated with liquefaction phenomena and cyclic mobility of soil, especially in the area of liquefaction potential evaluation by in-situ testing. Considering this, the evaluation and development of new methodologies associated with new geotechnical equipment is justified..

- The experimental setup necessary to carry out the dynamic penetration tests requires the consideration of a complex procedure that ensures the elimination of perturbations on both the sand specimen and the penetration equipment, since it was observed that the dynamic signals measured in the penetrometer are sensitive to factors not directly related to the soil-cone interaction, such as eccentric shocks or low energy impacts.

- In dynamic penetration tests on saturated specimens, it was necessary to design a modification to the K_0 calibration chamber to generate the necessary sealing conditions for the application of the saturation procedure and application of back pressure. The modification made allowed the reconstitution and saturation of specimens at different levels of density indices in a satisfactory manner; however, the applied procedure must be rigorous to avoid the application of consolidation pressures that generate overconsolidation conditions during the conduct of the dynamic penetration tests.

- The dynamic penetration resistance evaluated by the methodology adopted in this research (maximum resistance in the DCLT curve), is sensitive to the variation of the effective vertical stress applied to the sand specimen, and the sensitivity of the resistance to the variation of the density index of the sand specimens was also

verified. This characteristic allows the use of dynamic penetration resistance as a characteristic parameter of soil state.

- Although the effects of the penetration velocity of a body in a granular material have been proven in the literature (the higher the velocity, the higher the penetration resistance of the body), in the case of the results of variable energy dynamic penetration resistance, it was found that there is no relationship between penetration velocity and magnitude of the maximum shear resistance mobilized by the soil, this implies that in the range of cone displacement velocities (1 to 8 m/s), the dynamic penetration resistance can be considered independent of the effects of velocity during penetration. Moreover, based on the results of the reconstructed signals at the cone-soil interface, it was found that the maximum soil resistance and the maximum penetration velocity are not in phase and the mobilization of the maximum soil shear resistance occurs in a phase of decreasing penetration velocity. This indicates that the generation of the plastic flow phase during penetration is not related to the maximum penetration velocity. This conclusion is valid for the equipment used in this investigation and the velocity ranges mentioned, so further investigation is required.

- The independence of the penetration resistance with respect to the cone penetration velocity opens the possibility of a line of research that allows the establishment of a frame of reference to compare the results of dynamic penetration tests of variable energy and the penetration resistance obtained from penetration tests considered of static type such as the CPT, in line with the results of previous studies in which an equivalence relation between the dynamic penetration resistance q_d and the static penetration resistance is established q_c.

- Regarding the penetration energy, it was concluded that it is not related to the maximum shear resistance mobilized by the soil during the displacement of the cone, but it is related to the penetration work performed. It was observed that the higher the driving energy, the greater the penetration work done by the cone. This observation allows establishing that the dynamic penetration resistance considered as the maximum resistance in the DCLT curve is an intrinsic mechanical parameter of the soil response.

- The occurrence of a plastic flow state associated with a maximum resistance during cone displacement in the soil suggests the occurrence of a dynamic grain interaction

state in which the granular structure is modified and affected. This observation suggests an extension of the present investigation to the micromechanical analysis of the cone-soil interaction during dynamic driving of penetrometers.

- The analysis of the dynamic signals measured in the penetrometer and the decoupling and wave reconstruction methodology applied to these signals to obtain the force and velocity signals at the soil-soil interface, allow a multiparametric evaluation of the soil. These parameters can be extracted from the DCLT curves by analyzing the soil response or through the application of rheological models. It is also possible to parametrically evaluate the soil response through dynamic signals in the frequency spectrum by analyzing parameters such as dynamic modulus. Other parameters can be defined, however, their evaluation requires further investigation.

- The dynamic modulus E_{kd} has been identified as a parameter sensitive to the state of the soil and the applied boundary conditions, therefore it has been chosen to use this parameter to establish relationships that allow soil classification. This parameter has advantages over other parameters because its evaluation is based on the dynamic signals without the application of frequency filters, reducing the uncertainty associated with the application of treatment to the dynamic signals.

- By conducting cyclic triaxial tests, it has been concluded that Hostun HN31 sands exhibit liquefaction properties that make them more resistant than Fontainebleau NE34 sands when subjected to cyclic shear stresses. Considering this, it is possible to conclude that Hostun HN31 sands are less liquefiable than Fontainebleau NE34 sands.

- Regarding the identification of two different types of soil by means of the dynamic penetration test of variable energy, it is concluded that it is not possible to differentiate the two types of sands tested in this research by means of a single parameter; however, it is possible to establish a methodology based on a multi-parametric approach that relates two or more geotechnical parameters to identify soils of similar characteristics

- A liquefaction potential evaluation method has been established based on variable energy dynamic penetration tests and database records. This method allows the evaluation of the cyclic resistance ratio of a sand, but its initial applicability is limited because it was developed on the basis of two different types of sands, however, the

addition of new types of soils to the database would allow more applicability and increasingly accurate analysis.

- The liquefaction potential evaluation method makes it possible to evaluate the cyclic strength of the two types of sands tested in this study (Hostun HN31 and Fontainebleau NE34) and to establish a difference in the cyclic resistance ratio between the two soils, this implies that it is possible to obtain different liquefaction safety factor values associated with the state and type of soil.

- Finally, it is concluded that the use of a variable energy dynamic penetrometer in the liquefaction potential evaluation of sands is possible; However, the accuracy of the results is based both on the evaluation of the penetrometer dynamic signals and on the robustness of the database with results from dynamic penetration test and cyclic laboratory tests.

7 BIBLIOGRAPHY

AFNOR. 2000a. *NF P94-059 Soils : Investigation and Testing - Determination of Minimal and Maximal Density of Cohesionless Soils*. Association française de Normalisation.

AFNOR. 2000b. *XP P 94-105 Contrôle de La Qualité Du Compactage*. Francia.

Alam, Md Jahangir, Abul Kalam Azad, and Ziaur Rahman. 2008. "Prediction of Liquefaction Potential of Dredge Fill Sand by DCP and Dynamic Probing." Pp. 413–18 in *Seismic Engineering Conference Commemorating the 1908 Messina and Reggio Calabria Earthquake*. Vol. 1020.

Ambraseys, N. N. 1988. "ENGINEERING SEISMOLOGY." *EARTHQUAKE ENGINEERING AND STRUCTURAL DYNAMICS* 17(1):1–105.

Andrus, R. 1994. "In Situ Characterization of Gravelly Soils That Liquefied in the 1983 Borah Peak Earthquake."

Andrus, Ronald D., and Kenneth H. Stokoe. 1998. "Liquefaction Resistance Based on Shear Wave Velocity." in *NCEER Workshop on Evaluation of Liquefaction Resistance of Soils*. Biffalo, New York, United States.

Andrus, Ronald, and Kenneth Stokoe. 2000. "Liquefaction Resistance of Soils from Shear-Wave Velocity." *Journal of Geotechnical and Geoenvironmental Engineering* 126(11):1015–25. doi: 10.1061/(ASCE)1090-0241(2000)126:11(1015).

Anh Tran, Quoc, Miguel Angel Benz Navarrete, Pierre Breul, Bastien Chevalier, Philippe Moustan, Quoc Anh TRAN, and Miguel Angel BENZ NAVARRETE. 2019. "Soil Dynamic Stiffness and Wave Velocity Measurement through Dynamic Cone Penetrometer and Wave Analysis." Pp. 401–8 in *XVI Congreso Panamericano de Mecánica de Suelos e Ingeniería Geotécnica*.

Anh TRAN, Quoc, Miguel Angel BENZ NAVARRETE, and Marta Guardeño Garcia. 2018. "Détermination Du Module Dynamique À Partir Du Panda3® Et L'Analyse Spectrale Des Signaux Determination of Soil'S Dynamic Stiffness Trough Panda 3® and Spectrum Signal Processing." Pp. 1–9 in *Journées Nationales de Géotechnique et de Géologie de l'Ingénieur*.

Aoki, Nelson, and Jose Carlos Angelo Cintra. 2000. "The Application of Energy Conservation Hamilton's Principle to the Determination of Energy Efficiency in SPT Test." Pp. 457–60 in *6th International Conference on the Application of Stress-Wave Theory to Piles*, edited by S. Niyama and J. Bein. Sao Paulo, Brazil.

Arango, Ignacio. 1996. "MAGNITUDE SCALING FACTORS FOR SOIL LIQUEFACTION EVALUATIONS." *Journal of Geotechnical Engineering* 122(11):929–36.

Arbaoui, Hakim, Roland Gourvès, Philippe Bressolette, and Laurent Bodé. 2006. "Mesure de La Déformabilité Des Sols in Situ à l'aide d'un Essai de Chargement Statique d'une Pointe Pénétrométrique." *Canadian Geotechnical Journal* 43(4):355–69. doi: 10.1139/T06-013.

Aussedat, Georges. 1970. "Sollicitations Rapides Des Sols." Grenoble.

Azzedine, Oularbi. 1989. "Applicabilité Des Mesures Dynamiques Au Calcul Des Pieux." Nantes, France.

Bazhenov, V. G., A. M. Bragov, V. L. Kotov, and A. v Kochetkov. 2003. “An Investigation of the Impact and Penetration of Solids of Revolution into Soft Earth.” *Journal of Applied Mathematics and Mechanics* 67(4):611–20.

Benahmed, Nadia. 2001. “Comportement Mécanique d’un Sable Sous Cisaillement Monotone et Cyclique : Application Aux Phénomènes de Liquéfaction et de Mobilité y Cylique.” PhD. These, Ecole Nationale des Pont et Chaussees.

Benz, Miguel. 2009a. “Mesures Dynamiques Lors Du Battage Du Penetrometre Panda 2.” Université Blaise Pascal Clermont II.

Benz, Miguel. 2009b. *Méthodologie d’évaluation d’ouverture et Fermeture Des Pistes En Herbe d’aérodromes d’ADP à l’aide d’un Pénétromètre Dynamique Ultraléger Sur Mesure*. Riom.

Benz Navarrete, M. A., E. J. Escobar Valencia, R. Gourvès, Y. Haddani, P. Breul, and C. Bacconnet. 2013. “Mesures Dynamiques Lors Du Battage Pénétromètrique – Détermination de La Courbe Charge-Enfoncement Dynamique En Pointe.” Pp. 499–502 in *Proceedings of the 18th International Conférence on Soil Mechanics and Geotechnical Engineering*. Paris, France.

Benz Navarrete, Miguel Angel, Pierre Breul, and Roland Gourvès. 2022. “Application of Wave Equation Theory to Improve Dynamic Cone Penetration Test for Shallow Soil Characterisation.” *Journal of Rock Mechanics and Geotechnical Engineering* 14(1):289–302. doi: 10.1016/j.jrmge.2021.07.004.

Boguslavskii, Yu., S. Drabkin, I. Juran, and A. Salman. 1996. “Theory and Practice of Projectile’s Penetration in Soils.” *Journal of Geotechnical Engineering* 122(10):806–12. doi: 10.1061/(ASCE)0733-9410(1996)122:10(806).

Boulanger, Ross W. 2003. “High Overburden Stress Effects in Liquefaction Analyses.” *Journal of Geotechnical and Geoenvironmental Engineering* 129(12):1071–82. doi: 10.1061/(ASCE)1090-0241(2003)129:12(1071).

Boulanger, Ross W. 2004. “High Overburden Stress Effects in Liquefaction Analyses.” *Journal of Geotechnical and Geoenvironmental Engineering* 129(12):1071–82.

Boulanger, Ross W., and I. M. Idriss. 2004. “State Normalization of Penetration Resistance and the Effect of Overburden Stress on Liquefaction Resistance.” *11th ICSDEE and 3rd ICEGE Conference, University of California, Berkeley, January* (3):484–91.

Boulanger, Ross W., and I. M. Idriss. 2007. “Evaluation of Cyclic Softening in Silts and Clays.” *Journal of Geotechnical and Geoenvironmental Engineering* 133(6):641–52. doi: 10.1061/(ASCE)1090-0241(2007)133:6(641).

Boulanger, Ross W., and Izzat M. Idriss. 2014. *CPT and SPT Based Liquefaction Triggering*. California.

Boulanger, Ross W., Daniel W. Wilson, and I. M. Idriss. 2012. *Examination and Re-Evaluation of SPT-Based Liquefaction Triggering Case Histories SUPPLEMENT FOR THE PAPER : EXAMINATION AND RE-EVALAUTION OF SPT-BASED LIQUEFACTION TRIGGERING CASE HISTORIES*. doi: 10.1061/(ASCE)GT.1943-5606.0000668.

Canou, J., N. Benahmed, J. C. Dupla, and V. de Gennaro. 2002. “Liquefaction Instabilities and Cyclic Mobility Phenomena in Sands.” *Revue Française de Géotechnique* (98):29–46.

Canou, Jean. 1989. “Contribution à l’étude et à l’évaluation Des Propriétés de Liquéfaction d’un Sable.” PhD, Ecole des Ponts ParisTech, Paris.

Carlsson, J., K. G. Sundin, and B. Lundberg. 1990. “A Method for Determination of In-Hole Dynamic Force-Penetration Data from Two-Point Strain Measurement on a Percussive Drill Rod.” *International Journal of Rock Mechanics and Mining Sciences And* 27(6):553–58. doi: 10.1016/0148-9062(90)91006-S.

Casagrande, Arthur. 1975. “Liquefaction and Cyclic Deformation of Sands a Critical Review.” Pp. 1–55 in *Fifth Panamerican Conference on Soil Mechanics and Foundation Engineering*. Buenos Aires, Argentina.

Casem, D. T., W. Fourney, and P. Chang. 2003. “Wave Separation in Viscoelastic Pressure Bars Using Single- Point Measurements of Strain and Velocity.” *Polymer Testing* 22:155–64.

Castro, Gonzalo. 1969. “Harvard Soil Mechanics Series N° 81, Liquefaction of Sands.”

Castro, Gonzalo. 1975. “Liquefaction and Cyclic Mobility of SatCastro, G. (1975). Liquefaction and Cyclic Mobility of Saturated Sands. ” *Journal of the Geotechnical Engineering Division* 101(6):551–69.

Castro, G., and S. Poulos. 1977. “Factors Affecting Liquefaction and Cyclic Mobility.” *Journal of Geotechnical Engineering, ASCE* 103(June):501–16.

Cetin, K. Onder, and Raymond B. Seed. 2004. “Nonlinear Shear Mass Participation Factor (Rd) for Cyclic Shear Stress Ratio Evaluation.” *Soil Dynamics and Earthquake Engineering* 24:103–13. doi: 10.1016/j.soildyn.2003.10.008.

Cetin, K. Onder, Raymond B. Seed, Armen der Kiureghian, Kohji Tokimatsu, Leslie F. Harder, Robert E. Kayen, and Robert E. S. Moss. 2004. “Standard Penetration Test-Based Probabilistic and Deterministic Assessment of Seismic Soil Liquefaction Potential.” *Journal of Geotechnical and Geoenvironmental Engineering* 130(12):1314–40. doi: 10.1061/(ASCE)1090-0241(2004)130:12(1314).

Chaigneau, L. 2001. “Caracterisation Des Mileux Granulaires de Surface al’aide d’un Penetrometre.”

Clough, Ray W., and Joseph Penzien. 2003. *Dynamics of Structures*. Third edit. Berkeley, California, U.S.A.

CSN. 2014. “Centro Sismológico Nacional.” Retrieved May 18, 2022 (http://evtdb.csn.uchile.cl/event/6c5752b76db0f46280949a79863b4d67).

Dupla, Jean-claude. 1995. “Application de La Sollicitation d’expansion de Cavité Cylindrique à l’évaluation Des Caractéristiques de Liquéfaction d’un Sable.”

Escobar, Esteban, Miguel Angel Benz, Younes Haddani, Francisco Lamas-, Nicolas Calon, Sofia Costa D. Aguiar, and Pôle Innovation. 2014. “Reconnaissance Dynamique Des Sites Ferroviaires a l’aide Du Penetrometre PANDA 3®.” in *Journées nationales de géotechnique et de géologie de l’ingénieur*. Beauvais.

Escobar Valencia, E. J., M. A. Benz Navarrete, R. Gourvès, P. Breul, and B. Chevalier. 2016. “In-Situ Determination of Soil Deformation Modulus and the Wave Velocity Parameters Using the Panda 3®.” Pp. 279–84 in *5th Geotechnical and Geophysical Site*

Characterisation, ISC5, edited by Acosta-Martínez and Kelly. Sydney, Australia: Australian Geomechanics Society.

Espinace A, Raul, Gabriel Villavicencio A, Juan Palma, P. Breul, C. Bacconnet, Blaise Pascal, M. A. Benz, and R. Gourvès. 2013. "Pénétromètre Panda ®Stability of Chilean's Tailings Dams with the Panda® Penetrometer. Experiences of the Last 10th." Pp. 519–22 in *18th International Conference on Soil Mechanics and Geotechnical Engineering*.

Gansonré, Y., P. Breul, C. Bacconnet, M. Benz, and R. Gourvès. 2019. "Prediction of In-Situ Dry Unit Weight Considering Chamber Boundary Effects on Lateritic Soils Using Panda® Penetrometer." *International Journal of Geotechnical Engineering*. doi: 10.1080/19386362.2019.1698211.

GEONET. 2022. "GeoNet: M 6.2 Christchurch Tue, Feb 22 2011." Retrieved May 17, 2022 (https://www.geonet.org.nz/earthquake/3468575).

Goble, G., G. Likins, and F. Rausche. 1975. *Bearing Capacity of Piles from Dynamic Measurements*. Columbus, Ohio.

Golesorkhi, Ramin. 1989. "Factors Influencing the Computational Determination of Earthquake-Induced Shear Stresses in Sandy Soils."

Gourvès, Roland. 1991. *Le PANDA : Pénétromètre Dynamique Léger à Énergie Variable Pour La Reconnaissance Des Sols*. Clermont-Ferrand.

Graff, Karl. 1991. *Wave Motion in Elastic Solids*. edited by D. Publications. Bew York.

Haddani, Y. 2001. "Développement de La Géoendoscopie Aux Sols Saturés et Au Diagnostic d'ouvrages Enterrés."

Haddani, Y. 2004. "Caractérisation et Classification Des Milieux Granulaires Par Géoendoscopie." Clermont Ferrand 2, Clermont Ferrand.

Haddani, Younes, Pierre Breul, Gilles Saussine, Miguel Angel Benz, Fabien Ranvier, and Roland Gourvès. 2016. "Trackbed Mechanical and Physical Characterization Using PANDA ® / Geoendoscopy Coupling." Pp. 1201–9 in *International Conference on Transportation Geotechnics (ICTG 2016)*. Vol. 143. Elsevier B.V.

Harder, Leslie. 1993. "Application of the Becker Penetration Test for Evaluating the Liquefaction Potencial of Gravelly Soils." Pp. 129–39 in *NCEER Workshop on evaluation of liquefaction resistance of soils*, edited by T. Youd and I. Idriss. Salt Lake City, Utah: National Center for Earthquake Engineering Research.

Holtz, Robert, and William Kovacs. 1981. *An Introduction to Geotechnical Engineering*. edited by P. Hall. New Jersey.

Idriss, I. M., and R. W. Boulanger. 2003. " Relating K_α and K_σ to SPT Blow Count and to CPT Tip Resistance for Use in Evaluating Liquefaction Potential. Proceedings of the 20th Annual Conference of Association of State Dam Safety Officials, ASDSO, Lexington, 8-10 September 2003, 7-10. - References - Scientific Research Publishing." Pp. 7–10 in *Proceedings of the 20th Annual Conference of Association of State Dam Safety Officials, ASDSO*. Lexington.

Idriss, I. M., and R. W. Boulanger. 2004. “Semi-Empirical Procedures for Evaluating Liquefaction Potential During Earthquakes.” Pp. 32–56 in *3rd International Conference on Earthquake Geotechnical Engineering*.

Idriss, I. M., and R. W. Boulanger. 2006. “Semi-Empirical Procedures for Evaluating Liquefaction Potential during Earthquakes.” *Soil Dynamics and Earthquake Engineering* 26(2-4 SPEC. ISS.):115–30. doi: 10.1016/j.soildyn.2004.11.023.

Idriss, I. M., and R. W. Boulanger. 2008. *Soil Liquefaction during Earthquakes*. Vol. 1. Oakland, California, USA.

Idriss, I. M., and R. W. Boulanger. 2010. *SPT-Based Liquefaction Triggering Procedures, UCD/CGM-10-02*. Davis, California. doi: UCD/CGM-10/02.

Idriss, Izzat. 1999. “An Update to the Seed-Idriss Simplified Procedure for Evaluating Liquefaction Potential.” in *Proceedings of TRB Workshop on New Approaches to Liquefaction*. Washington DC: Federal Highway Administration.

Ishihara, Kenji. 1977. “Simple Method of Analysis for Liquefaction of Sand Deposits during Earthquakes.” *Soil and Foundations* 17(3):1–17. doi: https://doi.org/10.3208/sandf1972.17.3_1.

Ishihara, Kenji. 1985. “Stability of Natural Deposits during Earthquakes.” Pp. 321–76 in *11th International Conference on Soil Mechanics and Foundation Engineering*. San Francisco.

Ishihara, Kenji, and Yasuyuki Koga. 1981. “Case Studies of Liquefaction in the 1964 Niigata Earthquake.” *Soils and Foundations* 21(3):35–52. doi: 10.3208/SANDF1972.21.3_35.

Ishihara, Kenji, Fumio Tatsuoka, and Susumu Yasuda. 1975. “Undrained Deformation and Liquefaction of Sand under Cyclic Stresses.” *Soil and Foundations* 15(1):29–44. doi: https://doi.org/10.3208/sandf1972.15.29.

Iskander, Magued, Stephan Bless, and Mehdi Omidvar. 2015. *Rapid Penetration into Granular Media : Visualizing the Fundamental Physics of Rapid Earth Penetration.*

ISO 22476-2. n.d. *ISO 22476-2:2005 - Geotechnical Investigation and Testing — Field Testing — Part 2: Dynamic Probing*.

Iwasaki, Toshio, Fumio Tatsuoka, Ken-ichi Tokida, and Susumu Yasuda. 1978. “A Practical Method for Assessing Soil Liquefaction Potential Based on Case Studies at Various Sites in Japan.” Pp. 885–96 in *Proceedings of the 2nd International Conference on Microzonation*. San Francisco, California.

Jara, Felipe. 2013. “Etude d’une Nouvelle Méthodologie Pour La Détermination Du Potentiel de Liquéfaction Des Sols à l’aide Du Panda 3® et de La Géoendoscopie: Cas Des «tranques de Relave» Au Chili.” Polytech’Clermont Ferrand.

Jradi, Layal. 2018. “Study of the Influence of Fine Particles on the Properties of Liquefaction of Sands Study of the Influence of Fine Particles on the Properties of Liquefaction of Sands Draft Thesis.”

Juang, C. Hsein, Tao Jiang, and Ronald D. Andrus. 2002. “Assessing Probability-Based Methods for Liquefaction Potential Evaluation.” *Journal of Geotechnical and Geoenvironmental Engineering* 128(7):580–89. doi: 10.1061/(ASCE)1090-0241(2002)128:7(580).

Jung, Byungbo, Youngjin Park, and Youn-sik Park. 2006. “Longitudinal Acceleration Wave Decomposition in Time Domain with Single Point Axial Strain and Acceleration Measurements.” in *The 8th International Conference on Motion and Vibration Control*.

Kang, Xin, Zhao Xia, Renpeng Chen, Louis Ge, and Xiaoming Liu. 2018. “The Critical State and Steady State of Sand: A Literature Review.” *Marine Georesources and Geotechnology* 0(0):1–14. doi: 10.1080/1064119X.2018.1534294.

Karimpour, Hamid, and Poul v Lade. 2010. “Time Effects Relate to Crushing in Sand.” *Journal of Geotech-Nical and Geoenvironmental Engineering* 136(9):1209–19. doi: 10.1061/ASCEGT.1943-5606.0000335.

Karlsson, L. G., B. Lundberg, and K. G. Sundin. 1989. “Experimental Study of a Percussive Process for Rock Fragmentation.” *International Journal of Rock Mechanics and Mining Sciences And* 26(1):45–50. doi: 10.1016/0148-9062(89)90524-X.

Kayen, R., J. Mitchell, R. Seed, A. Lodge, S. Nishio, and R. Coutinho. 1992. “Evaluation of SPT-, CPT-, and Shear Wave-Based Methods for Liquefaction Potential Assessment Using Loma Prieta Data.” Pp. 177–204 in *Proceedings from the fourth Japan-U.S. workshop on earthquake resistant design of lifeline facilities and countermeasures for soil liquefaction*.

Kayen, R., and K. Mitchell. 1997. “Assessment of liquefaction potential during earthquakes by arias intensity.” *Journal of Geotechnical and Geoenvironmental Engineering* 123(12):1162–74.

Lambe, W., and R. Whitman. 1969. *Soil Mechanics*. edited by John Wiley & Son.

Langton, DD. 1999. “The Panda Lightweight Penetrometer for Soil Investigation and Monitoring Material Compaction.” *Ground Engineering* (September).

Latini, Chiara, and Varvara Zania. 2016. *Triaxial Tests in Fontainebleau Sand*. Lyngby, Denmark.

Lee, Kenneth L., Bolton Seed, and P. Dunlop. 1969. “Effect of Transient Loading on the Strength of Sand.” in *7th International Conference on Soil Mechanics and Foundation Engineering (Mexico)*.

Lepetit, Luc. 2002. “Etude d’une Méthode de Diagnostic de Digues Avec Prise En Compte Du Risque de Liquéfaction.” Université Blaise Pascal.

Le, van Cuong. 2014. “Étude Sur Modèle Physique Du Renforcement Des Sols Par Colonnes En « Soil-Mix » : Application Aux Plates-Formes Ferroviaires.” PhD, Université Paris - Est, Champs sur Marne.

Liao, S. S. C., and R. v Whitman. 1986. *A Catalog of Liquefaction and Non-Liquefaction Occurrences During Earthquakes*. Department of Civil Engineering, MIT.

Li, Zheng, Sandra Escof, and Panagiotis Kotronis. 2013. “Using Centrifuge Tests Data to Identify the Dynamic Soil Properties : Application to Fontainebleau Sand.” *Soil Dynamics and Earthquake Engineering* 52:77–87.

Lodygowski, T., and A. Rusinek. 2014. *Constitutive Relations under Impact Loadings*. Vol. 552. edited by T. Łodygowski and Alexis Rusinek. Vienna: Springer Vienna.

López Retamales, Sebastian, Jean Canou, Jean Claude Dupla, and Miguel Benz Navarrete. 2020. "Penetrometre dynamique et indice de densite des sables. Application a l'evaluation du risque de liquefaction des massifs sableux." in *Journées Nationales de Géotechnique et de Géologie de l'Ingénieur 2020*. Lyon, Francia.

López, S, Jean Canou, Jean-Claude Dupla, and Miguel Benz. 2021. "Development of a Liquefaction Risk Assessment Methodology Using an Instrumented Lightweight Dynamic Penetrometer: Calibration Chamber Tests." in *6th International Conference on Geotechnical and Geophysical Site.*

López, Sebastián, and Miguel Benz. 2019. "Comparación de Los Ensayos de Penetrómetro de Cono Dinámico de Energía Variable PANDA® Ensayo de Placa de Carga Estática y Dinámica." Pp. 1562–71 in *XVI Pan-American Conference on Soil Mechanics and Geotechnical Engineering*. Cancún, México.

López, Sebastián, Miguel Benz, and Philippe Moustan. 2019. "Comparación de Los Ensayos de Penetración de Cono Dinámico (DCP) y Penetrómetro de Cono Dinámico de Energía Variable PANDA®." *XVI Pan-American Conference on Soil Mechanics and Geotechnical Engineering*. doi: 10.3233/STAL190206.

López, Sebastián, Miguel Benz, Jose Navarro, and David Zamora. 2018. "Control Geotécnico de Obras Viales Mediante Penetrómetro Dinámico Ligero de Energía Variable PANDA 2." *X Congreso Chileno de Geotecnia*.

López, Sebastián, Jean-Claude Dupla, Jean Canou, and Miguel Benz. 2021. "Evaluation of Soil Liquefaction Resistance with Variable Energy Dynamic Penetration Test, PANDA®: State of the Art." in *6th International Conference on Geotechnical and Geophysical Site*.

Lukiantchuki, Juliana Azoia. 2012. "Interpretação de Resultados Do Ensaio Spt Com Base Em Instrumentação Dinâmica."

Lundberg, B., and A. Henchoz. 1977. "Analysis of Elastic Waves from Two-Point Strain Measurement." *Experimental Mechanics* 17(6):213–18. doi: 10.1007/bf02324491.

Lunne, Tom, Peter K. Robertson, and John J. M. Powell. 1997. *Cone Penetration Testing in Geotechnical Practice*.

Luong, P. 1978. "Etat Caracteristique Du Sol." *C.R.Ac.Sc., Paris, t. 287* 305–7.

Luong, P. 1980. "Phénomènes Cycliques Dans Les Sols Pulvérulents Par." *Revue Française de Géotechnique* (10):39–53.

Manassero, M. 1994. "Hydraulic Conductivity Assessment of Slurry Wall Using Piezocone Test." *Journal of Geotechnical Engineering* 120(10):1725–46.

Meunier, Jacques. 1974. "Contribution à l'étude Des Ondes et Des Ondes de Choc Dans Les Sols / Jacques Meunier - Beluga - Université Grenoble Alpes." Grenoble.

Nishida, Yoshichika, Hideo Sekiguchi, and Tatsunori Matsumoto. 1986. "Stress Wave Monitoring for a Friction Pile During Driving: A New Analysis Procedure." *Soil and Foundations* 26(4):111–26. doi: https://doi.org/10.3208/sandf1972.26.4_111.

Odebrecht, Edgar. 2003. "Medidas de Energia No Ensaio SPT."

Odebrecht, Edgar, Fernando Schnaid, Marcelo Maia Rocha, and George de Paula Bernardes. 2005. “Energy Efficiency for Standard Penetration Tests.” *Journal of Geotechnical and Geoenvironmental Engineering* 131(10):1252–63. doi: 10.1061/(asce)1090-0241(2005)131:10(1252).

Olsen, R. 1988. “Using the CPT for Dynamic Response Characterization.” Pp. 111–17 in *Proceedings of the Earthquake Engineering and Soil Dynamics II Conference*. New York: American Society of Civil Engineers.

Olsen, Richard, and Joseph Koester. 1995. “Prediction of Liquefaction Resistance the CPT.” Pp. 251–56 in *Proceedings of the International Symposium on Cone Penetration Testing, CPT’95*.

Olsen, R., and P. Malone. 1988. “Site Characterization Using the Cone Penetrometer Test.” Pp. 887–93 in *First International Symposium on Penetration Testing, ISOPT-1*. Orlando.

Olsen, R., and J. Mitchell. 1995. “CPT Stress Normalization and Prediction of Soil Classification.” Pp. 257–62 in *Proceedings international symposium on cone penetration testing*.

Omidvar, Mehdi, Magued Iskander, and Stephan Bless. 2014. “Response of Granular Media to Rapid Penetration.” *International Journal of Impact Engineering* 66:60–82. doi: 10.1016/J.IJIMPENG.2013.12.004.

OULARBI, Azzedine, and Daniel LEVACHER. 2009. “Réponse Dynamique de La Pointe d’un Modèle de Pieu Dans Un Sol Granulaire.” Pp. 49–52 in *Coastal and Maritime Mediterranean Conference*. Centre Francais du Littoral.

Paquet, J. 1968. “Etude Vibratoire Des Pieux En Béton Réponse Harmonique et Impulsionnelle Application Au Contrôle.” *Annales ITBTP* 789–803.

Pecker, Alain. 2007. *Advanced Earthquake Engineering Analysis*. Vol. 494. edited by A. Pecker. Springer-Verlag Wien.

Robertson, Peter, and Richard Campanella. 1985. “Liquefaction Potentia of Sands Using the CPT.” *Journal of Geotechnical Engineering* 111(3):384–403.

Robertson, P., and Catherine Fear. 1995. “Liquefaction of Sands and Its.” Pp. 1253–89 in *IS Tokyo ‘95, Proceedings of the 1st International Conference on Earthquake Geotechnical Engineering*.

Robertson, P. K. 1990. “Soil Classification Using the Cone Penetration Testing.” *Canadian Geotechnical Journal* 27(1):151–58. doi: doi.org/10.1139/t90-014.

Robertson, P. K. 2009. “Interpretation of Cone Penetration Tests - a Unified Approach.” *Canadian Geotechnical Journal* 46:1337–55. doi: 10.1139/T09-065.

Robertson, P. K. 2010. “Evaluation of Flow Liquefaction and Liquefied Strength Using the Cone Penetration Test.” *Journal of Geotechnical and Geoenvironmental Engineering* 136(6):842–53. doi: 10.1061/(ASCE)GT.1943-5606.0000286.

Robertson, P. K., and R. G. Campanella. 1983. “Interpretation of Cone Penetration Tests. Part I: Sand.” *Canadian Geotechnical Journal* 20(4):718–33. doi: 10.1139/t83-078.

Robertson, P. K., R. G. Campanella, D. Gillespie, and J. Greig. 1986. “Use of Piezometer Cone Data.” Pp. 1–18 in *IN-SITU ’86 Use of in-situ testing in geotechnical engineering, ASCE specialty conference*, edited by S. P. Clemence. Syracuse, New York.

Robertson, P. K., D. J. Woeller, and W. D. L. Finn. 1992. “Seismic Cone Penetration Test for Evaluating Liquefaction Potential under Cyclic Loading.” *Canadian Geotechnical Journal* 29:686–95.

Robertson, P. K., and C. E. Wride. 1998. “Evaluating Cyclic Liquefaction Potential Using the Cone Penetration Test.” *Canadian Geotechnical Journal* 35(3):442–59. doi: https://doi.org/10.1139/t98-017.

Rollins, K. M., T. L. Youd, and M. Talbot. 2016. “Liquefaction Resistance of Gravelly Soil from Becker Penetrometer (BPT) and Chinese Dynamic Cone Penetrometer (DPT).” Pp. 645–50 in *5th International conference on geotechnical and geophisical site characterisation*. Queensland, Australia.

Schmertmann, John. 1978. “The Statics and Dynamics of the Standard Penetration Test.” Pp. 145–205 in *Proceedings of a symposium on site exploration in soft ground using in situ techniques*. Alexandria, Virginia, EEUU.

Schmertmann, John, and Alejandro Palacios. 1979. “Energy Dynamics of SPT.” *Journal of Geotechnical Engineerin Division* 105(8):909–26.

Schnaid, F., E. Odebrecht, and M. M. Rocha. 2007. “On the Mechanics of Dynamic Penetration Tests.” *Geomechanics and Geoengineering* 2(2):137–46. doi: 10.1080/17486020701383825.

Schreyer, H. L., and C. P. Ehiu. 1991. “The Effects on Penetrator Deceleration of Material Features Exhibited in Soils.” *International Journal of Solids and Structures* 27(10):1327–46.

Seed, B. 1983. “Earthquake-Resistant Design of Earth Dams.” Pp. 41–64 in *Seismic Design of Embankments and Caverns*. Pennsylvania: ASCE.

Seed, B., and I. Idriss. 1971. “Simplified Procedure for Evaluating Soil Liquefaction Potential.” *Journal of the Soil Mechanics and Foundations Division* 97(9):1249–73.

Seed, B., and L. Lee. 1966. “Liquefaction of Saturated Sands During Cyclic Loading.” *Journal of the Soil Mechanics and Foundations Division* 92(6):105–34.

Seed, Bolton. 1983. “EARTHQUAKE-RESISTANT DESIGN OF EARTH DAMS.” Pp. 41–64 in *Seismic Design of Embankments and Caverns*.

Seed, Bolton. 1986. *REPORT NO. UCB/EERC-86/02 DESIGN PROBLEMS IN SOil LiQUEFACTION*.

Seed, Bolton, and Pedro de Alba. 1986. “Use of SPT and CPT Tests for Evaluating the Liquefaction Resistance of Sands.” *Se of In Situ Tests in Geotechnical Engineering, Geotechnical Special Publication 6*, 281–302.

Seed, Bolton, and I. Idriss. 1967. “Analysis of Soil Liquefaction: Niigata Earthquake.” *Journal of the Soil Mechanics and Foundations Division* 93(3):83–108. doi: 10.1061/JSFEAQ.0000981.

Seed, Bolton, and I. M. Idriss. 1982. *Ground Motions and Soil Liquefaction During Earthquakes*. edited by Earthquake Engineering Research Institute. Berkeley, California, U.S.A.: Earthquake Engineering Research Institute.

Seed, H. 1979. "Soil Liquefaction and Cyclic Mobility Evaluation for Level Ground during Earthquakes." *Journal of the Geotechnical Engineering Division* 105(2):201–55.

Seed, H. Bolton, and I. M. Idriss. 1970. *A Simplified Procedure for Evaluating Soil Liquefaction Potential. Report No. EERC 70-9*. Berkeley, California, U.S.A.

Seed, H. Bolton, Kohji Tokimatsu, L. F. Harder, and Riley M. Chung. 1985. "Influence of SPT Procedures in Soil Liquefaction Resistance Evaluations." *Journal of Geotechnical Engineering* 111(12):1425–45. doi: 10.1061/(ASCE)0733-9410(1985)111:12(1425).

Serratrice, J. F. 2002. "Essais de Laboratoire Sur Le Sable de Fontainebleu."

Shibata, Toru, and Wanchai Teparaksa. 1988. "Evaluation of Liquefaction Potentials of Soils Using Cone Penetration Tests." *JSME International JJournal* 28(2):49–60. doi: https://doi.org/10.3208/sandf1972.28.2_49.

Sladen, J. A., R. D. D. Hollander, and J. Krahn. 1985. "The Liquefaction of Sands, a Collapse Surface Approach." *Canadian Geotechnical Journal* 22(4):564–78.

Smith, E. A. L. 1960. "Pile Driving Analysis by the Wave Equation." *J. Soil Mech. Found. ASCE* 86:35–61.

Stokoe, K. H., J. M. Roesset, J. G. Bierschwale, and M. Aouad. 1988. "Liquefaction Potential of Sands from Shear Wave Velocity." Pp. 213–18 in *Proceedings, 9nd World Conference on Earthquake Engineering*.

Suzuki, Y., K. Tokimatsu, K. Koyamada, Y. Taya, and Y. Kubota. 1995. "Field Correlation of Soil Liquefaction Based on CPT Data." Pp. 583–88 in *Proceedings of the International Symposium on Cone Penetration Testing, CPT '95,*.

Suzuki, Y., K. Tokimatsu, Y. Taya, and Y. Kubota. 1995. "International Conferences on Recent Advances in Geotechnical Earthquake Engineering and Soil Dynamics." Pp. 249–52 in *nternational Conferences on Recent Advances in Geotechnical Earthquake Engineering and Soil Dynamics*. Vol. 13.

Sy, A., and R. G. Campanella. 1991. "An Alternative Method of Measuring SPT Energy." Pp. 499–505 in *International Conferences on Recent Advances in Geotechnical Earthquake Engineering and Soil Dynamic*. St. Louis, Missouri.

Tatsuoka, Fumio, and Kenji Ishihara. 1974. "Drained Deformation of Sand Under Cyclic Stresses Reversing Direction." *Soils and Foundations* 14(3):51–65.

Thiet, Trung le. 2005. "Étude Du Processus de Vibrofonçage d ' Inclusions Cylindriques En Chambre d ' Étalonnage . Application Au Pieux." PhD. Thesis, Ecole des Ponts ParisTech.

Timoshenko, Stephen P., and J. N. Goodier. 1975. *Teoria de La Elasticidad*. Vol. 7. 2a Spanish. edited by URMO. New York, United States.

Timothy Stark, By D., and Scott M. Olson. 1995. "Liquefaction resistance using CPT and field case histories." *Journal of Geotechnical Engineering* 121(12):856–69.¿*

Tokimatsu, Kohji, Y. Oshiaki, and Y. Oshimi. 1983. “Empirical correlation of soil liquefaction based on SPT n-value and fines content.” *Soil and Foundation* 23(4):56–74.

Tokimatsu, Kohji, Shuji Tamura, and Shinichi Kuwayama. 1991. “Liquefaction Potential Evaluation Based on Rayleigh Wave Investigation and Its Comparison with Field Behavior Investigation.” Pp. 357–64 in *International Conferences on Recent Advances in Geotechnical Earthquake Engineering and Soil Dynamics.*

Toki, Shosuke, Fumio Tatsuoka, Seiichi Miura, Yoshiaki Yoshimi, Susumu Yasuda, and Yorio Makihara. 1986. “Cyclic Undrained Triaxial Strength of Sand by a Cooperative Test Program.” *Soils and Foundations* 26(3):117–28. doi: 10.3208/SANDF1972.26.3_117.

UCD. 2022. “Becker Drilling & Penetration Testing – Geotechnical Photo Album.” *University of California at Davis*. Retrieved May 22, 2022 (https://research.engineering.ucdavis.edu/gpa/site-characterization/becker-drilling-penetration-testing/).

USGS. 1989. “Lateral Spread Caused by Liquefaction | U.S. Geological Survey.” Retrieved May 17, 2022 (https://www.usgs.gov/media/images/lateral-spread-caused-liquefaction).

Villavicencio A, Gabriel. 2009. “Methodologie Pour Evaluer La Stabilite Des Barrages de Residus Miniers.” Phd. Thesis, Université Blaise Pascal Clermont II.

Villavicencio A, Gabriel, Pierre Breul, Claude Bacconnet, Andy Fourie, and Raul Espinace A. 2016. “Liquefaction Potential of Sand Tailings Dams Evaluated Using a Probabilistic Interpretation of Estimated In- Situ Relative Density.” *Revista De La Construccion* 15(2):9–18. doi: 10.4067/S0718-915X2016000200001.

Villavicencio, G., P. Breul, R. Espinace, and P. Valenzuela. 2012. “Control de Compactación Con Penetrómetro Ligero En Tranques de Relaves, Considerando Su Variabilidad Material y Estructural.” *Revista de La Construccion* 11(1):119–33. doi: 10.4067/S0718-915X2012000100011.

Youd, Leslie, Izzat M. Idriss, Ronald D. Andrus, Ignacio Arango, Gonzalo Castro, Ricardo Dobry, Liam Finn, Leslie F. Harder, Mary Ellen Hynes, Kenji Ishihara, Joseph P. Koester, Sam S. C. Liao, William F. Marcuson, Geoffrey R. Martin, James K. Mitchell, Yoshiharu Moriwaki, Maurice S. Power, Peter K. Robertson, Raymond B. Seed, and Kenneth H. Stokoe. 1997. “Summary Report.” Pp. 1–40 in *NCEER Workshop on Evaluation of Liquefaction Resistance of Soils*. Vol. Rept. NCEE. Salt Lake City, Utah.

Youd, T., and I. Idriss. 1997. “Proceedings of the NCEER Workshop on Evaluation of Liquefaction Resistance of Soils.” in *NCEER Workshop on Evaluation of Liquefaction Resistance of Soils*. Salt Lake City, Utah.

Youd, T., and I. Idriss. 2001. “Liquefaction Resistance of Soils: Summary Report from the 1996 NCEER and 1998 NCEER/NSF Workshops on Evaluation of Liquefaction Resistance of Soils.” *Journal of Geotechnical and Geoenvironmental Engineering* 127(4):297–313. doi: 10.1061/(ASCE)1090-0241(2001)127:4(297).

Zhou, Shuhua. 1997. “Caracterisation Des Sols de Surface a l’aide Du Penetrometre Dynamique Leger a Energie Variable Type ‘Panda.’” Clermont Ferrand.

Zhu, Zhehao, Feng Zhang, Qingyun Peng, Jean Claude Dupla, Jean Canou, Gwendal Cumunel, and Evelyne Foerster. 2021. “Assessment of the Loading Waveform on the Cyclic

Liquefaction Resistance with Hostun 31 Sand." *Soil Dynamics and Earthquake Engineering* 150. doi: 10.1016/j.soildyn.2021.106919.